Electromechanical control of ferroelectric domains in Pb(Zr,Ti)O3 and BiFeO3 thin films

Sergio Gonzalez Casal

N° d'ordre NNT : xxxx

THESE de DOCTORAT DE L'UNIVERSITE DE LYON
opérée au sein de
l'INSA de Lyon

Ecole Doctorale N° 160
Electronique, Electrotechnique et Automatique

Spécialité/ discipline de doctorat :

Electronique, micro et nanoélectronique, optique et laser

Soutenue publiquement le 28/01/2022, par :
Sergio GONZALEZ CASAL

Electromechanical control of ferroelectric domains in $Pb(Zr,Ti)O_3$ and $BiFeO_3$ thin films

Devant le jury composé de :

Mme	**LEMEE**	**Nathalie**	Maître de Conférences - HDR	*Université Picardie Jules Verne*	Rapporteur
Mme	**PARUCH**	**Patrycja**	Professeur des Universités	*Université de Genève*	Rapporteur
Mme	**MERCONE**	**Silvana**	Professeur des Universités	*Université de Tours*	Examinateur
M.	**BOROWIK**	**Łukasz**	Ingenieur-Chercheur, HDR	*CEA*	Examinateur
Mme	**MATZEN**	**Sylvia**	Maître de Conférences	*Université Paris Saclay*	Examinateur
M.	**DELERUYELLE**	**Damien**	Professeur des Universités	*INL, Lyon*	Examinateur
M.	**AGNUS**	**Guillaume**	Maître de Conférences, HDR	*Université Paris Saclay*	Invité
M.	**BUGNET**	**Matthieu**	Chargé de Recherche	*MATEIS, Lyon*	Invité
Mme	**CAÑERO INFANTE**	**Ingrid**	Chargé de Recherche	*INL, Lyon*	Co-directeur
M.	**GAUTIER**	**Brice**	Professeur des Universités	*INL, Lyon*	Directeur de thèse

Département FEDORA – INSA Lyon - Ecoles Doctorales

SIGLE	ECOLE DOCTORALE	NOM ET COORDONNEES DU RESPONSABLE
CHIMIE	**CHIMIE DE LYON** **https://www.edchimie-lyon.fr** Sec. : Renée EL MELHEM Bât. Blaise PASCAL, 3e étage secretariat@edchimie-lyon.fr	**M. Stéphane DANIELE** C2P2-CPE LYON-UMR 5265 Bâtiment F308, BP 2077 43 Boulevard du 11 novembre 1918 69616 Villeurbanne **directeur@edchimie-lyon.fr**
E.E.A.	**ÉLECTRONIQUE, ÉLECTROTECHNIQUE, AUTOMATIQUE** **https://edeea.universite-lyon.fr** Sec. : Stéphanie CAUVIN Bâtiment Direction INSA Lyon Tél : 04.72.43.71.70 secretariat.edeea@insa-lyon.fr	**M. Philippe DELACHARTRE** INSA LYON Laboratoire CREATIS Bâtiment Blaise Pascal, 7 avenue Jean Capelle 69621 Villeurbanne CEDEX Tél : 04.72.43.88.63 **philippe.delachartre@insa-lyon.fr**
E2M2	**ÉVOLUTION, ÉCOSYSTÈME, MICROBIOLOGIE, MODÉLISATION** **http://e2m2.universite-lyon.fr** Sec. : Sylvie ROBERJOT Bât. Atrium, UCB Lyon 1 Tél : 04.72.44.83.62 secretariat.e2m2@univ-lyon1.fr	**M. Philippe NORMAND** Université Claude Bernard Lyon 1 UMR 5557 Lab. d'Ecologie Microbienne Bâtiment Mendel 43, boulevard du 11 Novembre 1918 69 622 Villeurbanne CEDEX **philippe.normand@univ-lyon1.fr**
EDISS	**INTERDISCIPLINAIRE SCIENCES-SANTÉ** **http://ediss.universite-lyon.fr** Sec. : Sylvie ROBERJOT Bât. Atrium, UCB Lyon 1 Tél : 04.72.44.83.62 secretariat.ediss@univ-lyon1.fr	**Mme Sylvie RICARD-BLUM** Institut de Chimie et Biochimie Moléculaires et Supramoléculaires (ICBMS) - UMR 5246 CNRS - Université Lyon 1 Bâtiment Raulin - 2ème étage Nord 43 Boulevard du 11 novembre 1918 69622 Villeurbanne Cedex Tél : +33(0)4 72 44 82 32 **sylvie.ricard-blum@univ-lyon1.fr**
INFOMATHS	**INFORMATIQUE ET MATHÉMATIQUES** **http://edinfomaths.universite-lyon.fr** Sec. : Renée EL MELHEM Bât. Blaise PASCAL, 3e étage Tél : 04.72.43.80.46 infomaths@univ-lyon1.fr	**M. Hamamache KHEDDOUCI** Université Claude Bernard Lyon 1 Bât. Nautibus 43, Boulevard du 11 novembre 1918 69 622 Villeurbanne Cedex France Tél : 04.72.44.83.69 **hamamache.kheddouci@univ-lyon1.fr**
Matériaux	**MATÉRIAUX DE LYON** **http://ed34.universite-lyon.fr** Sec. : Yann DE ORDENANA Tél : 04.72.18.62.44 yann.de-ordenana@ec-lyon.fr	**M. Stéphane BENAYOUN** Ecole Centrale de Lyon Laboratoire LTDS 36 avenue Guy de Collongue 69134 Ecully CEDEX Tél : 04.72.18.64.37 **stephane.benayoun@ec-lyon.fr**
MEGA	**MÉCANIQUE, ÉNERGÉTIQUE, GÉNIE CIVIL, ACOUSTIQUE** **http://edmega.universite-lyon.fr** Sec. : Stéphanie CAUVIN Tél : 04.72.43.71.70 Bâtiment Direction INSA Lyon mega@insa-lyon.fr	**M. Jocelyn BONJOUR** INSA Lyon Laboratoire CETHIL Bâtiment Sadi-Carnot 9, rue de la Physique 69621 Villeurbanne CEDEX **jocelyn.bonjour@insa-lyon.fr**
ScSo	**ScSo*** **https://edsciencessociales.universite-lyon.fr** Sec. : Mélina FAVETON INSA : J.Y. TOUSSAINT Tél : 04.78.69.77.79 melina.faveton@univ-lyon2.fr	**M. Christian MONTES** Université Lumière Lyon 2 86 Rue Pasteur 69365 Lyon CEDEX 07 **christian.montes@univ-lyon2.fr**

*ScSo : Histoire, Géographie, Aménagement, Urbanisme, Archéologie, Science politique, Sociologie, Anthropologie

Résumé

Les matériaux ferroélectriques montrent une polarisation spontanée qui peut être basculée par l'application d'un champ électrique. Cette polarisation à l'échelle nanométrique est localisée dans des régions appelées domaines ferroélectriques. Récemment, il a été rapporté que les domaines peuvent être contrôlés par une stimulation mécanique. Ce travail est centré sur l'étude des domaines au moyen de la microscopie à force atomique (AFM) et des techniques dérivées comme la microscopie à force piézoélectrique (PFM), qui permet l'application simultanée des stimulations électriques et mécaniques. Dans ce contexte, deux matériaux ferroélectriques différents ont été considérés : $Pb(Zr,Ti)O_3$ (PZT) et $BiFeO_3$ (BFO).

PZT a permis l'étude de la distribution des domaines hors du plan et des paramètres qui affectent leurs basculements électrique et mécanique, comme l'influence de la méthode de synthèse sur les propriétés ferroélectriques d'un matériau de même composition, ainsi que de l'atmosphère de mesure (humidité) et de l'épaisseur de l'échantillon. Nos résultats montrent qu'il est possible de contrôler la force nécessaire pour faire basculer mécaniquement les domaines. En parallèle, BFO a permis l'étude de la polarisation dans le plan et sa manipulation avec la composante du champ électrique localisée dans le plan de l'échantillon. Nous avons mis en évidence par la spectroscopie à commutation PFM (SS-PFM) un phénomène de contamination de la pointe qui rend l'interprétation des mesures difficile.

Puisque l'AFM et la PFM sont des techniques de surface, ce travail a été complété par des analyses structurales des échantillons en utilisant des techniques comme la diffraction des rayons X (x-ray diffraction, XRD), la microscopie électronique en transmission à balayage (scanning transmission electron microscopy, STEM) et la spectrométrie de rétrodiffusion Rutherford (Rutherford backscattering spectrometry, RBS).

Abstract

Ferroelectric materials show a spontaneous polarization that can be switched by applying an electric field. This polarization at the nanoscale is ordered in regions called ferroelectric domains. Recently, it has been reported that domains can also be controlled by a mechanical stimulus. This work is focused on the study of domains with atomic force microscopy (AFM) and derived techniques such as piezoresponse force microscopy (PFM), which allows for the application of electrical and mechanical stimuli. In this context, two different ferroelectric materials belonging to the family of perovskites were considered: $Pb(Zr,Ti)O_3$ (PZT) and $BiFeO_3$ (BFO).

PZT allowed for the study of the distribution of out-of-plane domains and the parameters affecting electrical and mechanical switching, such as different synthesis methods, different atmospheres and different thicknesses. The results illustrated the successful tuning of the threshold force needed to mechanically switch ferroelectric domains. Meanwhile, BFO allowed for the study of an in-plane polarization and its manipulation by trailing fields. These results were affected by AFM tip contamination, which was observed by switching spectroscopy PFM.

Since AFM and PFM are surface techniques, this work was complemented by structural analysis of the sample using techniques such as x-ray diffraction (XRD), scanning transmission electron microscopy (STEM) or Rutherford backscattering spectrometry (RBS).

Résumé étendu

Les matériaux ferroélectriques montrent une polarisation spontanée qui peut être basculée par l'application d'un champ électrique. La direction et la valeur de cette polarisation dépend du matériau. Cependant, la polarisation est stable seulement en dessous d'une certaine température connue sous le nom de température de Curie, au-dessus de laquelle le matériau entre dans la phase paraélectrique, qui ne présente pas de polarisation spontanée.

En 1921 Valasek (Valasek, 1921) a été le premier a découvrir expérimentalement un matériau ferroélectrique, les sels de Rochelle. Néanmoins, l'existence des matériaux ferroélectriques a été prédite quelques années avant par Schrödinger (Schrödinger, 1912), qui a utilisé le mot "ferro" à cause de la similarité avec les matériaux ferromagnétiques.

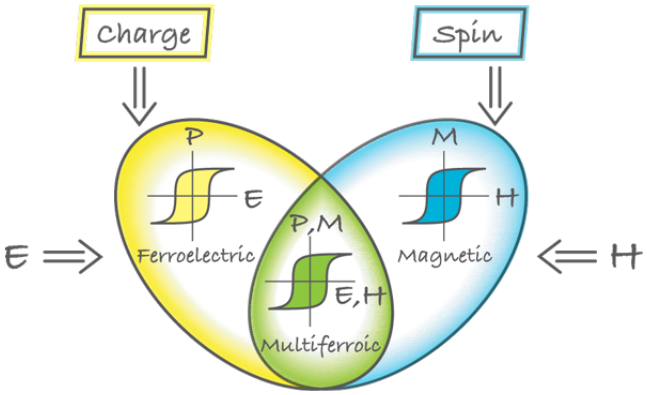

FIGURE 1 : Cycle d'hystérésis pour les matériaux ferroélectrique et ferromagnétique. (Khomskii, 2009)

Les matériaux ferroïques montrent un couplage entre un paramètre d'ordre et un stimulus. Les matériaux ferroïques peuvent être classifiés dans une ou plus de ces trois catégories : ferroélectrique (paramètre d'ordre : polarisation - stimulus : champ électrique), ferromagnétisme (paramètre d'ordre : aimantation - stimulus : champ magnétique) et ferroélastique (paramètre d'ordre : déformation - stimulus : contrainte). Quand un matériau peut être classifié dans plus d'une de ces catégories, il est appelé multiferroïque. Cependant, multiferroïque est communément utilisé

pour se référer aux propriétés électrique et magnétique. Tous les matériaux ferroïques sont caractérisés par un cycle d'hystérésis (Fig 1) qui relie le paramètre d'ordre et le stimulus.

À l'échelle nanométrique, la polarisation des matériaux ferroélectriques est ordonnée en régions de polarisation uniforme appeleés domaines, qui sont séparées par des parois de domaines. La taille des domaines peut être de quelques microns ou nanomètres en fonction du matériau et de son épaisseur. En plus, la polarisation des domaines peut être basculée par l'application d'un champ électrique. Par contre, la taille des parois des domaines est toujours de l'ordre du nanomètre. Les parois des domaines peuvent présenter des propriétés différentes du reste du matériau. Par exemple, sous certaines conditions, les parois des domaines peuvent être conductrices.

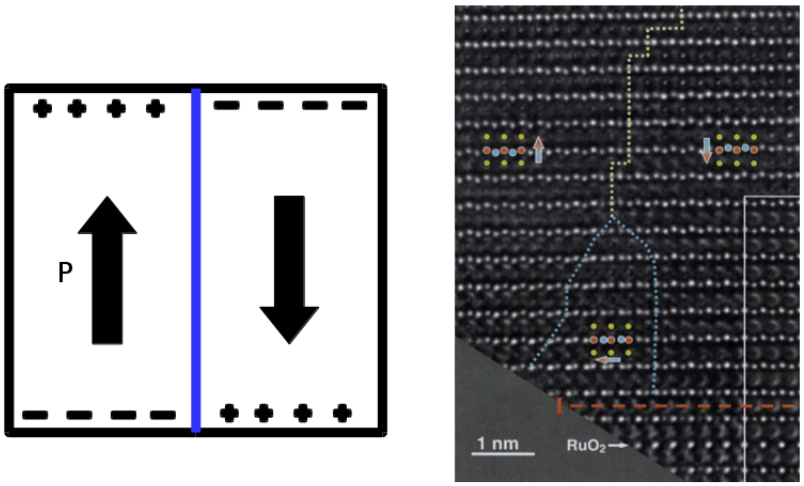

FIGURE 2 : À gauche, un schéma de deux domaines séparés par une paroi de domaine (bleu). À droite, image de microscopie électronique en transmission à haute résolution avec trois domaines et leurs parois de domaine (ligne à points) sur $PbZr_{0.2}Ti_{0.8}O_3$ (Jia et al., 2011).

Dans cette thèse, deux matériaux ferroélectriques seront étudiés le $PbZr_{0.2}Ti_{0.8}O_3$ (PZT) et $BiFeO_3$ (BFO).

PZT est une solution solide entre $PbTiO_3$ et $PbZrO_3$. À température ambiante et pour un contenu élevé de Ti, PZT a une structure tétragonale. Lorsque le pourcentage de Ti est entre 50 % et 40 %, le matériau est à la frontière entre la structure tétragonale et rhombohédrique. Dans ce travail, la composition 20% Zr/80% Ti est utilisée. Cette structure est tétragonale et a seulement deux directions de polarisation possibles.

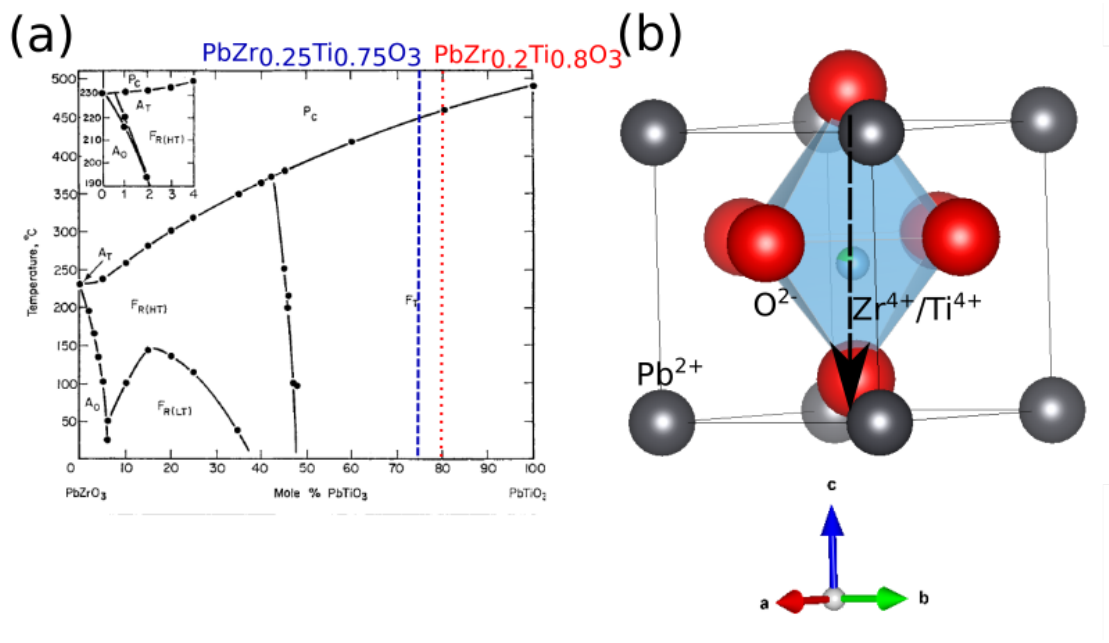

FIGURE 3 : (a) Differentes phases de PZT (Jaffe et al., 1971) et (b) structure tetragonale de $Pb[Zr_{0.2}Ti_{0.8}]O_3$

BFO est un matériau rhombohédrique, ferroélectrique et antiferromagnétique à température ambiante. Cependant, ce travail est centré sur ses propriétés ferroélectriques. Dans la littérature, on peut trouver trois angles possibles entre la polarisation des domaines ferroélectriques du BFO (70°, 109°and 180°) (Seidel et al., 2009). Cela signifie que BFO a toujours une composante de la polarisation dans le plan des films minces, ce qui va permettre l'étude du basculement latéral des domaines. De plus, BFO ne contient pas de plomb, ce qui est bénéfique du point de vue environnemental.

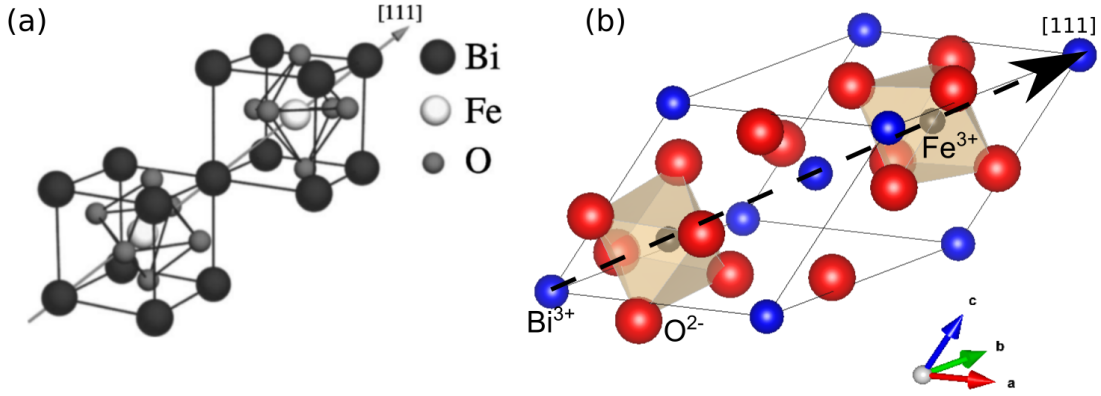

FIGURE 4 : (a) Structure pseudocubique (Ederer and Spaldin, 2005) et (b) structure rhombohédrique de $BiFeO_3$.

Pour étudier ces matériaux et la polarisation, un microscope à force atomique

(AFM) a été utilisé pour ce travail. L'AFM a été inventé en 1986 par Gerd Binnig et al (Binnig, 1986), après l'invention du microscope à effet tunnel (STM), qui était le premier microscope à sonde locale ((Binnig and Rohrer, 1983). En fait, AFM et STM sont basés sur le même concept : une petite sonde est placée très proche de la surface d'un matériau grâce à un actionneur piézoélectrique. La différence est que le STM fait une mesure de courant tandis que l'AFM fait une mesure de la force appliquée.

Plus spécifiquement, l'AFM possède trois composants : la sonde, qui consiste en un levier avec une pointe de taille nanométrique, un laser qui va se réfléchir sur le levier et être détecté par une photodiode et un actionneur piézoélectrique, qui va contrôler la position relative de la sonde et l'échantillon. Même si le principe est simple, il est important de noter que l'AFM ne serait pas possible sans les matériaux piézoélectriques qui permettent un contrôle précis pour balayer la surface jusqu'à l'échelle nanométrique.

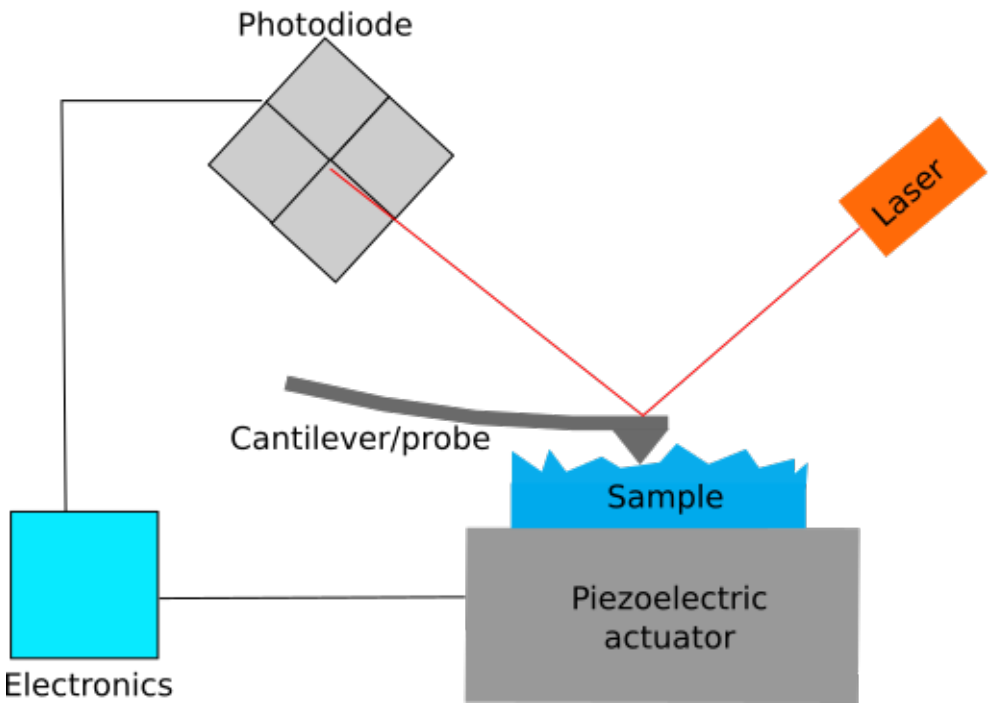

FIGURE 5 : Schéma d'un AFM avec ses composants principaux.

Pour imager les domaines ferroélectriques, il est possible de profiter du fait que les matériaux ferroélectriques sont aussi piézoélectriques. Cela veut dire qu'une contrainte produit une polarisation. De la même façon, un champ électrique produit une déformation, ce qui s'appelle l'effet piézoélectrique inverse. Cet effet est la base du microscope à force piézoélectrique (PFM), une technique dérivée de l'AFM inventée en 1992 par Güthner et Dransfeld (Güthner and Dransfeld, 1992).

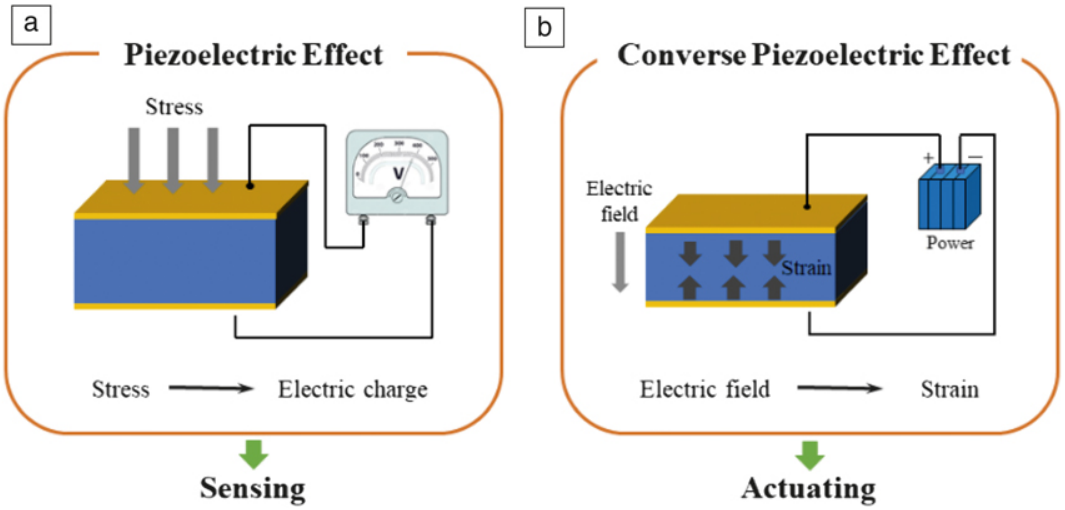

FIGURE 6 : Schéma de l'effet piézoélectrique (a) direct et (b) inverse (Rödel and Li, 2018).

Le PFM utilise une pointe conductrice pour appliquer un champ électrique alternatif. Si le matériau est piézoélectrique, il se déforme. Cette déformation peut être mesurée comme une vibration par la photodiode. Selon la direction de la déformation détectée, il est possible de mesurer la composante dans le plan et hors du plan. Dans ce cas, nous parlerons de PFM verticale ou latérale. Pour différencier entre ces deux modes, il est possible de choisir les fréquences de résonance correspondant aux mouvements latéraux et verticaux de la pointe.

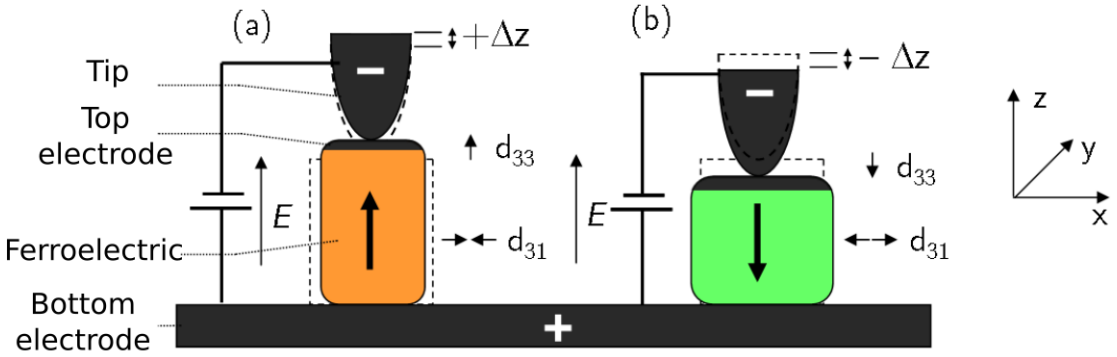

FIGURE 7 : Schéma pour le PFM vertical . (a) élongation d'un matériau ferroélectrique quand la polarisation est dans la même direction du champ électrique et (b) contraction quand la polarisation est opposée au champ électrique. (Brugère, 2011)

Le signal détecté est traité par un amplificateur lock-in pour éviter le cross-talk avec la topographie et les artefacts. De ce traitement il est possible d'obtenir l'amplitude de l'oscillation et la phase avec le champ électrique appliqué. L'amplitude permet de voir les parois de domaines, tandis que la phase permet de différencier

les domaines. De cette façon, il est possible d'observer les deux : les domaines et les parois, comme le montre les images sur la Fig. 8

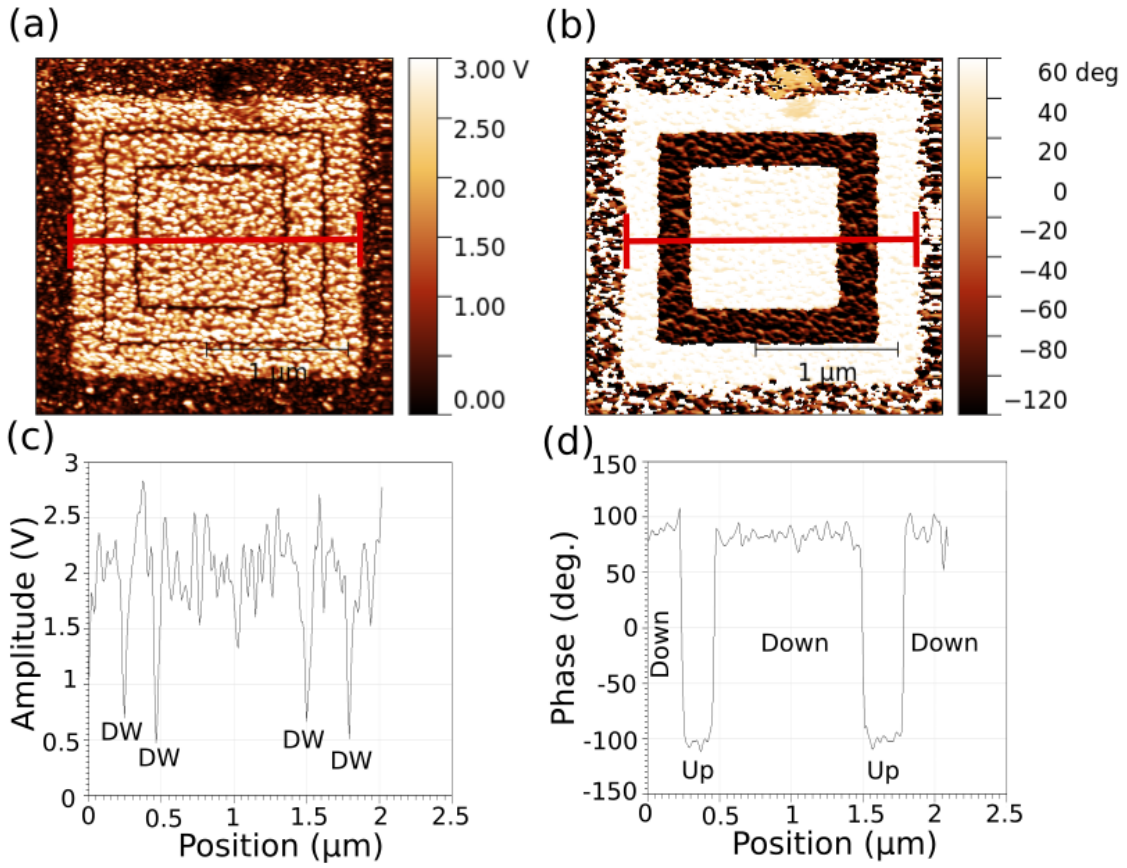

FIGURE 8 : Image (a) d'amplitude et (b) de phase d'un échantillon de 33 nm d'épaisseur de PZT, avec un motif qui a été fait avec un champ électrique. La ligne rouge montre où les données ont été obtenues pour (c) l'amplitude où le minimum représente les parois de domaines (DW) et (d) la phase où les domaines up et down peuvent être observés.

La PFM est capable de faire des études de spectroscopie. Ce mode s'appelle spectroscopie à commutation PFM (SS-PFM) et permet d'appliquer un champ électrique tandis que la mesure PFM se produit. De cette façon, des cycles d'hystérésis sont obtenus pour la phase et l'amplitude PFM. Ces cycles donnent une information sur l'état ferroélectrique de l'échantillon, comme par exemple la tension coercitive, et ils permettent aussi d'observer des artefacts provenant par exemple d'effets électrostatiques.

Cette thèse presente le travail effectué sur des échantillons de PZT et BFO étudiés par PFM et AFM, qui ne permettent pas seulement d'observer les domaines, mais aussi de les manipuler électriquement et mécaniquement. Pour ces études une série d'échantillons de PZT a été fabriqué par deux méthodes différentes : le pro-

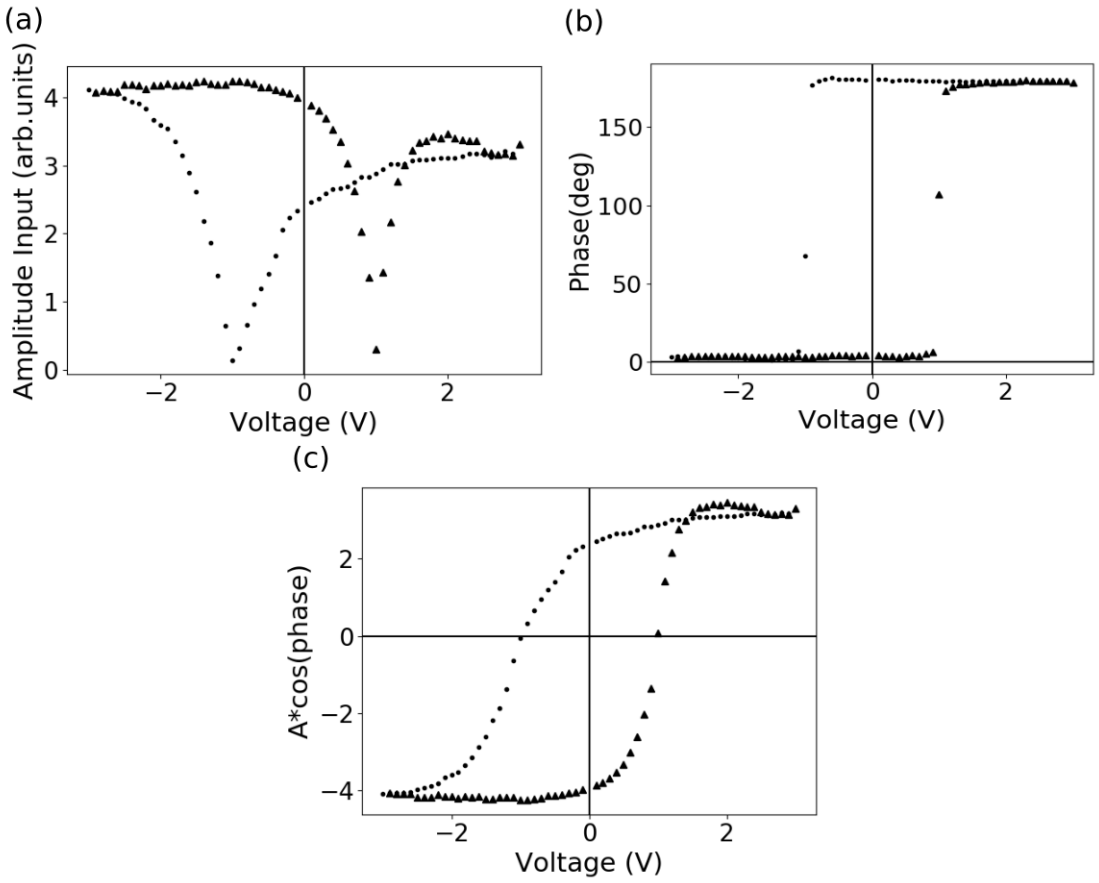

FIGURE 9 : Cycles de SS-PFM sur PZT. (a) Amplitude, (b) phase et (c) signal X. La tension coercitive peut être observée comme les points avec le minimum de signal pour (a) et les points où la phase change pour (b).

cédé solution-gélification (sol-gel) et l'ablation laser pulsé (PLD). La première est un méthode chimique tandis que la deuxième est un méthode physique. Il est communément admis que les films minces fabriqués par voie sol-gel présentent plus de défauts que les films fabriqués par PLD. Finalement, l'échantillon de BFO a été élaboré par PLD.

Les études électriques opérées sur les films de PZT montrent un comportement en accord avec la ferroélectricité. On peut observer au moins deux états de polarisation possibles sans champ électrique appliqué pour tous les films. De plus, les régions dont la polarisation a été changée conservent la nouvelle polarisation pendant plusieurs jours comme le montre la Fig. 10, la seule exception étant les films PZT fabriqués par PLD où la polarisation peut se retourner plus rapidement (quelques heures) et retourner à sa valeur initiale. Ce comportement des films de PZT par PLD peut être lié au fait qu'ils sont plus minces, et par conséquent la polarisation est moins stable.

Ce travail a aussi permis d'étudier les différents paramètres qui affectent les domaines. Dans ce sens, il peut être observé que pour les films plus minces il y a

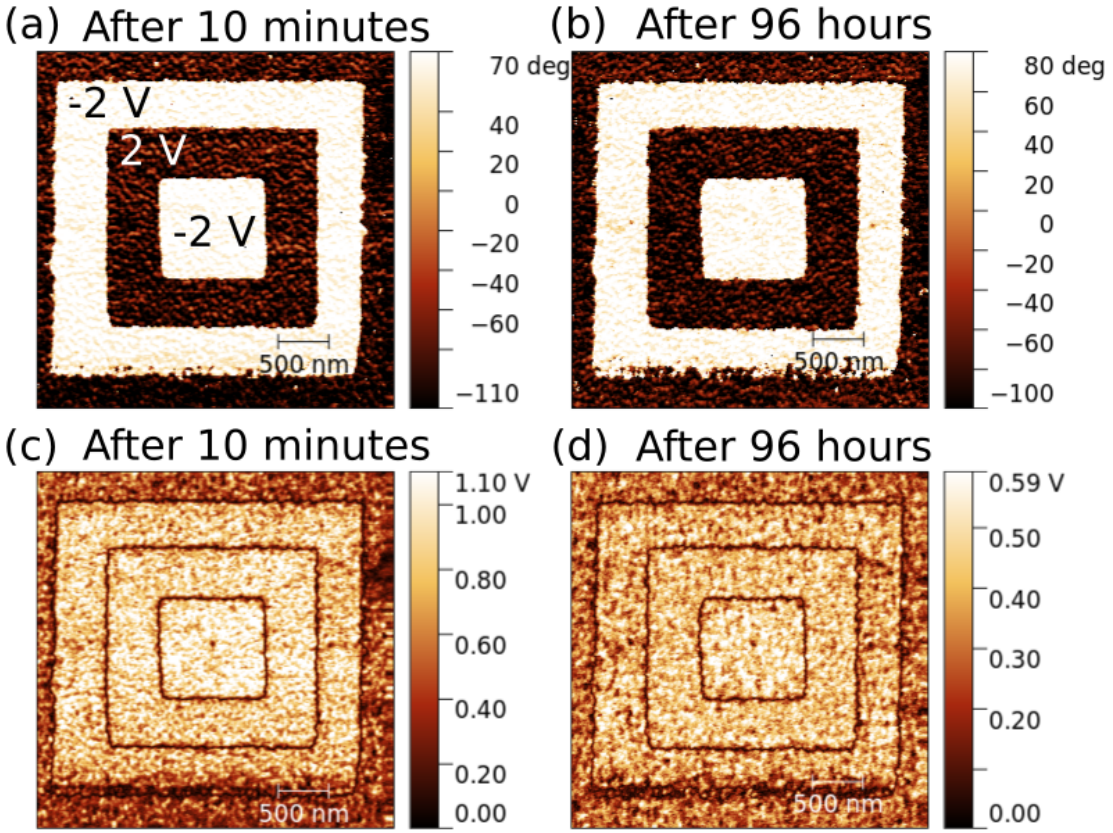

FIGURE 10 : (a) et (c) images de l'amplitude et phase verticale pour un motif créé avec 2 V et -2 V après 10 minutes. (b) et (d) images de l'amplitude et phase vertical pour le même motif après 96 heures.

toujours une polarisation majoritaire (up). Plus les films sont épais, plus la distribution est égalitaire entre polarisation up (vers la surface) et down (vers le substrat). En même temps, cette thèse montre que l'atmosphère affecte le basculement électrique de la polarisation. En effet, dans une atmosphère avec plus d'humidité, les domaines créés par un champ électrique sont plus grands que dans une atmosphère avec peu d'humidité. Finalement, des artefacts comme des protubérances qui apparaissent après un stress électrique ont été observés pour les échantillons PLD de PZT.

Le film de BFO était le seul à présenter une polarisation dans le plan. Il a permis l'étude de la manipulation latérale de la polarisation par la composante du champ électrique localisée dans le plan de l'échantillon ("trailing field" (Crassous et al., 2015)). En fait, appliquer un champ électrique tandis que la pointe se déplace permet la création des domaines dans le plan par basculement de la polarisation. En fonction de la direction du déplacement, il est observé que les directions des polarisation créées sont différentes. Un exemple peut être observé sur la Fig. 11. Dans cette figure, deux expériences sont présentées où des domaines sont crées avec

le même champ électrique mais différentes directions. Il ressort de cette étude que la direction de l'axe lent de l'AFM change les domaines écrits sur l'échantillon.

Finalement, la manipulation mécanique des domaines ferroélectriques a été étudiée. Depuis une dizaine d'années plusieurs études sur le basculement de la polarisation par application d'une pression avec une pointe AFM ont été reportées (Lu et al., 2012a). Cet effet est lié à la flexoélectricité pour films de moins de 30 nm. Cependant, d'autres mécanismes peuvent en être responsables pour des films plus épais. Parmi ces mécanismes il faut noter la piezoélectricité, les effets de surface (l'écrantage), les effets électrochimiques et la ferroélasticité (Cao et al., 2017).

Le basculement mécanique de la polarisation a été possible pour des échantillons d'épaisseur jusqu'à 200 nm avec une pointe non conductrice, ce qui n'est pas commun. Cependant avec une pointe conductrice moins dure, le basculement était observé jusqu'à 66 nm. De plus, il était possible de déterminer la force nécessaire pour faire basculer 75 % des domaines, ce point sert de référence pour montrer comment cette force augmente avec l'épaisseur.

La force nécessaire pour le basculement mécanique peut être modifiée par différentes méthodes. A part l'épaisseur, le nombre de défauts joue un rôle essentiel pour ce basculement. Les résultat obtenus dans cette thèse montrent que les films avec plus de défauts sont plus faciles à basculer. De plus, dans les films les plus minces, l'application d'un champ électrique avant le basculement mécanique peut augmenter la force nécessaire comme le montre la Fig. 13. Par conséquent, il est possible de combiner le champ électrique avec la force appliquée pour contrôler les domaines.

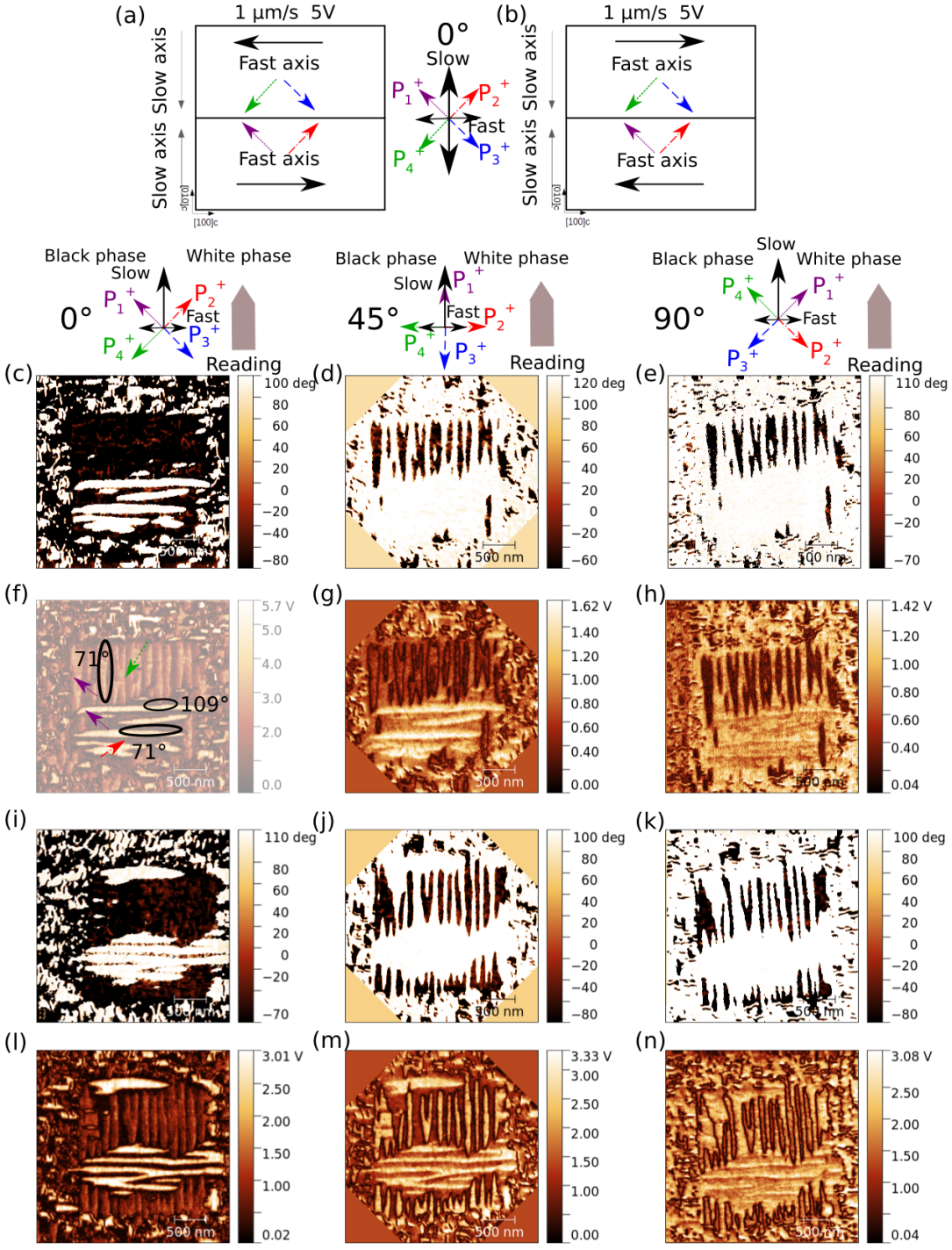

FIGURE 11 : (a)Schéma pour l'expérience 1 et (b) schéma pour l'expérience 2 sur BFO à 0°. Image de phase latérale pour l'expérience 1 à (c) 0°, (d) 45° et (e) 90°, et les images respectives d'amplitude (f),(g) and (h). Image de phase latérale pur l'expérience 2 à (i) 0°, (j) 45° and (k) 90°, et les images respectives d'amplitude (l),(m) and (n). L'image (f) montre les differentes directions de polarisation obtenues pour les expériences.

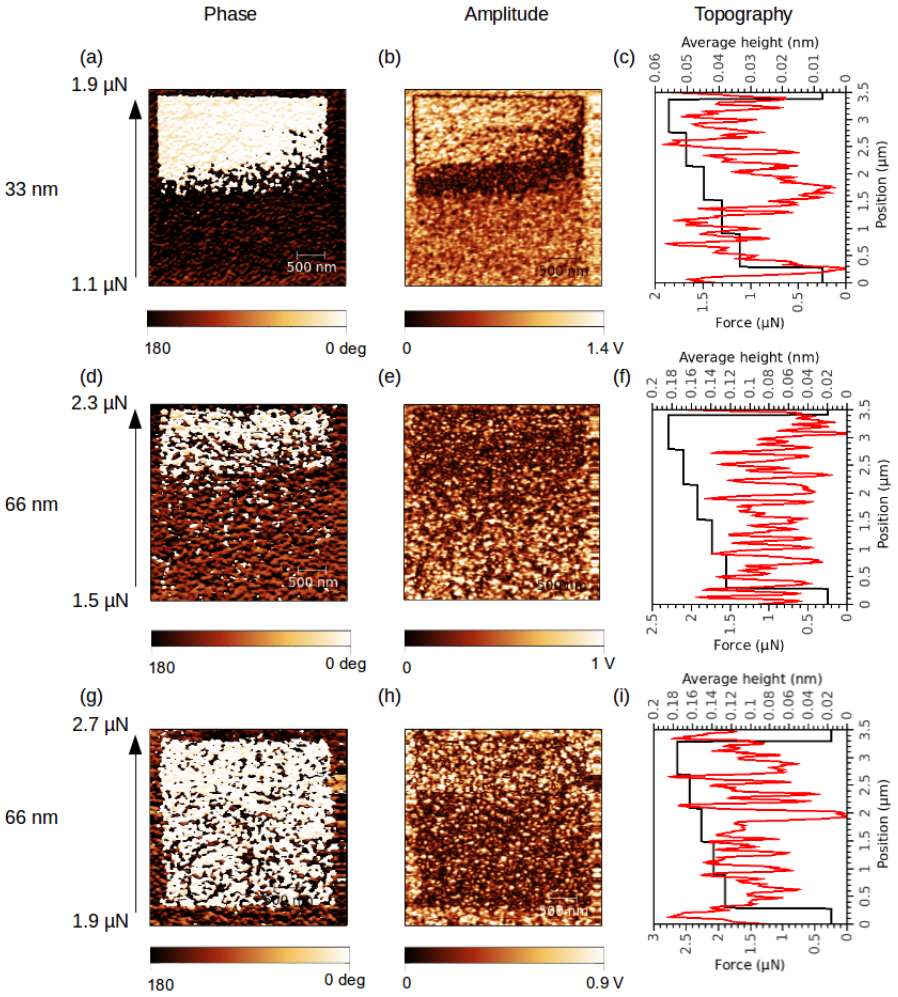

FIGURE 12 : Basculement de la polarisation des domaines ferroélectriques par application d'une force. (a), (d) et (g) images de phase (b), (e) et (h) image d'amplitude et (c), (f) et (i) L'évolution spatiale de la force appliquée (ligne noire) est montrée avec la topographie (ligne rouge), en fonction de la position de la pointe. La taille des images est 3,5 μm.

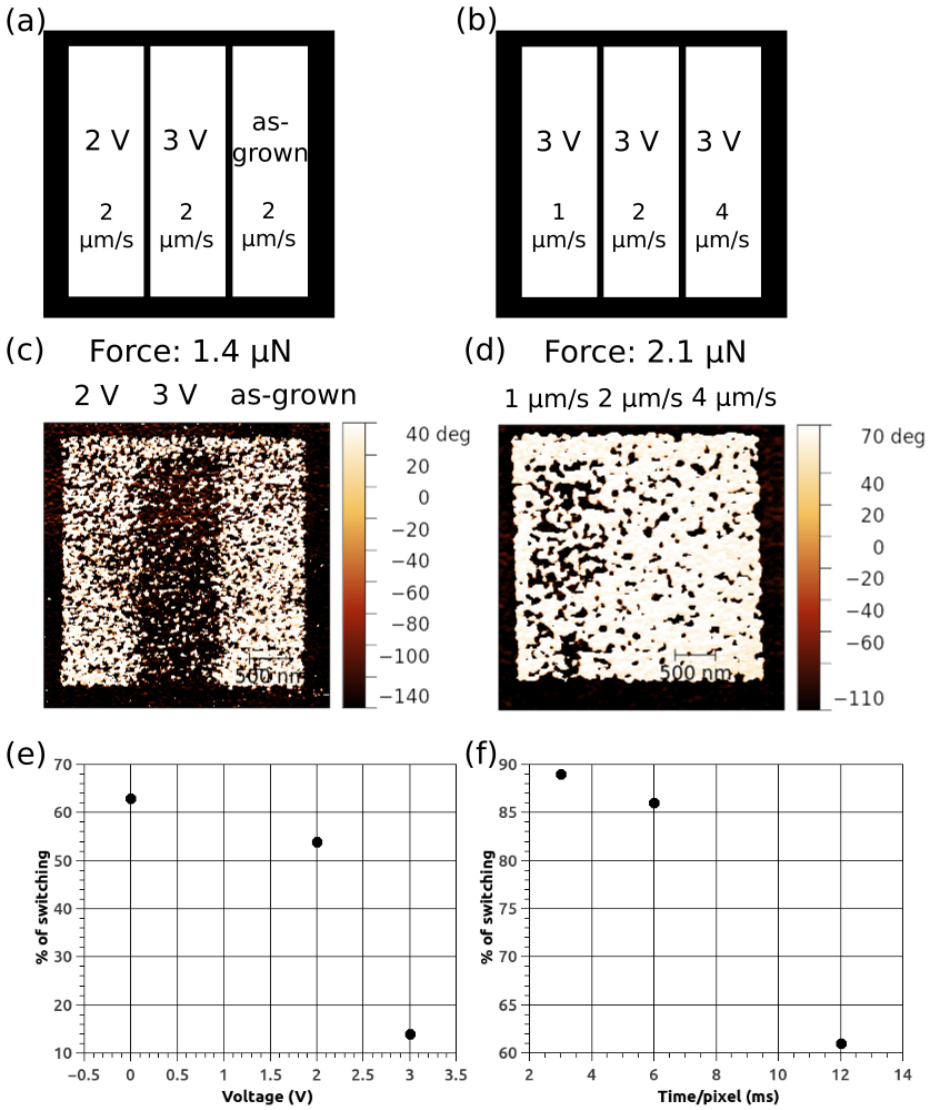

FIGURE 13 : Schémas pour (a) la première expérience et (b) la deuxième expérience sur un échantillon de 33 nm de PZT. Images de phase PFM obtenues après (c) la première et (d) la deuxième expérience. Graphique du pourcentage de basculement contre (e) la tension appliquée préalablement et (d) la vitesse avec laquelle la tension est appliquée.

Contents

Acknowledgements

This work would have not been possible without the supervision of Brice Gautier, Ingrid Cañero Infante and Matthieu Bugnet. Their guidance was key to develop this work, they taught me how to be a scientist and for that I will be forever thankful.

I am deeply grateful to Patrycja Paruch and Nathalie Lemée for accepting being referees of this work.

I would like to thank David Albertini for teaching my how to do PFM and for valuable discussions that help in the interpretation of my results. I do not want to forget to thank Xiaofei Bai who made most of my sol-gel sample and contributed to this work in a direct way. At the same time, I wish to thank the staff of INL, specifically some people that helped in this work in a way or another: Nicolas Baboux, Bruno Canut, Solene Brottet, Bertrand Vilquin, Pedro Rojo-Romeo and Benjamin Fornacciari.

I would also like to remark the support of Prabir Mahato and Alexander Singaevsky, PhDs of INL. They were there during my PhD to share the good things but also the suffering of a PhD life.

At a more personal level, I have to thank my small "family" in Lyon composed of Selma, Barbara, Hussein and Corentin. They made my stay in Lyon something pleasant and made it feel like a home.

Finally, I thank my family in Barcelona who has always been my support in life. Thank you dad, mum, Fran, Puri and my lovely nephews.

In conclusion, thanks to everyone who helped me. This work would have not been possible without you.

Introduction

Ferroelectric materials have attracted much attention for their potential applications in electronic devices (Scott and Paz De Araujo, 1989) due to their capability to switch between two or more possible polarization states by applying an electric field. Since their discovery in 1921 by Valasek (Valasek, 1921), ferroelectric materials have been envisaged in numerous applications as they are at the same time dielectric, piezoelectric and pyroelectric. Besides the applications on nanoelectronics such as memories (Sharma et al., 2017; Scott et al., 1988), diodes (Whyte and Gregg, 2015) or tunnel junctions (Sanchez-Santolino et al., 2017), their piezoelectric and pyroelectric properties can be used for applications such as acoustic transducers (Tressler, 2008) or energy harvesters (Thakre et al., 2019; Covaci and Gontean, 2020).

The polarization of ferroelectric materials at the nanoscale is distributed in regions called domains with different polarizations. The domains can be observed using different tools such as scanning probe, electron or optical microscopes (Waser et al., 2005). This work was carried out using an atomic force microscope (AFM) (Binnig, 1986) and its derived mode piezoresponde force microscope (PFM) (Soergel, 2011), which allows for the observation of ferroelectric domains. Furthermore, the polarization of domains can be switched by applying an electric field with an AFM tip, thus allowing the manipulation of domains.

Recently, it was shown that the polarization can be switched by applying a force with an AFM tip (Lu et al., 2012a). Although the mechanisms responsible for the switching are still being discussed, it is thought that for ultra-thin films (less than 30 nm) the main mechanisms are flexoelectricity and surface electrochemistry. For thicker films, other mechanisms such as ferroelasticity, Vegard strain or piezoelectricity (Cao et al., 2017) are expected to be at the origin of the switching. Indeed, mechanical switching has mostly been evidenced in films of less than 100 nm. All these discoveries can open the door to a new generation of force sensors or electromechanical devices (Lu et al., 2012b) based on the mechanical switching of ferroelectric domains.

In this work, thin films of $Pb[Zr_xTi_{1-x}]O_3$ (x=0.2, x=0.25) (PZT), which is a well known tetragonal ferroelectric material (Cattan et al., 1999; Polla and Francis, 1998; Xu et al., 2001) where mechanical switching has been observed for x=0.2 (Guo et al., 2014), will be studied under electrical and mechanical stimuli to control the ferroelectric polarization at the nanoscale.

In a similar manner, thin films of $BiFeO_3$, an extensively studied ferroelectric material that can be grown with stable polarization depicting in-plane and out-of-plane polarization components, will be studied to explore in-plane polarization switching, which can be obtained by trailing fields (Crassous et al., 2015). In this material mechanical switching has also been observed (Park et al., 2018).

This work aims at understanding how to control electrically and mechanically ferroelectric domains in PZT and BFO with AFM and other complementary techniques. The influence of parameters such as the thickness of the sample, the relative humidity, the defects in the sample or the previous application of electrical and mechanical stimuli on the electrical and mechanical switching will be studied. Furthermore, for the mechanical switching the force needed to switch will be quantified by defining a threshold force for each of the samples studied, which will allow to compare the switching between different samples. Thus, this work is focused on investigating whether mechanical switching can be tuned and if the electromechanical control of domains is possible with an AFM.

This work is structured as a first chapter dedicated to explain basic concepts of ferroelectricity, followed by a second chapter focused on the growth and structural characterization of the ferroelectric thin films used for this work. The third chapter is dedicated to AFM-related techniques. The results obtained in this experimental work are presented in the fourth and fifth chapters, which are dedicated to the studies of electrical and mechanical switching respectively.

Chapter 1

Ferroelectric materials

1.1 Dielectric polarization

This section will be dedicated to dielectric polarization, a key concept to understand ferroelectric materials.

1.1.1 Definition

Dielectric polarization exists anytime fixed charges of opposed sign and equal absolute value are separated by a distance d. Therefore, dielectric polarization is a phenomenon related with the separation of charge in a dielectric material. The electric dipole moment between two charges q and -q is defined as:

$$\vec{p} = q\vec{d} \tag{1.1}$$

where $\vec{p}$ is the dipole moment vector and $\vec{d}$ is the vector distance from the negative to the positive charge.

At the atomic scale a dipole moment appearing because of a local electric field ($\vec{E}_{loc}$) can be written in terms of the atomic polarizability α :

$$\vec{p} = \alpha\vec{E}_{loc} \tag{1.2}$$

Dielectric polarization arises from dipole moment. Indeed, polarization is the sum of the dipole moments per unit of volume. This sum can be expressed with the concept of polarization vector $\vec{P}$:

$$\vec{P} = \frac{d\vec{p}}{dV} \tag{1.3}$$

In most materials, $\vec{P}$ is null at a null electric field. In this situation, a dielectric has all dipoles randomly oriented, which means that $\vec{P}$ is null. When an electric

field $\vec{E}$ is applied, the polarization vector of a dielectric material is proportional to the electric field due to dipoles aligning with it. However, since not all dielectric materials polarize the same way, there must be a factor corresponding to the properties of the material. This factor is called electric susceptibility χ. Therefore, it is possible to write the polarization vector as:

$$\vec{P} = \varepsilon_0 \chi \vec{E} \tag{1.4}$$

where ε_0 is the vacuum permittivity and χ is the dielectric susceptibility. ε_0 and χ are related to the atomic polarizability and can be seen as their macroscopic counterparts. Furthermore, χ can be defined as:

$$\chi = \epsilon_r - 1 \tag{1.5}$$

Where ϵ_r is the relative permittivity of the material.

1.1.2 Polarization mechanisms

Dielectric materials can be polarized under the influence of an electric field, following four polarization mechanisms (Fig. 1.1) :

1. Electronic polarization: When an atom is under the influence of an electric field, its electron cloud is slightly displaced to the opposite direction of the field, while its nucleus is slightly displaced in the opposite direction. In this state, a dipole moment will appear in the atom. This mechanism is present in all dielectric materials for small and linear electric fields.

2. Ionic polarization: It is present inside ionic crystals, where atoms are held together by the electrostatic interaction. Therefore, there are positively and negatively charged ions that will be slightly displaced in opposite directions by an electric field. In this way a dipole moment is created.

3. Orientation polarization: This type of polarization is only present in materials that contain polar molecules, which means that molecules already have a dipole moment. However in the absence of an electric field, the orientation of the molecules is random and the total polarization vector is null. When an electric field is applied, all dipole moments align with it, which changes the total polarization vector.

4. Interfacial polarization or space charge: This type of polarization mechanism appears when there is an interface between two materials of different conductivity or inside the material. For example a dielectric between two electrodes. This mechanisms is related with free charge (Kao, 2004).

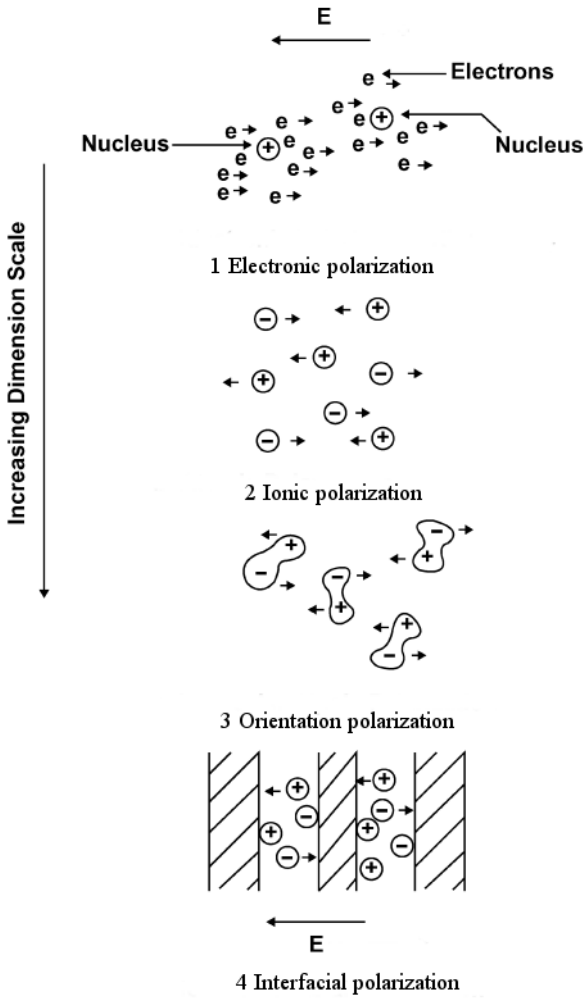

Figure 1.1: Different mechanisms of polarization (Dakin, 2006)

The total polarization inside a material must be the sum of all 4 mechanisms, therefore:

$$\vec{P} = \vec{P}_{electronic} + \vec{P}_{ionic} + \vec{P}_{orientation} + \vec{P}_{interfacial} \tag{1.6}$$

1.1.3 Charge and electric displacement field

The appearance of polarization in a dielectric material can also be represented as a volume charge associated with a surface charge appearing on the material. However, the total charge of the material will be 0 since polarization is a phenomenon related with the reorganization of charges rather than the creation of free charge because polarization charge is a bound charge. This surface charge σ and volume charge ρ can be expressed mathematically by the relation:

$$\sigma = \vec{P} \cdot \vec{n} \tag{1.7}$$

$$\rho = -\vec{\nabla} \cdot \vec{P} \tag{1.8}$$

where $\vec{n}$ is the vector normal to the surface.

The electric displacement field $\vec{D}$ is a representation of the electric field taking into account the polarization of the material. Mathematically it is written as:

$$\vec{D} = \varepsilon_0 \vec{E} + \vec{P} \tag{1.9}$$

but since dielectric materials have the relation shown in Eq. 1.4 and χ can be expressed as function of the relative permittivity ϵ_r as seen in Eq. 1.5. The electric displacement field can be written for dielectrics under small electric fields as:

$$\vec{D} = \varepsilon_0 \varepsilon_r \vec{E} \tag{1.10}$$

1.2 Ferroelectricity

1.2.1 Definition

The property by which a material shows a spontaneous electric polarization that can be switched by applying an external electric field is known as ferroelectricity. This polarization will remain even after the external electric field is removed and can have different orientations and magnitudes. However, ferrolectricity is only stable under a certain temperature known as Curie Temperature, over which the material is in a paraelectric phase with no spontaneous polarization.

Since ferroelectric materials are polarized, it is expected that they have a surface charge. This charge creates an electric field called the depolarizing field (Fig. 1.2). To compensate this depolarizing field, a ferroelectric material requires an electrode or a source of electric field Fig. 1.2. The effect of the depolarizing field will be commented more extensively in Section 1.3.2.

From the mathematical point of view, the description of ferroelectric polarization is more complex than in the case of dielectric materials. In a first approximation, the polarization can be described as the composition of a linear part proportional to the electric field and a non linear part with a dependence with the temperature. In that way, ferroelectric polarization can be written as:

$$\vec{P} = \vec{P}_s + \epsilon_0(\epsilon_r - 1)\vec{E} \tag{1.11}$$

Where $\vec{P}$ is the polarization and $\vec{P}_s$ the spontaneous polarization. However, as seen in Fig. 1.3 this model does not reproduce accurately the real behavior of ferroelectric materials. The spontaneous polarization, also known as remnant

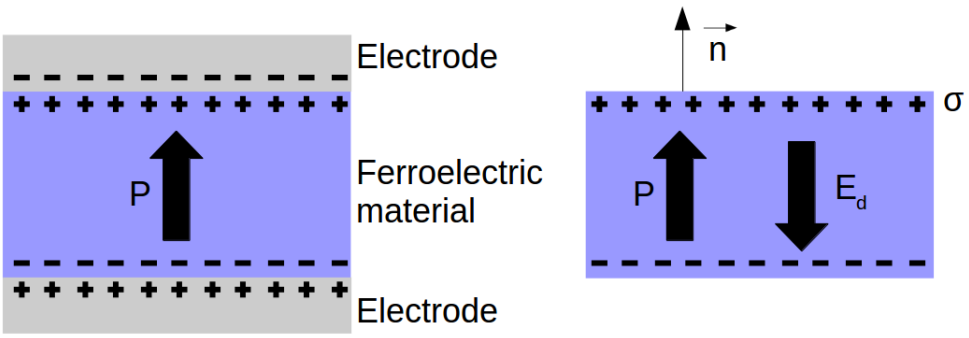

Figure 1.2: On the left a polarized material with electrodes, depolarization field is compensated by charges from the electrodes so that the electric field is null in the material in the absence of external applied field. On the right, a polarized material with no electrodes and a depolarizing field is not compensated.

polarization, corresponds to the polarization at null electric field. In a similar way, the coercive field E_c is the electric field where null polarization is achieved. Other more accurate models exist (Skaliukh, 2018) such as the Preisach model (Preisach, 1935) or modern variations of it (Sutor et al., 2010; Bartic et al., 2001), but they are more complex and out of the scope of this work. Nevertheless, it is important to know that concepts available for dielectric materials can also be applied to ferroelectrics, just with a nonlinear mathematical description.

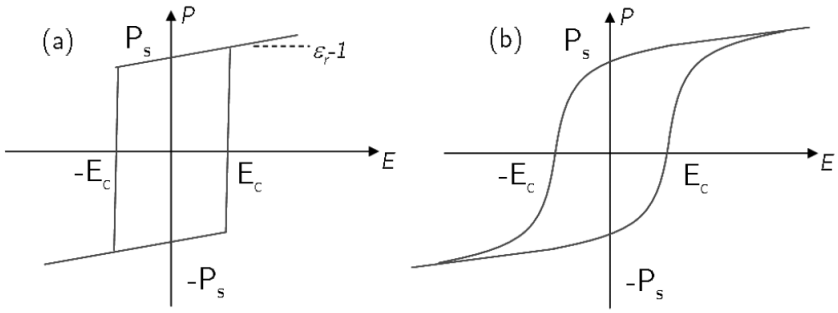

Figure 1.3: (a) Polarization in ferroelectric materials with a simplified model (b) Real behavior of polarization in a ferroelectric material.

The first experimentally discovered ferroelectric material was the Rochelle's salt, which was found by Valasek in 1921 (Valasek, 1921). Nonetheless, the existence of ferroelectric materials had already been theorized by Schrödinger (Schrödinger, 1912), who used the term "ferro" due to the similarities with ferromagnetic materials.

The field of ferroic materials is of remarkable importance, in which a coupling between an order parameter and a stimulus can be evidenced. Ferroic materials can be

classified in one or more than one of the three categories: ferroelectricity (parameter: polarization-stimulus: electric field), ferromagnetism (parameter: magnetization-stimulus: magnetic field) and ferroelasticity (parameter: strain-stimulus: stress). When one material can be classified in more than one of these categories, it is called multiferroic. However, most of the time, multiferroic refers to electric and magnetic properties, since they are the ones of interest for electronics. All ferroic materials are characterized by an hysteresis loop (Fig. 1.4) that describes the relationship between the order parameter and stimulus.

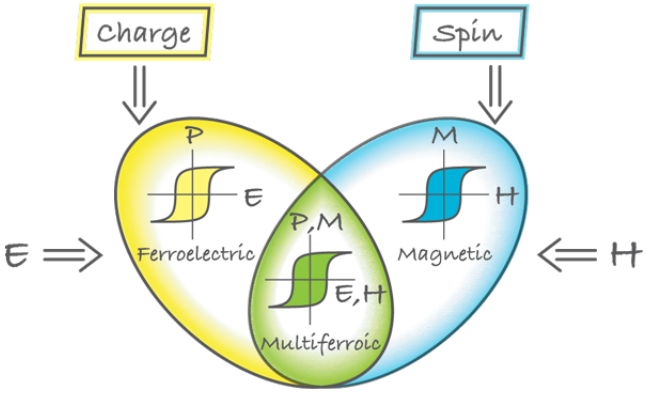

Figure 1.4: Ferroelectric/ferromagnetic multiferroic materials (Khomskii, 2009).

Ferroelectricity, as long as we consider only bound charge, is only present in crystalline materials either monocrystalline or polycrystalline and it has not been observed in amorphous compounds. Crystalline structures displaying ferroelectricity are the focus of the next subsection.

1.2.2 Crystalline origin of ferroelectricity

There are 32 point groups in crystallography, however any centrosymmetric group cannot be ferroelectric. This leaves 21 groups that are not centrosymmetric, however not all of them are ferroelectric. 20 groups are piezoelectric, which means that a polarization will appear whenever a mechanical stress is applied and among them 10 point groups are ferroelectric. Therefore any ferroelectric material is piezolectric (Fig. 1.5). Furthermore, any ferroelectric material is pyroelectric, in other words, the polarization changes with temperature.

This thesis focuses on a specific crystal structure that can give rise to ferroelectricity, the perovskite structure. Perovskites are formed by three different atoms in a ABO_3 chemical formula, where A and B are metallic cations and O is the oxygen anion. In the paraelectric phase, the A atom is positioned at the corner of the cubic cell while the B atom is at the center surrounded by an octahedron of oxygen atoms.

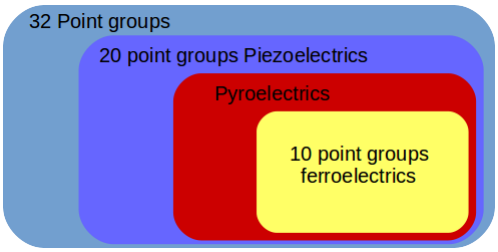

Figure 1.5: All ferroelectric materials are piezo and pyroelectrics.

However, in the ferroelectric phase, the relative position of atoms is displaced in a way that creates a polarization in the unit cell as shown in Fig. 1.6. When an electric field is applied, the relative position of atoms may change, which in turn changes the direction of the polarization.

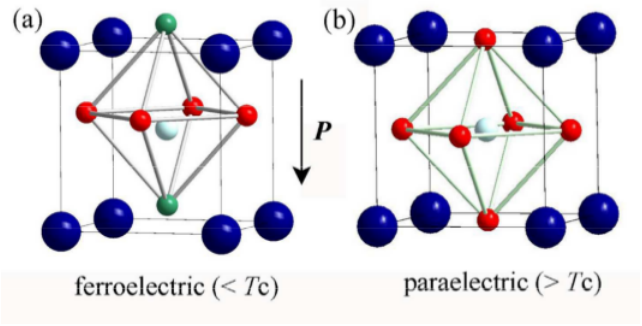

Figure 1.6: (a) Under Curie's temperature a displacement of the atoms creates a polarization (b) Over Curie's temperature the material goes back to a paraelectric phase. (Wang et al, 2017)

1.2.3 Ferroelectric domains and domain walls

Most of the time, the polarization in a given material is arranged in regions of constant polarization that are called domains, which are separated by domain walls:

- Ferroelectric domain: A ferroelectric domain is a group of unit cells with the same polarization. The size of these domains ranges from a few microns (Merz, 1954), which is observable with an optical microscope, down to few nanometers and depends on conditions such as the thickness of the material and the compensation of the polarization. Ferroelectric domains can be switched from one direction of polarization to another by the application of an electric field.

- Ferroelectric domain wall: A ferroelectric domain wall is the region separating two domains. Its size is in the range of nms but it depends on the type of

domain wall. Special properties can arise in these regions due to their position between two regions with a different polarization. For example, certain configuration of domain walls can show higher conductivity than the rest of the sample (Seidel et al., 2009).

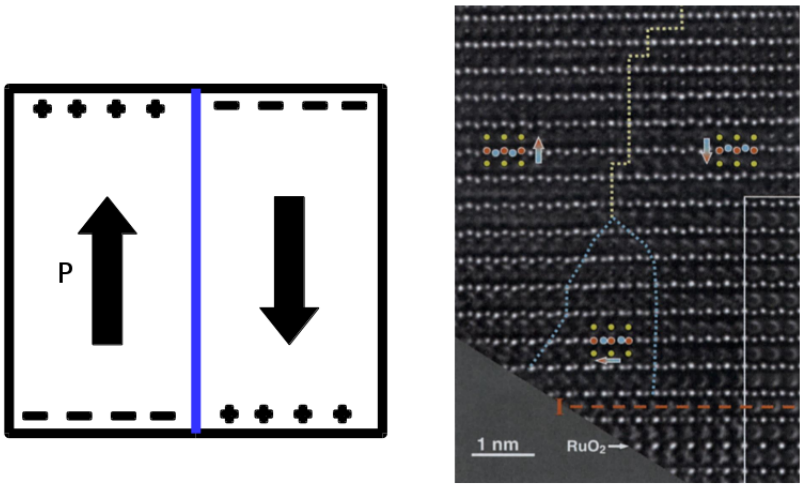

Figure 1.7: On the left, schematic of two domains separated by a domain wall (in blue). On the right, high-resolution transmission electron microscope image at the atomic scale of three domains and their domain walls in $Pb[Zr_{0.2}Ti_{0.8}]O_3$, domain walls are represented by the dotted line (Jia et al., 2011).

1.3 Compensation of ferroelectric domains

Many compensation mechanisms have been proposed and studied on ferroelectric materials. Indeed, the formation of domains in a material is itself a compensation mechanism. In order to decrease the energy of the material, domains are created. Their size and distribution ensure that the material remains in a stable state. In the same way, screening by electrodes or atmospheric adsorbates may stabilize domains

1.3.1 Domain formation

In 1935 Landau and Lifshitz (Landau and Lifshitz, 1935) studied the stability of ferromagnetic domains from an energetic point of view. They found that a specific domain distribution with closed domains like the one shown in Fig. 1.8 (e) decreases the energy and stabilizes domains. Later on, Kittel (Kittel, 1946) continued this work and found that the size of a domain is proportional to the square root of the

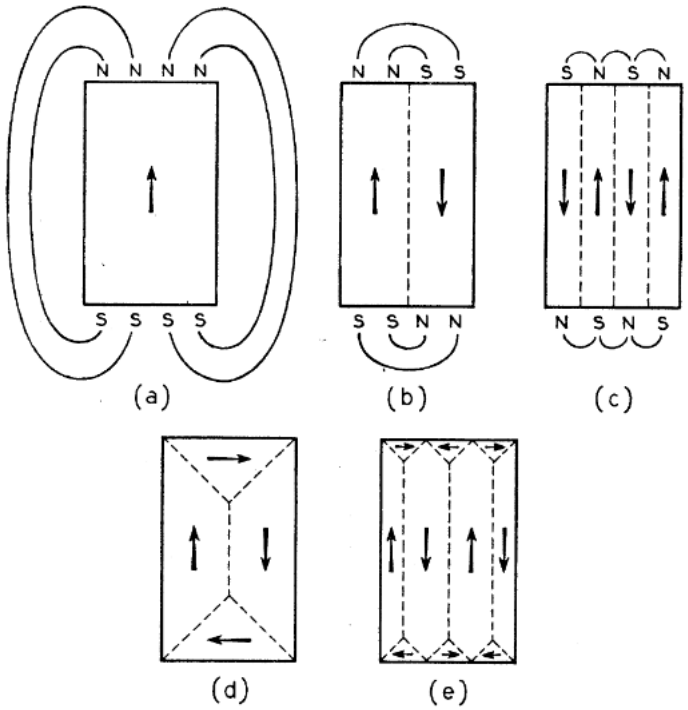

Figure 1.8: A single domain (a) shows higher magnetic field, which is associated with a higher energy. Creating more domains (b) and (c) decreases the field and the energy (as proposed by Kittel). (d) and (e) distributions like the ones proposed by Landau and Lifshitz have no field associated, decreasing their energy and becoming more stable. Similar effects appear in ferroelectric domain walls, (Kittel, 1949)

film thickness. Indeed, domains could be stable even without closing as long as they were opposing (Fig. 1.8 (c)) and their is size small enough. These results were shown to apply to ferroelectric materials as well (Mitsui and Furuichi, 1953).

Nowadays, these results are still being applied to study of ferroelectric domains (Catalan et al., 2007; Prosandeev et al., 2010). However, ferroelectric domains have to take into account screening and atmospheric effects that compensate electric fields and were not considered for ferromagnetic materials, which means that domain formation only represents one method of compensation. Furthermore, for multiferroic materials such as $BiFeO_3$ (BFO), there are cases more complex were domain size may not follow Landau, Lifshitz and Kittel's behavior(Catalan et al., 2008).

In conclusion, domains of different sizes and shapes are created in a ferroelectric thin film thereby minimizing its total energy. The distribution and nature of these domains will depend on parameters such as the crystalline structure of the material and its thickness.

1.3.2 Atmospheric, electrode compensation and surface electrochemistry

This section will exclusively focus on compensation by screening with atmospheric adsorbates, surface electrochemistry and metallic electrodes. Indeed, the most typical configuration for ferroelectric thin films is to have a bottom electrode and either a top electrode or atmospheric conditions over the surface. In this situation under ambient conditions, a thin water layer will lie on the material. This water layer can change the material in a reversible or irreversible way depending on the water vapor partial pressure. It has been shown that for high water partial pressures hydrolysis can take place resulting in the creation of an hydroxide layer and oxygen vacancies on the surface of BTO ultra thin films (Shin et al., 2009). Therefore, the water layer has an effect on screening and also introduces electrochemical changes on the surface.

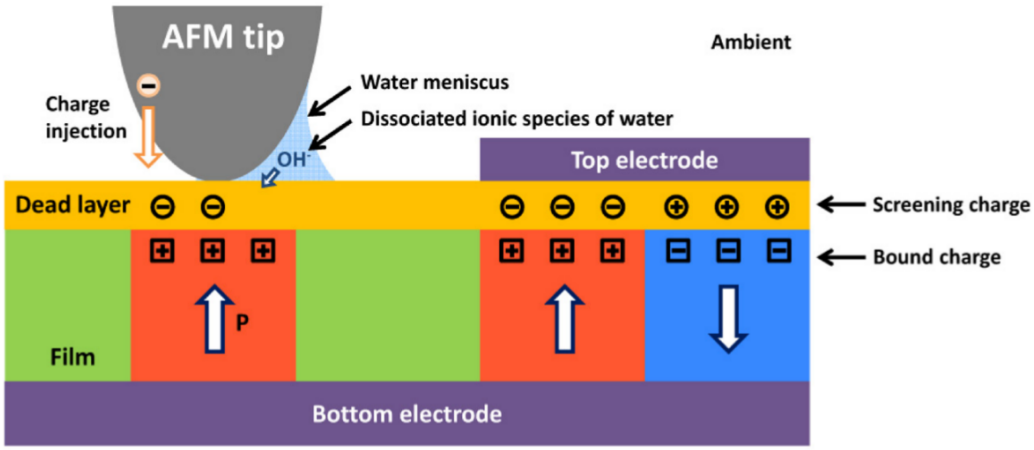

Figure 1.9: Schematic of the different screening mechanisms in ferroelectric materials. (Kalinin et al., 2018)

More studies show that the application of a voltage by an Atomic Force Microscope (AFM) tip may change ferroelectric properties due to redox reactions (mainly reduction or oxidation depending on the voltage applied). The products of these reactions may disappear with time but a small quantity of ions from the material may get desorbed due to these reaction, which with time leads to a loss of the polarization (fatigue) on ferroelectric thin films (Genenko et al., 2015; Domingo et al., 2019).

In Fig. 1.9 a summary of screening mechanisms are shown. Besides the role of the water on the surface that has already been discussed in this section, it can be observed that an electrode can stabilize a domain under it. Indeed, when a

top metallic electrode is deposited on the film, the screening comes from the free charges of the electrode. The choice of electrodes can affect the coercive voltages observed in ferroelectric materials by changing the electrostatic boundary conditions (Lichtensteiger et al., 2016). Furthermore, it has been shown that using a dielectric spacer it is possible to control the depolarizing electric field, since in this way the screening is less effective. This approach gives a way to change the distribution of domains and the coercive voltage (Lichtensteiger et al., 2014).

In conclusion, the choice of electrodes in the case of a thin film is of importance for the control of ferroelectric domains, and the electrochemical phenomena taking place at the surface of a ferroelectric thin film must be taken into account.

1.4 Ferroelectric domain walls

Domain walls exist in ferroelectric, ferroelastic and ferromagnetic materials (Thomas et al., 2007), even in antiferromagnetic materials (Privratská and Janovec, 1997). In this section, the classification of domain walls is detailed, as well as their properties.

1.4.1 Classification of domain walls

The main difference between ferroelectric and ferromagnetic domain walls is that the former is related with a change in polarization while the latter with a change in magnetization. However, how these changes happen is of importance to understand why the width of domain walls is different between ferromagnetics and ferroelectrics.

The size of a ferromagnetic domain wall is around tens of nanometers (Wade, 1962) while the width of a ferroelectric domain wall is around one nanometer (Foeth et al., 1999). Domain walls between ferroelectric and ferromagnetic materials are of different types. In ferroelectric materials, domain walls are of Ising type like the one shown in Fig. 1.10 (a). It can be observed that approaching the domain wall, the polarization in a domain decreases while keeping the same direction, and switches to the opposite direction once the domain wall is crossed. This means that the ferroelectric domain wall is a small region without polarization. In ferromagnetic materials, the magnetization does not change in module at a domain wall, only the direction moves perpendicularly (Néel type) or parallel (Bloch type) to the domain wall, in this case the domain wall is the region where the magnetization rotates.

Phase-field calculations have shown that it is possible to have a combination of an Ising-Néel type domain wall in ferroelectrics. This type of domain wall would decrease its polarization while rotating it at the same time (Lee et al., 2009).

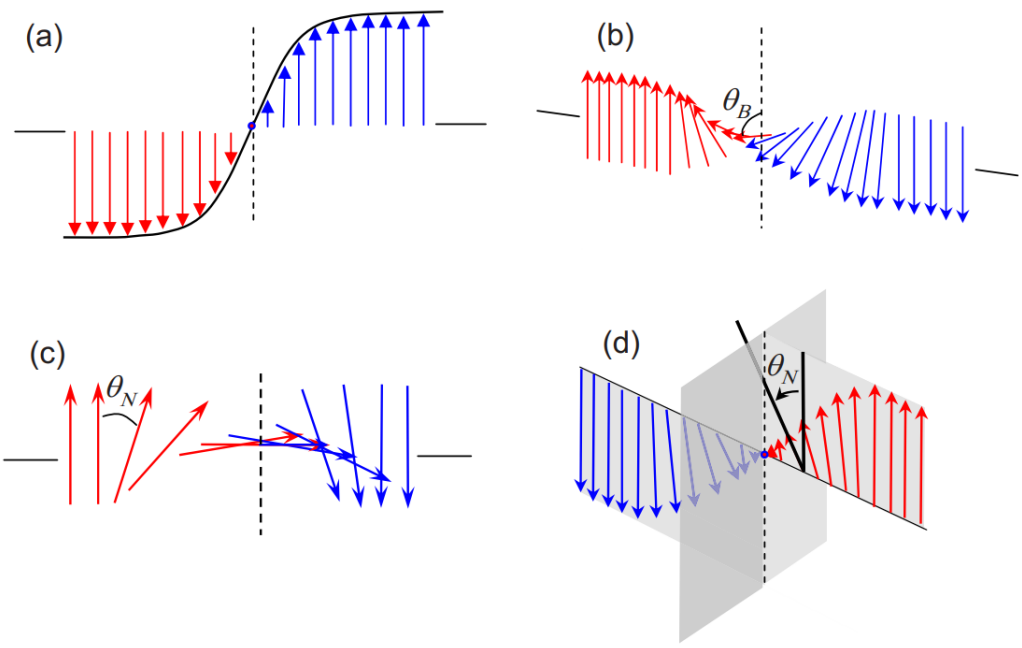

Figure 1.10: Different types of domain walls (a) Ising (b) Bloch (c) Néel d) Mixing Ising-Néel. (Lee et al., 2009).

1.4.2 Charged and neutral ferroelectric domain walls

In a tetragonal ferroelectric material like $Pb[Zr_{0.2}Ti_{0.8}]O_3$, it is possible to have an in-plane polarization, called a, and out-of-plane polarization, called c. Two types of domain walls are defined, the ones with 180° (between c-c or a-a) or the ones with 90° (a-c) (Damjanovic, 2006), as can be seen in Fig.1.11.

Nevertheless, for non tetragonal materials like BFO, other angles between domains exist and this may affect their stability, since all the domain walls obey the following rules to diminish energy (Fousek and Janovec, 1969):

- The domains creating the domain wall must be electrically compatible, in other words, there should not be any charge at the domain walls. However, in certain situations, charged domain walls exist if a source of compensating charge such as free oxygen vacancies or compensation from an electrode is present (Sluka et al., 2012).

- The domains must be mechanically compatible. Here, the strain of domains and ferroelasticity play an important role and can allow charges at the domain wall if this means a decrease of the mechanical energy (Sluka et al., 2016).

In summary, domains will organize themselves in a way that they reach their minimum electrical and mechanical energy. As a function of the electrical properties, we will distinguish neutral domain walls (NDW) and charged domain walls (CDW).

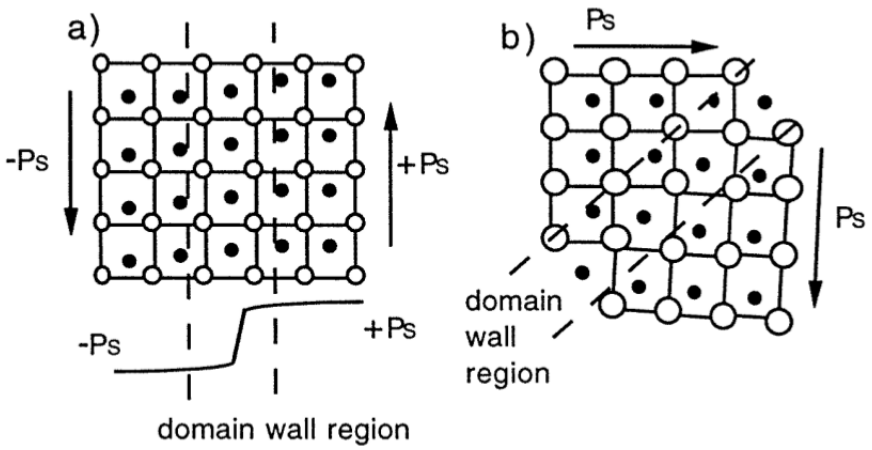

Figure 1.11: (a) 180° domain wall, the position of the middle atom gives the polarization in the region (b) 90° degrees domain wall (Damjanovic, 1998).

The charge of the domain wall can be calculated by making the difference in surface charge created by two domains, taking Eq. 1.7. for adjacent domains:

$$\sigma_p = (\vec{P}_2 - \vec{P}_1) \cdot \vec{n}_1 \tag{1.12}$$

Where $\vec{P}_2$ and $\vec{P}_1$ are the polarization of the domains, $\vec{n}_1$ is the wall normal vector into domain 1 and σ_p the surface charge at the domain wall. Fig.1.12 shows that the charge of the domain walls will depend on the angle between domains.

Domain walls with positive charge are called head-to-head (H-H) while the ones with negative charge are called tail-to-tail (T-T). This is of importance to understand the phenomena of conduction in domain walls.

1.4.3 Conductive domains walls

The most important property of domains for nanoelectronics would probably be the conductivity of domains. Indeed, as shown in Fig. 1.13, domain walls can show higher conductivity than the rest of the sample. This conductivity depends on the angle between domains. With conductive domain walls it would be possible to control current in small regions, which is of interest for nanodevices.

1.4.3.1 Mechanisms of conduction

The mechanisms allowing the existence of conductive domain walls are still discussed. Depending on the material and nature of domain walls, three mechanisms are proposed:

- Defects: Ferroelectric domain walls can attract or repel defects like oxygen

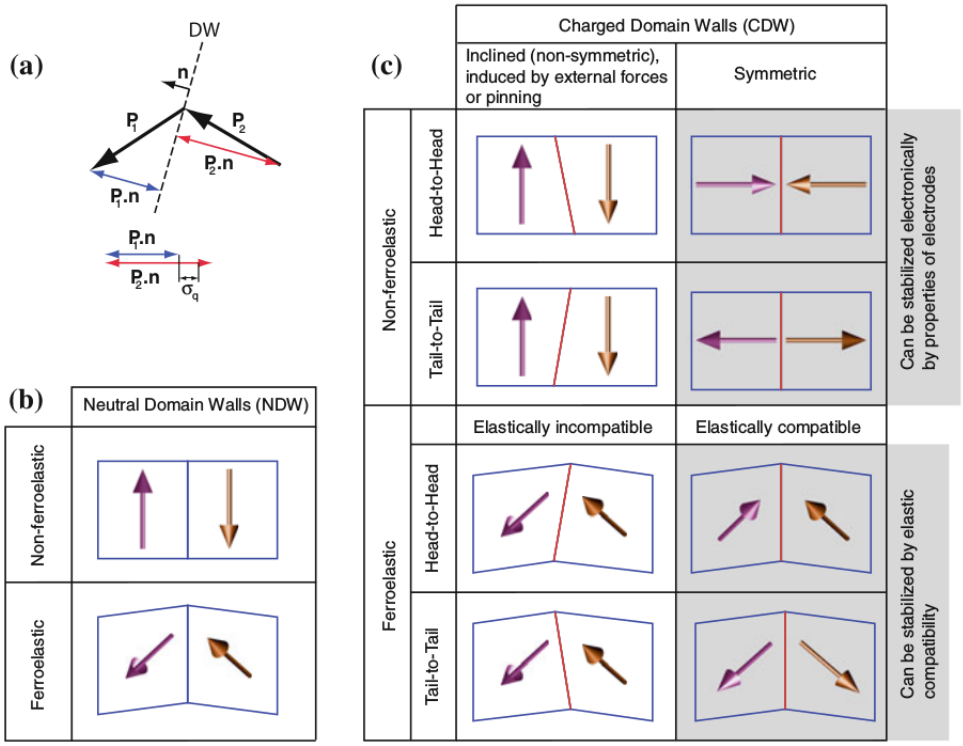

Figure 1.12: (a) Visual calculation of the charge of a domain wall (b) Orientations of neutral domain walls (c) Orientation of charged domain walls (Sluka et al., 2016).

vacancies. In this case conduction is possible thanks to these vacancies either through ionic movement or defects acting as donors/acceptor. It has been proved that the concentration of oxygen can affect the conductivity on domain walls(Seidel et al., 2010).

- Decreased band-gap: Since the nature of domain walls is different from the domains themselves, this can imply a decrease of the band-gap, which would facilitate electrons moving to the conduction band (Farokhipoor and Noheda, 2011).

- Electric fields due to charged domain walls: The local electric fields created by charged domain walls can allow conduction in domains. These electric fields can be controlled by the charge at domain walls, by changing the tilt of domains it is possible to change their conductivity (Lu et al., 2019). In this case charge carrier can be either electrons or oxygen vacancies depending if the configuration of domains (H-H or T-T).

The conduction can be due to more than one of these mechanism at the same time.

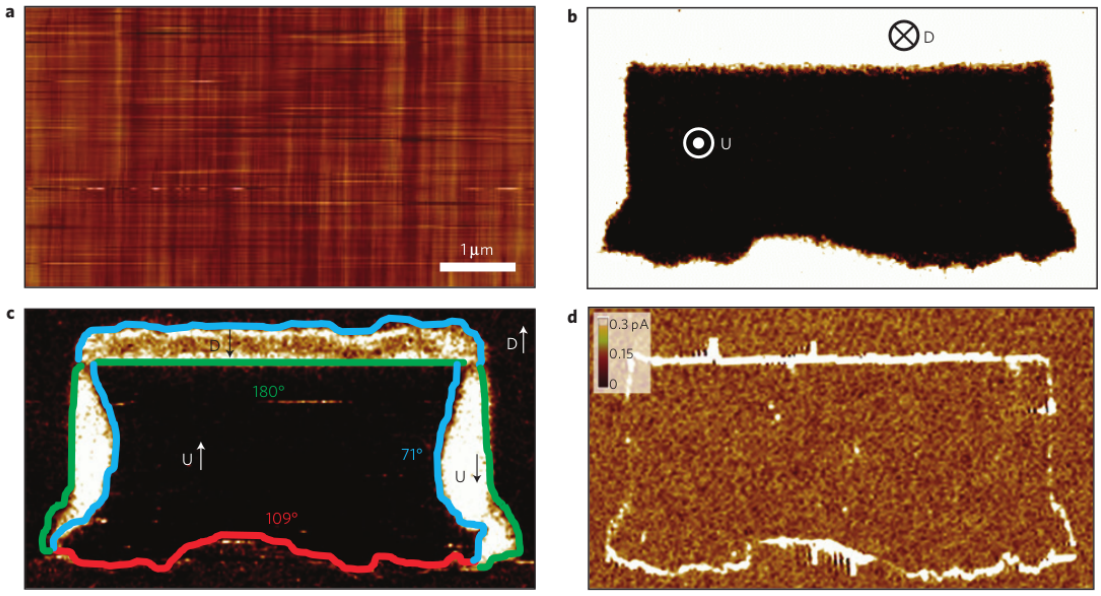

Figure 1.13: (a) Topography of a BFO sample (b) Vertical PFM of the same sample (c) Lateral PFM and the angle between domains d) Conductivity at domain walls. (Seidel et al., 2009)

1.4.3.2 Results on conductive domain walls

One of the first results that shows conductivity in ferroelectric domains was obtained in BFO, where the angle between domains gives rise to different conductivity (Seidel et al., 2009). This is one of the main ways to control conductivity of domain walls, others involve changing the screening condition. For example, it has been shown that the conductivity of a specimen can be altered by thermal annealing, while the bottom electrodes used (Gaponenko et al., 2015) also change the screening conditions and can change the conductivity. Changing the atmospheric condition and working in ultra high vacuum is also a way to obtain conductive domain walls (Guyonnet et al., 2011). Another route to obtain conductive domain walls is the photoconductivity present in some domain walls on $LiNbO_3$ (Schröder et al., 2012). Indeed, applying a light of appropriate frequency increases the current measured in domains walls.

All these discoveries open the door to new devices based on domain wall conductivity. Some attempts have been already performed, for example domain walls in manganites have been used as half wave rectifying device (Fig. 1.14) (Schaab et al., 2018). In this case, the conduction was thought to be due to oxygen vacancies accumulated at domain walls. Another example is the diode-like device created by (Whyte and Gregg, 2015), where the authors can control the movements of domain walls by the geometry of the top electrode. As a final example, the velocity of domain walls movement can also be controlled by the thickness of the top electrode

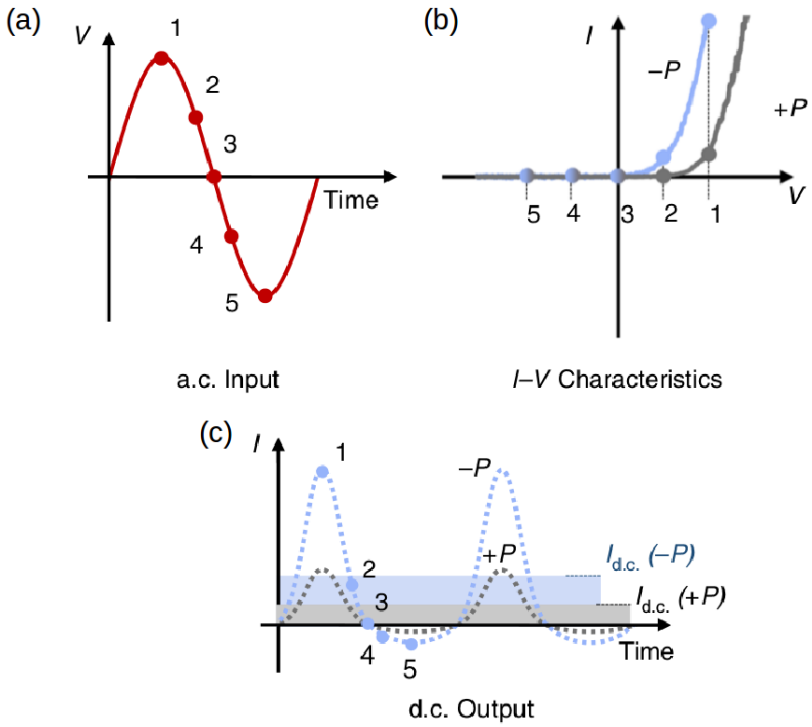

Figure 1.14: (a) AC input in a domain wall in $ErMnO_3$ (b) I-V curve of the domain wall for both polarizations (c) Final output of the domain wall for both polarizations where the signal is half wave rectified(Schaab et al., 2018).

as shown by (McGilly et al., 2016). All these examples show the possibilities for the control of domains and domain walls conductivity for electronics.

1.5 Ferroelectric materials studied in this work

The two ferroelectric perovskites compounds studied in this work are $Pb[Zr_xTi_{1-x}]O_3$ (PZT) and $BiFeO_3$ (BFO)

1.5.1 $Pb[Zr_xTi_{1-x}]O_3$

$Pb[Zr_xTi_{1-x}]O_3$, abreviated PZT, is a perovskite compound from the solid solution of end members $PbTiO_3$ (ferroelectric) and $PbZrO_3$ (antiferroelectric). For room temperature and a high content of Ti, PZT crystallizes in a tetragonal lattice. When the Ti percentage is between 50% and 40%, the morphotropic phase boundary (Goldschmidt, 1929; Ahart et al., 2008) occurs and the material changes from a tetragonal to a rhombohedral structure, while remaining ferroelectric as shown in Fig. 1.15 (a).

$Pb[Zr_{0.2}Ti_{0.8}]O_3$ and $Pb[Zr_{0.25}Ti_{0.75}]O_3$ are the compositions of interest for this thesis. For these compositions, PZT depicts a tetragonal structure (Fig. 1.15 (b)),

which can be stabilised to depict in epitaxial films grown on (001)-pseudocubic perovkiste oxides only two components of the polarization against the thin film surface.

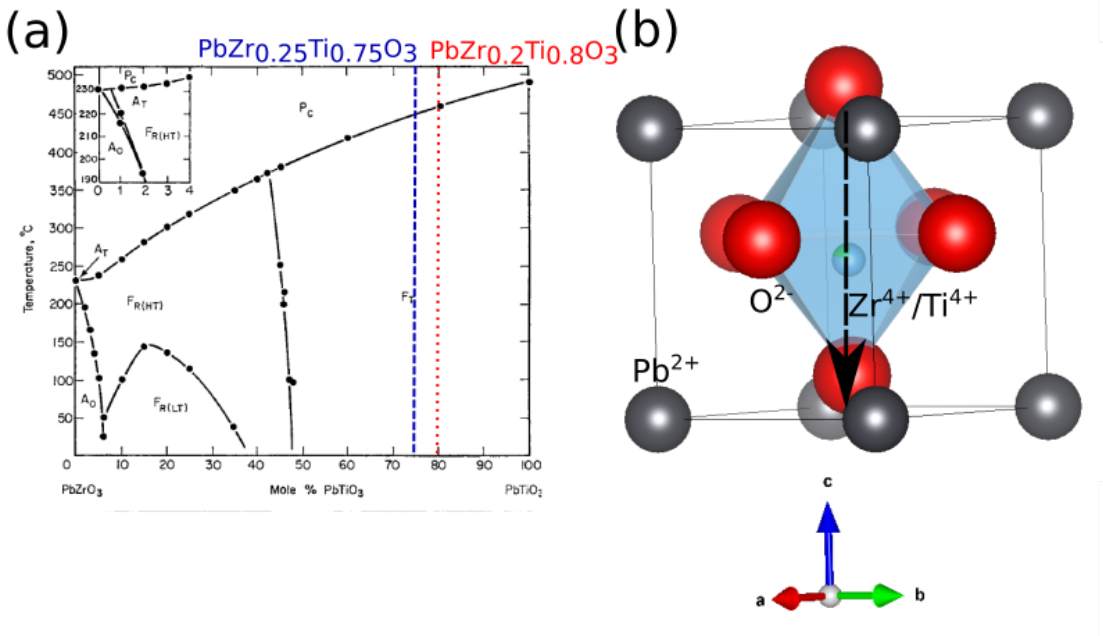

Figure 1.15: (a) Phase diagram of the transition temperature and structure of PZT (Jaffe et al., 1971) and (b) sketch of the tetragonal structure of $Pb[Zr_{0.2}Ti_{0.8}]O_3$, the black arrow indicates the direction of the ferroelectric polarization.

1.5.2 $BiFeO_3$

BFO is a rhombohedral ferroelectric and antiferromagnetic material at room temperature, hence a prototypical multiferroic. This work is focused on its ferroelectric properties. Previous studies have shown that it is possible to create ferroelectric domain walls with different angles (71°, 109° and 180°) (Seidel et al., 2009).

What makes this material interesting compared to PZT is the in-plane polarization, which allows for studies on lateral switching of domains. Even if the material is rhombohedral in its bulk form, in this work we will use the pseudocubic notation (see Fig. 1.16 (a)) that simplifies our notation for the projections of the polarization. Furthermore, BFO is a ferroelectric without Pb, in line with current environmental concerns.

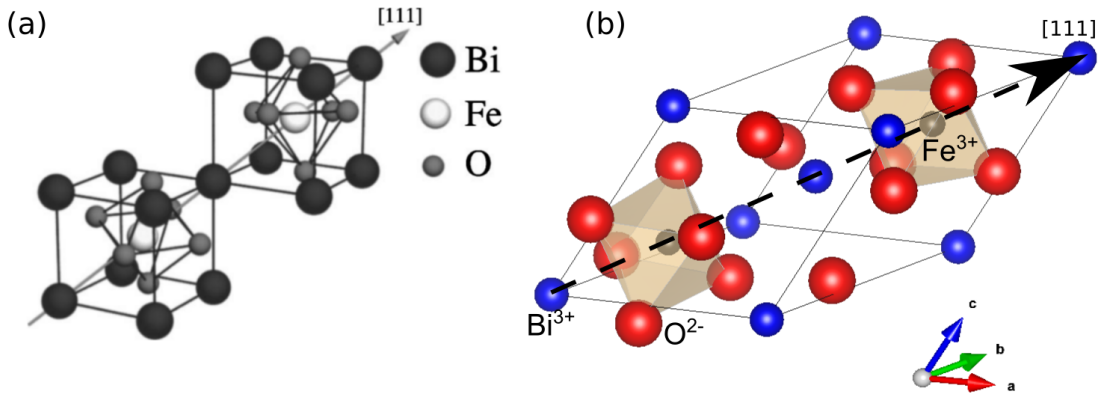

Figure 1.16: (a) Pseudocubic structure (Ederer and Spaldin, 2005) and (b) sketch of the rhombohedral structure of $BiFeO_3$, the black arrow indicates the direction of the ferroelectric polarization.

1.6 Conclusions

It has been 100 years since the discovery of ferroelectric materials and 70 since the beginning of studies on domains. Since then, ferroelectricity has become of great interest for research, especially for its applications in electronics in a similar way to ferromagnetism (Baibich et al., 1988). However, this field has advanced greatly during the last years thanks to the technological improvements like the creation of AFMs (1986). These improvements allowed a study in depth of domains and domain walls, which could be useful for their special properties such as their small size (smaller than ferromagnetic) and conductivity.

This work will focus on the control of domains by electrical and mechanical stimuli in PZT and BFO. The former is chosen because of its well known polarization that simplifies the study of domain switching, while the latter is used to study domains with in-plane polarization.

Chapter 2

Synthesis and characterization of ferroelectric thin films

This chapter is devoted to the techniques used to grow PZT and BFO and the characterization techniques used to study the structural and chemical composition of the materials obtained. While piezoresponse force microscope (PFM) is the main tool used in this thesis, it is a surface microscope that can essentially provide information from the surfaces of materials. The techniques and results presented in this chapter, complement the PFM results that are the focus of the next chapters.

2.1 Synthesis of ferroelectric materials

In this work, a series of PZT samples was synthesized by soft chemistry (sol-gel), and by a physical method, pulsed laser deposition (PLD). The BFO sample was also prepared by PLD. This section aims at showing the two different techniques used to prepare these samples and point out their differences.

2.1.1 Deposition of $SrRuO_3$ electrodes by sputtering

In order to characterize ferroelectric material electrically, a $SrRuO_3$ (SRO) bottom electrode is deposited between the substrate of $SrTiO_3$ (STO) (001) and the ferroelectric films for most of the samples in this work. This bottom electrode is grown by sputtering, a technique based on the creation of a plasma that sputters a target of the desired material. This plasma is created by the ionization of a gas (Ar, although other gases can also be used in a gas mixture, e.g. oxygen or nitrogen) by a DC or AC voltage. The sputtered atoms from the target are then deposited on the substrate.

For this work, radio frequency (RF) magnetron sputtering was performed at a frequency of 13.56 MHz with the substrate facing the target (on axis configuration). RF sputtering is used because of its compatibility with reactive gases such as oxygen, that allows the deposition of oxides and also allows to reduce the charging effects at the target level. Furthermore, sputtering uses a magnetron that confines the charged particles of the plasma near the target, which improves the efficiency of the milling. A schematic of the whole process is shown in Fig. 2.1.

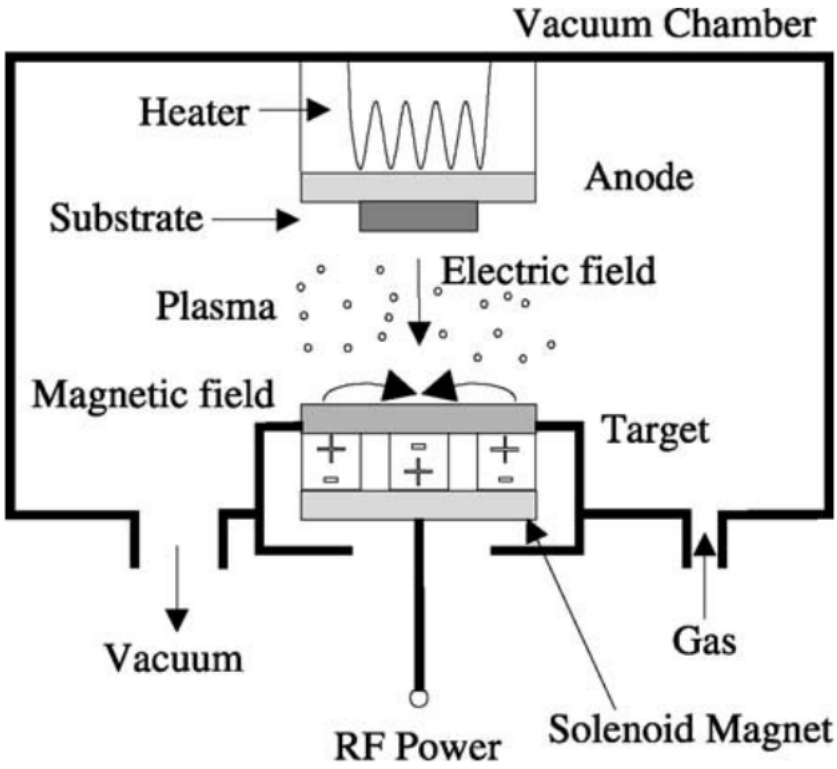

Figure 2.1: Schematic for the sputtering deposition process (Tsuchiya et al., 2003)

While sputtering represents only a small part of this work, the interested reader can find more information in specialized books (Mattox, 2010). In this work, RF sputtering of SRO electrodes (as bottom electrodes, grown at high temperature, as top electrodes, grown at room temperature) was performed by Bertrand Vilquin and Pedro Rojo-Romeo in École Centrale de Lyon (ECL) at Nanolyon platform. Detail of the deposition conditions and procedure can be found in (Liu, 2014).

For macroscopic measurements of the polarization, SRO top electrodes were deposited on the ferroelectric films. The deposition was done by reversal lift-off, a procedure explained in Fig. 2.2, nanotechnological processing performed by Bertrand Vilquin and Pedro Rojo-Romeo.

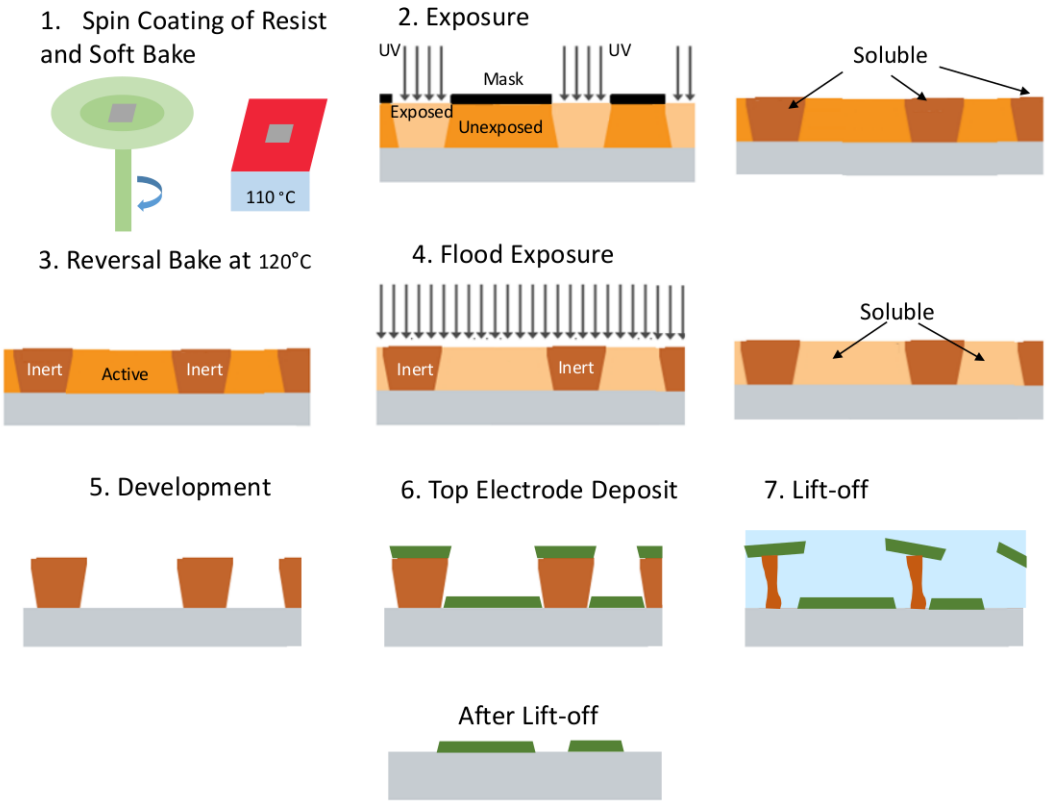

Figure 2.2: Reversal lift-off process (Liu, 2014)

2.1.2 Sol-gel

Sol-gel is a chemical method used to fabricate solid materials like the PZT 20/80 thin films (Budd et al., 1985) of this work. In this method, a solution (sol) is used as a precursor for the material. In our case, it is a commercial solution from Mitsubishi Corp. A small quantity of precursor is deposited over a flat substrate (the SRO electrode) and spin-coated. Then, the material is heated two times, the first one to dry and obtain an amorphous gel and the second one to do a pyrolisis process. Finally, the material is heated one last time at higher temperatures and during a longer time to crystallize in the expected perovskite structure.

The whole process, with the corresponding surface preparation routine, deposition conditions, steps for obtaining different thickness, used instruments, and processing temperatures, is shown in Fig. 2.3 a. For most of our samples, the crystallization process was done once for samples of 100 nm or less, and twice for thicker samples. There was only one exception, a sample of 100 nm that underwent three crystallizations, in order to study the effect of changing the crystallization process. The whole process and crystallization conditions were inspired by the work of Bennecka et al. (Fig. 2.3 b)

Sol-gel method is a technique that does not require expensive vacuum systems, in contrast with other physical vapor deposition techniques such as molecular beam epitaxy or pulsed laser deposition (PLD), where high temperature and high vacuum is required to stabilize the pure perovskite PZT phase. Soft chemistry-derived films are also of technological interest for the reduction of processing temperatures and its corresponding processing time (Fig. 2.3 a), and thus open the path to device integration. Sol-gel grown films are typically more defective for what accounts to grain boundaries, PZT sol-gel films will depict crystalline extension of shorter size compared to those of high temperature physical vapor deposited thin films. Profiting from this particular nanocrystalline state in PZT sol-gel films, and having means to control them, sol-gel films provides an ideal platform to study the effect of higher defect concentration in films on their ferroelectric properties.

All the PZT sol-gel thin films used in this work were fabricated in the clean room (NanoLyon facilities) of École Centrale de Lyon (ECL) by Xiaofei Bai and Ingrid Cañero Infante.

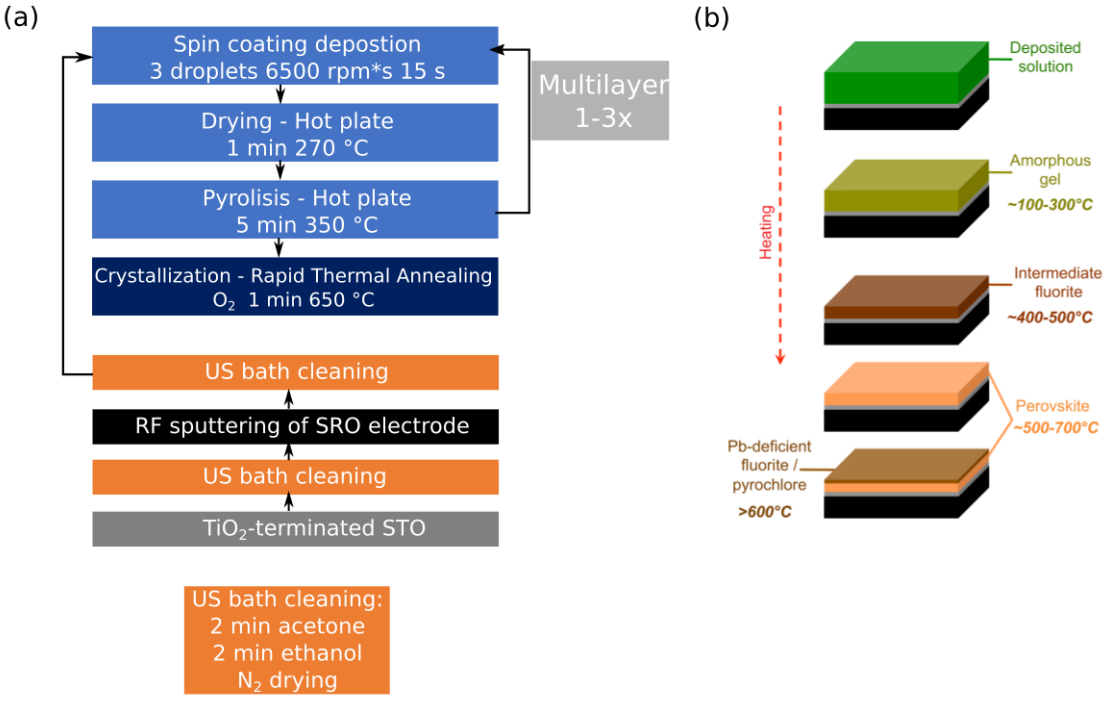

Figure 2.3: (a) Process of sol-gel fabrication for the sol-gel PZT samples at INL. (b) Schematic for the different phases of sol-gel fabrication of PZT thin films (Brennecka et al., 2010)

2.1.3 Pulsed laser deposition

The pulsed laser deposition (PLD) is a physical vapor deposition technique based on the use of a high power pulsed laser to melt and vaporize a solid target of the material that has to be deposited. For the process to succeed it is important to work at low pressures or under vacuum. In these conditions, the short pulses of the laser create a plasma plume perpendicular to the surface of the target like the one shown in Fig. 2.4. The ions from this plasma will then be deposited on the substrate. Since the materials studied in this work are oxides, the whole process happens in an atmosphere with a certain percentage of oxygen to obtain the oxidation.

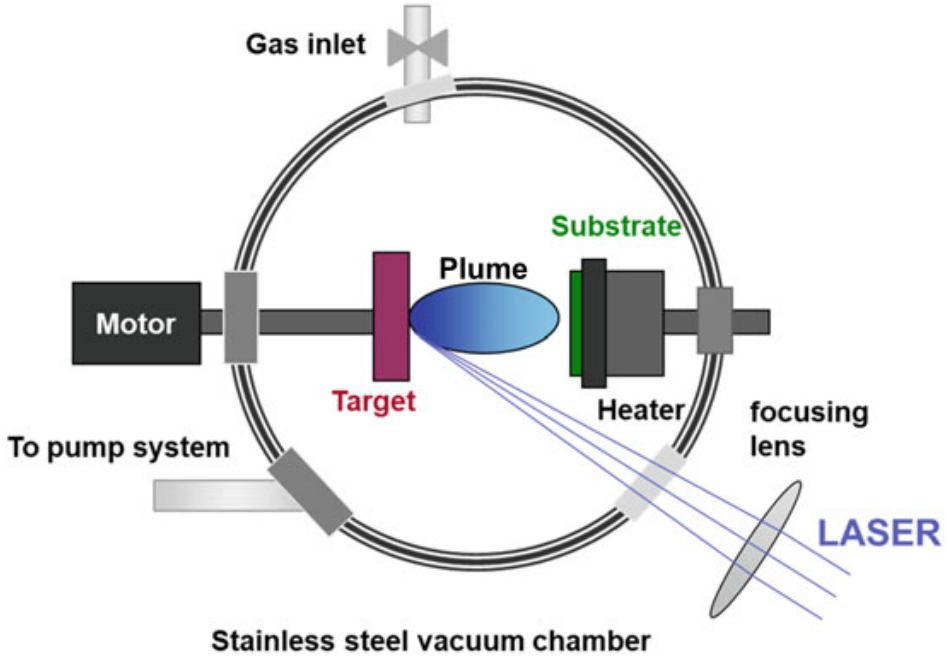

Figure 2.4: Schematics of PLD system (Craciun et al., 2020).

While this technique allows a higher control on the growth of the materials and even the synthesis of metastable phases not possible with other techniques, it is still an expensive technique compared with sol-gel. Furthermore, a high number of parameters need to be controlled to assure the growth of the materials such as the atmosphere.

For this work, tetragonal PZT samples with a 25:75 composition were prepared by PLD with a KrF excimer laser at 248 nm wavelength, a laser-repetition rate of 4Hz, and an energy density of 2.7 J/cm2. PZT piezoelectric films with a thickness of 40 and 20 nm were deposited with 0.12 Torr (0.16 bar) of nitrous oxide (N_2O) and at a substrate temperature of 640°C. The substrate was the same than the one used for sol-gel samples, with an SRO electrode. The process was carried out by Guillaume Agnus at Centre de Nanosciences et de Nanotechnologies (C2N) in Saclay.

In a similar manner, the BFO sample used in this work was grown by PLD in a Pascal system using a KrF excimer laser at 248 nm wavelength. First, the substrate (STO (001)) was heated to 750 °C (at 30 °C/min) using a laser heater, while inserting 100 mTorr (0.133 mbar) of flowing O_2, then a LSMO target was ablated with 175 laser pulses at 5 Hz to deposit 5 nm of LSMO, which acts as the bottom electrode. The temperature was then reduced to 590 °C at 20 °C/min, with oxygen pressure staying at 100 mTorr (0.133 mbar), and the BFO target ($Bi_{1.1}FeO_3$, excess bismuth to account for volatility) was ablated with 10,000 pulses at 10 Hz. After the deposition the sample was cooled to room-temperature at 20 °C/min in 5 Torr (6.65 bar) of static O_2. The process was carried out by Oliver Paull at the University of New South Wales in Sydney.

2.2 Structural and chemical characterization of the tetragonal $Pb[Zr_xTi_{1-x}]O_3$ thin films

2.2.1 Structural and chemical characterization of the sol-gel $Pb[Zr_{0.2}Ti_{0.8}]O_3$ thin films

2.2.1.1 X-ray diffraction

The study of x-ray diffraction patterns can be used to determine the crystalline structure of materials. Indeed, when a x-ray beam gets diffracted by a crystalline structure, a constructive interference occurs when the rays have the appropriate difference in the optical path. The conditions for a constructive interference can be obtained by Bragg's law:

$$2d\sin\theta = n\lambda \tag{2.1}$$

Where d is the lattice spacing, λ the wavelength, θ is the diffraction angle and n is the diffraction order, which is always an integer. With Bragg's law it is possible to link the diffraction pattern and the maximum intensity at particular θ values with the inter-planar distance d.

For the sol-gel PZT samples, the x-ray diffraction obtained in the experimental diffractometer setting described in detail in Appendix B under the name of configuration 2. The results are shown in Fig. 2.5 and the films exhibit the expected tetragonal structure over the SRO electrode and the STO substrate. From PZT peak position, we deduce a value for inter-planar distance (d_{001}) between 4.07 Å and 4.10 Å, for the 66 nm and 100 nm samples (grown on SRO (30 nm)//STO

(001)), respectively. From the shape of the (001) peak, depicting large intensity for low 2θ angle than for higher angle, we cannot rule out a range of d_{001} within the film thickness indicating a distribution of d_{001} between 4.07 Å and 4.10 Å.

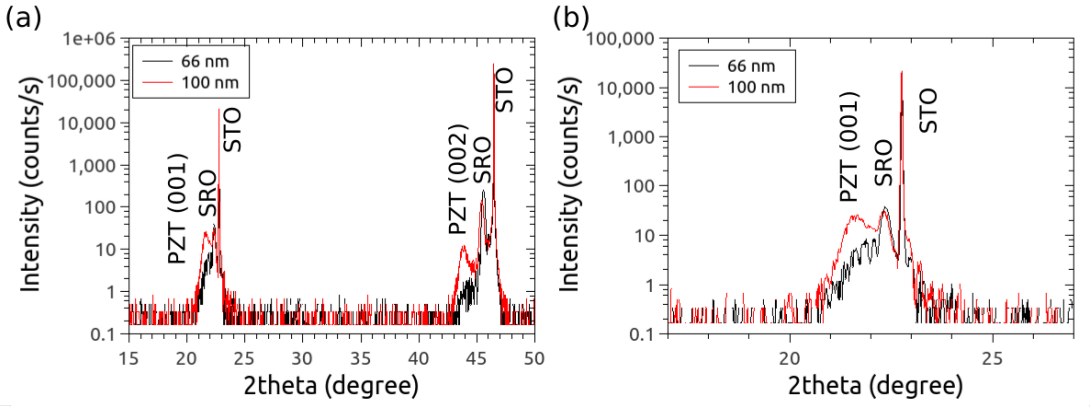

Figure 2.5: (a) $2\theta/\omega$ scans around 001 and 002 STO reflections. (b) Zoom of the scan around 001 STO reflections.

2.2.1.2 Scanning transmission electron microscopy

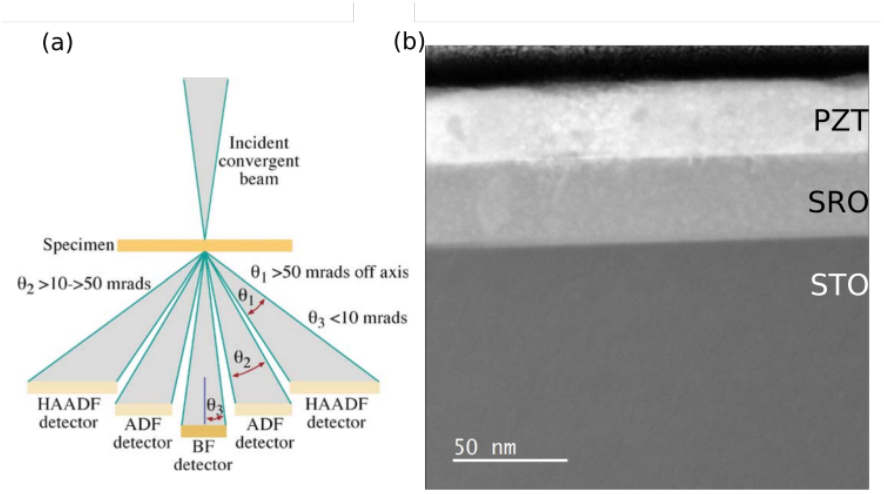

Figure 2.6: (a) Schematic of the beam geometry and the angular range for the different imaging modes in STEM where HAADF and bright field are shown (Williams and Carter, 2009). (b) HAADF imaging of one of the sol-gel-grown samples (33 nm-thick) studied in this work, which consists of PZT over a SRO electrode and a STO substrate. The regions with higher Z atoms show higher intensity.

In scanning transmission electron microscopy (STEM), a beam of electrons is focused on a specimen, which is usually in the form of a thin (few tens on nms) lamella prepared by focused ion beam (see Appendix D), and scans the specimen as a raster. For each beam position, the scattered electrons can be collected using

a set of detectors located below the specimen. Different types of contrast can be obtained as a function of the scattering angle θ, as shown in Fig. 2.6. All STEM images presented in this work were obtained by using the high angle annular dark field (HAADF) detector (see Fig. 2.7). In a first approximation, the intensity in the HAADF image is proportional to the atomic number squared ($\propto Z^2$).

STEM-HAADF imaging has become very popular over the last decade with the availability of aberration correctors of the probe forming lenses, which provide Z-contrast images at atomic resolution. Furthermore, the HAADF image can be correlated with spectroscopic signals, such as electron energy-loss spectroscopy (EELS) and energy-dispersive x-ray spectroscopy for the most common ones.

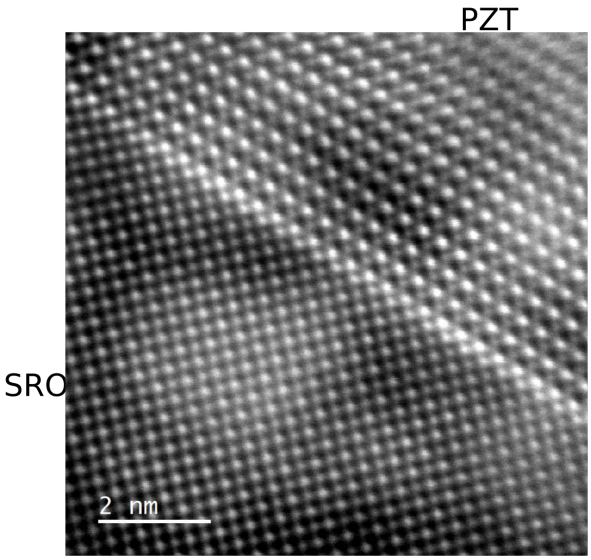

Figure 2.7: Atomic resolution STEM-HAADF image of the interface between a 200 nm PZT 20:80 sol-gel thin film and the SRO electrode, highlighting the epitaxial growth of PZT on SRO.

STEM is a complex technique and here only the details relevant for this work are explained. However, the reader interested in knowing more about this technique can refer to the book of Williams and Carter (Williams and Carter, 2009).

The microscope used for this work was a Cs corrected Jeol JEM-ARM200F NeoARM, which is equipped with a high brightness cold-FEG, a CEOS ASCOR aberration corrector of the condenser lenses, a Gatan imaging filter QUANTUM, and was operated at 200 keV. All STEM-HAADF images presented in this thesis were recorded using the annular dark field detector located at the entrance of the EEL spectrometer, and the Gatan microscopy suite software.

2.2.1.3 Rutherford backscattering spectrometry

The Rutherford backscattering spectrometry (RBS) is an analytical technique in which an ion beam of high energy (MeV) is used to study a material. When the ions of the beam arrive to the sample, there is a chance that they will collide elastically with the nucleus of atoms present in the specimen. The probability that an ion from the beam encounters an elastic collision after colliding an atom of the target gives rise to a secondary ions flux composed of retro-diffused ions. RBS is based on this phenomenon. The energy of the retro-diffused ions is measured, which allows to record energy spectra like the one showed in Fig. 2.8, which gives information about the composition and thickness of the layers in the sample. RBS has already been used to analyse the composition of PZT thin films (Natali et al., 2011).

An RBS instrument consists of an ion source, a linear particle accelerator and a detector to measure the energy of backscattered electrons. In this work, the ions used will be $^4He^+$ that will be accelerated up to an energy of 2 MeV. The studies will be carried out with different incidence angles to change the penetration depths and be able to study thinner films. The RBS will provide data on the composition of the PZT thin films grown at INL.

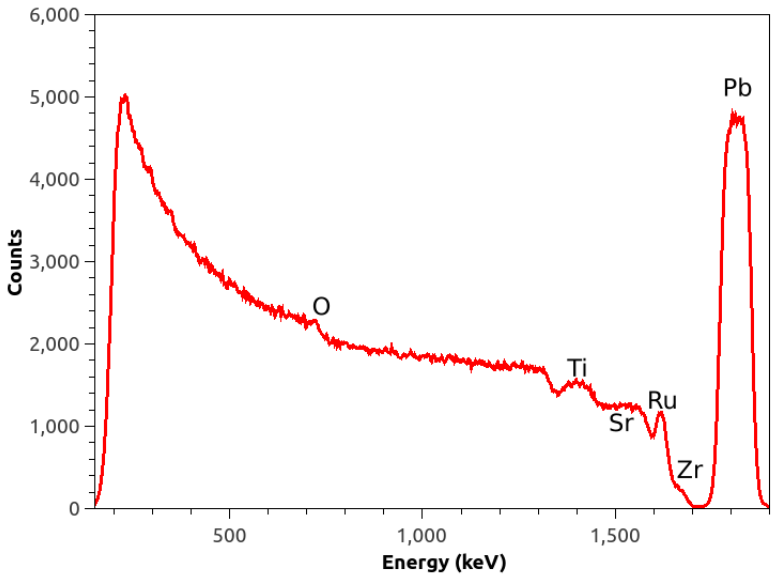

Figure 2.8: Example of an RBS spectrum from a 100 nm thick PZT sample on a SRO electrode and a STO substrate. From the spectrum it is also possible to obtain the atomic fraction of each specimen.

RBS experiments were carried out by Bruno Canut at the SAFIR (Système d'Analyse par Faisceaux d'Ions Rapides) platform, which is part of the Institut des Nanosciences de Paris (INSP) and is located at the Université de Jussieu. More

information about the technique can be found in specialized books (Feldman et al., 1987; Chu et al., 1978).

2.2.1.4 Time of flight secondary ion mass spectrometry

The secondary ion mass spectrometry (SIMS) is an analytical technique, which consist of a focused ion beam sputtering a material and a mass spectrometer that collects the secondary ions released during the sputtering. In the case of this work, a time of flight detector was used, which is why this technique will be written as ToF SIMS. The main property that differentiate the ToF from other detectors is the ability to register the activity of all ions sputtered, while other detectors are only able to register one specimen at a time. It is possible to reconstruct the depth profile of the material and its composition by collecting the secondary ions. However, it is not possible to know the thickness of the material without a calibration to know the erosion speed.

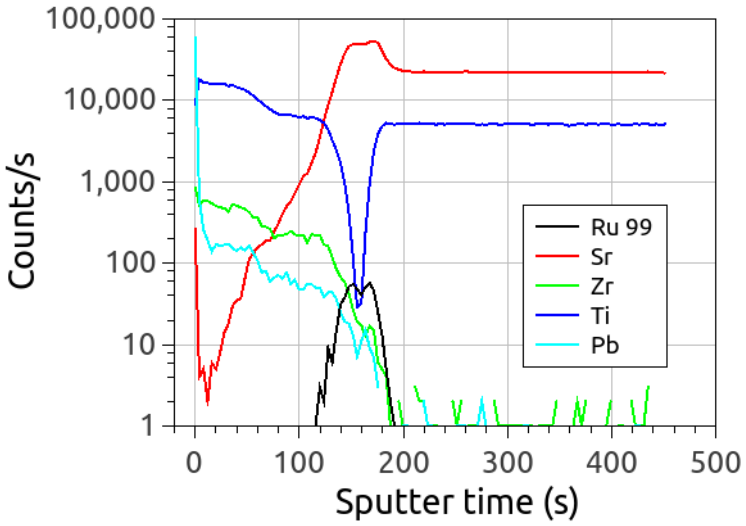

Figure 2.9: Example of a TOF SIMS signals as a function of the sputter time for a 100 nm thick PZT sample on a SRO electrode and a STO substrate. Notice that the x axis represents the sputtering time and not the thickness. For Ru the 99 isotope is followed to univocally determine the presence of Ru in the sample, avoiding mass interference in the signal.

In this work, the PZT samples grown by sol-gel were studied by ToF SIMS with a ion beam of Cs^{+}. The results shown in Fig. 2.9 suggest that the thin film heterostructure is as expected with a PZT layer over SRO and STO substrate. The Ru signal is followed using Ru^{99} to avoid problems of mass interference with SrO. The ToF SIMS analyses were conducted in CEA LETI by Jean-Paul Barnes in

Grenoble. More information about the technique can be found in the bibliography (Fearn, 2015).

2.2.1.5 Macroscopic characterization of the polarization

There are different ways to measure ferroelectricity at the macroscopic scale. Most of them are based on the measurement of transitory current created when the polarization switches. In this thesis the method called Positive Up Negative Down (PUND) was used.

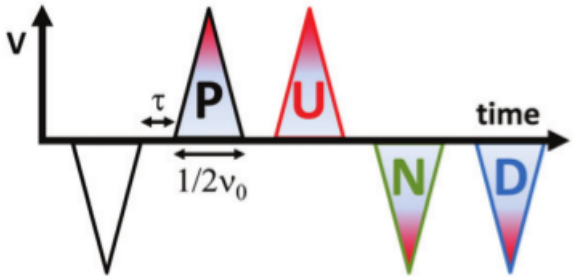

Figure 2.10: Schematic of voltage pulses used for PUND measurements (Fina et al., 2011).

PUND was developed by J. Scott (Scott et al., 1988) and consists of prepolarizing the sample with a negative voltage, then apply two positive voltage pulses (P and U) followed by two negative voltage pulses (N and D), as shown in Fig. 2.10. The currents measured during the P and N voltage pulses are related with the ferroelectric switching. However, they also present non ferroelectric contributions, which are dielectric and leakage currents. These contributions can be eliminated by subtracting the currents measured during U and D pulses that only present the non ferroelectric contributions, since the polarization switching current has occurred during the previous pulse and it only appears when switching the polarization. If the result is integrated during the time of the pulses, it is possible to obtain the charge displaced during the switching event and from that the polarization as:

$$P^{+} = \frac{1}{S}\int (I_P - I_U)dt + k_1 \tag{2.2}$$

$$P^{-} = \frac{1}{S}\int (I_N - I_D)dt + k_2 \tag{2.3}$$

Where P^{+} and P^{-} are the positive and negative polarization respectively, S is the surface of the electrode, I are the different currents, and k_1 and k_2 are integration constants that can be determined from plotting P.

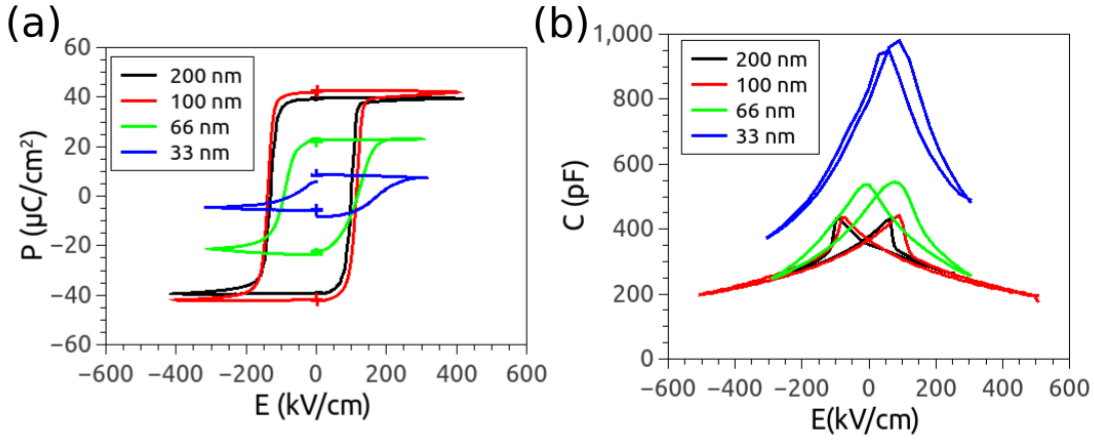

Figure 2.11: (a) Polarization and (b) capacitance against electric field for sol-gel samples. The polarization measurements were obtained for a frequency of 5 kHz, while the capacitance was measured with a frequency of 100 kHz and small amplitude signal of 50 mV.

In this work, PUND was performed in the PZT samples grown by sol-gel after lithographic processing was performed on them to define micro-capacitors, as explained in Section 2.1.1, with bottom and top electrodes being of SRO. The results shown in Fig. 2.11 present a ferroelectric behavior for the four samples studied. However, the thinnest sample has a loop slightly deformed and a different behavior for the capacitance, which could be related to the appearance of leakage currents in the sample.

All experiments were carried out on a microprobe station where samples were electrically contacted in a top-bottom capacitor configuration. The bottom electrode was accessed either using silver paste on the sample side, or using short-circuited top contacts after dielectric breakdown. For positive up negative down experiments, a NF WF1966 function generator, a Femto DLPCA-200 current amplifier and a Nicolet INTEGRA-40 oscilloscope were interfaced through a home made program. Capacitance versus voltage characteristics were obtained using a HP 4284A LCR meter. The experiments were carried out at INL by Nicolas Baboux.

2.2.2 Structural characterization of the PLD $Pb[Zr_{0.25}Ti_{0.75}]O_3$ thin films

The experimental diffractometer settings are described in detail in Appendix B under the name of configuration 1.

The results in Fig. 2.12 show a tetragonal lattice for the PZT films. From the PZT peak position, we deduce a value for inter-planar distance (d_{001}) between 4.10

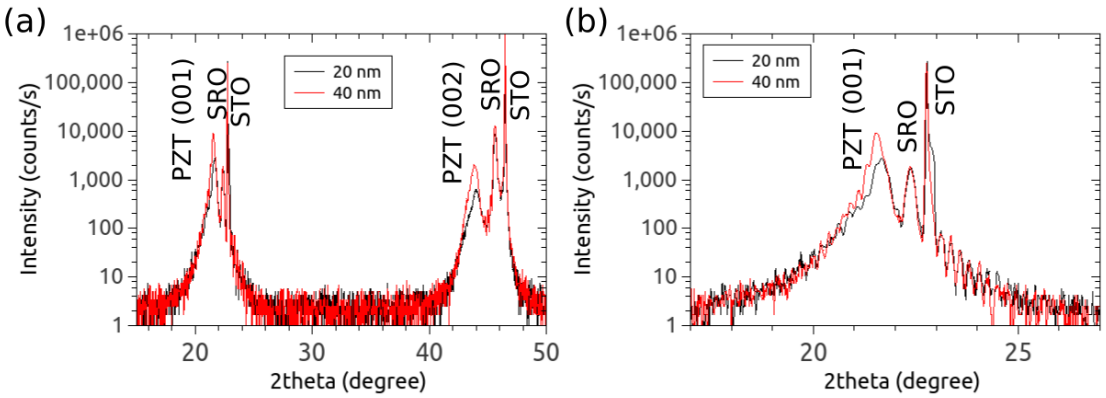

Figure 2.12: (a) $2\theta/\omega$ scans around 001 and 002 STO reflections. (b) Zoom of the scan around 001 STO reflections.

Å and 4.12Å, for the 20 nm and 40 nm sample, respectively. From the (001) peak shape (Fig. 2.12 b), depicting a center peak with intensity angular spread towards low angle, we cannot rule out a range of d_{001} within the film thickness indicating a distribution of d_{001} between 4.10 Å and 4.12 Å in a similar way to those obtained for the PZT sol-gel samples. Furthermore, the appearance of Laue's oscillations are an evidence of the quality of the interface.

2.2.3 Comparison of x-ray diffraction in tetragonal $Pb[Zr_xTi_{1-x}]O_3$ thin films

The mosaicity of (002) planes for 66 nm PZT 20:80 sol-gel and 40 nm PZT 25:75 PLD films has been studied (PZT films grown on SRO (30 nm)//STO (001)), using samples with reduced areas (approximately 2 × 5 mm^2) and with an x-ray beam of lateral size of 0.5 mm using the diffractometer in configuration 1 (see Appendix B). The corresponding experimental results are presented in Fig. 2.13. We note that the inter-planar distance (d_{001}) previously suggested a larger value for the PLD sample compared to the corresponding sol-gel ones (see Section 2.2.1.1 and Section 2.2.2), although from compositional aspects, bulk PZT 20:80 should depict larger tetragonal distortion than PZT 25:75 (Jaffe et al., 1971). As shown from the larger spread along the in-plane direction q_{100} of the PZT in-plane scans (Fig. 2.13 b and c), the (002) planes in the sol-gel sample depict larger mosaicity, which can be seen as a signature of the lower coherence length along the in-plane direction for the sol-gel samples, and consequently a reduced size of the crystallites as compared to the PLD sample ones.

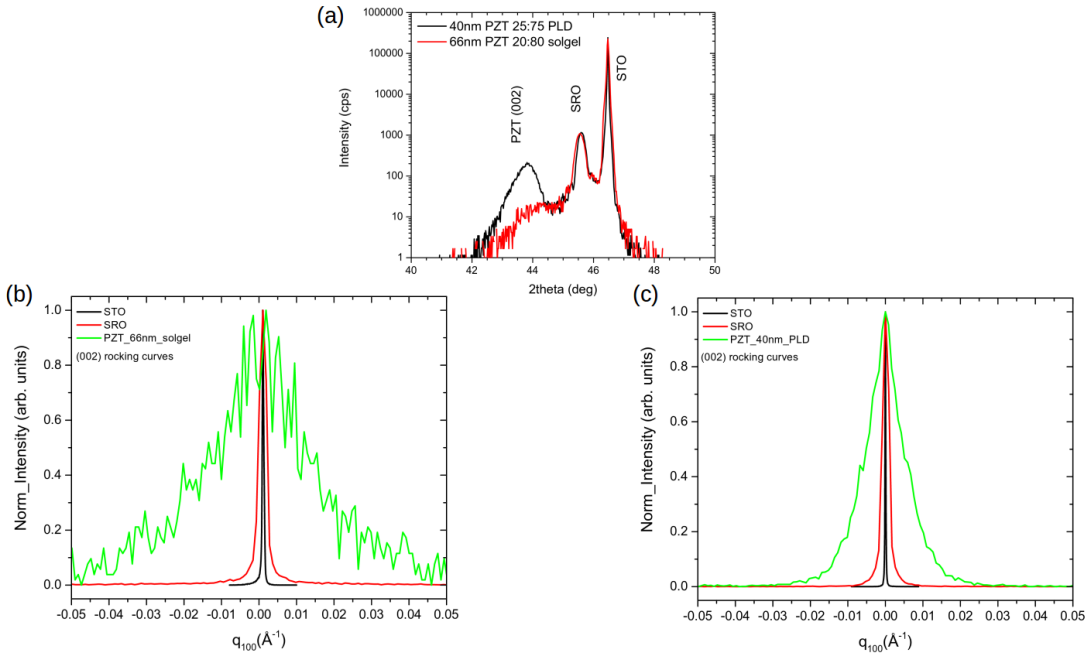

Figure 2.13: (a) $2\theta/\omega$ scans around 002 STO reflections for the 66 nm sol-gel and the 40 nm PLD samples (grown on SRO (30 nm)//STO (001)). (b) and (c) rocking curves or in-plane diffraction profiles, along [100] for (002) reflections corresponding to PZT, SRO, STO (reflection indexed in pseudocubic notation, for simplicity) for (b) the 66 nm PZT 20:80 sol-gel and (c) the 40 nm PZT 25:75 PLD films, collected with fixed 2θ values deduced from the peak center position for PZT, SRO and STO determined from the $2\theta/\omega$ scans shown in (a).

2.3 Structural characterization of the PLD $BiFeO_3$ thin films

X-ray diffraction of the BFO sample was carried out by Oliver Paull at the University of New South Wales in Sydney, Australia. The experiments were performed with a Rigaku SmartLab diffractometer (9kW rotating anode x-ray generator operating at 200 mA, 45 kV) with a 2 mm slit before the sample.

The results in Fig. 2.14 present a film with a good crystallinity in a similar way to the PZT PLD films. It is interesting to note that the peak for the electrode of the sample (LSMO) is located on the other side of the STO peak. Therefore, the BFO films may present a different strain state than those of PZT shown so far, as well as different electrical properties from different nature of the used electrodes, i.e. LSMO and SRO.

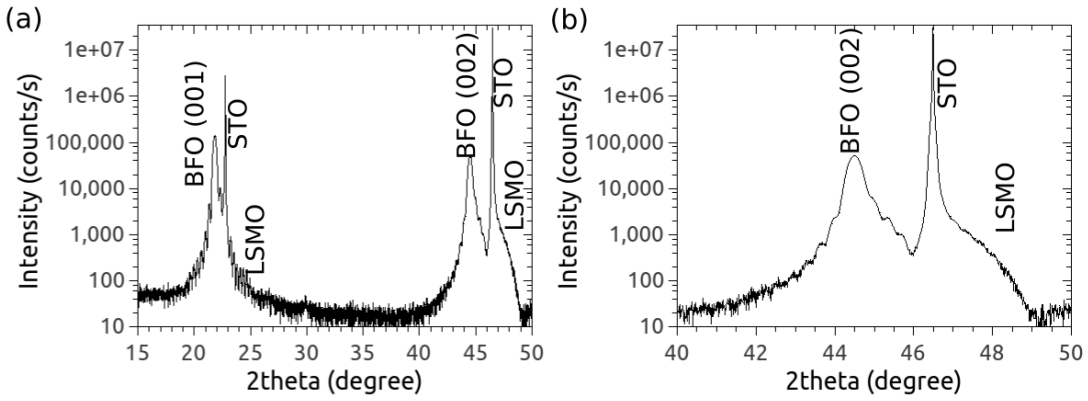

Figure 2.14: (a) $2\theta/\omega$ scans around 001 and 002 STO reflections and (b) zoom to the 002 reflection for the BFO sample. Pseudocubic notation was used for BFO indexing.

2.4 Conclusions

The AFM and more specifically the PFM are the main tools used for this work. They allow for imaging and spectroscopy studies of ferroelectric domains and domain walls. However, the information obtained is exclusively from the surface of the sample. To complement PFM measurements, XRD, STEM, RBS and SIMS were performed to provide information about the whole volume of the samples.

The materials studied consist of a series of PZT 20:80 samples synthesized by sol-gel, and two PZT 25:75 samples and one BFO grown by PLD. In the PZT case, SRO electrodes were grown by RF sputtering at INL on STO (001) substrates, and in the BFO case the LSMO electrode was grown *in situ* by PLD before the BFO deposition, all over STO (001) substrate. A list of all the samples can be found in Appendix A

Chapter 3

Atomic force microscopy for the study of ferroelectric thin films

The atomic force microscope (AFM) is a mechanical device that is used to make different kinds of measurements on a sample's surface. It differs from the optical and electron microscope in that it uses a physical probe instead of photons or electrodes to obtain an image. This section will be dedicated to the description of the AFM and the modes used for this thesis.

3.1 Description

The AFM was invented in 1986 by Gerd Binnig et al. (Binnig, 1986; Binnig et al., 1986), after the breakthrough invention of the scanning tunneling microscope (STM) as the first scanning probe microscope (Binnig and Rohrer, 1983). Indeed, both AFM and STM share the same basic idea: a small probe is placed very close to a surface thanks to a piezoelectric actuator. The main difference between STM and AFM is that the former measures a current when a voltage is applied, while the latter measures a force applied on the probe.

Specifically, an AFM is composed of three components: the probe, which consists in a cantilever with a nanometric size tip, a laser that will reflect on the cantilever top surface and be detected by a photodiode to measure the deflection of the tip, and a piezoelectric actuator, which will control the relative position of the probe and the sample. A schematic of an AFM is shown in Fig. 3.1. While the design seems simple, it is important to notice that piezoelectric materials are necessary to reach the fine control needed to scan surfaces down to the nanometer scale.

The tip of the AFM scans the surface in order to produce a topographic image. However, there are four different ways to proceed depending on the tip-sample

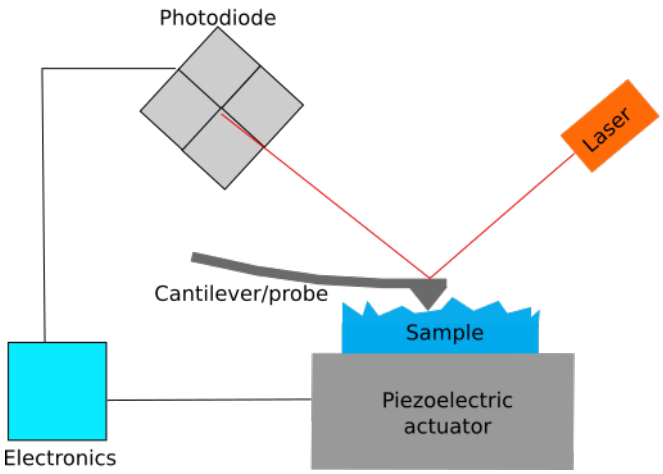

Figure 3.1: Schematic of an AFM with its main components.

interaction. This interaction can be represented by a Lennard-Jones potential:

$$V_{LJ} = \frac{C_1}{r^{12}} - \frac{C_2}{r^6} \tag{3.1}$$

Where C_1 and C_2 are constants and r is the distance between the sample and the tip. The first fraction of the equation corresponds to the repulsive forces while the second one corresponds to the attractive forces. Depending on the distance, the attractive interaction will prevail or not on the repulsive interaction, which gives rise to different operating modes described in the next section.

3.2 AFM imaging modes

These different modes are defined depending on which force governs the tip-sample interaction. Accordingly, there are four main different modes available: contact, tapping, non contact and peak-force tapping.

3.2.1 Contact mode

In contact mode, the tip is in contact with the surface. In this situation, the force acting on the tip is repulsive, as a result of the inter-atomic interaction (Coulomb forces), mainly electron clouds repelling each other. The AFM probe can be modeled as a spring with a mass at its end. In this model, the cantilever/tip system behaves like an elastic spring, where the applied force is described by Hooke's law:

$$F = k\delta \tag{3.2}$$

Where F is the force, k is the spring constant of the cantilever and δ is the displacement with respect to the equilibrium position of the cantilever. In contact

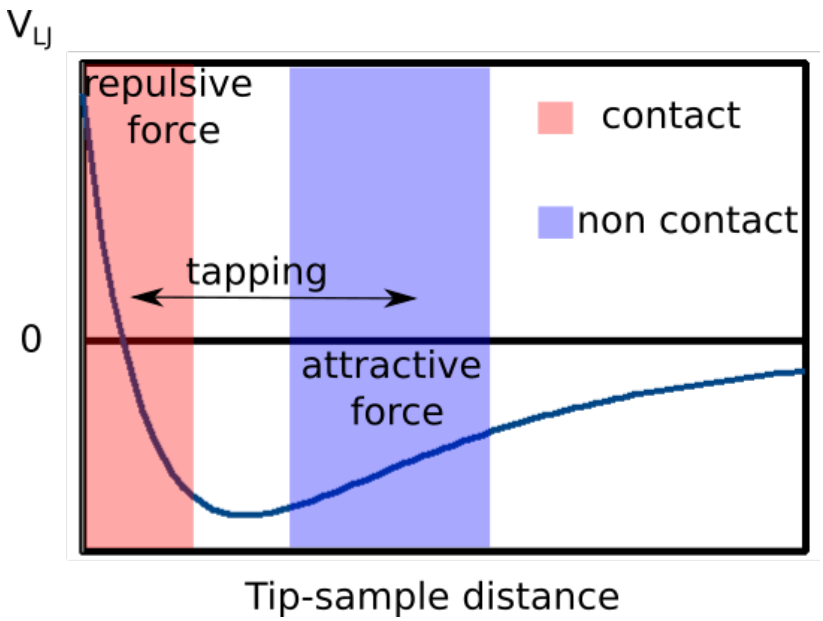

Figure 3.2: Lennard-Jones potential for the tip-sample interaction. In the repulsive force region the AFM operates in contact mode (red region), while in the attractive force region the AFM operates in non contact mode (blue region, although it can also be operated further to the right). Tapping mode operates in both regions.

mode, F is kept constant and the electronic feedback assures to move the tip accordingly. However, in this mode it can be interesting to obtain the pressure applied by the tip. Therefore, it is important to know the area of contact between the tip and the sample. Different contact models can be used:

- **Flat disc model**: the tip is a disc of a finite radius. In this case, no deformation of the tip is considered as the disc is supposed to be flat. In general, this model can be applied to worn tips whose contact area with the surface of the sample is a flat disc. While simple, this model cannot be applied to most tips. Examples of this model can be found in the literature for mechanical switching experiments (Wang et al., 2020).

- **Hertz's model**: both the tip and surface deform when in contact, therefore the surface in contact changes as a function of the force. Following this model, the radius of the contact area between two spheres can be written as (Jacobs et al., 2013):

$$a = \left(\frac{3F_{applied}R_{eff}}{4E^*}\right)^{1/3} \tag{3.3}$$

  Where a is the contact area radius, $F_{applied}$ the force applied, R_{eff} the effective radius and E^* the effective Young's modulus. These two last parameter can

be written as:

$$R_{eff} = \left(\frac{1}{R_1} + \frac{1}{R_2}\right)^{-1} \tag{3.4}$$

$$E^* = \left(\frac{1-\nu_1}{E_1} + \frac{1-\nu_2}{E_2}\right)^{-1} \tag{3.5}$$

Where R_1 (R_2) is the radius of the sphere 1 (2), for a flat surface it can be considered infinite and therefore R_{eff} is the radius of the tip. E and ν are the Young's modulus and the Poisson's ratio of the materials. Therefore, a good knowledge of the mechanical properties is necessary to apply this model. While this model is more precise than the flat disc model and better determines the area of contact, it still has some limitations. For example, it assumes that the material exhibits a linear elastic behavior and the surfaces are smooth. At the same time it does not take into account any friction or adhesion force.

- **Derjaguin-Müller-Toporov (DMT) (Muller et al., 1983) and Johnson-Kendall-Roberts (JKR) (Johnson et al., 1971) models**: the area of contact between the sample and the tip is the same as the one obtained by the Hertz's model, but the force applied is different due to the adhesive forces (Tabor, 1977). These two models obtain different adhesive forces. Experimentally, the adhesive forces are a complex problem to take into account in an AFM and these models or even mixture of them are only some of the possible approaches (Barthel, 2008).

The contact mode will be the main scanning mode used in this work since it ensures a good electrical contact and at the same time allows for the constant application of a mechanical load. Nevertheless, the contact mode may damage the tip and the sample, which means that it can hardly be used on soft surface. For the experiments presented in this thesis, Hertz's model will be applied since the flat disc model is too simple to describe experiments with diamond tips and the DMT and JKR models require a precise measurement of elastic parameters in the sample that can be obtained with other AFM modes.

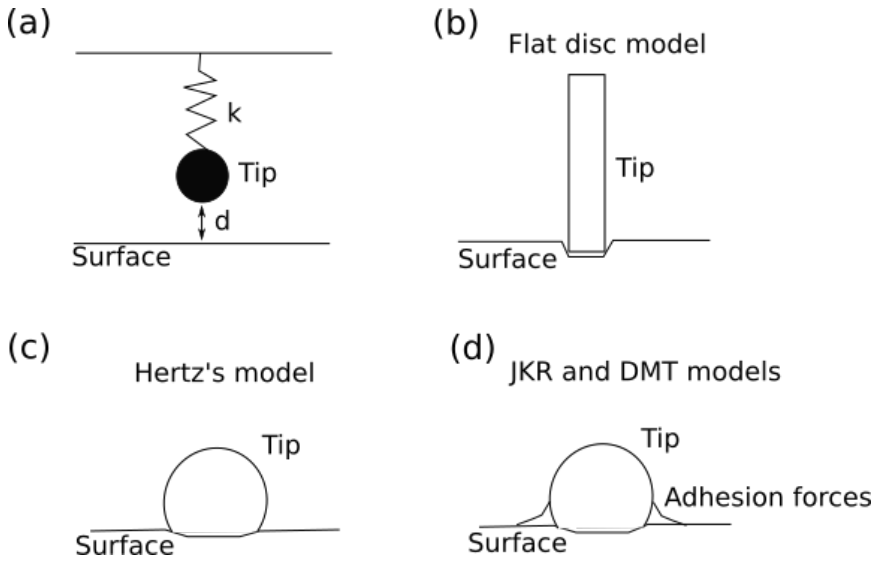

Figure 3.3: Models of the tip and cantilever for AFM imaging in contact mode. (a) Model of an AFM probe where the cantilever can be seen as a spring with constant k with the tip bottom at a distance d of the surfce (d may change depending on the mode). (b) Flat disc model (c) Hertz's model and (d) JKR and DMT models for the tip-sample interaction.

3.2.2 Tapping mode

In this mode the AFM probe is oscillating at or close to the resonance frequency while tapping constantly on the sample. The parameter used to control the position of the tip is the amplitude of oscillation, which is in the range of tens of nm. When a change in the amplitude is detected, the electronic feedback moves the tip accordingly to maintain a constant amplitude. In this mode, repulsive and attractive forces play a role.

This mode allows for a better spatial resolution down to the detection of molecules (Klinov and Magonov, 2004). This mode is common for AFM in liquids and fluids (García and Pérez, 2002; García and Paulo, 1999). Even if the contact during tapping occurs with a higher force than in contact mode, the tip is in contact with the surface for a short time and does not move laterally, which leads to smaller tip and sample degradations.

3.2.3 Non contact mode

In non contact mode the tip is close to the surface of the material (tip-sample distance ranging from nm to tens of nm (Martin et al., 1987)) and oscillates with a small amplitude without touching the surface. In this mode, the parameter used to con-

trol the distance between the tip and the sample is the resonance frequency. Indeed, the attractive force (Van der Waals) between the tip and the sample will change the resonance when the tip is sensitive to the attractive part of the Lennard-Jones potential. The electronic feedback will modify the tip-surface distance to maintain a constant resonance frequency. Therefore, this mode works in the attractive regime of forces (see Fig 3.2).

This is the best mode to work on soft and biological samples since there is no damage either to the tip or the sample. For instance, it has been shown that non contact AFM can resolve the structure of molecules under the right conditions (Gross et al., 2009). However, it is usually perform in ultra high vacuum or in a low environment to benefit from a better sensitivity. This mode was not used for this thesis since it is not compatible with the main techniques of study.

3.2.4 Peak-force tapping mode

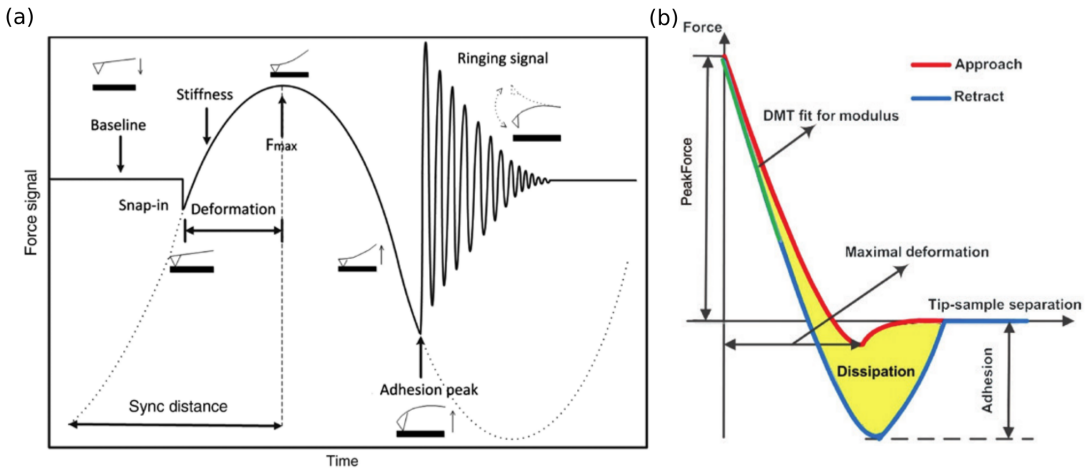

Figure 3.4: (a) Movement and force applied by the tip during peak force tapping mode. (b) Force curve and the information obtained from different regions of the force curve. (Xu et al., 2018)

One of the main resulting applications of the AFM capability to measure force is force spectroscopy. Indeed, by engaging and disengaging the tip it is possible to obtain the force applied on the tip as a function of the tip-sample distance, where the contact and the adhesion forces can be evaluated. Peak-force tapping mode is an AFM mode, which works as a combination of force spectroscopy and tapping mode. In this mode, the piezoelectric actuator goes up and down moving the tip over the sample. The tip-sample distance is reduced until a certain force, called “peak force“, is reached. Then, the piezoelectric retracts to disengage the tip. Therefore, the

parameter used to control the tip over the sample is the force applied during the contact. In a way, this mode can be described as performing multiple force curves over the sample.

In peak-force tapping mode it is possible to obtain mechanical information such as the adhesion force, the stiffness and the dissipation besides the topography. Furthermore, it is possible to fit the DMT contact model to obtain the effective Young's modulus.

3.3 Piezoresponse force microscopy

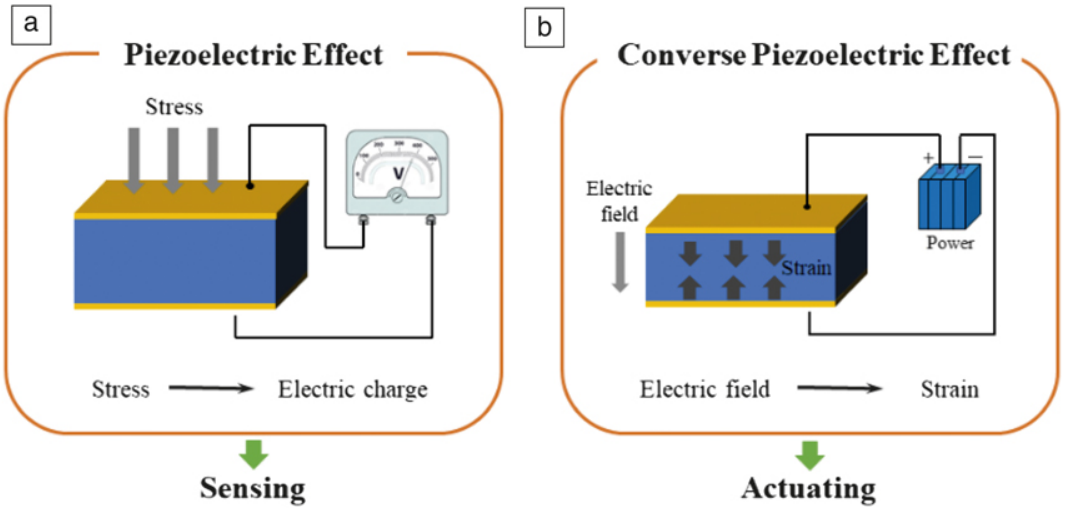

Figure 3.5: Schematics for the (a) direct and (b) converse piezoelectric effect (Rödel and Li, 2018).

Piezoresponse force microscopy (PFM) is an electrical mode of AFM that allows to map piezoelectric activity, and thus ferroelectric activity. This technique was invented in 1992 (Güthner and Dransfeld, 1992), although it was named later in 1996 (Gruverman, 1996), and is based on the converse piezoelectric effect. While for the direct piezoelectric effect a stress creates an electric displacement, for the converse piezoelectric effect an electric field creates a strain. This can be represented mathematically as:

$$S_{ij} = d_{ijk} E_k \tag{3.6}$$

Where S_{ij} is the deformation tensor, d_{ijk} is the piezoelectric tensor and E_k is the applied electric field. With an AFM and a conductive tip, an electric field can be applied to a ferroelectric material, which in turn will deform. If an alternating electric field (an ac voltage) is applied, the ferroelectric material will vibrate either

following or opposing the electric field depending on the polarization direction of the domain. In this way, ferroelectric domains can be imaged. However, ferroelectric materials may have an in-plane and an out-of-plane component of polarization. As a function of which signal is being recorded we can differentiate between vertical and lateral PFM, as described in the next section.

3.3.1 Vertical PFM

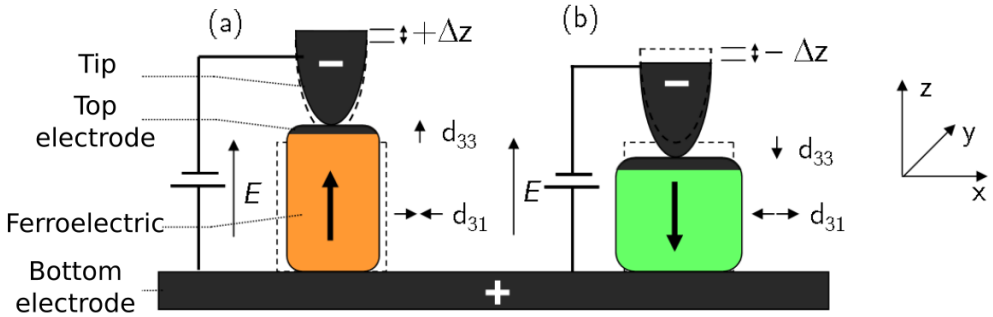

Figure 3.6: Schematics for vertical PFM. (a) elongation of the ferroelectric material when the polarization is in the same direction as the electric field and (b) contraction when the polarization is opposed to the electric field. A top electrode is not necessary, but can be used. (Brugère, 2011)

In vertical PFM an out-of-plane electric field (generated by a voltage V) creates a vertical strain in the ferroelectric material. Depending on the polarization of the material, the domains will elongate or contract. However, the interpretation of the motion of the surface should take into account the electrostriction effect, which appears in all crystalline structures, and relates to a quadratic deformation of the material under the applied electric field (while the piezoelectric deformation is linear). If both phenomena are taken into account, the vertical deformation (Δz) of a ferroelectric material when a voltage is applied can be written as (Kholkin et al., 2007):

$$\Delta z = d_{33}V + \frac{M_{333}}{t}V^2 \tag{3.7}$$

Where V is the voltage applied, d_{33} is the piezoelectric coefficient, M_{333} is the electrostrictive constant that does not depend on the direction of the polarization, and t is the thickness of the sample. d_{33} sign changes as a function of the polarization. The quadratic term of the equation corresponds to electrostriction, and is smaller than the piezoelectric effect defined by the first term. In the situation of a sinusoidal voltage being applied, the frequency of electrostriction becomes 2 times the

frequency ω of the voltage. If the signal is filtered by the frequency ω, only the piezoelectric term remains:

$$\Delta z = \pm d_{33} V_{ac} \sin(\omega t) \tag{3.8}$$

This signal can be recorded with the help of a lock-in amplifier in order to obtain two types of images. However, this signal suffers from cross-talk (Jesse et al., 2010) between the topography and electrostatic effects. All this will be explained in next sections.

3.3.2 Lateral and vector PFM

While in vertical PFM the vertical movement of the tip is measured (deflection and buckling) in lateral PFM the lateral movement is measured (torsion). Usually, the photodiode of an AFM is divided in four different sections to differentiate these movements as shown in Fig. 3.7.

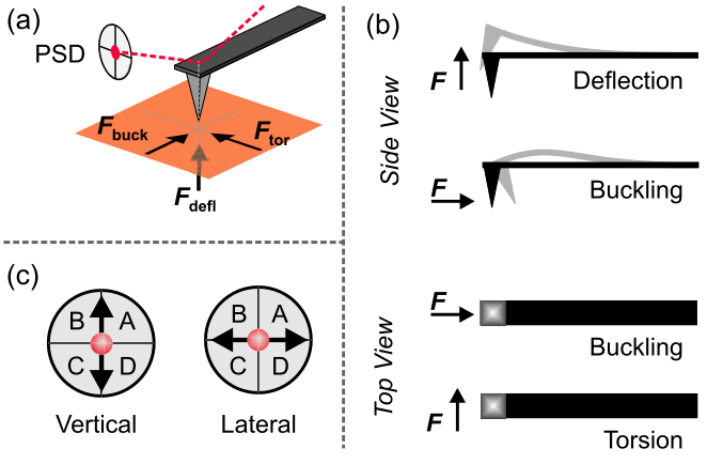

Figure 3.7: (a) The three different forces acting on an AFM tip leading to three different kinds of movements: deflection, buckling and torsion. (b) Side and top views of the cantilever movement. (c) Possible movements of the laser on the segmented photodiode. The torsion movement of the cantilever is registered as lateral displacement in the photodiode while buckling and deflection are seen as vertical movement (Soergel, 2011).

Indeed, applying a vertical electric field to a ferroelectric material with an in-plane polarization will create a shear stress. This stress will make the ferroelectric material vibrate laterally, which will create torsional forces acting on the tip and the cantilever. This vibration can be expressed mathematically in a similar way as the vertical displacement:

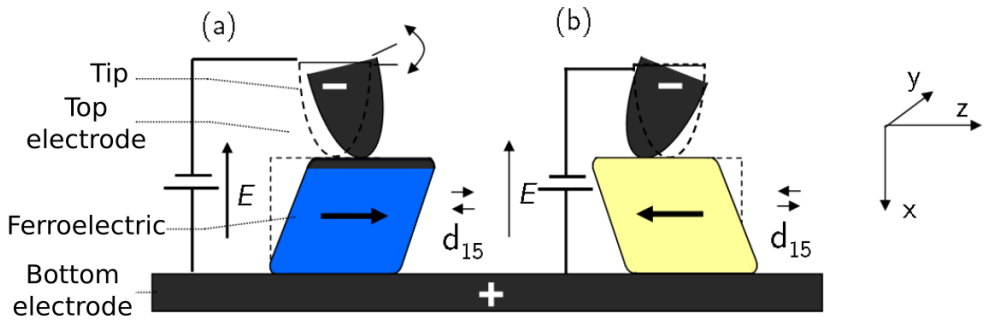

Figure 3.8: Schematics for lateral PFM. Like in vertical PFM, different directions of the polarization create different deformations in the material. (Brugère, 2011)

$$\Delta x = \pm d_{15} V_{ac} \sin(\omega t) \tag{3.9}$$

Where in this case Δx is the lateral deformation and the coefficient d_{15} represents a shear stress. However, this equation gives information only about one axis in-plane, which means that even with lateral and vertical PFM it would not be possible to know exactly the three dimensional direction of the polarization in the material. In order to solve this issue, vector PFM was proposed as an optimized approach (Rodriguez et al., 2004; Kalinin et al., 2006).

In vector PFM, the surface is scanned two times rotating the sample by 90°, thus giving two different images of lateral PFM, one corresponding to Δx and another to Δy. If the possible directions of polarization are known, it is possible to combine these two images with a vertical PFM image to determine the three dimensional direction of the polarization in a ferroelectric material.

3.3.3 Signal processing in PFM

As explained in previous sections, PFM provides the signal of lattice displacement due to the converse piezoelectric effect. However, this signal is mixed with the topography, and a lock-in amplifier is needed to separate them. The lock-in will help to demodulate the signal, filter the topography and provide two types of information: amplitude and phase (compared with a reference signal).

A lock-in is different from other amplifiers by the fact that it amplifies a signal of a specific frequency with a precision of 0.01 Hz. This allows for the measurement of very noisy signals, as long as the frequency of the signal is known. To achieve this, the lock-in takes a reference signal and multiplies it by another signal, filtering only the frequency of the reference signal. In the case of PFM, the reference signal

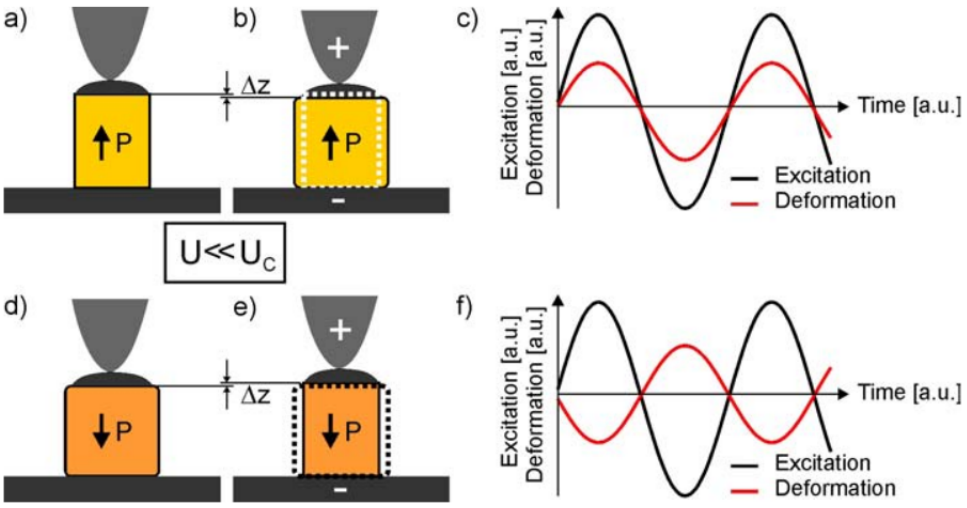

Figure 3.9: (a),(b), (d) and (e): schematics showing a ferroelectric material elongating or contracting under an electric field depending of its polarization. (c), (f) Signal input and deformation as a function of time. In the case of the polarization pointing upwards the signal should be in phase (c), while in the case of the polarization downwards it should be in opposition of phase (f). (Peter, 2006)

will be the ac voltage applied to the tip, which can be written as:

$$V_{ref} = V_{ac}\cos(\omega t) \tag{3.10}$$

While the signal measured by the photodiode can be expressed as:

$$V_{sig} = \Delta z_{topo} + A\cos(\omega t + \phi) \tag{3.11}$$

Where A is the amplitude of oscillation, ϕ is the phase that will depend on the material sense of polarization and $\Delta\ z_{topo}$ is the signal change due to topography. Multiplying V_{sig} and V_{ref} leads to:

$$V_{out} = \frac{1}{2}V_{ac}A\cos(\phi) + \frac{1}{2}V_{ac}A\cos(2\omega t + \phi) + \Delta z_{topo}V_{ac}\cos(\omega t) \tag{3.12}$$

Where only the first term of the equation is a dc signal, therefore, filtering the signal or averaging it only this term remains as:

$$X = \frac{1}{2}V_{ac}A\cos(\phi) \tag{3.13}$$

This is already a pure signal of the ferroelectric response, nevertheless, if the phase is 90°, the signal would be zero. To avoid this, modern lock-in have a second demodulator that uses the same reference signal but with a phase of 90°, which gives the following signal as a result:

$$Y = \frac{1}{2}V_{ac}A\cos(\phi + \frac{\pi}{2}) = \frac{1}{2}V_{ac}A\sin(\phi) \tag{3.14}$$

With these two outputs, X and Y, from the lock-in amplifier, it is possible to obtain the amplitude of oscillation independently of the phase by computing:

$$R = \sqrt{X^2 + Y^2} \tag{3.15}$$

Finally, it is also possible to obtain the phase between the reference signal and the photodiode signal by using the following equation:

$$\Phi = \tan^{-1}\left(\frac{Y}{X}\right) \tag{3.16}$$

In practice, it is thus possible to obtain two images: the amplitude and the phase image.

3.3.4 Amplitude and phase

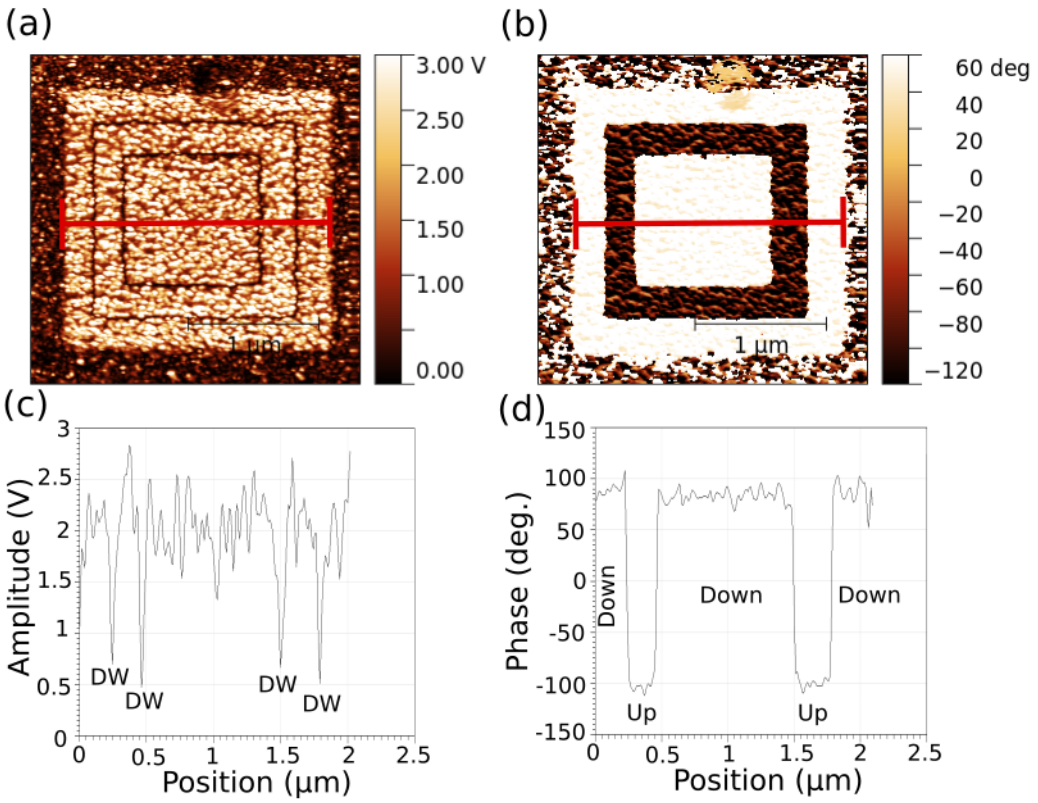

Figure 3.10: (a) amplitude and (b) phase image of 33 nm thick PZT sample that has been poled electrically to create a ferroelectric pattern. The red line indicates the position of the profiles obtained for (c) the amplitude where the minimum represents domain walls (DW) and (d) the phase where the up and down domain can be seen.

The PFM signal from the vibration of the ferroelectric material gives two complementary outputs:

- **Amplitude signal**: It gives information about piezoelectric activity under the tip. The amplitude will depend on the piezoelectric coefficient, but will decrease at domain walls where there is no polarization. With this kind of image it is possible to observe domain walls, but not to determine the direction of the polarization.

- **Phase signal**: It provides information about the direction of the polarization. As shown in Fig. 3.9, the PFM signal arising from down polarization should be in phase opposition with the reference signal, while the PFM signal arising from the up polarization should be in phase. However, in Fig. 3.10 both up and down polarizations have a phase, which is neither 0° nor 180°. This can be explained due to background noise (Jungk et al., 2007) and configurations of the electronics. Furthermore, the image (b) in Fig. 3.10 has all signals inverted with respect the reference signal due to the electronics used in our microscope, therefore the up polarization has a negative sign. Nevertheless, the difference between up and down polarizations should always be around 180°, which is the case in Fig. 3.10.

3.3.5 Dual frequency resonance tracking

Initially, PFM was performed using single frequency PFM, where one frequency is chosen for the ac voltage. However, Okino et al. showed that measurements at the contact resonance frequency improved the signal to noise ratio of the PFM signal (Okino et al., 2003). A direct consequence of this result is that it is possible to work with smaller voltages, thus decreasing electrostatic artifacts. Since other techniques such as non-contact AFM depend entirely of the frequencies used, the different resonance frequencies were already studied (Caron et al., 2004), which provides references of lateral resonance modes to increase the signal of in-plane polarization. The first vertical contact resonance frequency ($f_{contact}$) can be obtained from the free resonance frequency (f_{free}) (Rabe, 2006):

$$f_{contact} = 4.4 f_{free} \tag{3.17}$$

However, this equation is an approximation since the contact resonance frequency also depends on the force applied and the adhesion between the tip and the surface, which will change while scanning. Due to this, the frequency shifts constantly and working in single frequency mode at the contact resonance frequency is challenging. Results suggest that it is better to work near the resonance frequency rather than exactly at it (Harnagea et al., 2003), to avoid problems such as not having a

phase contrast. The dual frequency resonance tracking (DFRT) allows following the resonance frequency while scanning.

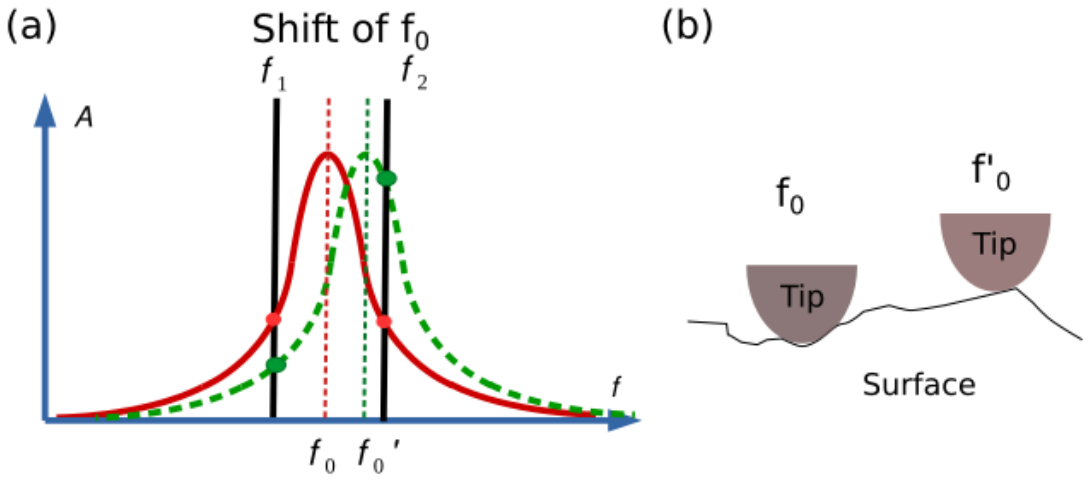

Figure 3.11: (a) Plot of two resonance amplitude peaks where the different frequencies and amplitudes involved in DFRT can be observed. When f_0 shifts to f_0', A_1 and A_2 are not equal, f_1 and f_2 will change until their difference is null. (b) Schematic of a tip over the surface. Different contacts between sample and tip will create a change in the resonance frequency as the one shown in (a).

DFRT was developed in 2007 by Rodriguez et al. (Rodriguez et al., 2007a). In this technique, the resonance frequency (f_0) is followed by applying two signals (referred as satellites) with frequencies (f_1,f_0) close to f_0:

$$f_1 = f_0 - \Delta f \tag{3.18}$$

$$f_2 = f_0 + \Delta f \tag{3.19}$$

Where f_1 and f_2 are the frequencies measured by lock-in 1 and 2, respectively, and Δf is the difference to f_0. Δf can be obtained by finding the point where the amplitude decreases to half of the amplitude at f_0. Since the amplitude peak is supposed to be symmetric, the amplitudes (A_1 and A_2) at f_1 and f_2 should be the same. However, moving the tip will change f_0, and A_1 and A_2 will also change. In this situation, a proportional-integral-derivative (PID) controller will impose that A_1 and A_2 are equal. Therefore if $A_1 > A_2$, the PID sends a signal to change f_0 until A_1-A_2=0, which is the example of Fig. 3.11 (a). In this way it is possible to obtain a better PFM signal than in single frequency PFM without amplitude changes due to the shift of f_0. When working with DFRT, the obtained f_1 and f_2 signals are equally good for imaging domain and domain walls.

DFRT PFM will be the technique most used during this thesis. It is important to note that in the literature, DRFT is sometimes referred to as dual ac resonance tracking (DART).

3.3.6 Switching spectroscopy PFM

As AFM, PFM is not limited to imaging and is able to perform spectroscopy. Indeed, since the discovery of PFM, spectroscopy studies have been performed in an effort to better understand ferroelectric switching (Eng, 1999). Different techniques such as switching spectroscopy PFM (SS-PFM) and time spectroscopy PFM have been developed (Rodriguez et al., 2007b), but this work will focus on SS-PFM.

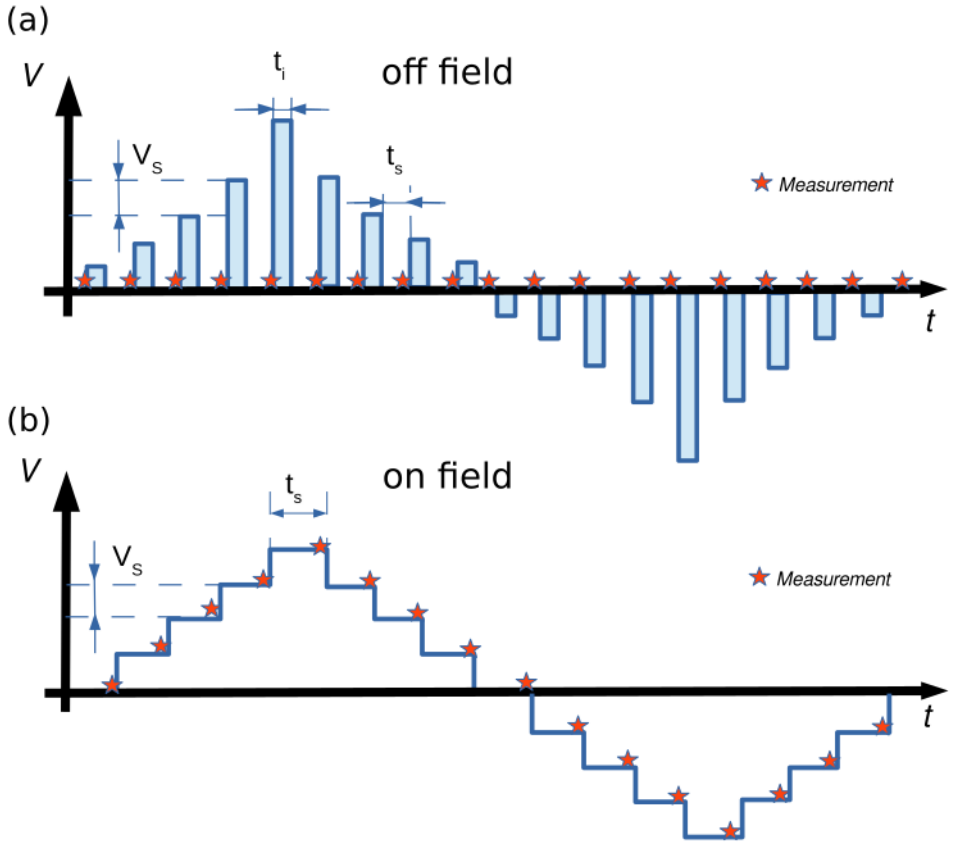

Figure 3.12: (a) Plot of the dc voltage applied during off-field SS-PFM cycles and (b) during on-field cycles. At the same time, a small ac voltage is always applied, but it is smaller than the coercive voltage.

As its name implies, SS-PFM is optimized to study the PFM signal of a ferroelectric material during switching events. This is achieved by applying a triangular dc voltage ramp that increases over the positive coercive voltage and decreases below the negative coercive voltage. At the same time, the small ac signal used for PFM is

being applied to the sample and recorded with the lock-in. Finally, the PFM signal is plotted against the dc voltage used to obtain a phase, amplitude or even X and Y signal detailed in Section 3.3.3. However, there are two different ways to apply the dc voltage, which give two possible modes for SS-PFM:

- **On-field SS-PFM**: In this mode, the dc voltage is always on, even when measuring the PFM signal. The voltage changes following a voltage step (V_s) and time step (t_s) that are kept constant. At the end of a time step, before the voltage is changed, the PFM signal for the corresponding voltage is measured. Fig 3.12 (b) shows the step and the corresponding measurement point. This mode does not allow the material to relax, which means that polarization will not have the possibility to switch back, and that electrostatics and leakage effects will play a bigger role than in off-field. Usually, these effects appear in the shape of the hysteresis loops. For example, a phase loop will be inverted if electrostatic effects are involved (Balke et al., 2015). A normal phase loop is shown in Fig. 3.13 b, while an electrostatic one is shown in Fig. 3.14 b.

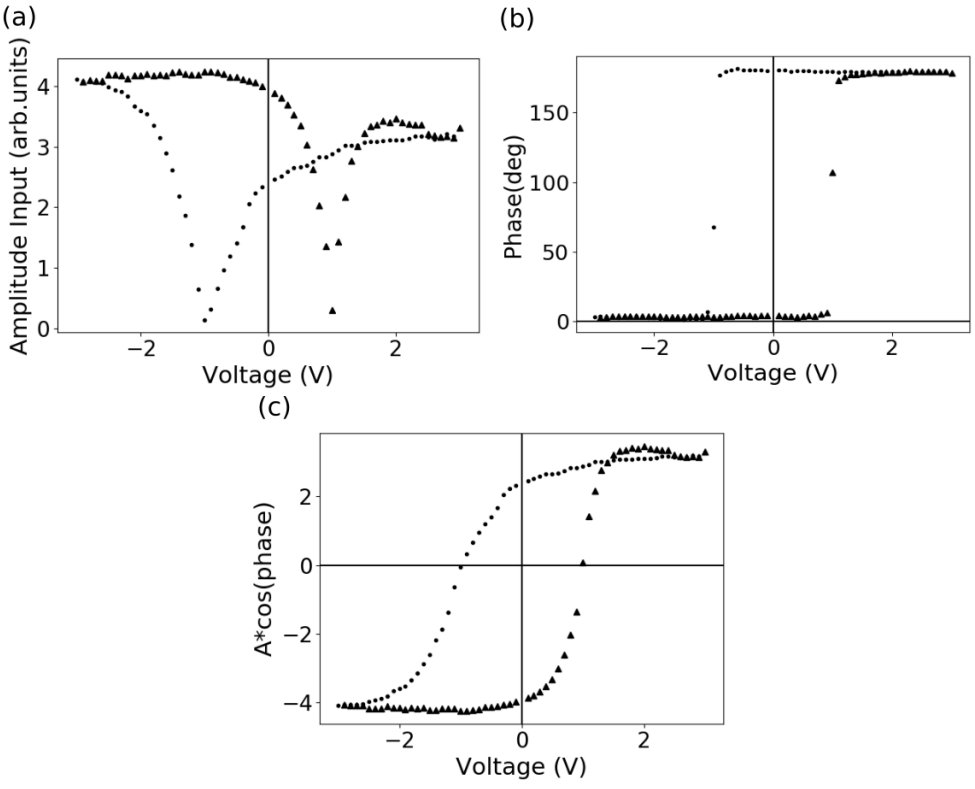

Figure 3.13: Loops of off-field SS-PFM in PZT. (a) Amplitude, (b) phase and (c) X signal. The coercive voltage can be seen as the points of minimum signal in (a) and the points where the phase sign changes in (b).

- **Off-field SS-PFM**: In this mode, the voltage is applied by pulses that last al-

ways the same time (t_i) and are separated by a time step (t_s). After each pulse, when the dc voltage is null, the PFM signal is measured. The duration of the pulse and the step that separates pulses can be changed to study the remnant polarization. Because the measurement is performed without dc voltage, the electrostatic and leakage effects are less important than in the on-field mode and the signal presents less parasitic contributions. However, some materials switch back to their original polarization faster than few milliseconds, so that hysteresis loops cannot be recorded using this experimental protocol.

Both on-field and off-field modes will be used for this thesis, since they provide complementary information about the ferroelectric nature of the materials studied. The amplitude and phase images in Fig. 3.13 (a) and (b), as well as the X-signal in (c) are typical examples.

3.3.7 PFM artifacts

Since PFM is an electromechanical technique, plenty of artifacts must be taken into account. These effects are mainly electrostatic and electrochemical, although electrostriction and flexoelectricity should also be considered (Seol et al., 2017).

- **Electrostatic force**: Since there is a voltage applied to the AFM probe, the appearance of electrostatic forces between the probe and the material may change the amplitude measured. These forces can be separated between the local electrostatic forces that are applied to the tip and the non-local electrostatic forces that are applied to the cantilever. These forces can be expressed as:

$$F_{ES} = \frac{1}{2}\frac{dC}{dz}V^2 \tag{3.20}$$

Where F_{ES} is the electrostatic force, C is the capacitance, V is the voltage applied and z the distance between the tip and the sample for the local force and the distance along the z axis between the cantilever and the sample for the non-local force. When an ac and a dc voltage are applied, this force gives rise to an additional surface displacement:

$$x_{ES} = \frac{F_{ES}}{k} = \frac{1}{2k}\frac{dC}{dz}(V_{dc} + V_{cpd} + V_{ac}\sin(\omega t))^2 \tag{3.21}$$

Where k is the cantilever spring constant and V_{cpd} the contact-potential between the tip and the sample. Since the PFM signal is measured by a lock-in amplifier, only the components with the same ac frequency will be obtained, which means that the electrostatic deflection measured will be:

$$D_{ES,\omega} = \frac{1}{2k}\frac{dC}{dz}(V_{dc} + V_{cpd})V_{ac}\sin(\omega t) \tag{3.22}$$

Since this electrostatic interaction can occur between the tip and the surface, as well as between the cantilever and the sample, the deflections due to local and non-local forces must be considered. From the equation above, it is possible to decrease the electrostatic contribution in PFM in multiple ways. First by just applying a small voltage, which can be done using DFRT. A second option would be to increase the spring constant of the cantilever and use longer tips to increase the distance between the cantilever and the sample. Indeed, it has been demonstrated that using longer and stiffer tips decreases the electrostatic signal (Gomez et al., 2018). However, the signal also depends on the material studied since the deflection is a function of V_{cpd}. Furthermore, it also depends linearly on the applied dc voltage, which is of importance when performing SS-PFM experiments: a linear behavior (Fig. 3.14) can be related to electrostatic effects.

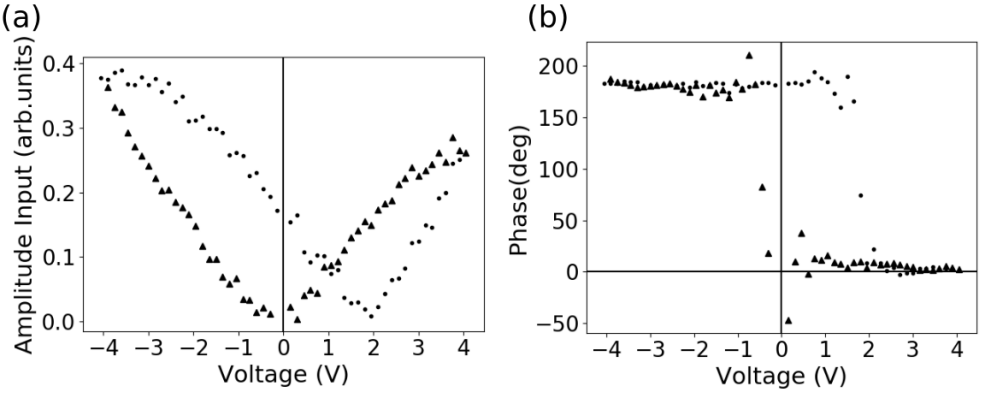

Figure 3.14: Electrostatic loops of on-field SS-PFM in PZT. (a) Amplitude, which shows a linear behavior due to electrostatic forces. (b) Phase, which shows an inverted loop. The up polarization is shown in the the negative voltage instead of the positive.

- **Electrochemistry**: The application of an electric field can change the chemistry of ferroelectric materials. These effects range from charging at the surface of the material, which can increase the PFM amplitude, to actual destruction of the surface.

  A common phenomenon observed in a variety of ferroelectric materials is the increase of height in the topography after applying a voltage, forming so-called hillocks (Hourani, 2011). The origin of these hillocks is related with the injection of oxygen vacancies or protons. Indeed, hillocks up to 100 nm have been observed in SS-PFM experiments with voltages higher than 4 V bias (Strelcov et al., 2012). While hillocks do not affect directly the PFM signal,

it does change the topography and may affect the shape of hysteresis loops of the material, which should be avoided.

Finally, Vegard strain, which is the strain appearing because of changes in the lattice parameter after a redistribution of defects due to the application of an electric field in the material, can modify the PFM signal. Indeed, it has been reported that Vegard strain can create an amplitude signal (Chen et al., 2014), which was used to create the electrochemical strain microscope.

While electrochemistry plays a big role in electrical modes of PFM, the processes involved are rather complex and can be challenging to differentiate from the PFM signal. It gives another reason to use small voltages and DFRT to decrease the contribution of these electromechanical effects.

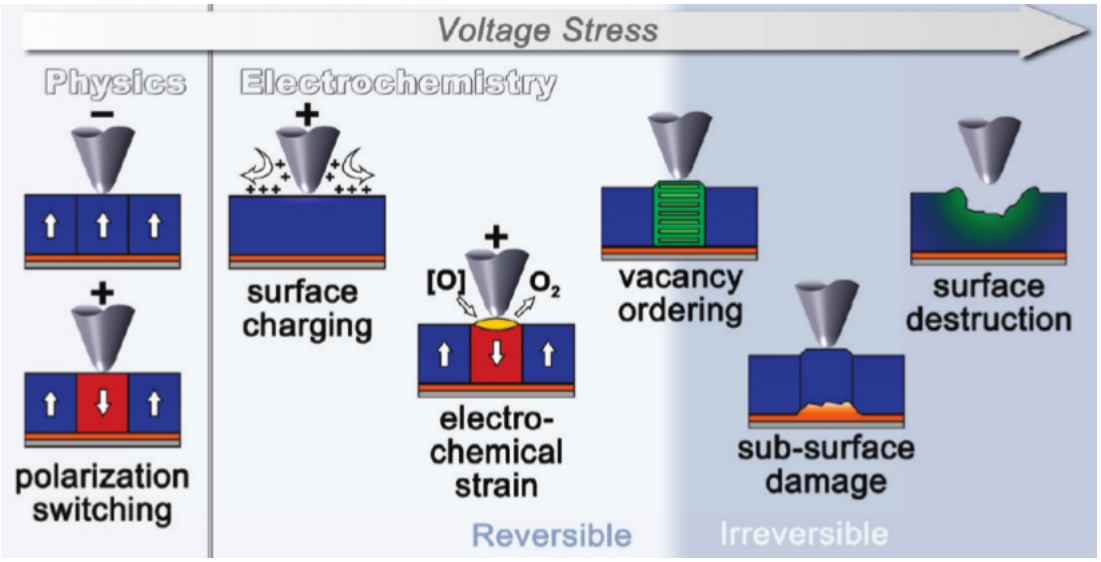

Figure 3.15: On the left ferroelectric switching, which is a pure physical effect. On the right electrochemical effects related with the application of a voltage. The higher the voltage, the more effects appear including irreversible effects that would damage the sample permanently (Kalinin et al., 2011).

- **Joule effect**: In ferroelectrics that present a considerable leakage current, the thermal expansion due to Joule effect should be considered. The expansion due to a leakage current can be computed from the next equation:

$$x_J = \beta I^2 R \tag{3.23}$$

Where x_J is the displacement is the expansion, I is the intensity, R is the resistance and β is the Joule heat transduction coefficient (Kim et al., 2011). If we consider a sinusoidal intensity, then it is possible to write the amplitude

of displacement at a frequency ω as:

$$x_{J,\omega} = -\beta \frac{RI_{ac}^2}{2} \cos(2\omega t) \tag{3.24}$$

This last equation shows that the frequency now is double the original frequency. Therefore, the signal will be filtered by a lock-in amplifier and will not alterate the PFM signal. However, during experiments it is important to consider that the Joule effect can exist and change things like the water layer on the surface of a material exposed in air.

Finally, electrostriction also plays a role in PFM. Nevertheless, this work has shown already in Section 3.3.1 that electrostriction can be filtered out by frequency from the PFM signal. Other phenomena such as flexoelectricity could affect the signal. Indeed it has been show that flexoelectricity produces a PFM signal (Abdollahi et al., 2019). Although on ferroelectric materials it is usually smaller than piezoelectric signal, it can still contribute to the signal (Seol et al., 2016).

3.4 Conductive AFM

Conductive AFM (C-AFM) is an electrical mode invented in 1993 (Murrell et al., 1993). C-AFM is used in contact mode and allows the measurements of currents in a material. C-AFM can be used in a spectroscopy mode or a scan mode.

In the scan operation mode, a dc voltage is constantly applied through a conductive tip while scanning a surface. The intensity measured in response is registered pixel by pixel. Finally, a map of the intensity recorded at each pixel is obtained. These maps give information about leakage currents, but can also be used to study the conductivity of topological defects such as domain walls.

In the spectroscopy operation mode, the tip is not moving and a dc voltage ramp is applied. Like in scan mode, the corresponding intensity is measured and an I-V curve is obtained. This is useful to understand conduction mechanisms and, specifically for this study to work below the voltage point where leakage currents start to appear.

In both modes, the intensity measured is proportional to the effective emission area A_{eff}, which is different from the contact area detailed in Section 3.2.1. Since a water meniscus is usually sticked to the tip that acts as an electrode, A_{eff} will be bigger than the contact area, and A_{eff} will change as a function of the water content in the atmosphere (Weeks et al., 2005). The total intensity I obtained by the tip can be written as:

$$I = JA_{eff} \tag{3.25}$$

Where J is the current density. However, this model considers that J is uniform over A_{eff}, which might not be always the case.

Finally, C-AFM can be operated in different current ranges. To measure ultra-low currents (<1 pA), it is possible to use the lowest range called tunneling AFM (TUNA). This C-AFM range has been used to study oxide thin films (Castle et al., 2011; Yanev et al., 2008) and complements other ranges that are less precise but reach currents in the μA range.

3.5 AFM implementation in INL

For this work, two different AFM were used. PFM was done with a NT-MDT Ntegra, and DFRT was performed thanks to the implementation of a Zurich Instruments HF2LI lock-in amplifier. In this microscope the force and PFM spectroscopy were also studied. SS PFM was done using a NI-DAQ 5261, which manages the voltage ramp and the acquisition of the PFM signal. The DAQ is controlled by a labview script in order to represent the data obtained and simplify the whole process.

Finally, all C-AFM experiments were carried out in a Bruker Dimension 3100.

Chapter 4

Electrical control of ferroelectric domains

4.1 Switching polarization electrically

The polarization of domains in a ferroelectric material can be switched by applying an electric field between a top and a bottom electrode. It is possible to deposit a conductive material or to use a conductive AFM tip as the top electrode as shown in references (Paruch et al, 2001) and (Molotskii, 2003). In the case of in-plane polarization, it is possible to use coplanar electrodes.

4.1.1 Electrical control of the out-of-plane polarization

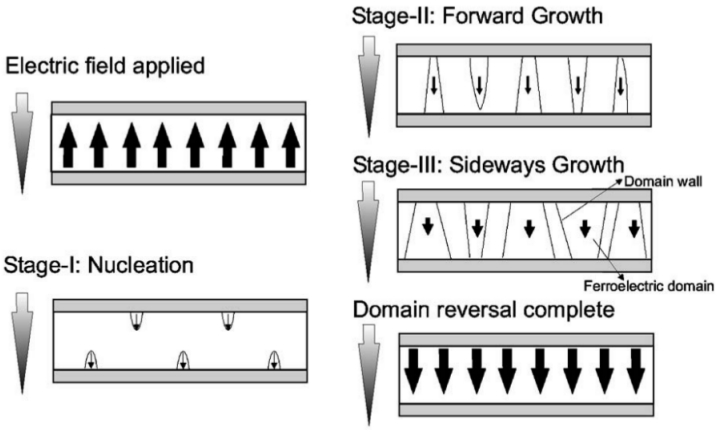

Figure 4.1: The three steps of ferroelectric switching when an electric field is applied (Dawber et al., 2005)

For this work, the out of plane polarization will be switched by using a bottom

electrode and an AFM tip. Many studies have been reported (Morozovska et al., 2006; Shin et al., 2007) to explain how the ferroelectric switching of domains occurs when an electric field is applied between a top and bottom electrode. This process is ilustrated in Fig. 4.1, and can be divided into three different steps (Dawber et al., 2005):

1. *Nucleation:* In this step small domains appear at the interfaces between the material and the electrodes. This is an inhomogenous process, which starts at defects or inhomogeneities on the surface (Shur, 2006).

2. *Forward growth*: The domains created at the surface begin to expand across the film until they reach the bottom electrode. During this process the domains take the form of needles (Shur et al., 2000) to minimize the depolarization field (Morozovska et al., 2009). From Eq. 1.7 the surface charge can be obtained as $\sigma = \vec{P} \cdot \vec{n}$. It can be deduced that σ will be large when $\vec{n}$ and $\vec{P}$ are parallel. Therefore, the needle shape means a smaller σ, thus decreasing the depolarization field. This vertical growth is faster than the radial growth that takes place at the next step.

3. *Sideways growth*: At this point domains have crossed the material from electrode to electrode and they start to grow laterally, merging with the other domains. Finally, the switching of the domains in the total volume of the layer will be achieved. This lateral movement of domains can continue beyond the sample-top electrode contact are. This phenomenon is known as: domain wall creep motion (Tybell et al., 2002).

In the example shown in Fig. 4.1 the only case considered is the out-of-plane polarization, nevertheless, ferroelectric materials can also have an in-plane polarization.

4.1.2 Electrical control of the in-plane polarization

The control of in-plane polarization is more difficult, however, a series of results in the literature were obtained through the use of two different techniques. Among them, only one can be achieved with an AFM tip:

- Coplanar Electrode: This configuration allows for some degree of control of the in-plane polarization by applying an electric field between the coplanar electrodes (Shafer et al., 2007). The control of the vertical polarization can be achieved by approaching an AFM tip as a top electrode, which will bend

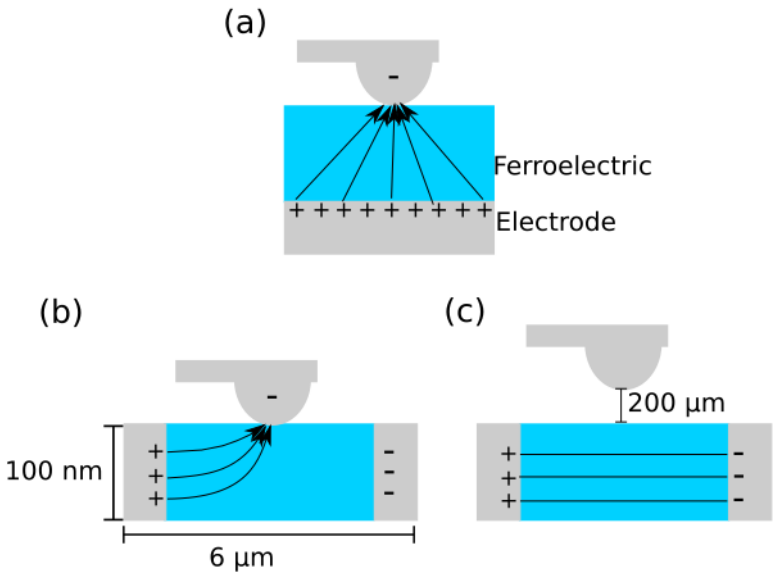

Figure 4.2: (a) AFM tip-bottom electrode configuration to control the out-of-plane polarization. (b) Planar electrode configuration with the AFM tip on the surface of the material to control the out-of-plane polarization. (c) Planar electrode configuration with the AFM tip far from the surface of the material to control the in-plane polarization. Based on the drawings of (Balke et al., 2010).

the field lines upwards and will change the polarization accordingly. However, when changing the in-plane polarization, the tip must be removed.

- Trailing fields: This technique uses the movement of an AFM tip to change the in-plane polarization in a sample with a bottom electrode. Indeed, the electric field applied by an AFM tip always has a radial component, which is able to switch domains laterally while scanning (Balke et al., 2009; Vasudevan et al., 2014; Crassous et al., 2015). However, a complete control of the in-plane polarization with trailing fields requires a good knowledge of the possible

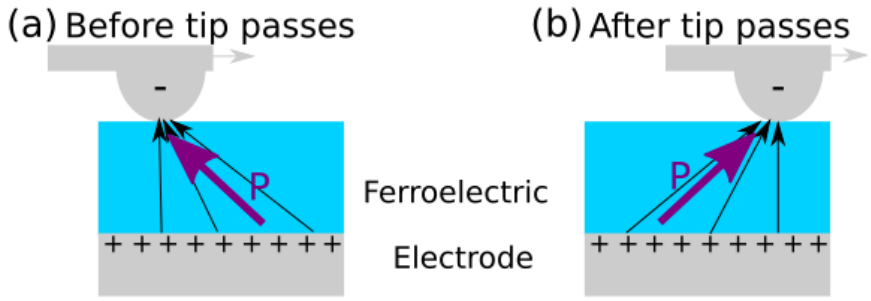

Figure 4.3: Trailing field for two lateral polarization states. The movement of the tip changes from state (a) to the state (b).(Crassous et al., 2015)

directions of polarization in the material.

4.2 Results on $Pb[Zr_{0.2}Ti_{0.8}]O_3$ sol-gel samples

Most of the work presented in this thesis was performed with the PZT thin films grown at INL by the sol-gel method introduced in chapter 2. These films have different thicknesses ranging from 33 to 200 nm and a distribution of down and up domains (out-of plane polarizatio). The experiments were consistently performed at the center of the samples since the sol-gel spin coating approach lead to non-uniform thicknesses at the edges of the substrate pieces.

4.2.1 Study of the As-Grown Domains

The observation of as-grown domains was possible by imaging with PFM without applying high voltages. The applied force was also controlled to avoid any effects related with mechanical switching or changes in the topography. The experiments were performed in the 33, 66, 100, 133 and 200 nm thick samples (from now on referred to as $sol_{thickness}$) as shown in Fig. 4.4.

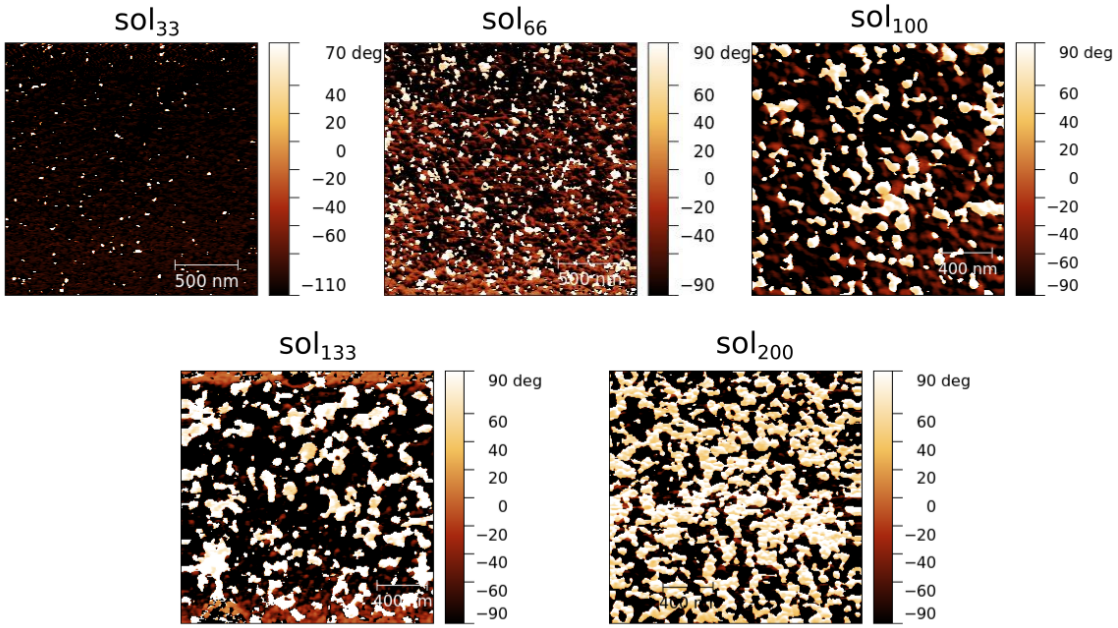

Figure 4.4: PFM phase images of the sol_{33}, sol_{66}, sol_{100}, sol_{133} and sol_{200} samples. The images are 2×2 μm^2 large and the scale at the bottom right represents 400 nm. In these images, the down polarization is represented in white, while the up polarization is represented in dark.

The preferable polarization of the as-grown domains is up (dark) in all samples

except the sol_{200} where an equilibrium between up and down is reached. To understand the origin of this as-grown polarization distribution among all specimens, the percentage of up and down domains was evaluated, as shown and plotted in Fig. 4.5. To obtain the percentages, all images were binarized using the Gwyddion software (Nečas and Klapetek, 2012). The results show a linear behavior of both the percentage and the size of down-polarized domains with the thickness of the samples. It should be noted that the preferentially upwards vertical polarization has been reported in the literature. It was proposed that this preferential orientation originates from a distribution of oxygen and cation vacancies (Pintilie et al., 2015), which helps to compensate the depolarization field and stabilize the direction of domains. Another possible origin is the substrate strain (Luo et al., 2013), which could switch domains up due to flexoelectricity.

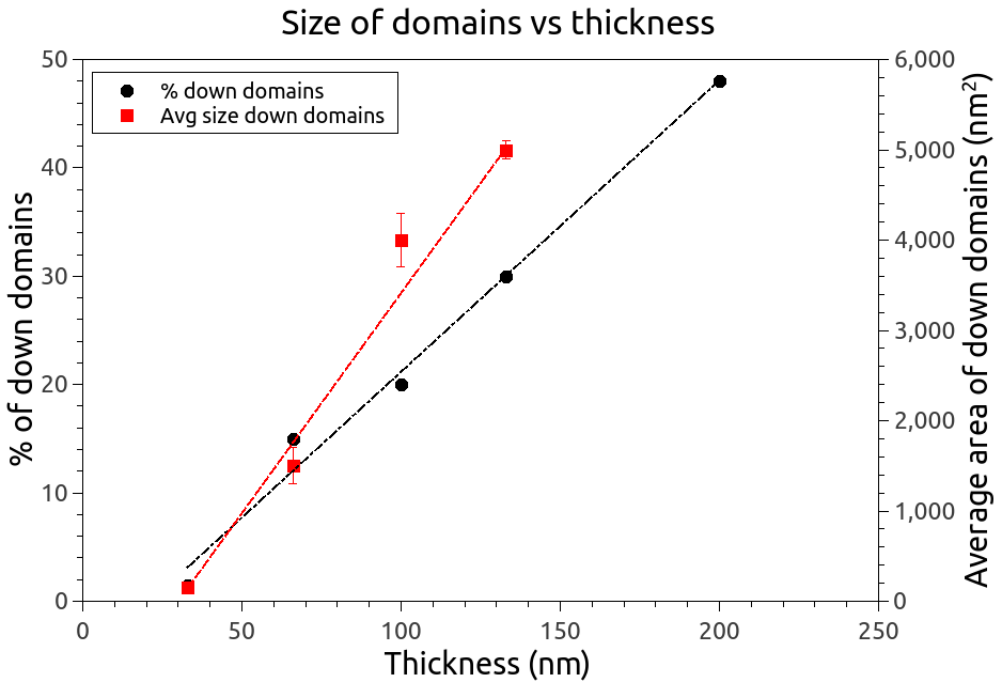

Figure 4.5: Plot of the percentage of down polarization against thickness (in black) and the average area of down domains against thickness (in red). A linear behavior can be observed for the percentage and the average area. The 200 nm point is excluded from the average area because domains coalesced for this thickness and it is not possible to clearly define the boundaries of domains.

Imaging of in-plane domains was possible in the samples considered in this thesis, but it seemed quite dependent on the region studied. In most cases, an in-plane signal was not observed. The in-plane polarization of domains will be discussed more extensively in Section 4.2.4.

4.2.2 Switching Spectroscopy PFM

SS PFM was performed with all the samples except the sol_{133} sample. The topography of the sol_{133} sample prevented us from implementing PFM systematically, although it was possible to obtain a few phase images. This is why it was not used extensively in this work. The ac voltage applied to the satellites was always between 250 and 300 mV to avoid leakage currents and electrostatic effects.

In Fig. 4.6 the off-field loops are presented for all the samples. The loops are almost symmetrical, which means that both up and down polarization are stable at null electric field. However, usually the voltage needed to switch to down polarization is slightly higher (a difference of 0.2 V for sol_{33} and 0.3 V for sol_{100}) than the one needed to switch to the up polarization. This is called an imprint, and can be related with the as-grown state of the samples having a majority of up domains. An imprint can originate from charge trapping in one of the interfaces or strain applied by the substrate. However, this work is not focused on the study of the imprint, the interested reader can find more information in the references (Grossmann et al., 2002; Warren et al., 1995).

For the off-field loops, the coercive voltage increases with the thickness, which is expected since thicker samples require higher voltage. However, this is not the case for the coercive fields, which was evaluated as an electric field between two plane electrodes, not considering any exaltation of the electric field due to the shape of the tip. The values obtained are 30 MV/m for the sol_{33}, 22 MV/m for the sol_{66}, 20 MV/m for the sol_{100}, and 23 MV/m for the sol_{200}. However, results show that the coercive field remains approximately constant around 20 MV/m, which is a proof of the reproducibility of the fabrication process.

In Fig. 4.7 the on-field loops are shown. Of special interest is the loop of the sol_{33} sample, where a linear behaviour for the high values of amplitude can be observed after the switching. This effect is thought to be related to electrostatic effects due to charge injected in this thin sample. To avoid this effect and other possible artifacts explained in Section 3.3.7, most of the work performed with the thinnest samples was in off-field SS PFM and using the smallest possible voltages for each sample. For the thicker film, the on-field loops usually presented a better ferroelectric-like behavior than the off-field since there are no leakage currents at the voltages applied, and a thicker sample requires higher voltage to switch.

For the on-field loops, a comparison of coercive voltages is not accurate due to electrostatic and leakage effects being able to affect the measurements, although a slight increase can be observed between the thinnest and the thicker samples, which can be linked to the behavior of the off-field loops.

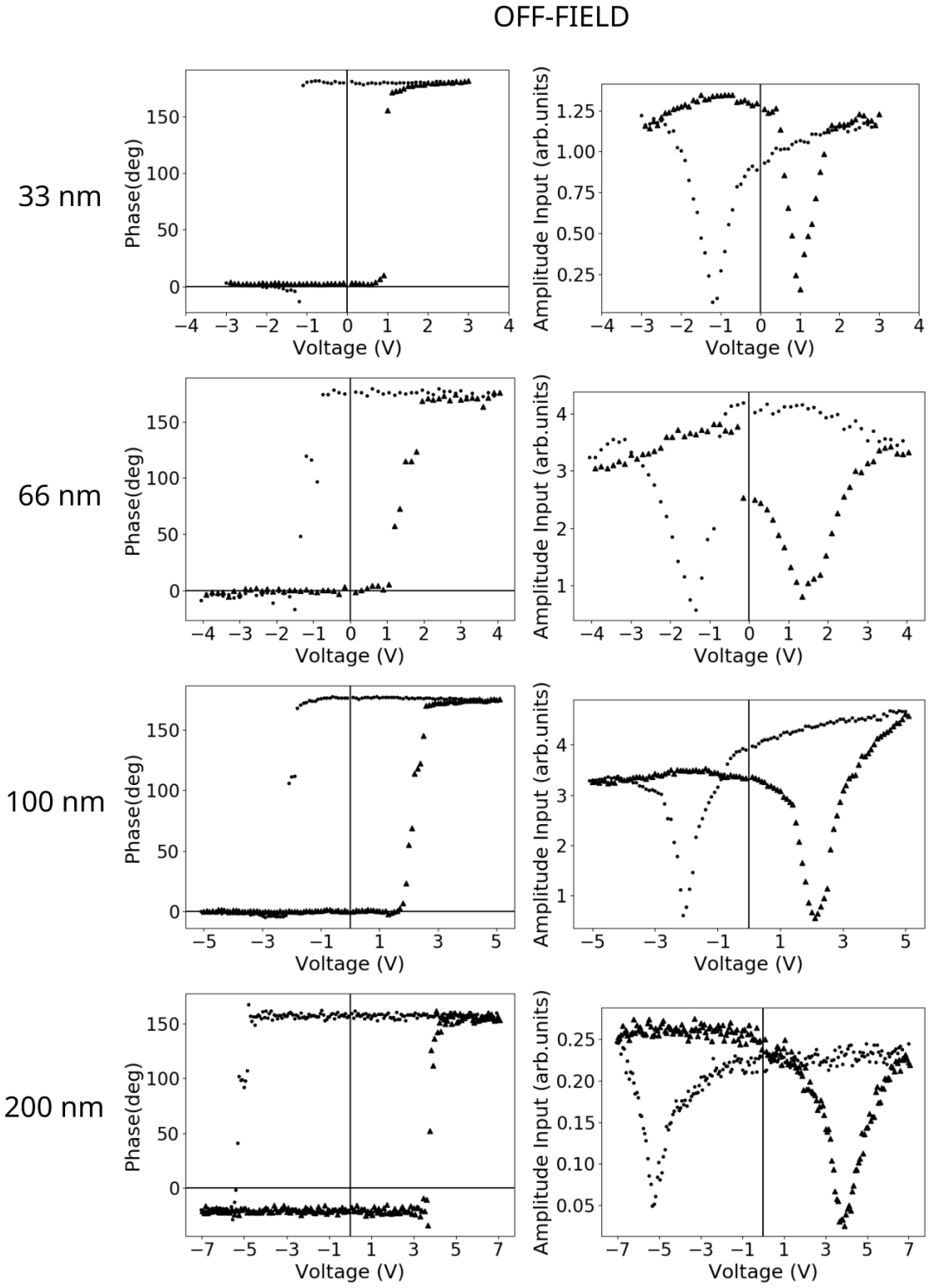

Figure 4.6: SS PFM off-field loops of phase and amplitude of the sol_{33}, sol_{66}, sol_{100} and sol_{200} samples. The ac voltage applied to the satellites to perform the PFM measurement was between 250 and 300 mV for all samples and the time steps in the range of a hundred ms.

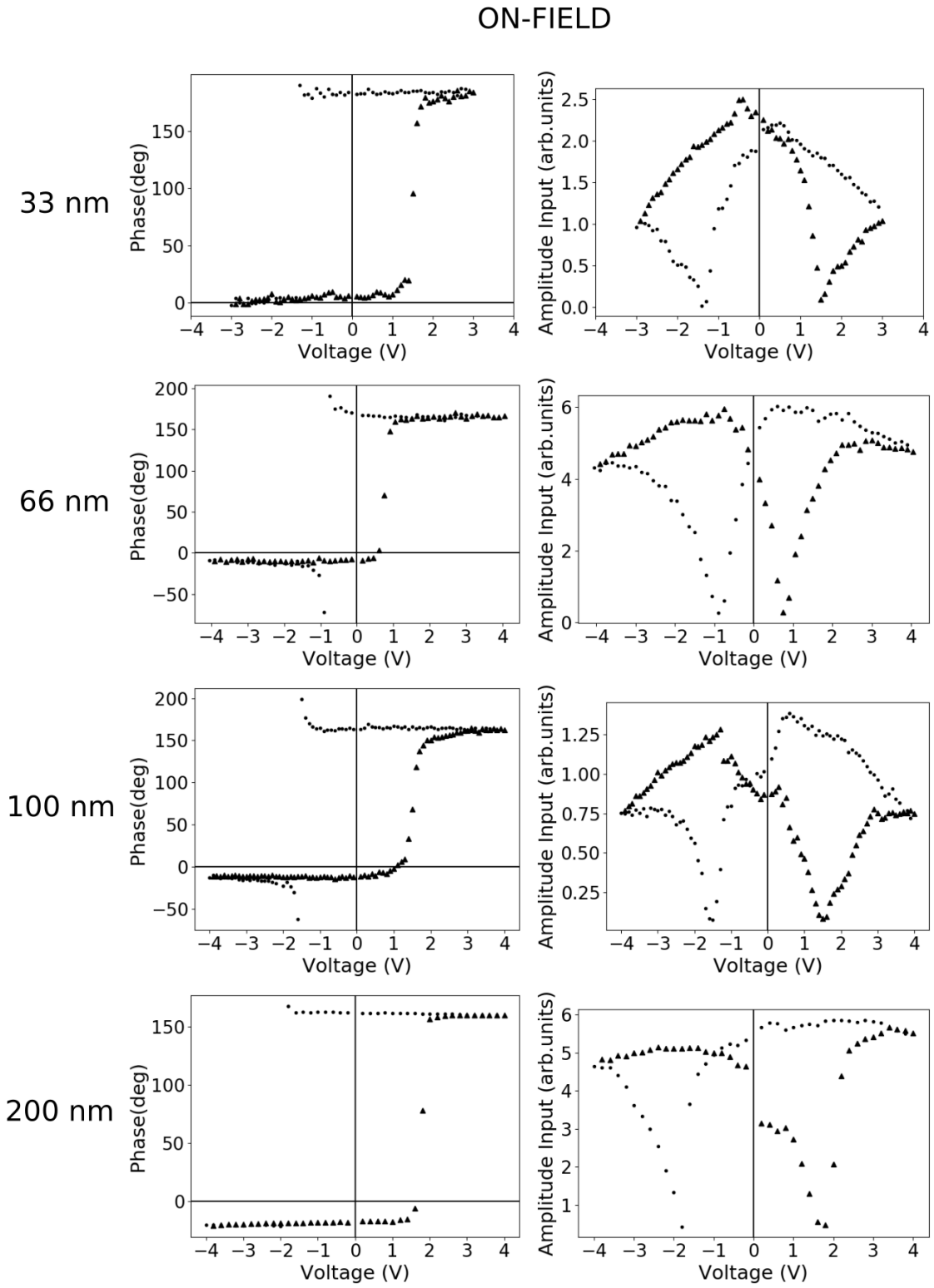

Figure 4.7: SS PFM on-field loops of phase and amplitude of the sol_{33}, sol_{66}, sol_{100} and sol_{200} samples. The ac voltage applied to the satellites to perform the PFM measurement was between 250 and 300 mV for all samples and the time steps in the range of a hundred ms.

In conclusion, all samples show symmetrical loops and behave as expected. Therefore, it should be possible to control domains by applying an electric field.

4.2.3 Study of the leakage by conductive AFM

C-AFM was performed in the sol_{33} and sol_{100} samples to relate the electrostatic effect observed in SS-PFM with leakage currents. The results shown in Fig. 4.8 confirm the presence of leakage currents appearing for the sol_{33} over 2.5 V. Since the voltage used for SS-PFM was 3 V, the linear effects observed can be attributed to leakage. On the contrary, sol_{100} does not show any leakage currents even after reaching voltages as high as 8 V.

It must be noted that in Fig. 4.8 a there is a remarkable difference between the forward (trace) and the backward (retrace) I-V curves. This change can be linked to charge trapping in the sample that modifies the threshold voltage for current injection. Therefore, the backward curve needs less voltage to reach the same intensities.

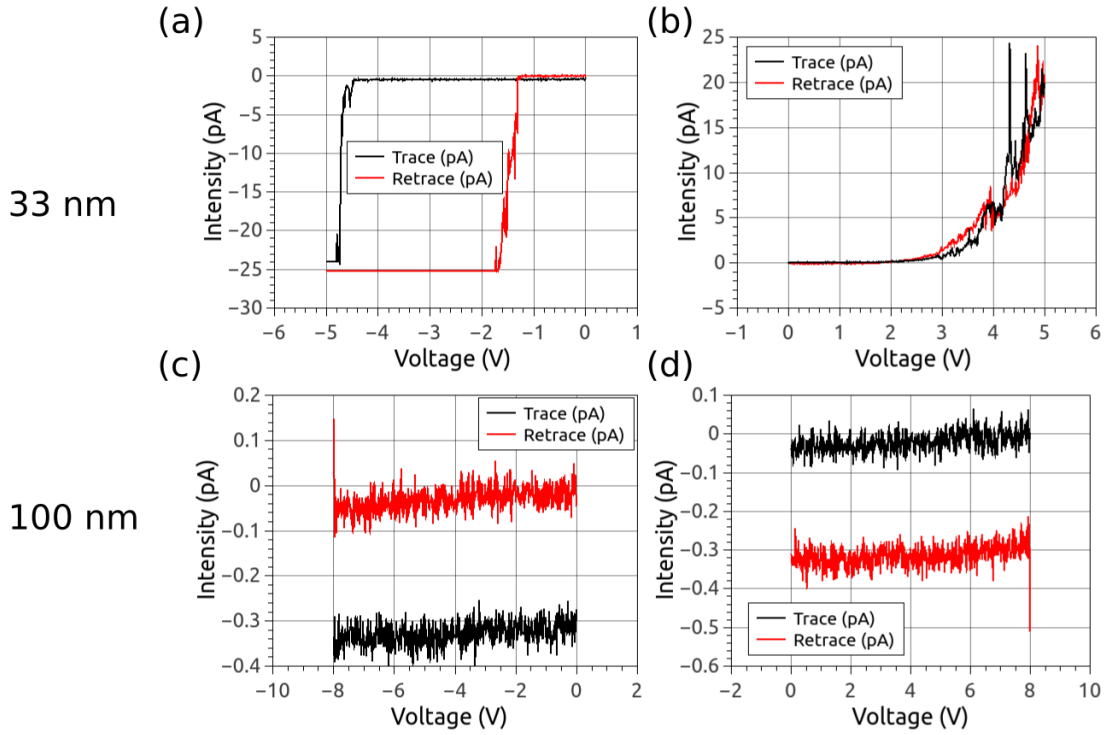

Figure 4.8: C-AFM I-V curves for the sol_{33} (a) and (b), and for the sol_{100} (c) and (d). The voltage ramps were performed at 0.5 V/s. The black lines represent the voltage going to 0 to the extreme (positive or negative), while the red lines represent the voltage going back to 0.

While these are local measurements, which result may vary from point to point,

different points show a similar behavior with leakage appearing in the sol_{33} over ± 3 v and no leakage for the sol_{100}.

4.2.4 Electrical patterning of domains

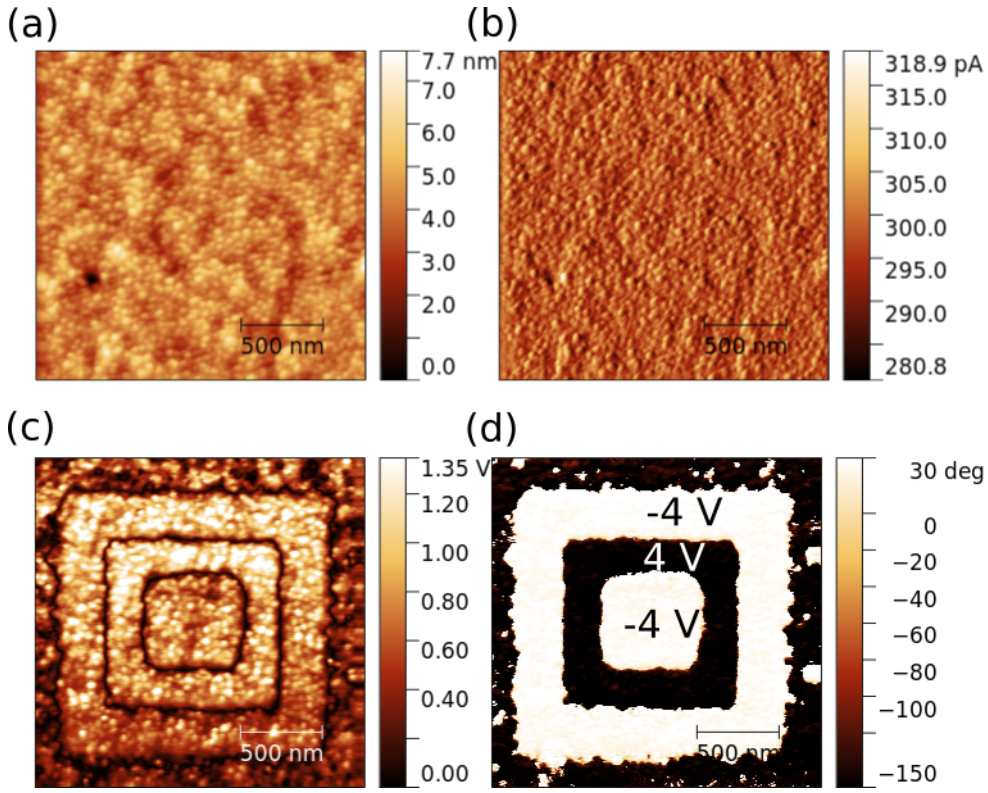

Figure 4.9: PFM images of the same region of the sol_{100} sample. (a) Topography, (b) deflection (c) vertical amplitude, and (d) vertical phase. All images are 2 × 2 μm^2 large.

As expected from the previous section, it was possible to write and rewrite domains in the out-of-plane direction for all the samples. For example, in Fig 4.9 are shown the PFM phase and amplitude images after writing different features in the sol_{100} sample without changing the topography. Firstly, a square of 1.5 μm with down polarization was written with -4 V at a speed of 2μm/s, then, the polarization was reversed by applying 4 V in a square of 1 μm at the same speed, and finally a square of 0.5 μm with down polarization was written reversing the polarization a third time with the same speed. In this case, the patterns were all squares, but more complex patterns can be achieved by using the lithography mode of the microscope.

In a 100 nm thick film, grown by sol-gel in a later batch ($sol_{100/new}$) prepared with two years difference, an in-plane polarization was observed inside of an electrically poled area, shown in Fig 4.10. We cannot rule out the evolution of the

sol-gel solution used for the synthesis, and thus its effects in the micro-structure obtained. This structure with out-of-plane domains separated by in-plane domains has been reported previously in $Pb[Zr_{0.2}Ti_{0.8}]O_3$ thin films (Roelofs et al., 2002), and is thought to be an effect of the depolarizing field. However, it was not possible to control electrically these in-plane domains and they were not observed for the others samples. Therefore, with PZT films we will focus on vertical polarization, while in BFO, where in-plane domains have been observed in a reproducible manner, in-plane domains will be included in the study (see Section 4.4).

From the point of view of remnant polarization, as shown in Fig 4.11, patterns created last for several days in the thinnest sample, sol_{33}. Indeed, after 4 days the polarization switches back only at some places near domain walls, as expected from the literature (Ganpule et al., 2002; Gruverman et al., 1998; Paruch et al., 2006; Paruch and Triscone, 2006). In thicker samples, the patterns should last longer since the down polarization is more stable than in the sol_{33} sample. Here, experiments were carried out up to 96 hours.

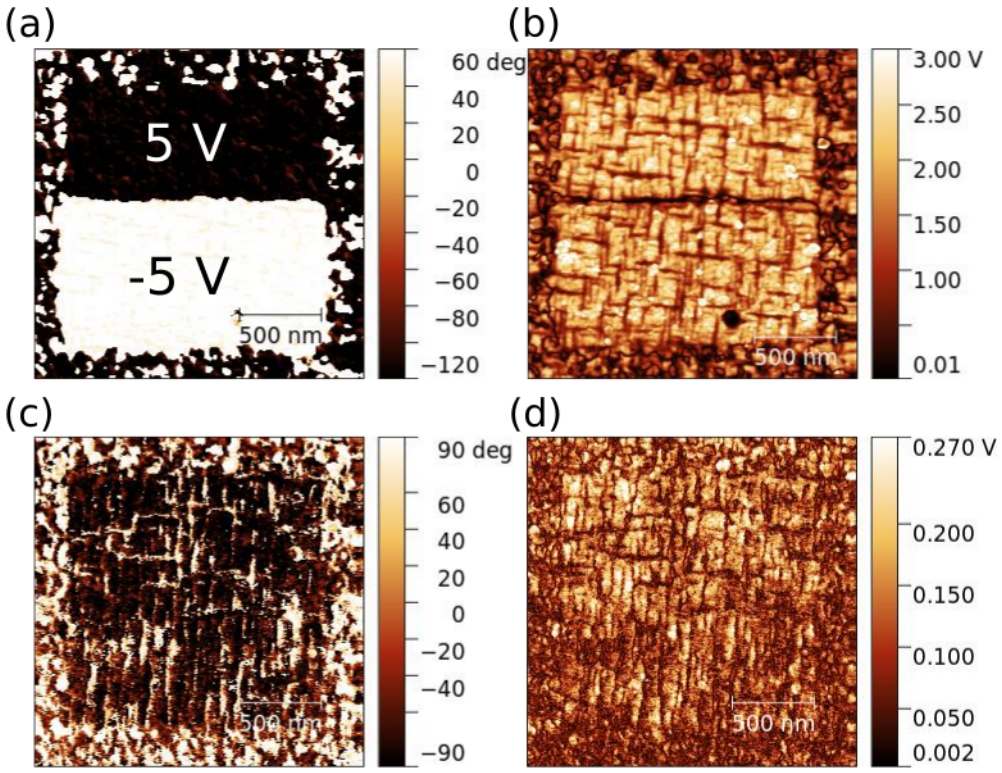

Figure 4.10: PFM images of the same region of a 100 nm thick PZT sol-gel film. (a) Vertical phase and (b) amplitude. (c) Lateral phase and (d) amplitude. All images are 2×2 μm^2.

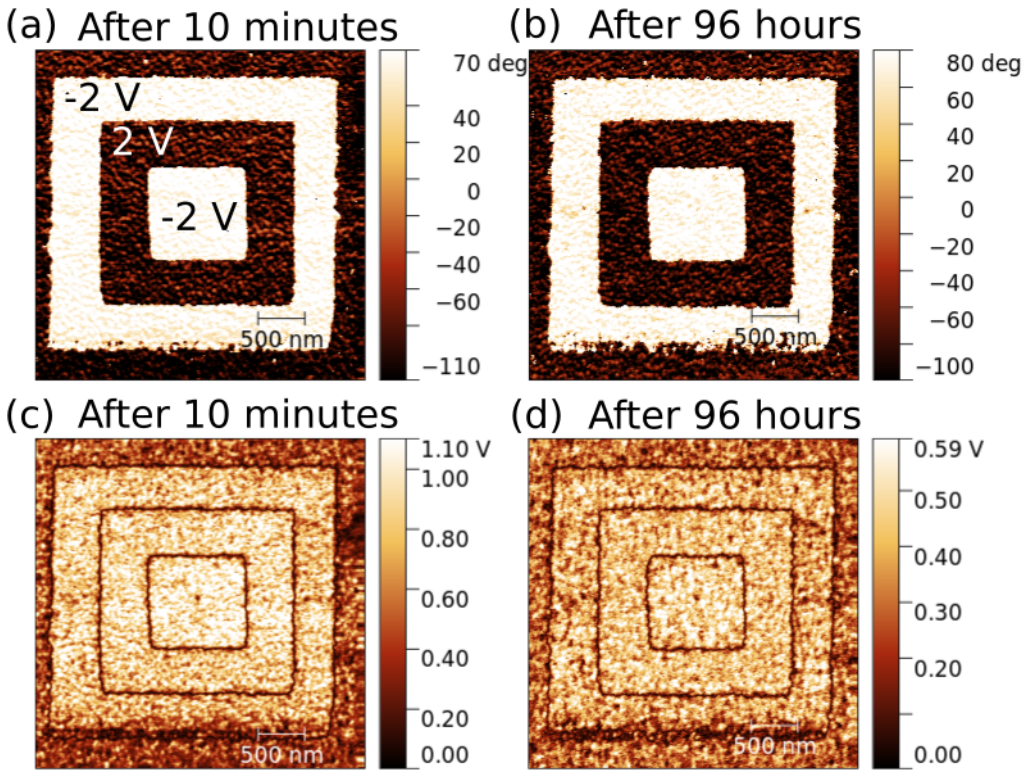

Figure 4.11: PFM images of the same region of a 33 nm thick PZT sol-gel film. (a) and (c) vertical amplitude and phase image of a pattern created with 2 V and -2 V after 10 minutes. (b) and (d) vertical amplitude and phase image of the same pattern after 96 hours.

4.2.5 Effect of the atmosphere on the growth of domains

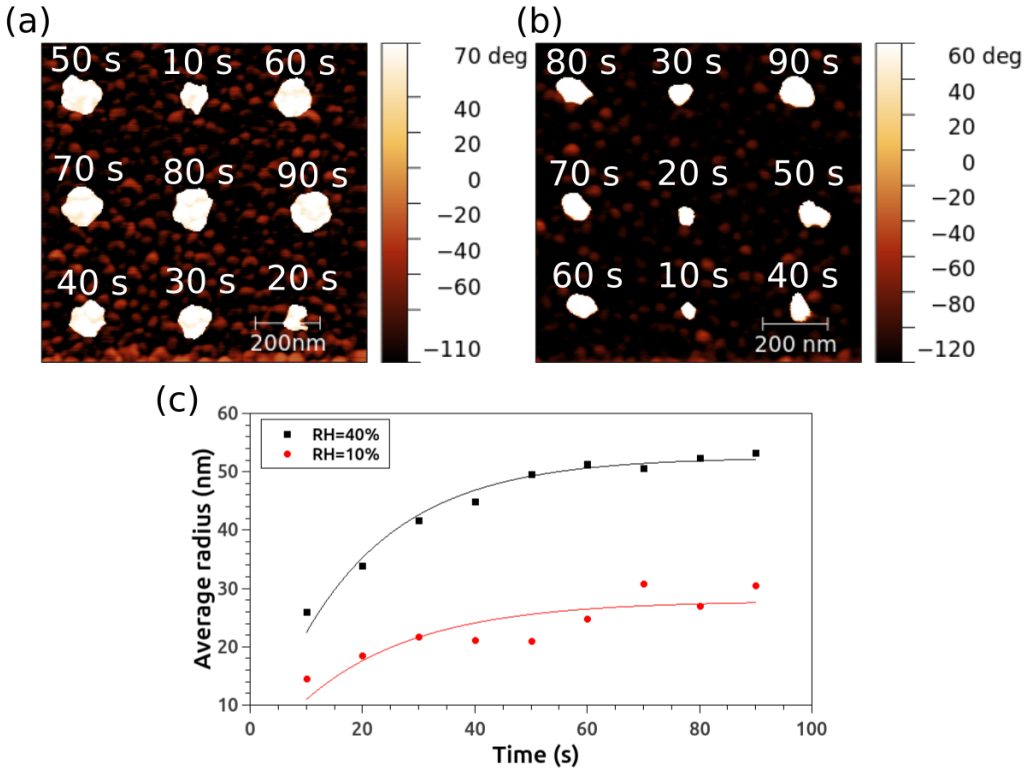

Figure 4.12: Phase PFM images of an experiment performed in sol_{33} with a relative humidity (RH) of (a) 40% and (b) 10%. (c) Plot of the average equivalent radius measured vs duration of the voltage pulse for a RH of 40% and a RH of 10% with the fitting of Eq. 3.1

The effect of different atmospheres in the electrical switching of ferroelectric domains was studied by increasing the nitrogen content inside the chamber that contains the AFM, which in turn decreases the relative humidity (RH). The RH can be obtained with a built-in system in the microscope chamber that measured the humidity. In a first step, an experiment under normal conditions and a RH of 40% was performed, then repeated in an atmosphere with more nitrogen and a RH of 10%. The experiment consisted in poling electrically with 2 V a region of the sol_{33} sample, then the voltage was maintained for 10 to 90 seconds in different points of the electrically poled region while applying -2 V. In this way, it is possible to relate the size of domains with the duration of application of the voltage and the RH.

As shown in Fig. 4.12, domains grow bigger and faster under an atmosphere with higher humidity. One possible explanation for this behavior, suggested by Brugere et al. (Brugère, 2011; Gautier et al., 2012), is that the electric field propagates through the water layer on the film surface, which act as an electrode. This water layer is

thicker for higher RH, thus decreasing the resistivity and increasing the speed of propagation. Another possible explanation, suggested by Blaser and Paruch (Blaser and Paruch, 2015), is that the modification of the water layer changes the screening conditions of ferroelectric polarization and nucleation sites as defects. This would affect stability of nucleated domains reducing their size. While the results in Fig. 4.12 do not allow to choose one of these two hypothesis, they show that the equivalent radius of domains increases with the time the voltage is applied and can be modelled as:

$$R = R_{final}(1 - e^{\frac{-t}{B}}) \tag{4.1}$$

Where R_{final} is the maximum radius reached by the domain and B is a time constant. This is in agreement with previous results found on $LiTaO_3$ (Gautier et al., 2012) samples, where the speed of domains growth is higher for domains of smaller radius. However, this model is only valid for the time scale studied, the literature on PZT shows that at a smaller time scale the domains growth behaves differently (Tybell et al., 2002). The model fits well the experiment with a RH of 40%, where the correlation coefficient is 0.95. However, the experiment with a RH of 10% has correlation coefficient of 0.7. This difference can be attributed to the relative error of the size of domains and the RH being higher for smaller measurements.

It must be noted that the results from the literature (Gautier et al., 2012; Blaser and Paruch, 2015) show a bigger radius for the same time, and thus a higher speed of growth. This can be explained by different factors that can affect the final size reached by domains such as the applied electric field, the radius of the tip and the material studied. For example, none of the materials from the literature were fabricated by sol-gel technique that should create more defects, which could affect the results.

4.2.6 Exceptions to the general behavior

This section has been devoted to describe the behavior of the the sol_{33}, sol_{66}, sol_{100}, sol_{133} and sol_{200} samples from the point of view of the electrical control of the polarization. However, two samples were made and showed different properties compared to the others.

The first exception is the sol_{166} sample that underwent 2 crystallization annealing steps. While the other samples had a majority of up domains, the sol_{166} sample had a reversed polarization with a majority of down domains. To understand this unexpected behavior, the chemistry of the film was investigated using Rutherford Backscattering Spectroscopy (RBS). As shown in Fig. 4.13, the Pb contribution

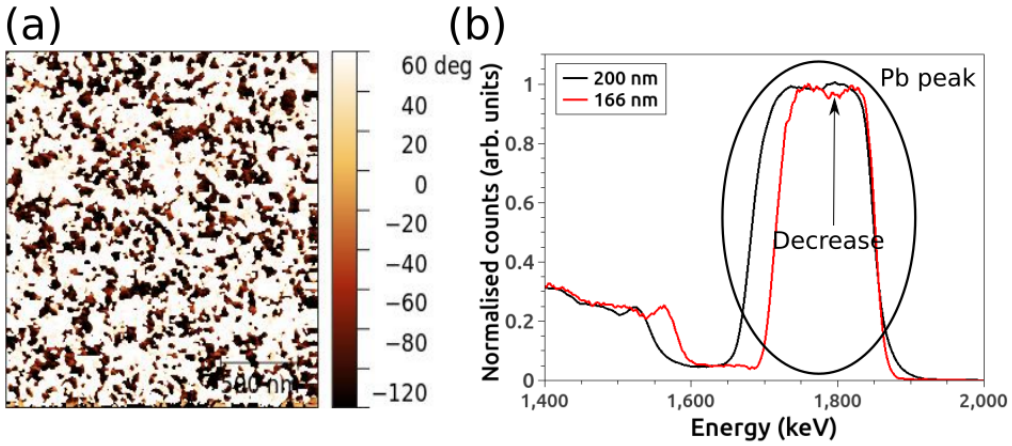

Figure 4.13: (a) Phase PFM image of the as-grown state of the sol_{166} sample. (b) RBS spectrum around the Pb peak for the sol_{200} and the sol_{166}. The arrow indicates the decrease of Pb signal for the sol_{166}, which can be related to a different composition in the middle of the sample. The peak width is related to the thickness of PZT.

shows a significant decrease (5 % of the maximum value) at around half the total thickness of the film. This decrease can be observed in other samples with two crystallizations, but never to the extent of this sample as exemplified by the sol_{200} sample in Fig. 4.13 (2 % decrease of the maximum value). Since the samples with two crystallizations are composed of two distinct layers (one for each crystallization), as described in Section 2.1.2, an interface with less Pb must have been created between the bottom 100 nm thick layer and the top 66 nm thick one in sol_{166}. This interface could either show a charge accumulation region or affect the strain of the top film. In the case of charge accumulation region, the screening conditions would change and this could reverse the polarization. In the case of a different strain, the literature has shown that the strain state can affect the polarization of a film (Schwarzkopf et al., 2017).

The second exception was a sample of 100 nm with three crystallizations ($sol_{100/3c}$), for this sample there was a crystallization every 33 nm. The sample had an as-grown state similar to the sol_{33} sample with a majority of up domains, but a coercive voltage similar to the sol_{100} sample. In Fig. 4.14 on-field and off-field loops are shown. On-field loops show electrostatic effects similar to those shown for the sol_{33} sample. Cross-section STEM-HAADF imaging in Fig. 4.14 b showed a line of cavities in the top third of the PZT thin film, corresponding to the last 33 nm crytallized. While cavities have also been observed in PZT films fabricated by sol-gel (Kiguchi et al., 2020), the high number and their position close to the surface could be related to the

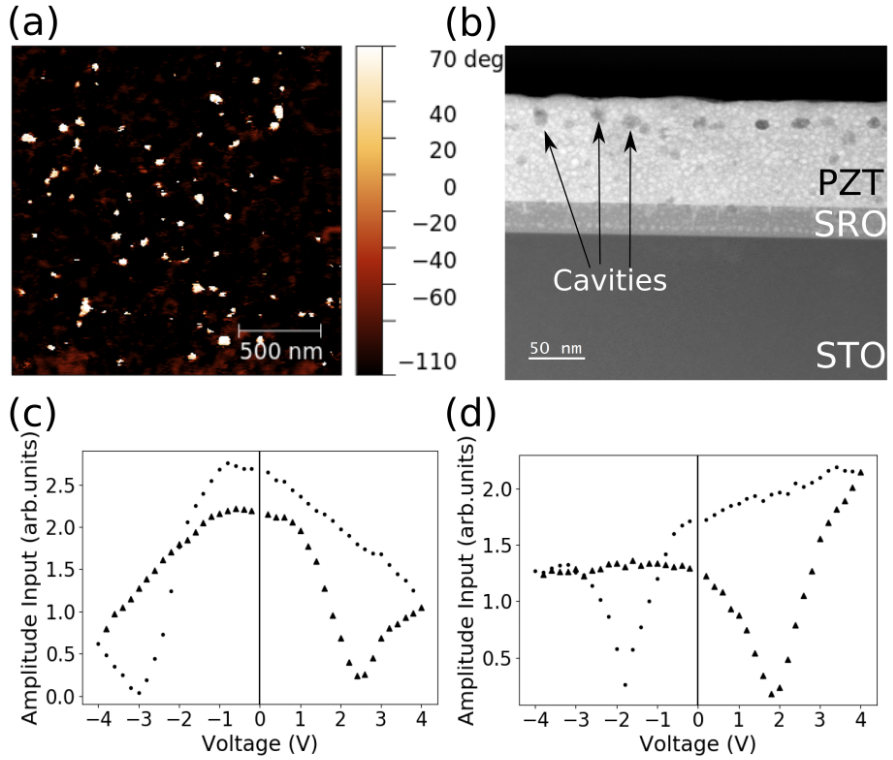

Figure 4.14: (a) Phase PFM image of the as-grown state of the $sol_{100/3c}$ sample. (b) Cross-section STEM-HAADF image of the same sample as (a) where a line of cavities is visible close to the surface. (c) On-field loop where electrostatic effect are observed and (d) off-field loop in the same sample.

special properties of the sample, since they are defects where domains can nucleate or be clamped. In chapter 5 a more thorough study of the effect of these cavities can be found.

4.3 Results on $Pb[Zr_{0.25}Ti_{0.75}]O_3$ PLD samples

The PZT samples grown by PLD at the C2N laboratory were used for comparison with the ones made by sol-gel, specifically their response to mechanical switching, which will be the main topic of chapter 4. However, the response of these PLD films to electrical switching was studied in a first step, and is presented in this section.

4.3.1 As grown state and patterning

Two PZT samples with a thickness of 20 nm and 40 nm were studied (from now on PLD_{20} and PLD_{40} respectively). As shown in Fig. 4.15, the as-grown state of the PLD_{20} sample is quite similar to the state of the sol_{33} (see Fig. 4.4 and Fig. 4.15)

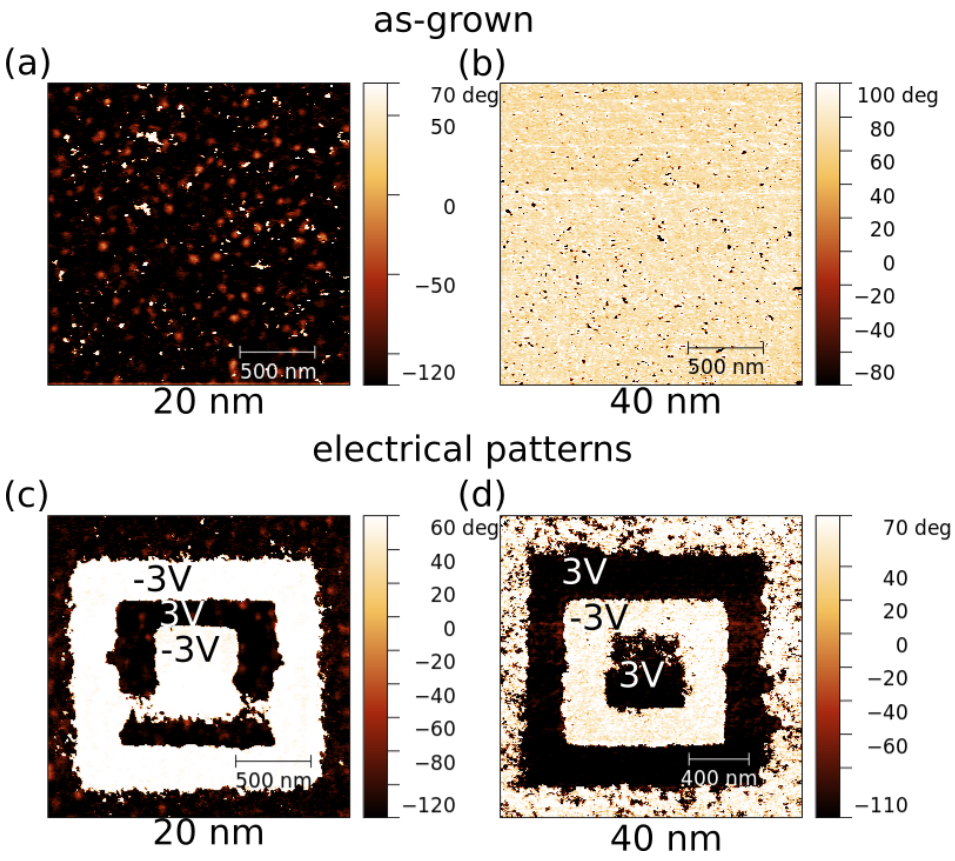

Figure 4.15: Phase PFM image of the as-grown state of the (a) PLD_{20} and the (b) PLD_{40} samples. Phase PFM image of patterns created with 3 V and -3 V in the (c) PLD_{20} and the (d) PLD_{40} samples.

sample with a majority of up polarization and small down domains. However, in the case of the PLD_{40} sample the polarization is reversed and there is a majority of down domains. At the moment, there is no clear explanation for this, but further structural and chemical studies with STEM in cross-section geometry and RBS could help determine the nature of this opposite behavior, which was also observed for the sol_{166}.

Nevertheless, it was possible to control the out-of-plane polarization in both PLD_{20} and PLD_{40} with electric fields higher than those needed for the sol_{33} sample (1 V and 30 MV/m for sol_{33}, 1 V and 50 MV/m for PLD_{20}, and 2.5 V and 63 MV/m for PLD_{40}). Indeed, it was possible to switch with smaller voltages but the polarization partially switched back within an hour as shown in Fig. 4.16. This different behavior may originate from different synthesis methods. Indeed, PLD thin films are not expected to present the same density of defects as sol-gel films (Arredondo et al., 2009; Vogel et al., 2021), defects from which domains can nucleate as explained in Section 4.1.1. The absence of these kind of defects for the PLD films can explain why domains are less stable than for sol-gel films.

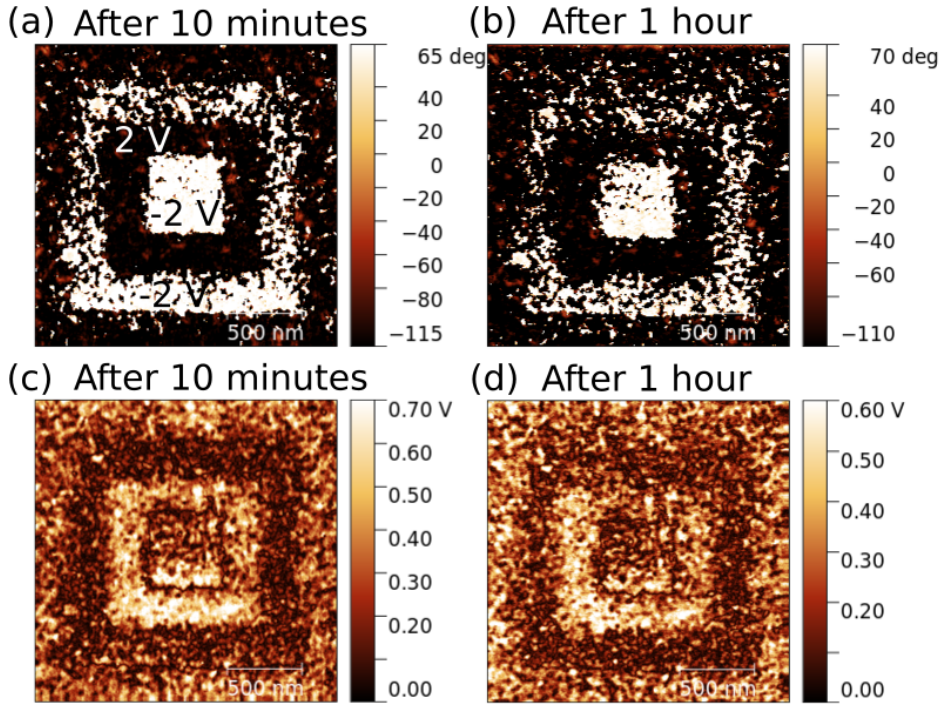

Figure 4.16: (a) and (c) vertical amplitude and phase image of a pattern created with 2 V and -2 V in the PLD_{20} after 10 minutes. (b) and (d) vertical amplitude and phase image of the same pattern after 1 hour.

4.3.2 SS-PFM and hillocks

SS PFM investigations carried out on PLD_{20} and PLD_{40} demonstrated that a higher coercive voltage was needed to switch in the off-field mode. However, the on-field and off-field signal of the PLD_{40} sample was asymmetric. Positive voltage have a considerably higher amplitude than the negative voltage of the loop, as shown in Fig. 4.17. From these experiments, hillocks as the ones shown in Fig. 4.17 appear only after the application of a positive voltage. The size of these hillocks varies as a function of the time the voltage has been applied, and they can be as tall as 3 nm.

It is know that the appearance of a hillock increases the deflection signal (Grandfond et al., 2014) of AFM measurements. However, PFM signal is filtered by frequency, which means that a change of the topography should not be enough to justify the increase of amplitude. The linearity of the on-field amplitude suggests that the increase of the signal is related to electrostatic effects, which means that the hillocks could be the result of a charge injection due to leakage currents. Leakage would occur only for positive voltages, which explains the normal behavior for negative voltages. The longer this current is passing through the sample, the more charges are injected at the interface between SRO and PZT and the bigger is the hillock and the damage of the sample (Hourani, 2011).

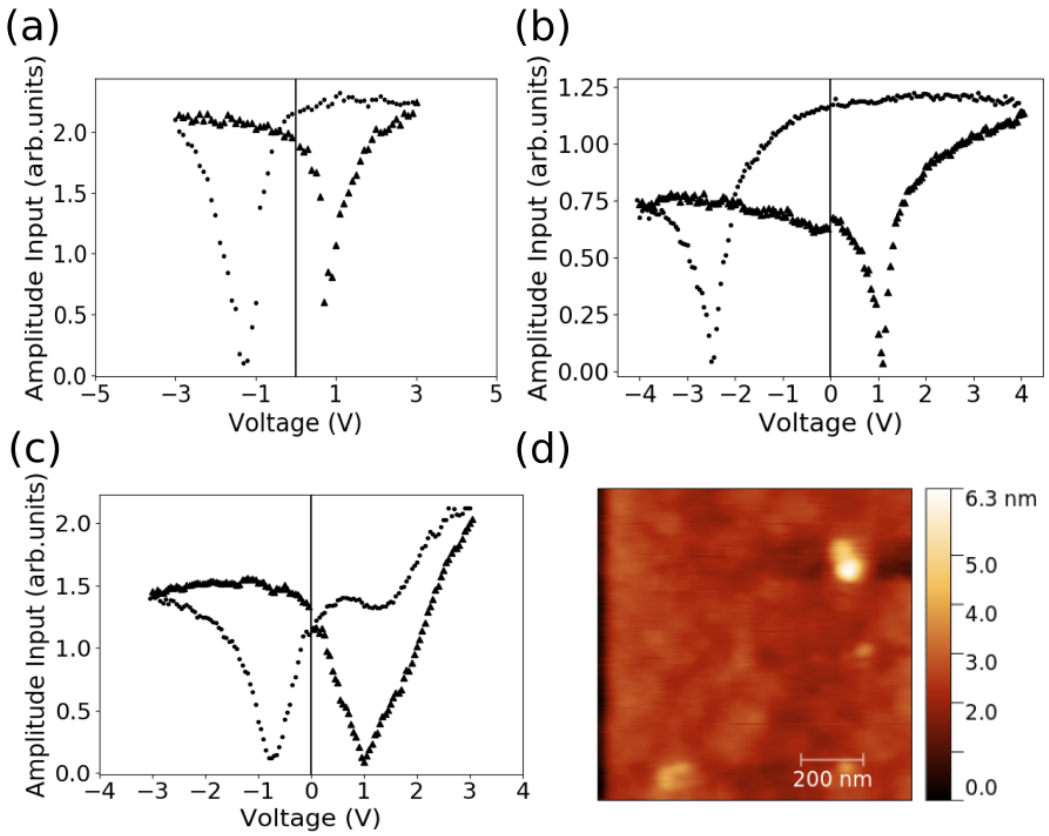

Figure 4.17: Off-field loops for the (a) PLD_{20} and the (b) PLD_{40} sample. (c) on-field loop of the 40 nm sample showing a deformation related with the growth of a hillock. (d) topo of the 40 nm sample with a hillock on it.

Therefore, the deformation observed in the positive branch of SS-PFM, specifically on-field loops, can be attributed to charge injection. The electrical switching is possible in both sample, but the time during which voltages are applied to the PLD_{40} sample must be controlled to not damage the sample permanently.

4.4 Results on $BiFeO_3$ PLD sample

A 30 nm thick BFO sample grown by PLD at University of New South Wales was studied. This sample allowed for the study and manipulation of in-plane domains, which was not possible in previous sections since PZT had mostly an out-of-plane polarization. This difference originates from the crystal structure of BFO as opposed to PZT. Contrary to PZT, which crystallizes in a tetragonal lattice, BFO is rhombohedral. In Fig. 4.18 the different directions of polarization for BFO in a pseudocubic structure are shown. As indicated by the schematics b and c of Fig. 4.18, rotating the sample changes the PFM signal obtained, which is why the same

region will be observed rotating the sample from 0 ° to 90 °.

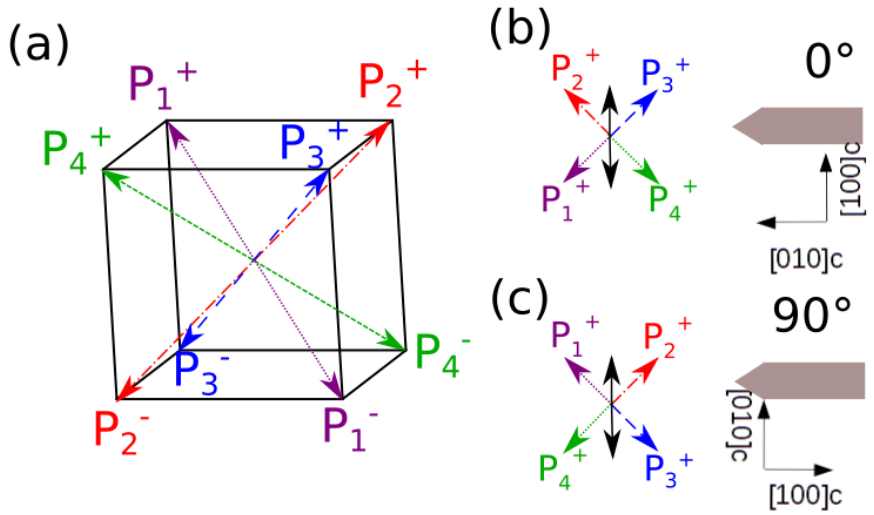

Figure 4.18: (a) Pseudocubic structure with the 8 possible directions of the polarization for BFO, 2 orientations are possible for the out-of-plane polarization and 4 for the in-plane polarization. Configuration of the tip and the up polarizations in the pseudocubic structure at (b) 0 ° and (c) 90°, the black arrow represents the lateral PFM signal.

4.4.1 As-grown domains

As shown in Fig. 4.19 the out of plane polarization has a majority of up domains as in the PZT samples. However, domains have an elongated shape different from the PZT samples, which can be related with the method of growth of the sample and its topography, which also shows elongated shapes. It could also be an effect of the rhombohedral phase of the film.

Contrary to the results on PZT samples, on BFO in-plane polarization can be clearly observed by lateral PFM as shown in Fig. 4.19. As shown in Fig. 4.18 (b) and (c), the rotation changes the lateral PFM signal, it must be noted that the rotation was done manually and an uncertainty of 10° is expected. For both lateral PFM images, a polarization seems to be predominant.

As interesting as the observation of the lateral polarization is in the as grown state, it is still challenging to determine the exact direction of polarization in each region. In Section 4.4.3, this will be achieved within regions where the lateral polarization is more uniform.

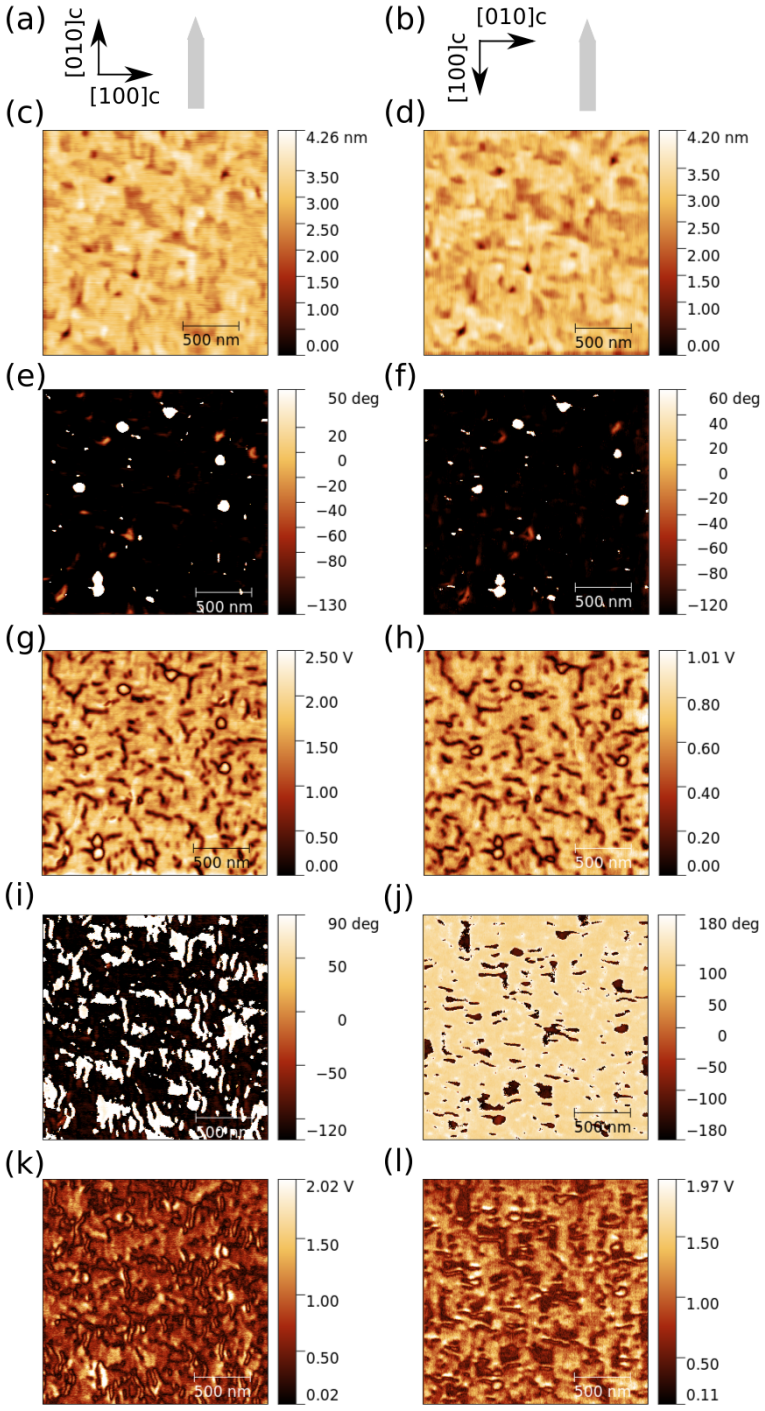

Figure 4.19: Schematics of the tip and pseudocubic directions for the measurements at (a) 0 ° and (b) 90 °. Topography of the BFO sample scanned with the tip at (c) 0° and (d) 90° as shown by Fig. 4.18. Vertical phase of the sample at (e) 0° and (f) 90°. Vertical amplitude of the sample at (g) 0° and (h) 90°. All domains are as-grown except the six down domains that were created electrically as a point of reference. Lateral phase of the sample at (i) 0° and (j) 90°. Lateral amplitude of the sample at (k) 0° and (l) 90°. Images at 90 ° were rotated for a better comparison.

4.4.2 SS-PFM and tip degradation

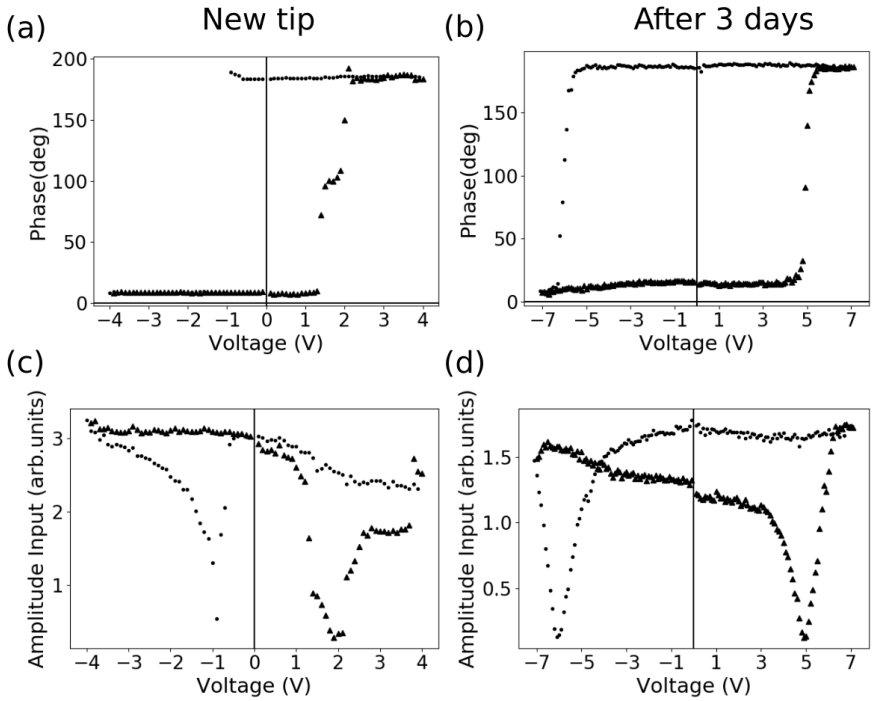

Figure 4.20: Off-field (a) phase and (c) amplitude loops of BFO with a new tip. Off-field (b) phase and (d) amplitude loops of BFO with a tip that has been used during three days.

SS-PFM lead to almost symmetrical off-field and on-field loops as shown in Fig. 4.20 and Fig. 4.21. However, in the on-field loops an important electrostatic effect is observed, which increases the amplitude proportionately to the voltage. This effect can be related with the leakage currents appearing in this type of films that have been already reported in the literature (Pabst et al., 2007).

Indeed, these currents may also cause the creation and deposition of oxides (either Fe or Bi) on the tip, which is an effect than can be observed after using the tip for a day. As shown in Fig. 4.20 and Fig. 4.21, the coercive voltage of off-field and on-field loops increases more than two times compared to the value measured with a brand new tip, after using that new tip for three days. This behavior disappears when working in the same region with a different tip, which verifies that the tip is being damaged and not the sample.

The problem of oxidation of the tip, either if it is an oxide pulled out from the surface of the material or from the oxidation of the tip coating, presents a series of challenges. Firstly, imaging the in-plane polarization can be quite challenging since the PFM signal is smaller than the out-of-plane, which means that higher voltages must be applied to increase it. This in turn means more degradation of the tip that

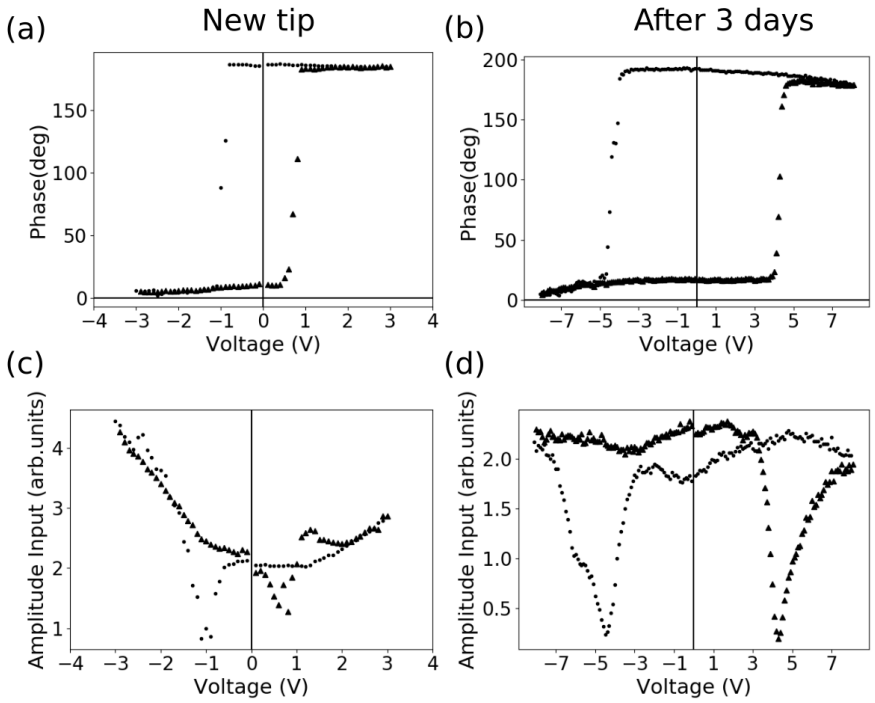

Figure 4.21: On-field (a) phase and (c) amplitude loops of BFO with a new tip. On-field (b) phase and (d) amplitude loops of BFO with a tip that has been used during three days.

requires even higher voltages for the imaging. Secondly, the electrical control of domains becomes problematic, since applying a dc voltage in the tip will favour its degradation. From the experimental point of view, negative voltages degrade the tip more than positive ones, therefore switching to the down polarization degraded the tip more. This is in agreement with Fig. 4.21, where electrostatic effects are more important for negative voltages on amplitude loops. Finally, measuring the conductivity of ferroelectric domains becomes almost impossible since the conductivity of the tip changes constantly with its continuous degradation.

However, solutions exist to minimize the oxidation and leakage currents. The first one is to work in a different atmosphere. Indeed, this work has shown already that the water meniscus plays a role in the electrical control of ferroelectric domains, and water must probably play a role in the oxidation. Another possible solution as mentioned by Pabst et al. (Pabst et al., 2007) is to change the materials of the electrodes used. This would change the potential between the tip and the surface and decrease leakage currents, however it could also reduce the PFM signal.

Exploring these different solutions has not been possible because of time constraints, and thus constitute relevant perspectives to further extend this work on BFO thin films. Therefore, the effects of leakage marked the limits of the results

presented in this work.

4.4.3 Control of in-plane polarization

It was possible to control the direction of in-plane polarization by applying a voltage while scanning a surface, in a similar way to trailing fields introduced in Section 4.1.2. To avoid the problem of the tip degradation, most experiments were performed by applying a positive voltage, which means that the final out-of-plane polarization was up in the whole scanned region.

As shown in Fig. 4.22, after poling a series of stripe domains appear in the region. To understand completely how the movement of the tip affected the creation of these domains, two experiments were performed moving the tip in different ways. In the first experiment, a half square was scanned with a slow axis up and a fast axis to the right, and the other half was scanned with a slow axis down and a fast axis to the left. In the second experiment, both half squares were scanned with the same slow axis, but opposite fast axis. From the results shown in Fig. 4.22, it can be concluded that the fast axis does not affect the in-plane domains created, since the patterns observed in experiment 1 and 2 are similar and the small differences can be a result of the error in the angle of rotation of the sample.

Since the fast axis is scanned forward and backward, it does not determine a clear direction of polarization. However, the slow axis only moves forward and determines the direction of the in-plane polarization. Since there are always four possible in-plane polarizations and the movement of the fast axis does not favour any, domains correspond to the two directions following the slow axis. This is verified by the stripe structure with two different polarization in each half square. Although it can be noticed that stripes of the opposite polarization can appear at the beginning of each half square. Similar results were obtained when doing the scanning with a 90° angle.

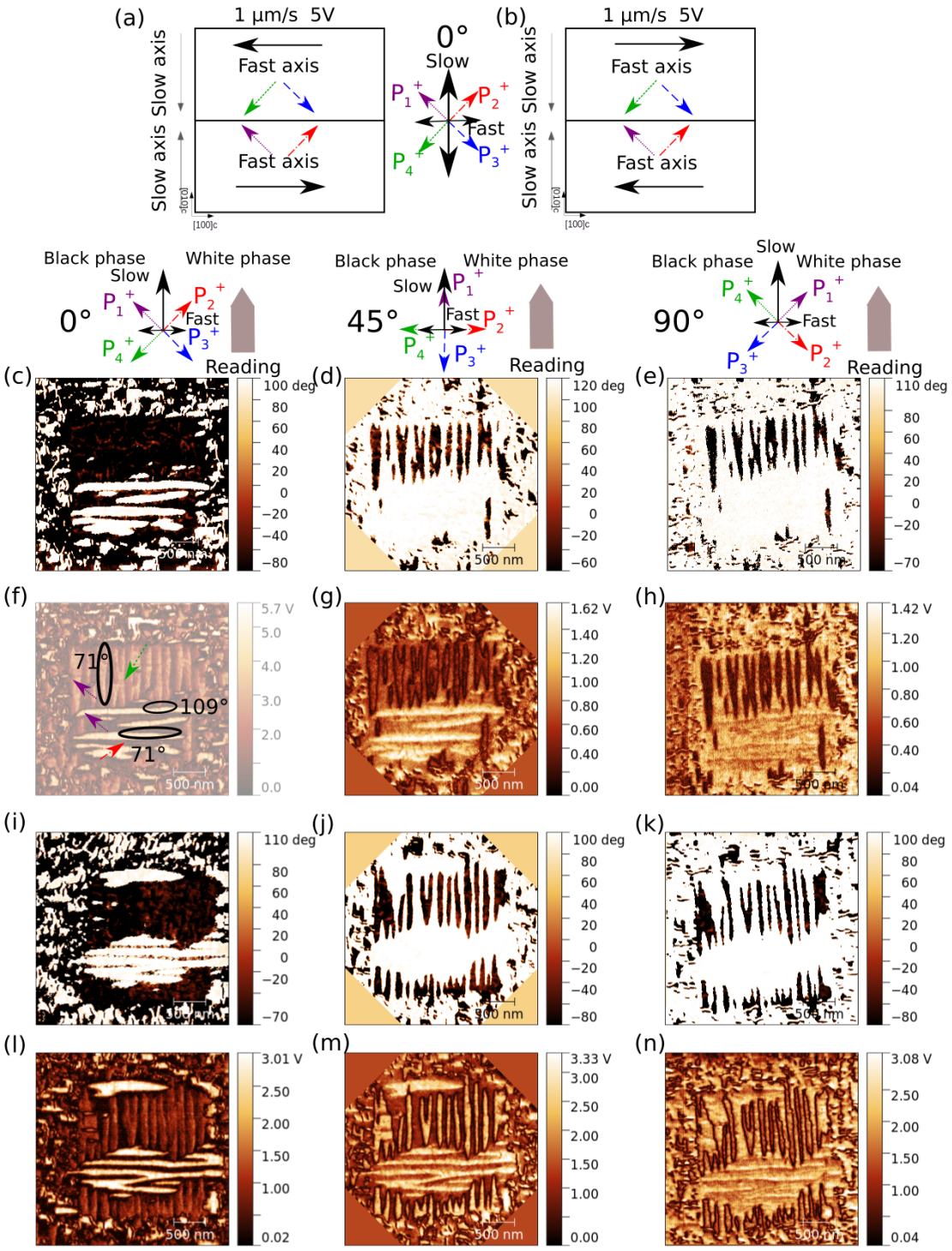

Figure 4.22: (a) Schematics for experiment 1 and (b) schematics for experiment 2 performed at 0° with the expected polarization. Lateral phase for experiment 1 at (c) 0°, (d) 45° and (e) 90°, and the corresponding amplitude images (f),(g) and (h). Lateral phase for experiment 2 at (i) 0°, (j) 45° and (k) 90°, and the corresponding amplitude images (l),(m) and (n). Image (f) also shows the different polarization directions and domain walls present in the experiment.

Angle	P_1^+ Phase	P_2^+ Phase	P_3^+ Phase	P_4^+ Phase
0° expected	Black	White	White	Black
0° observed	Black	White	Black	Black
45° expected	Unknown	White	Unknown	Black
45° observed	White	White	White	Black
90° expected	White	White	Black	Black
90° observed	White	White	White	Black

Table 4.1: Table of expected and observed colors in the phase images. Unknown means that the polarization is align with the cantilever, which means that it could be either white or black. Notice that only P_3^+ is not in agreement with what it is expected.

Angle	P_1^+ Amp	P_2^+ Amp	P_3^+ Amp	P_4^+ Amp
0° expected	Medium	Medium	Medium	Medium
0° observed	Low	High	Low	Medium
45° expected	Low	High	Low	High
45° observed	Low	High	Low	High
90° expected	Medium	Medium	Medium	Medium
90° observed	Medium	Medium	Medium	Medium

Table 4.2: Table of expected and observed amplitudes in the amplitude images. It seems more difficult to interpret the amplitude, however, most images follow the expected results.

By the direction of the scan while writing and the interpretation of results with tables 4.1 and 4.2, a majority of 71° domain walls can be determined inside a region scanned with the same slow axis. In the interface between two regions scanned with different slow axes, domains walls with 109° can be identified. To obtain 180° domain walls a negative voltage should be applied. It must be noticed that table 4.1 shows that there is no difference in contrast between P_1^+ and P_3^+ domains. It is possible that P_1^+ is favoured over P_3^+, thus only P_1^+ would be present in the results. This would not change the interpretation since both have a 71° angle with respect P_2^+ and P_4^+.

Following this reasoning, when the poling is done at -45° or 45°, the region should present three different polarizations, two aligned with the fast axis and one aligned with the slow axis. This experiment is shown in Fig. 4.23 were a region is poled with a positive voltage at -45° and observed at -45°, 0° and 90°. Three different polarizations can be observed in the same region, one for the slow axis direction and

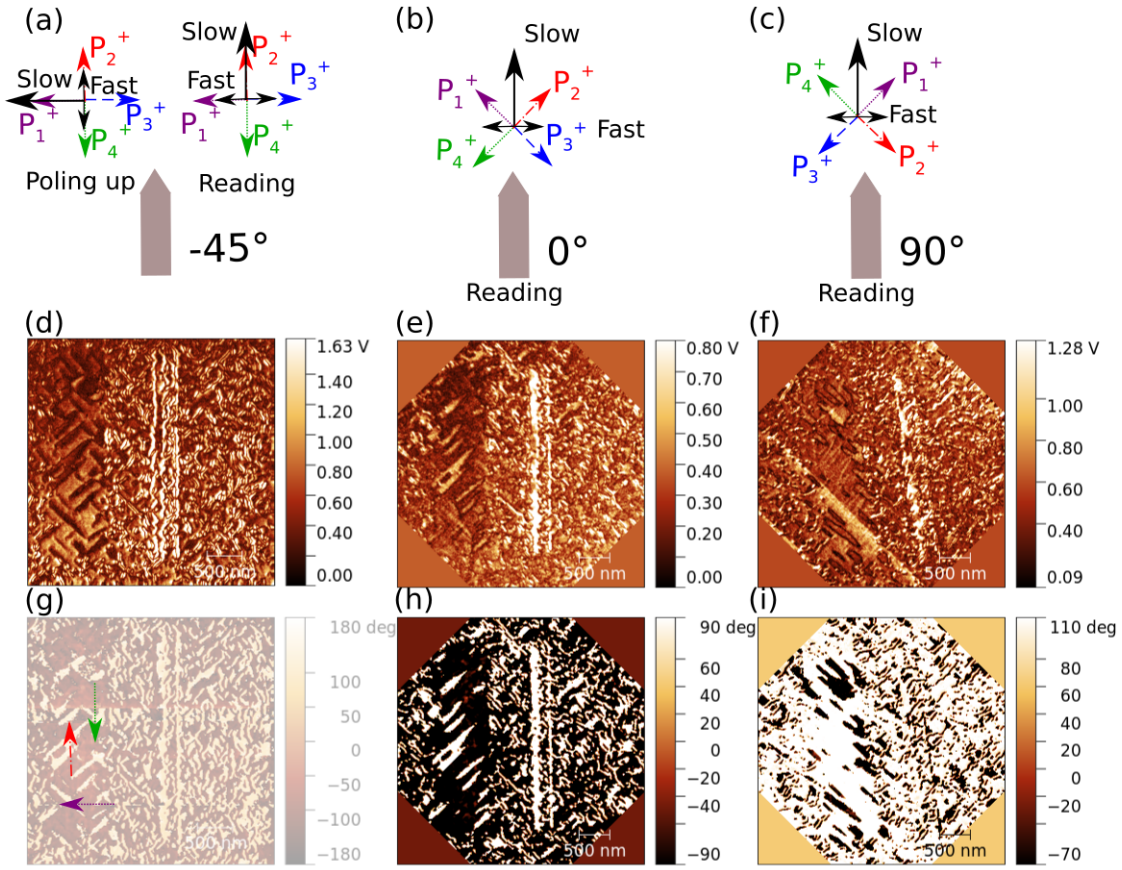

Figure 4.23: (a) Schematics of the tip and polarization for the (a) -45°, (b) 0° and (c) 90°. Lateral amplitude image of the sample at (d) -45°, (e) 0° and (f) 90°. Lateral phase image of the sample at (g) 45°, (h) 0° and (i) 90°. (g) Shows the different polarization directions present in the experiment.

two for the fast axis direction, which is in agreement with the previous experiment shown in Fig. 4.22.

However, all these results were obtained after poling an as-grown region with a positive voltage. Once the in-plane domains were created it was not possible to revert their polarization while scanning with a positive voltage, no matter the direction of scanning in the slow axis. The only way to revert the polarization was to apply a negative voltage as shown in Fig. 4.24. This means that it should be possible to control the in-plane polarization by changing the voltage applied and the direction of scanning. However, as explained in the previous section this method degrades the tip and affects future measurements.

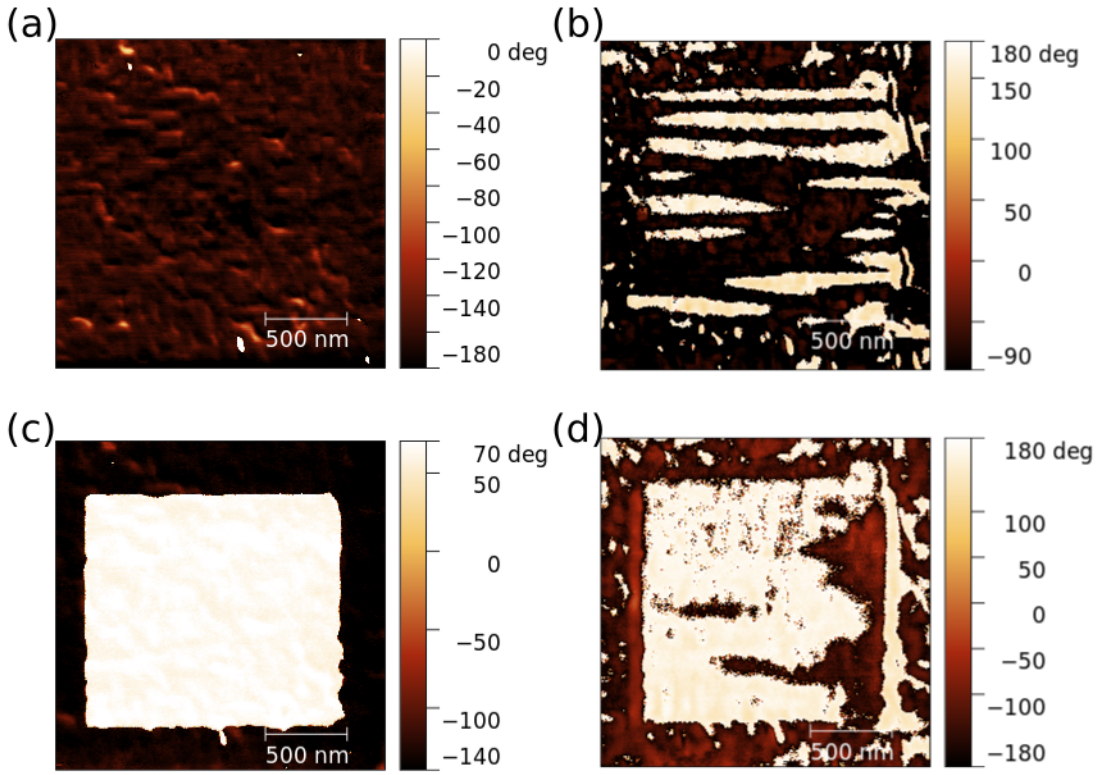

Figure 4.24: Vertical PFM phase image for the sample (a) after applying 5 V and (c) after applying -5 V. Lateral PFM phase image for the sample (b) after applying 5 V and (d) after applying -5 V.

Furthermore, as shown in Fig. 4.25, these kind of stripe patterns also appear when writing with a negative voltage. Again, following the scanning directions and with the images at different angles is possible to identify the possible directions of polarization. As in the case of the up domains, only P_1^-, P_2^- and P_4^- seems to be present. This is in agreement with previous results where P_3^+ could not be identified.

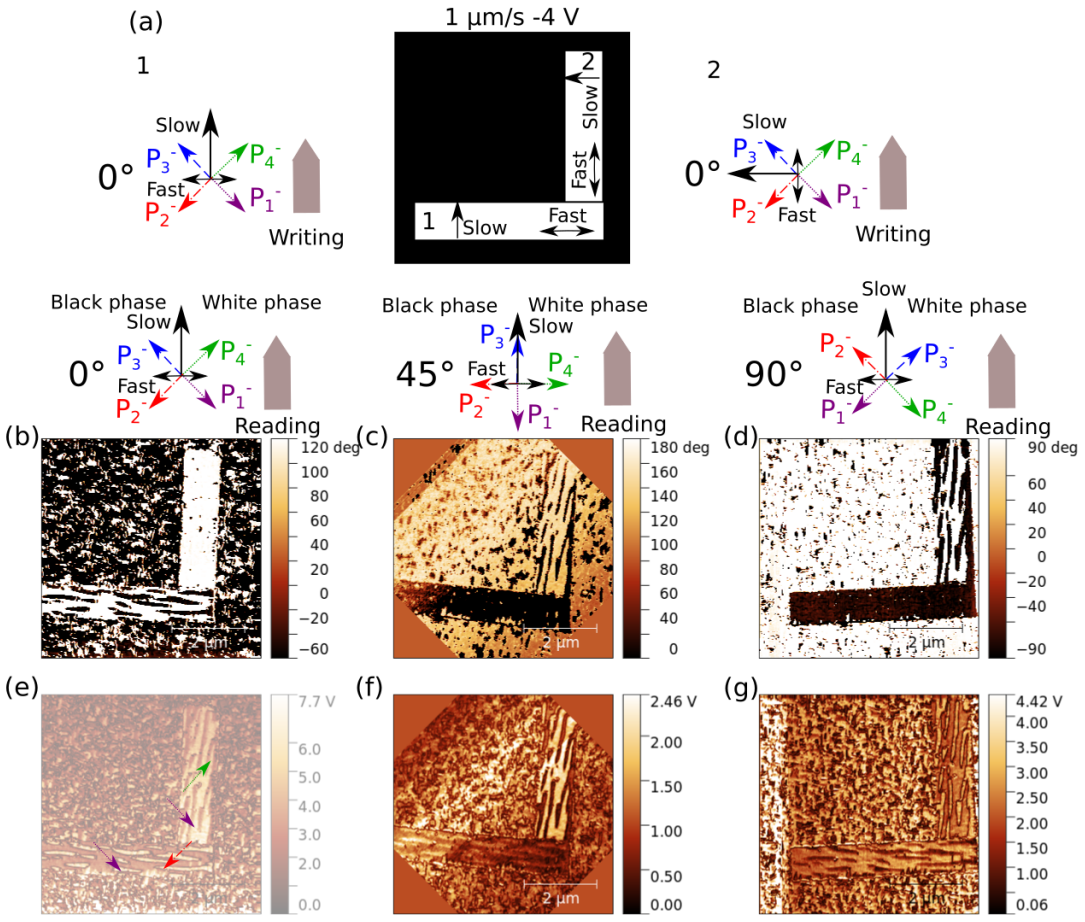

Figure 4.25: (a) Schematics for experiment 1 and 2 performed at 0° with the expected polarization. Lateral phase at (b) 0°, (c) 45° and (d) 90°, and the corresponding amplitude images (e),(f) and (g). Image (e) also shows the different polarization directions present in the experiment.

4.5 Conductivity of domain walls

Measurements with C-AFM were performed to see whether domain walls in the PZT sol-gel samples and the BFO sample had any conductivity. In the case of the PZT samples, no conduction was observed for the domains or the domain walls. In the case of BFO, conduction at domain walls should be expected by the polarization measured and the results in the literature (Seidel et al., 2009). However, the changes in the conductivity of the tip due to degradation did not allow for a clear measurement of conduction at domain walls and all currents measured could only be related with leakage currents.

4.6 Conclusions

In this chapter, the electrical switching was studied in a series of PZT thin films of different thickness grown by sol-gel and PLD, as well as in a BFO thin film grown by PLD. In the case of PZT, all of them showed the expected ferroelectric behavior and the possibility of controlling only the out-of-plane polarization. SS-PFM results in sol_{33} suggest that electrostatic effects are present and probably related with leakage currents. In that sense, the voltage applied to the sample must be controlled to avoid the injection of charge and the appearance of hillocks as in the case of the 40 nm thick film made by PLD. Furthermore, evidence that ferroelectric properties of the samples change when they present cavities or chemical inhomogeneities was found by RBS and STEM.

The BFO thin film allowed for the study of an in-plane polarization, contrary to PZT. In this sample it was possible to control both the in-plane and out-of-plane polarization. To rewrite in-plane polarization, changing the slow axis of scanning and the voltage applied was the only option. All these results also confirmed a ferroelectric behavior of the sample. Unfortunately, fast degradation of the tip occurred when working on this sample, preventing further analysis of the directions of polarization with a down component. This is thought to be related with leakage currents and oxidation on the tip.

Finally, results with C-AFM confirmed that there is no conductivity in the PZT domain walls and the degradation of the tip does not allow to investigate the conductivity in the BFO sample.

Chapter 5

Mechanical control of ferroelectric domains

5.1 How to switch ferroelectric domains mechanically ?

The mechanical switching of ferroelectric domains walls has been shown to be possible by applying pressure with an AFM tip (Lu et al., 2012a). However, several mechanisms play a role in this switching (Cao et al., 2017).

5.1.1 Mechanisms for mechanical switching

It should be noted that the importance of the mechanical switching mechanism varies as a function of the thickness of the film. Below are listed the mechanisms responsible of the mechanical switching of ferroelectric polarization:

- Flexoelectric and piezoelectric effect: Flexoelectricity (Huang et al., 2016) is the property of a dielectric material to create an inner polarization whenever a strain gradient is applied. This is close to the definition of piezoelectricity, which is the appearance of a polarization in piezoelectric materials due to an homogenous strain. These close definitions make it difficult to differentiate one effect from the other. In both cases, the polarization created can be written as:

$$P_i = d_{ijk}\varepsilon_{jk} + \mu_{ijkl}\frac{\partial \varepsilon_{jk}}{\partial x_l} \tag{5.1}$$

  Where d_{ijk}, μ_{ijkl}, ε_{jk} and x_l are the piezoelectric constant, flexoelectric constant, strain, and position coordinate, respectively. The first term of the equa-

tion corresponds to piezoelectricity, while the second one corresponds to flexoelectricity. The flexoelectric effect may be the main mechanism for ultra-thin films between 10 and 30 nm (Cao et al., 2015), because the strain gradient increases when the dimensions are reduced (Zubko et al., 2013). However, this mechanism is not predominant for thicker films.

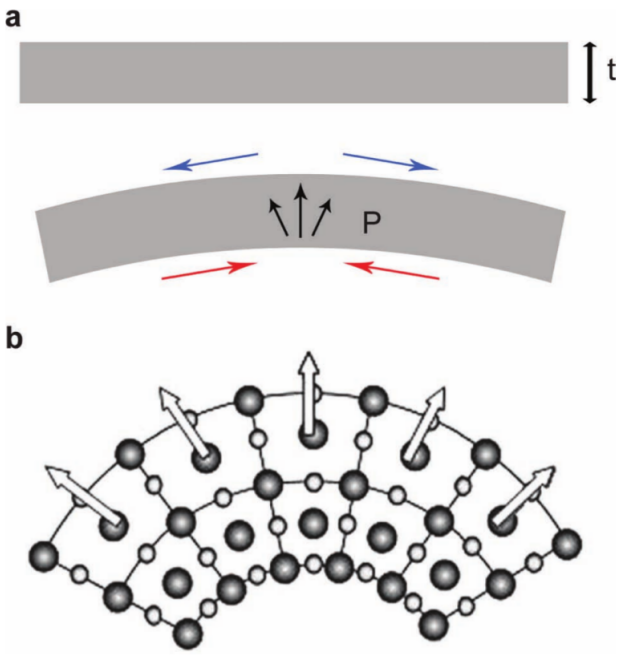

Figure 5.1: (a) film of thickness t without any strain and with a strain gradient applied creating a polarization due to flexoelectricity. (b) Effect of the gradient in the lattice, the strain gradient displaces the atoms, which generates a polarization. (Maranganti et al., 2006; Nguyen et al., 2013)

- Bulk vacancies and Vegard effect: Vegard's law (Vegard, 1921) states that in a solid solution the lattice parameter is a weighted mean of the component of this solution. Therefore, changes in the composition of the solution may also change the lattice parameter increasing the strain in the solid. Indeed, the movement of ions or ionic defects such as oxygen vacancies generates stress and strain. In the case of this work, it is important to differentiate between the direct Vegard effect where the ion concentration variation creates a stress or strain, and the converse Vegard effect where a strain or stress changes the ion concentration (Morozovska et al., 2011). Specifically, the converse Vegard effect may play a role in the mechanical switching of ferroelectric materials.

  For example, it has been reported that oxygen vacancies can be displaced in perovskites with a combination of converse Vegard effect and flexoelectric effect (Das et al., 2017). As a result an electric field in a ferroelectric material could

be created by the displaced oxygen vacancies, which may lead to a ferroelectric switching (Cao et al., 2017).

- Surface effects: As explained in Section 1.3.2, the surface of a ferroelectric material exposed to air will suffer screening from water on its surface. Applying a pressure on a material can change the electrostatic boundary conditions by affecting ions on the surface, which will change the screening conditions. Other surface effects such as triboelectricity should also be considered, since they can generate a voltage in the surface that could switch ultra-thin films. However, these surface effects are small and will be more prominent for very thin films (less than 10 nm) (Cao et al., 2017).

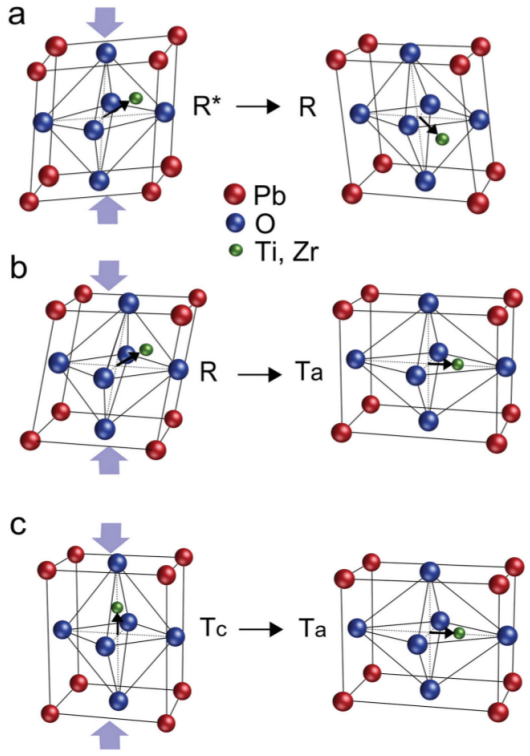

Figure 5.2: Schematic representation of polarization re-orientation (black arrow) and ferroelastic change in PZT as a result of an out-of-plane force. (a) Ferroelastic switching from a rhombohedral structure to another compatible rhombohedral structure and its change of polarization. (b) Ferroelastic switching from a rhombohedral structure to a tetragonal in-plane structure, and (c) tetragonal out-of-plane to in-plane(Tc $\rightarrow$ Ta) switching. None of these situations represent a 180° ferroelectric switching, and only c case could appear in the PZT thin films studied. The atomic displacements are exaggerated to highlight the resulting polarization direction and crystal deformation. (Edwards et al., 2016)

- Ferroelastic switching: In multiferroics (ferroelastic-ferroelectric), applying

pressure may induce a ferroelectric switching (Edwards et al., 2016) due to the ferroelastic properties. In this case, the switching is more influenced by the intrinsic properties of the material than its thickness in thin film form. This kind of ferroelastic switching usually does not involve 180° ferroelectric switching, as shown in Fig. 5.2 . However, the creation of in-plane domains by ferroelastic switching can help to achieve 180° ferroelectric switching. It has been reported in the literature that in-plane domains can reduce the energy to switch an out-of-plane polarization, this out-of-plane domains would be pinned at the interface with the in-plane domains (Li et al., 2021).

It is important to note that all these mechanisms can occur at the same time, sometimes even be coupled.

5.1.2 Recent evidence of mechanical control

The first evidence of mechanical control of ferroelectric domains was observed in PZT capacitors in 2003 by bending the substrate of the capacitors (Gruverman et al., 2003). In the same publication, a shift of the hysteresis loops that would change as a function of the direction of bending was found, which led to the conclusion that the switching was caused by flexoelectricity. Indeed, the bias created by flexoelectricity was large enough to displace the loops until only one polarization would be possible at null electric field. However, it was not before several years later that mechanical switching was observed for the first time by using an AFM tip in $BaTiO_3$ (BTO) (Lu et al., 2012a). Since then, the mechanical switching with an AFM tip has been reported in literature for materials such as PZT (Guo et al., 2014; Vats et al., 2020), BTO (Zheng et al., 2014) and BFO (Chen et al., 2016) and for thicknesses from a few nm to 100 nm. Most of these results show an out-of-plane switching. Nevertheless, some reports on BFO demonstrate switching of in-plane polarization by applying a stress and moving the tip in a determined direction in a similar way to what is done with trailing fields (Park et al., 2018). Furthermore, recent studies report switching by bending the sample instead of applying pressure with an AFM tip (Alsubaie et al., 2017).

While mechanical switching seems a promising way to control ferroelectric domains, some limitations are still present in the technique. The main one is that when switching is done by AFM tips instead of bending stage, switching is only possible in one direction (from up to down domains) due to the strain gradient being created in only one sense. To overcome this limitation, theoretical ideas such as working on ultrathin films where surface effects are the main mechanism have been proposed.

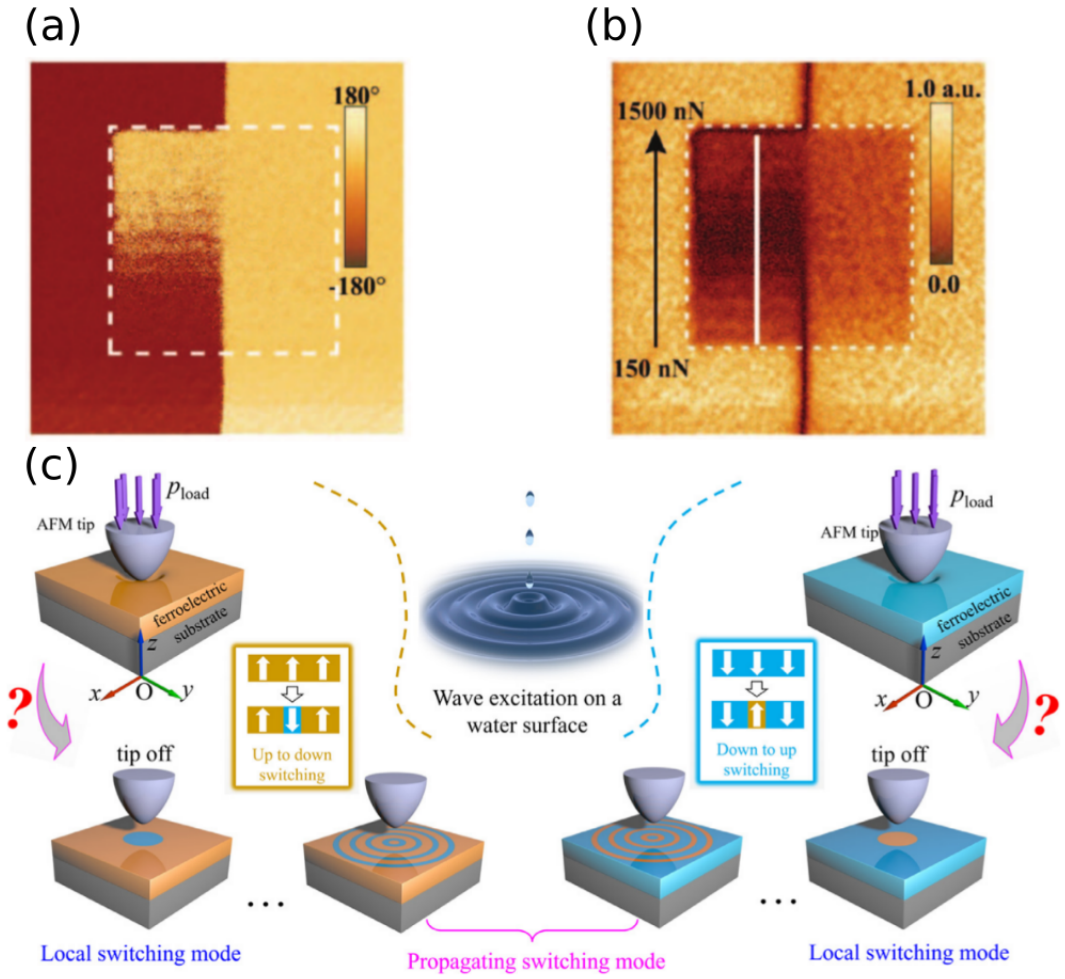

Figure 5.3: (a) PFM phase image and (b) PFM amplitude image of mechanical switching in BTO (Lu et al., 2012a). (c) Theoretical switching by mechanical waves proposed by Chen et al. (Chen et al., 2018). The only difference between left and right is the original polarization state.

One example is the work of Chen et al. (Chen et al., 2018) where it is theorize that it could be possible to create ripple-like patterns due to mechanical waves on the surface have, as shown in Fig. 5.3. The other limitation is that this switching is thickness dependent, therefore, the thickness of the sample would completely change the main mechanisms at play, see previous section.

All these results open the door to an electromechanical control of ferroelectric domains and derived electronic devices. For example, it has been proven possible to switch a ferroelectric tunnel junction just mechanically (Lu et al., 2012b). This approach to ferroelectric switching is quite recent, and holds the potential to bring new technologies in fields like pressure sensors.

Finally, the pressure induced by the tip or an external mechanical stress are not the only ways to modify the domain wall topology by non-electrical means

in ferroelectric materials. Strain engineering (Schwarzkopf et al., 2017; Catalan et al., 2011) also allows some control over domains and domain walls. However, the epitaxial strain is fixed by the growth conditions and is independent of any additional stress applied externally e.g. by an AFM tip. This kind of stress engineering will not be explored in this work.

5.1.3 Force measurement

In the NT-MDT Ntegra microscope used for this work the position of the tip is controlled by a setpoint obtained in nA. To translate this signal into an applied force, force curves presenting the deflection in nm against the setpoint in nA were performed as the one shown in Fig. 5.4. By performing a linear adjustment to the force curve, it was possible to obtain the relationship between the setpoint and the deflection. This allows us to obtain the deflection for a certain setpoint

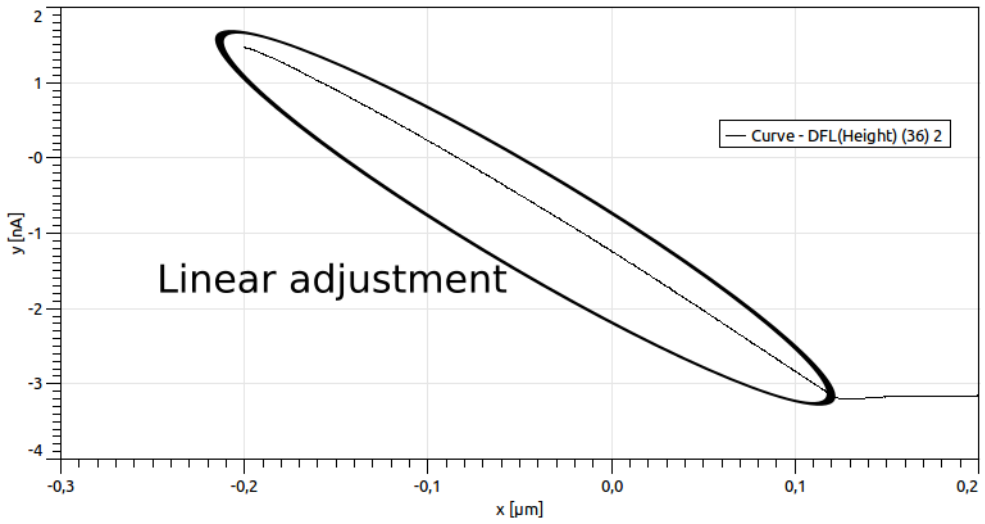

Figure 5.4: Force curve of the setpoint (y) against the displacement (x).

Once the deflection can be controlled, a calibration of the tip using thermal noise calibration (Hutter and Bechhoefer, 1993) can be performed to obtain the elastic constant k of the tip. With this information, it is possible to apply Hooke's law ($F = k\delta x$) to obtain the force applied by the tip on the surface.

5.2 Mechanical switching in PZT samples

Mechanical switching was observed in PZT samples by applying a force with an AFM tip. The switching was always from up to down polarization due to the direction of the stress applied.

Sol-gel samples were appropriate to study the mechanical switching due to the variety of thicknesses and samples available for the experiments. The next section is dedicated to experimental results on these samples, as well as and those obtained on the PLD samples.

5.2.1 Results obtained with a conductive tip

Most of the experiments presented in this chapter were obtained with a Pt-Ir tip of $\sim$ 25 nm radius of curvature and a stiffness (k) for the cantilever of 4.6 $\pm$ 0.5 N/m. This type of tip is the same used for PFM and electrical switching, which means that it was possible to perform electrical and mechanical experiments at the same time.

In the next sections, we will study the mechanical switching obtained in the two thinnest samples with this kind of tip.

5.2.1.1 Mechanical switching versus electrical switching

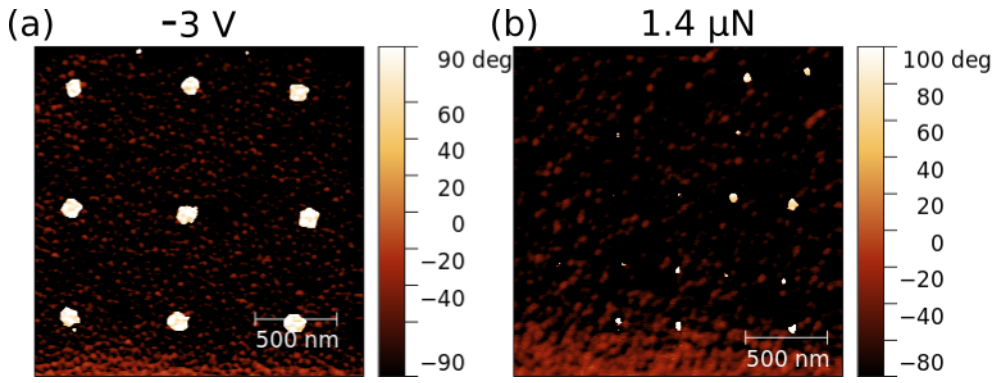

Figure 5.5: (a) Phase image of a region with 9 points switched by -3 V applied for 10 to 90 seconds (b) Phase image of a region where 1.4 μN were applied during 60 seconds in 25 points, not all points switched. Both images were obtained in sol_{33}.

Mechanical switching presents two advantages over electrical switching, the main one being the limitation of any charge injection and electrostatic effects like the ones observed in the previous chapter. For example, artifacts like hillocks do not appear after mechanical switching. The other advantage shown in Fig. 5.5 is that domains switched mechanically are barely affected by the layer of water on the surface. Therefore, a domain switches only under the contact area between the tip and the surface, allowing for the creation of smaller domains.

However, mechanical switching has also disadvantages compared with electrical switching. Firstly, switching with an AFM tip is only possible from up to down

domains, as already mentioned. Secondly, the switching depends on the stress rather than the force, which changes when the tip is contaminated or degraded with use, thereby decreasing the switching efficiency[1]. Thirdly, this switching depends more on the local state of the sample under the tip. Parameters like the topography or defects in the sample may change the contact area of the tip and the force applied, as shown in Fig. 5.5: not all domains switch with the same force or have the same size after switching. While a similar effect can be expected when applying an electric field, the water meniscus acting as an electrode should make the effect less remarkable. Finally, applying high forces could lead to indentation, and damage the tip and the surface of the sample.

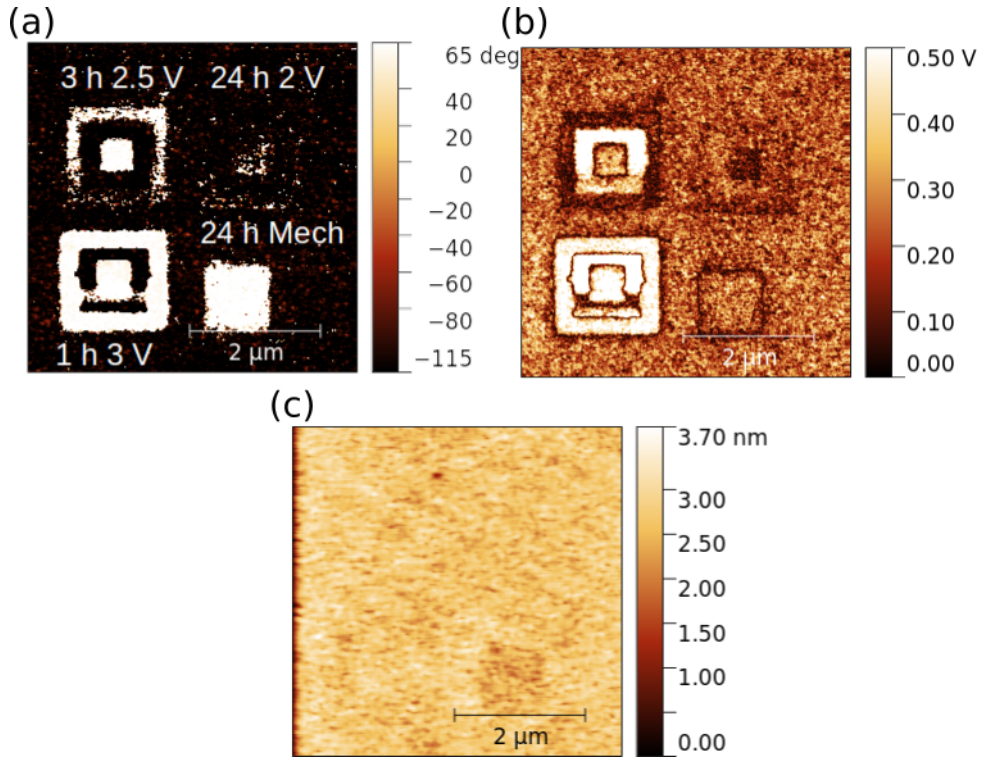

Figure 5.6: Comparison between four patterns, three created by the application of different electric fields (± 2, ± 2.5 and ± 3 V) and one created mechanically. (a) Phase image, (b) Amplitude and (c) topography images of the same region. All images were obtained in the PLD_{20} sample.

As an example, in the PLD_{20} sample it was observed that electrically written down domains with voltages of -2.5 and -2 V reverted back to the up polarization after tens of minutes. However, mechanically switched domains remained for longer periods of time as shown in Fig. 5.6, with the only disadvantage of slightly changing

[1]In fact, the degradation of the tip also changes the electric field produced. Higher voltages will be required in that case, but the effect seems more important in mechanical switching.

the topography, a phenomena also observed for the domain written with -3V, which in the electrical case can be link to electrostatic effects. In the amplitude image, electrically switched domains show a higher amplitude than mechanically switched domains, this is a clear sign of electrostatic effects as explained in Section 3.3.7. It is possible that this electrostatic effects reflect charges on the surface that, when evacuated, make the domains unstable, which leads to domains reversing. In that sense, experiments that were operated on this samples support the conclusion that the best way to control the orientation of the domains in this sample was a combination of electrical and mechanical switching, where mechanical stimulus are used to switch to the down polarization and the electrical stimulus to switch to the up polarization.

5.2.1.2 Effect of the scanning speed in the mechanical switching

The scanning speed is a important factor for both electrical and mechanical switching, however our experiments show that it is even more important for mechanical switching. Indeed, the time spent by the tip over each pixel is directly dependent on the scan speed. If it is too small due to a fast scanning speed, the pressure will not be applied during enough time to let the domain grow and increase its probability to be clamped and remain stable. Furthermore, higher speeds might damage and wear the tip, which can change its geometry and thus the applied stress during scanning.

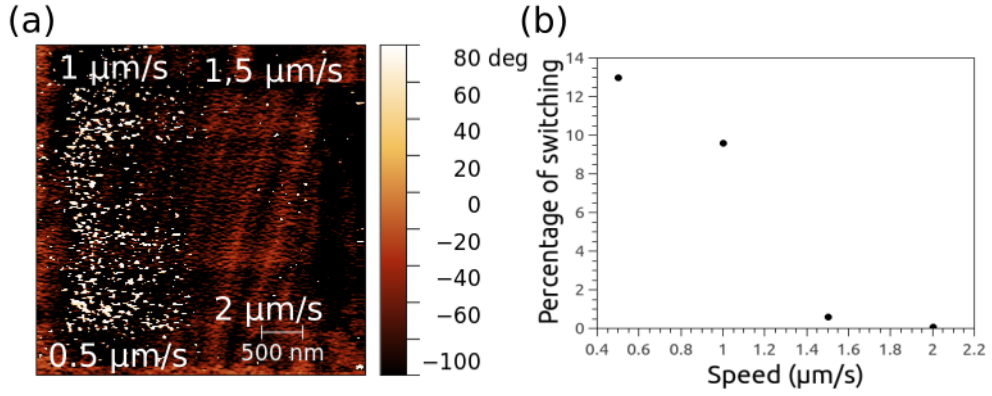

Figure 5.7: (a) Phase image of the four regions mechanically switched with a force of 1.3 μN and different speeds. (b) Plot of the percentage of switching against the scanning speed. The experiment was performed in sol_{33} sample.

To better understand the effect of the scanning speed on mechanical switching, an experiment was performed with sol_{33}. The experiment consisted on poling electrically a region of 3×3 μm^2 with 3 V to obtain a region with a uniform up

polarization. Then four squares of 1.5×1.5 μm^2 were written mechanically with the same force but different speeds inside the electrically poled square. As shown in Fig. 5.7, the slower the scanning speed, the bigger the switched area. For this reason, mechanical switching experiments shown in this work were performed with a scanning speed of 1 μm/s, since it is a good compromise between the time needed for the experiment, and a moderate speed to switch without damaging the tip too much. It is also important to remark that the voltage used to pole the sample before applying a mechanical pressure also affects the mechanical switching and will be the focus of future sections.

5.2.1.3 Determination of a threshold force on sol-gel samples

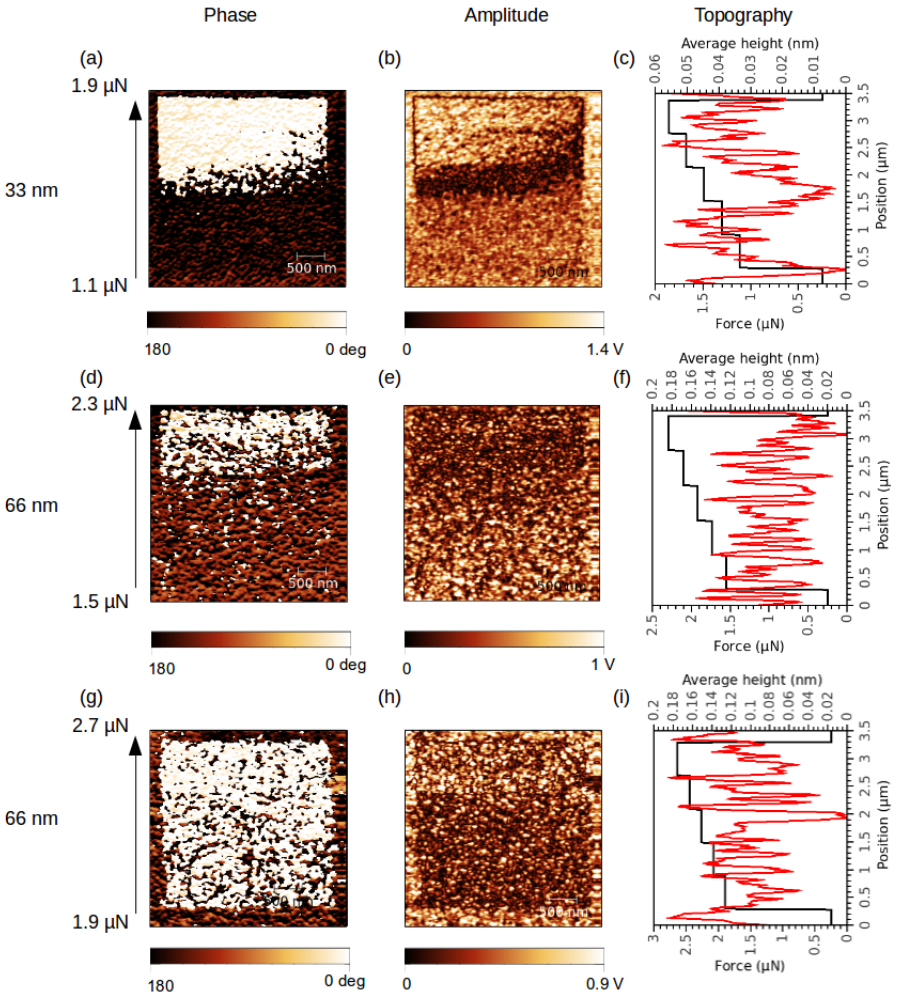

Figure 5.8: Ferroelectric domain switching using mechanical stress for PZT samples of different thickness (a), (d) and (g) phase image (b), (e) and (h) amplitude image and (c), (f) and (i) section profile and force plot. The size of all images is 3.5 μm. The spatial evolution of the applied force (black solid line) is shown alongside the topography (red solid line), as a function of the vertical tip position.

This work has shown that it is possible to switch domains mechanically, but not all points in a sample will switch for a given force. With this in mind, is there a threshold force for which most domains switch in a given sample?

An as-grown region of 3×3 μm^2 of a sol-gel sample was scanned at a speed of 1 μm/s while increasing the force applied every 600 nm. In this way, 5 different regions of 0.6×3 μm^2 were obtained where a different force is applied. Applying the same method used to measure the percentage of as-grown down domains, the percentage of domains that switched were computed for each force. Interpolating these points using a data analysis software (QtiPlot), the force for which 75% of domains switched can be evaluated, and defined as the threshold force for the switching.

The results of these experiments for the sol_{33} and sol_{66} samples are shown in Fig. 5.9. Above a given force the percentage of switched domains increases rapidly. This increase goes up to 80-90 % for both samples. After interpolation, the threshold forces obtained are 1.6 μN for sol_{33} and 2.3 μN for sol_{66}. As expected, the thicker films requires a higher force to switch the polarization of domains.

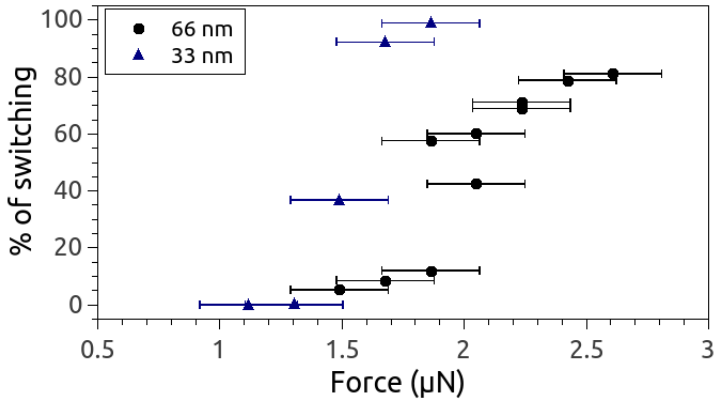

Figure 5.9: Plot of the percentage of switching against the force applied for sol_{33} and sol_{66}

Fig. 5.8 shows the phase and amplitude image after the switching in both samples and the average height of the topography. It is important to note that the topography is the same before and after switching, which means that the surface of the sample is not damaged. The amplitude in the 0.6×3 μm^2 area before the uniform switching (the point of 1.5 μN for sol_{33} and 2.1μN for sol_{66}) is almost null in all the region. The reason behind this observation is that only small domains start to nucleate at the beginning of the switching, hence creating a large number of domain walls, which have null amplitude.. When the force increases, domains become bigger and the number of domain walls decreases, which results in a higher amplitude.

5.2.1.4 Spectroscopy study of the mechanical switching

The previous section was focused on determining the threshold force needed to switch 75% of domains in a PZT thin film. This section will complement these findings by using SS-PFM to study the evolution of the coercive voltage while different forces are applied on the sol_{33} sample. In this way, it is possible to determine the force needed to switch the domains.

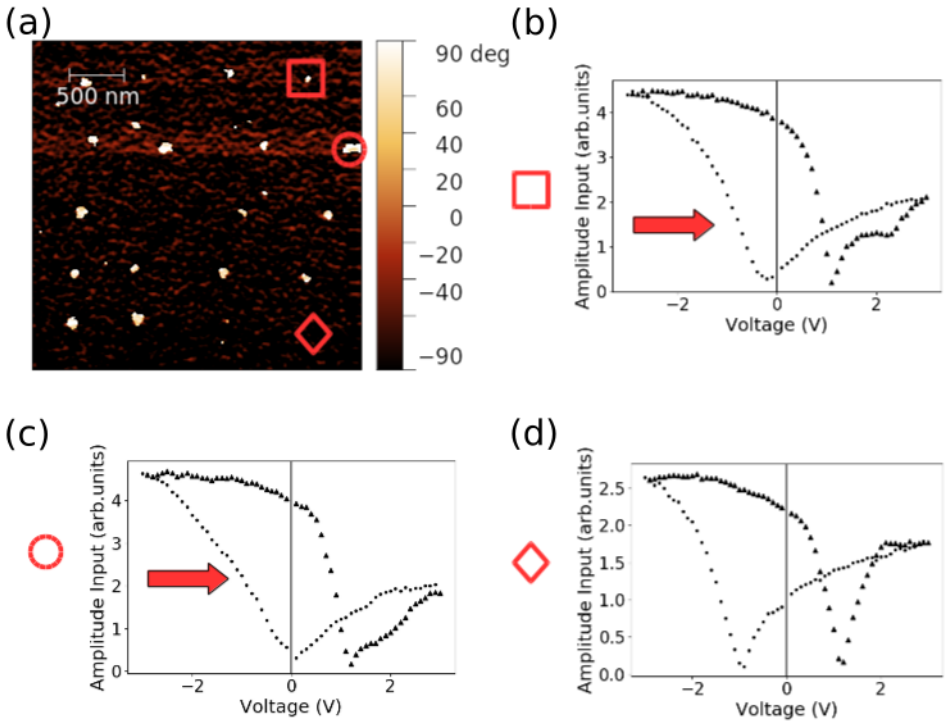

Figure 5.10: (a) Phase image of down domains created mechanically with 1.7 μN in sol_{33}, three points are marked by a square,a circle and a diamond. Amplitude off-field loops obtained while applying 1.7 μN of (b) the square point, (c) the circle point and (d) the diamond point.

Indeed, as shown in Fig. 5.10 a shift of more than 1 V in the coercive voltage is visible when an hysteresis loop is performed while applying a force. In this case, all points had the same force applied, but not all of them switched. Those points that did not switch were the ones that did not show a shift of the coercive voltage. Therefore, the shift of the coercive voltage is related to the mechanical switching.

In order to study the shift of the coercive voltage with the force, 20 loops were obtained at different points for each of the 9 different forces applied. In this way it was possible to plot the average coercive voltage measured against the force applied as shown in Fig. 5.11. While both coercive voltages shift, the negative one does it faster, which results in a decrease of the hysteresis loop width. For certain forces the

negative coercive voltage becomes positive. Therefore, with that force and at null electric field, only the down polarization state is stable, which is at the origin of the mechanical switching. Furthermore, the force where the average negative coercive voltage is null is 1.7 μN, which is not far from the threshold force determined for the sol_{33} sample in the previous section.

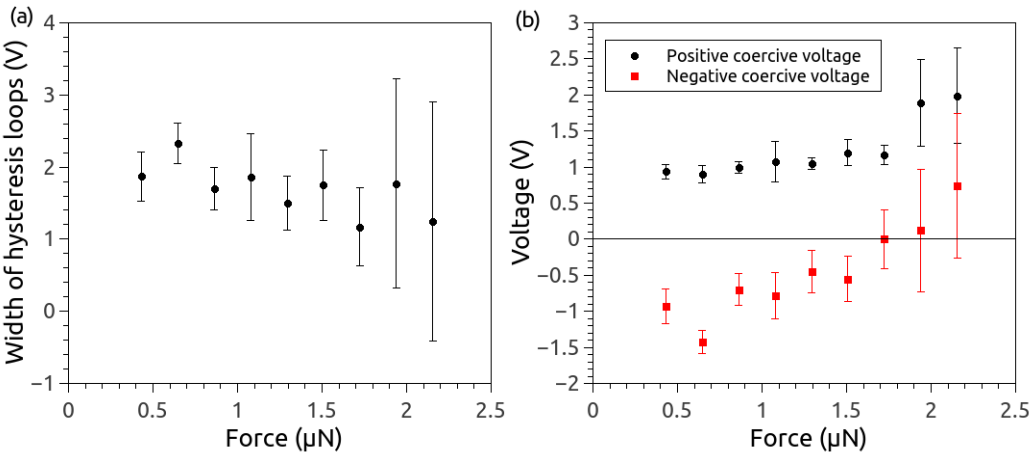

Figure 5.11: (a) Plot of the hysteresis loop width (the difference between positive and negative coercive voltage) against the force applied. (b) Plot of negative and positive coercive voltage against the force applied. All results obtained in sol_{33} sample.

The shift of the coercive voltages can be linked to flexoelectricity favouring the down polarization as expected from the sign of the strain gradient applied, while the fact that the width of hysteresis loops decreases can be associated with a decrease in the tetragonality of the film according to Lu et al. (Lu et al., 2012a). This decrease of tetragonality comes from the strain slightly changing the relative position of atoms and the relation between the lattice parameters. For the thinnest samples, it is expected that flexoelectricity is the main effect governing the mechanical switching (Cao et al., 2015). However, in thicker samples, flexoelectricity is not supposed to be able to switch the polarization (Cao et al., 2017), therefore it will be necessary to consider other mechanisms such as ferroelasticity (Edwards et al., 2016) or bulk electrochemistry(Morozovska et al., 2011).

5.2.1.5 Electrical tuning of the mechanical switching

Since mechanical switching with an AFM tip only switches domains from up to down, electrically switching an area to the up state is needed to erase mechanically written domains. To understand the effects of electrically poling an area before switching it mechanically, two different experiments were designed for the sol_{33} sample. One with

the purpose of studying the effect of different voltages applied before mechanical switching on the surface, and the other to study the effect of applying the same voltage during different times.

In the first experiment, two regions of 1×3 μm^2 were scanned at the same speed while applying 2 V and 3 V respectively, while a third region was scanned without applying a voltage as shown in Fig. 5.12 (a). After that, all regions were scanned while applying a force of 1.4 μN at 1 μm/s. The results presented in Fig. 5.12 (c) and (e) show that in the regions where a higher voltage was applied the percentage of switched area is lower. Since the sol_{33} is a leaky sample as shown in Section 4.2.3, it is possible that electrically poling a sample also injects charges in the sample. These charges, together with a possible redistribution of mobile defects (such as oxygen vacancies) (Pintilie et al., 2015), could screen the electric field created mechanically and change the threshold force needed to switch. Applying a higher voltage would mean injecting more charge and affecting more the distribution of defects, which explains why the region poled with 3 V has less domains switched that the one poled with 2 V. If this is true, applying a voltage during longer times will mean that more charges are injected and defects have more time to migrate, which means that a similar effect should be observed. To verify this hypothesis the second experiment was performed.

In the second experiment, three regions of 1×3 μm^2 were poled electrically with 3 V but with three different writing speeds (1, 2 and 4 μm/s) as shown in Fig. 5.12 (b). Then, all regions were scanned while applying a force of 2.1 μN at 1 μm/s. The force was higher than in the previous experiment to verify that it was still possible to switch regions poled with 3 V. The results presented in Fig. 5.12 (d) and (f) show that the slower the electrical poling the higher the force needed to switch domains mechanically. This is in agreement with the hypothesis of injected charges and defects screening the electrical field created mechanically.

All these results show that it is possible to tune the force needed to switch domains mechanically by previously applying an electric field. However, it also means that when combining electrical and mechanical switching, the voltage and speed of writing must be controlled carefully to avoid changing the threshold force. This is also the reason why the experiments in Section 5.2.1.3 were carried out in as-grown regions.

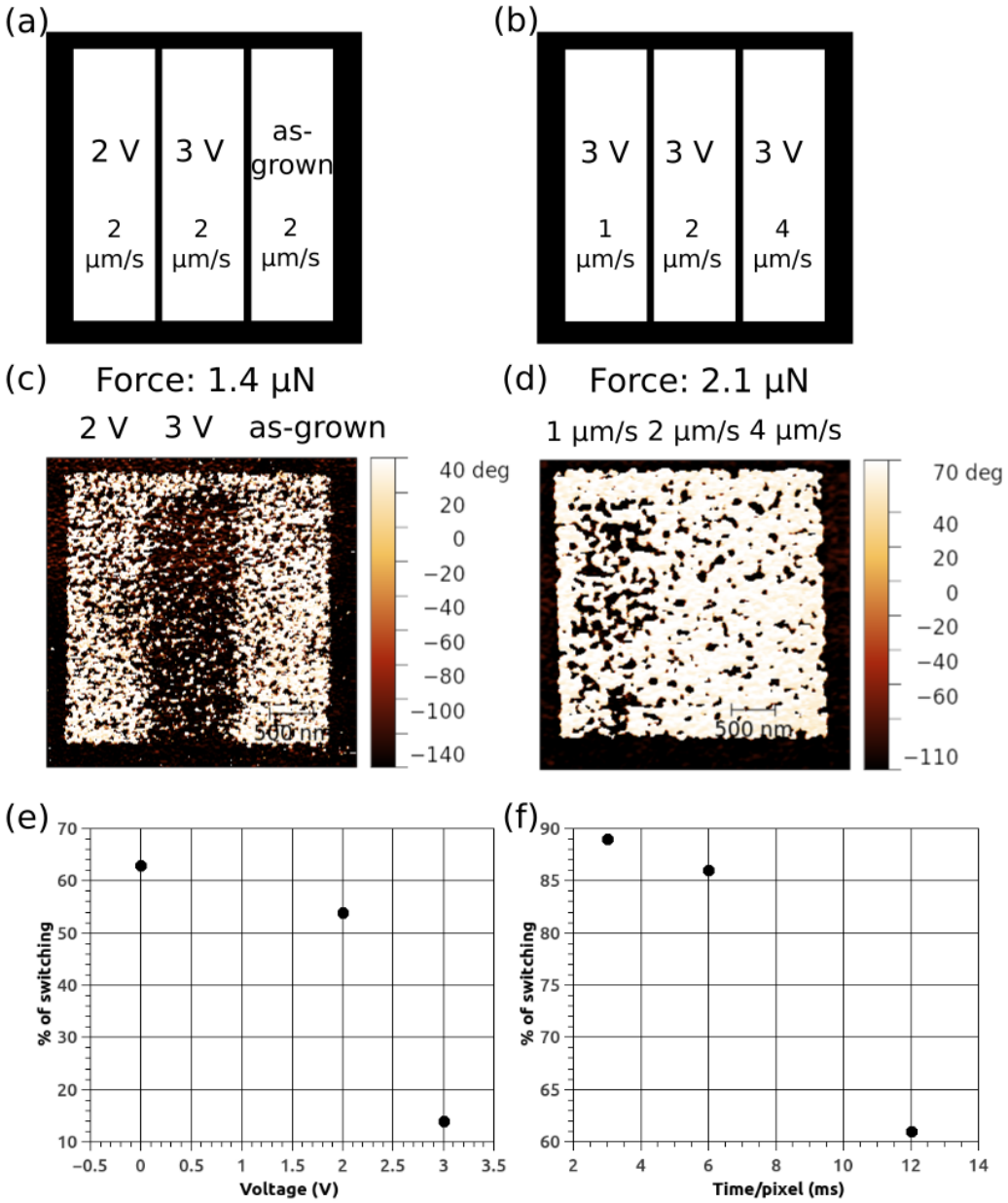

Figure 5.12: Schematics for (a) the first experiment and (b) the second experiment. PFM phase images obtained after (c) the first and (d) the second experiment. Plot of the percentage of switching against (e) the voltage previously applied in the first experiment and (d) the time per pixel the voltage is applied in the second experiment. All experiments were carried out in the sol_{33}.

5.2.1.6 Erasing mechanically written domains

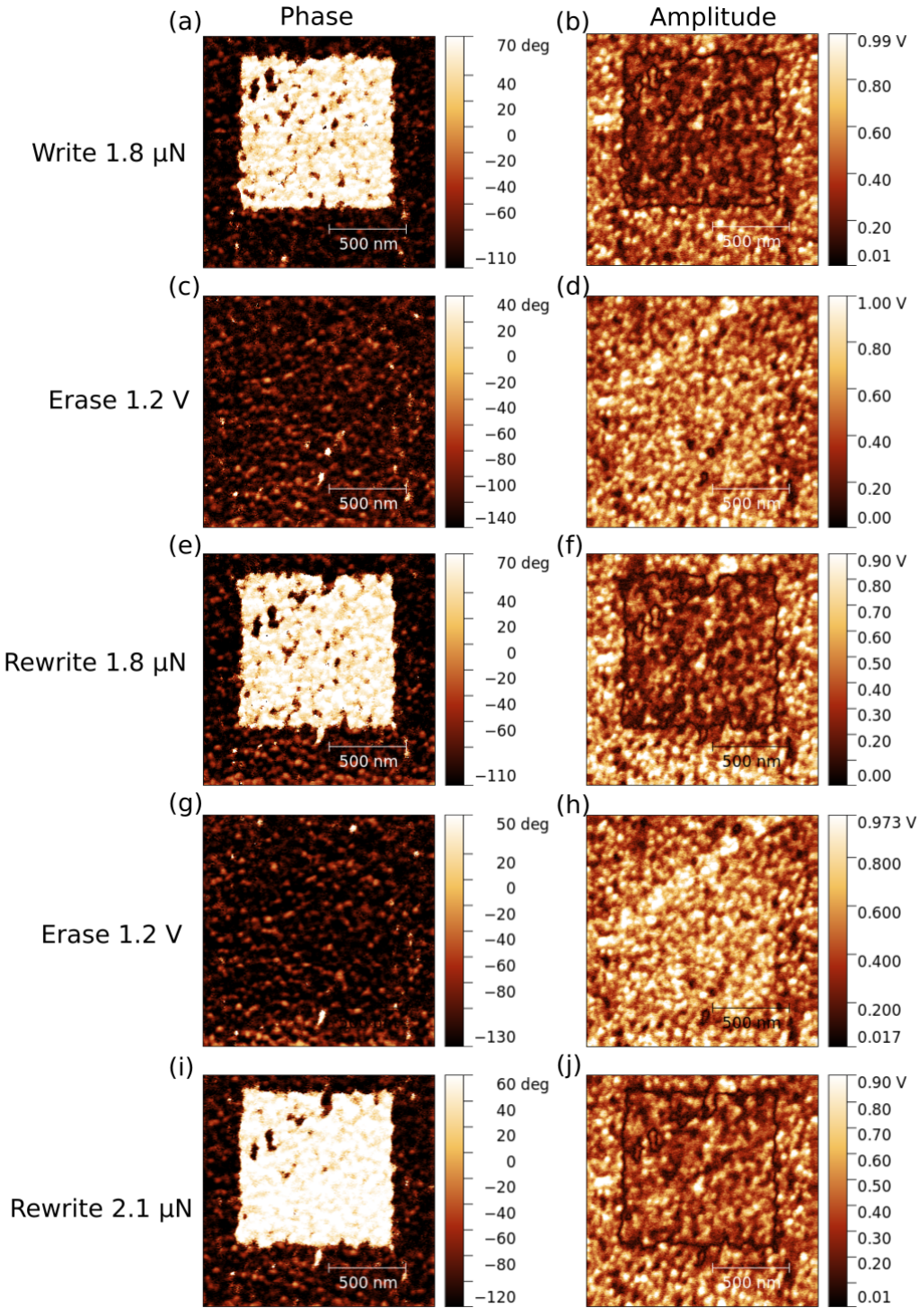

Figure 5.13: PFM phase and amplitude images of sol_{33} after (a) and (b) writing mechanically in an as-grown region with 1.8 μN, (c) and (d) erasing electrically the domain mechanically written with 1.2 V, (e) and (f) rewriting the same region with 1.8 μN, (g) and (h) erasing again with 1.2 V, and (i) and (j) rewriting with 2.1 μN to see if it was possible to switch the unswitched regions with 1.8 μN.

With the previous section showing that the threshold force increases after electrically poling the sample, it was necessary to study if it was possible to erase mechanically the domains that was written previously electrically. The sol_{33} sample was used and, as shown in Fig. 5.13, a domain was created by applying a pressure and scanning. This domain was later erased by applying 1.2 V, which is a voltage close to but higher than the coercive voltage (Fig. 4.6) and should not inject charges in the sample. Then, the domain was rewritten mechanically, and the whole process repeated a second time. It was again possible to switch the domain mechanically, with no apparent fatigue or damage of the surface, which proves that it is possible to control ferroelectric domains by combining electrical and mechanical switching.

It is interesting to notice two effects visible in Fig. 5.13. The first one is that the regions that do not switch mechanically are always the same ones every time the domain is written. Therefore, something makes these region more difficult to switch than the other. This can be related to the cavities observed in the sol-gel samples. Cavities could correspond to fragile regions with defect that may help stabilize domains and switching would require less force, while regions without defects would require a higher force or more time (Xiong et al., 2020) to switch the polarization. To verify that these regions can still be switched, the last mechanical switching was performed with a higher force (2.1 μN). The results show that the switching occurs, and suggest that an even higher force would switch the rest of unswitched areas. Finally, regions switched mechanically present a smaller amplitude signal due to the absence of electrostatic effects.

5.2.1.7 Comparison between PLD and sol-gel samples

To better understand the role of defects in mechanical switching, the PLD_{20} and the sol_{33} samples were compared. The experiment was performed in a similar way as the experiments presented in Section 5.2.1.3, but with a different tip that had a k constant slightly higher. Therefore, the range of force is higher for this experiment.

The results shown in Fig. 5.14 show that switching in the PLD_{20} sample requires a higher force than in the sol_{33} sample even if the sample is thinner. After interpolation, the threshold force for the PLD sample is 1.9 μN, while the one obtained earlier for the sol_{33} sample was 1.6 μN in agreement with the result presented in this section. This can be related to PLD samples being expected to present a higher coherence length, which means bigger crystalline grains, and a higher tetragonality than sol-gel samples (see Section 2.2.3), which means that defective films facilitate the mechanical switching of ferroelectric domains.

In Fig. 5.14 (d) the evolution of the coercive voltages with the applied force for

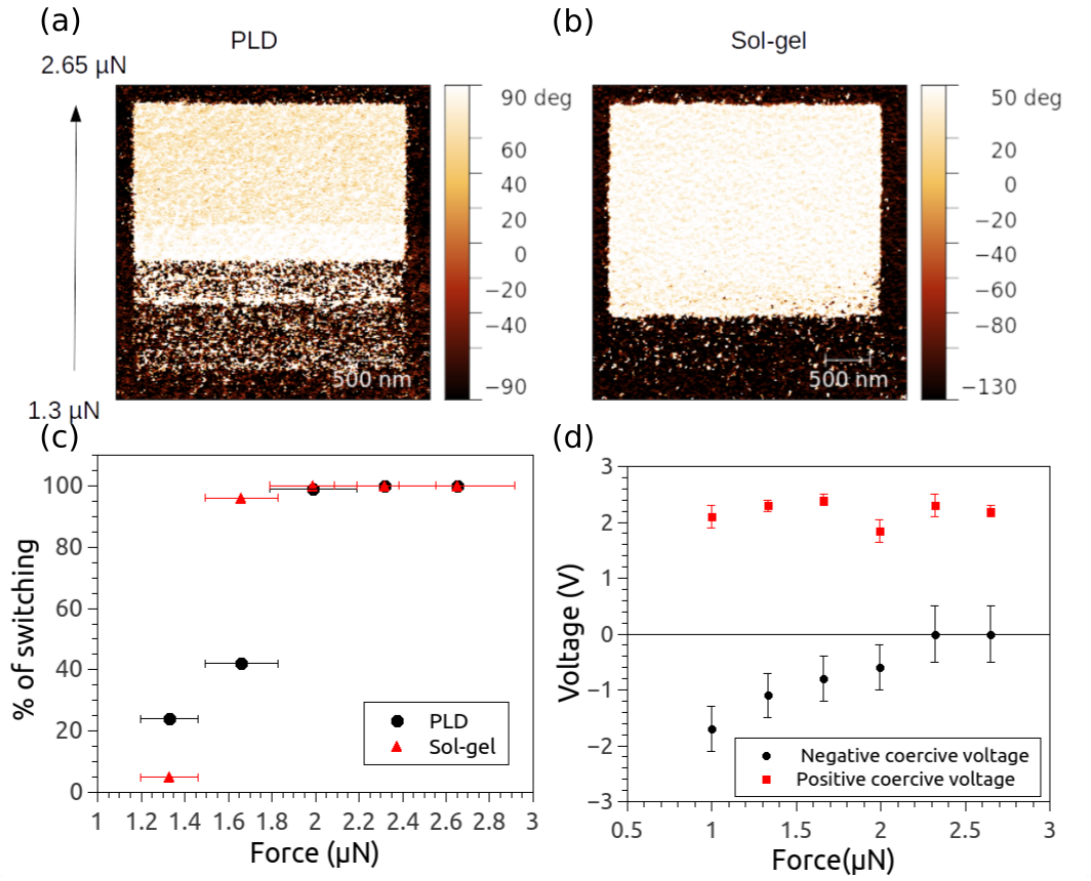

Figure 5.14: PFM phase images after mechanical domain switching of (a) 20 nm PLD sample and (b) 33 nm sol-gel sample. (c) Plot of the percentage of switching with force for each sample. (d) Plot of the evolution of the coercive voltage with force for the 20 nm PLD sample.

the PLD_{20} sample is shown. The negative coercive voltage is shifting as it happened with the sol-gel sample, which again can be related to flexoelectricity and a decrease of tetragonality. The threshold force, in this case, is slightly lower than the force needed to reach a null coercive voltage. Therefore, the results presented in (a),(c) and (d) are in agreement.

5.2.2 Results obtained with a badly conductive tip

To complement the results obtained with the soft conductive tip, badly conductive diamond tips were used. They allow to study the mechanical switching in a situation where a discharge from the sample should be slower and can be neglected, therefore the switching is completely mechanical. Furthermore, these tips prevent the current from the change of the compensation charge to flow through the tip when switching occurs, which changes the switching conditions. Finally, since these tips are harder,

they allowed for the study of mechanical switching in thicker films. They had a cantilever with a stiffness (k) of 90 ± 9 N/m, and a radius of curvature around 150 nm.

While these tips allow for the application of higher forces, they prevent from using PFM. This has challenging implications since the experiments must be performed without any knowledge about the actual ferroelectric state of the sample. Therefore, all the PFM images presented in this section were performed after changing the diamond tip to a conductive one.

5.2.2.1 Mechanical switching up to 200 nm

Mechanical switching of domains in as-grown areas was possible up to the 200 nm thick sample with the same badly conductive tip as shown in Fig. 5.15 and 5.16. However, switching in the sol_{200} sample was not as uniform as in the others samples. This can be related to the sample and the tip getting damaged after using a high force. Indeed, Fig. 5.15 shows how the sample starts to switch for a certain force, but for a higher force the percentage of switched domains decreases to the as-grown state. This is also supported by the topography in 5.16, which shows a decrease of the height with the force in agreement with indentation of the sample.

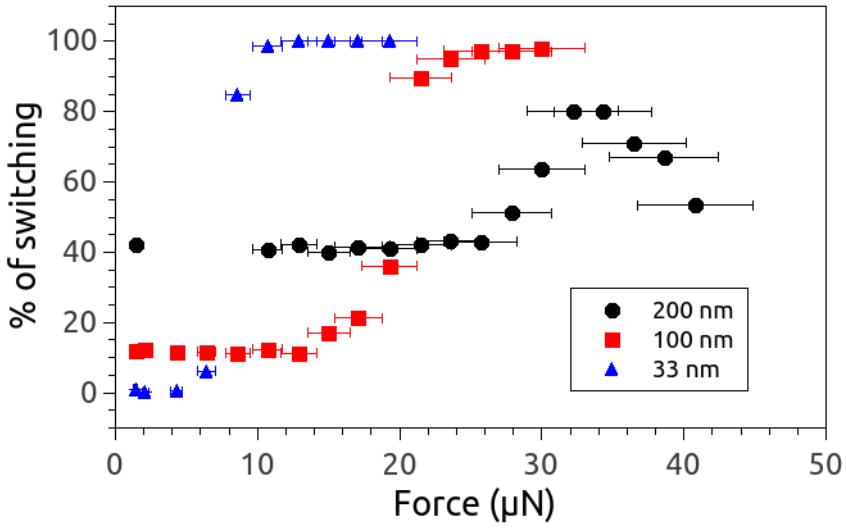

Figure 5.15: Plot of the percentage of switching against the force with a badly conductive tip for the sol_{33}, sol_{100} and sol_{200} samples.

From Fig. 5.15 it is possible to determine the threshold forces for the three samples as reported previosly in Section 5.2.1.3. The results show a threshold force of 8.3 μN for the sol_{33} sample, 20.9 μN for the sol_{100} sample and 31.5 μN for the sol_{200} sample. The force needed for the sol_{33} sample is much higher compared to

previous results since flexoelectricity depends of the strain gradient, in other words pressure is the pertinent parameter to consider for switching, not force. Since the tip used has a bigger radius of curvature the force needed to apply the same pressure is higher for the same applied force.

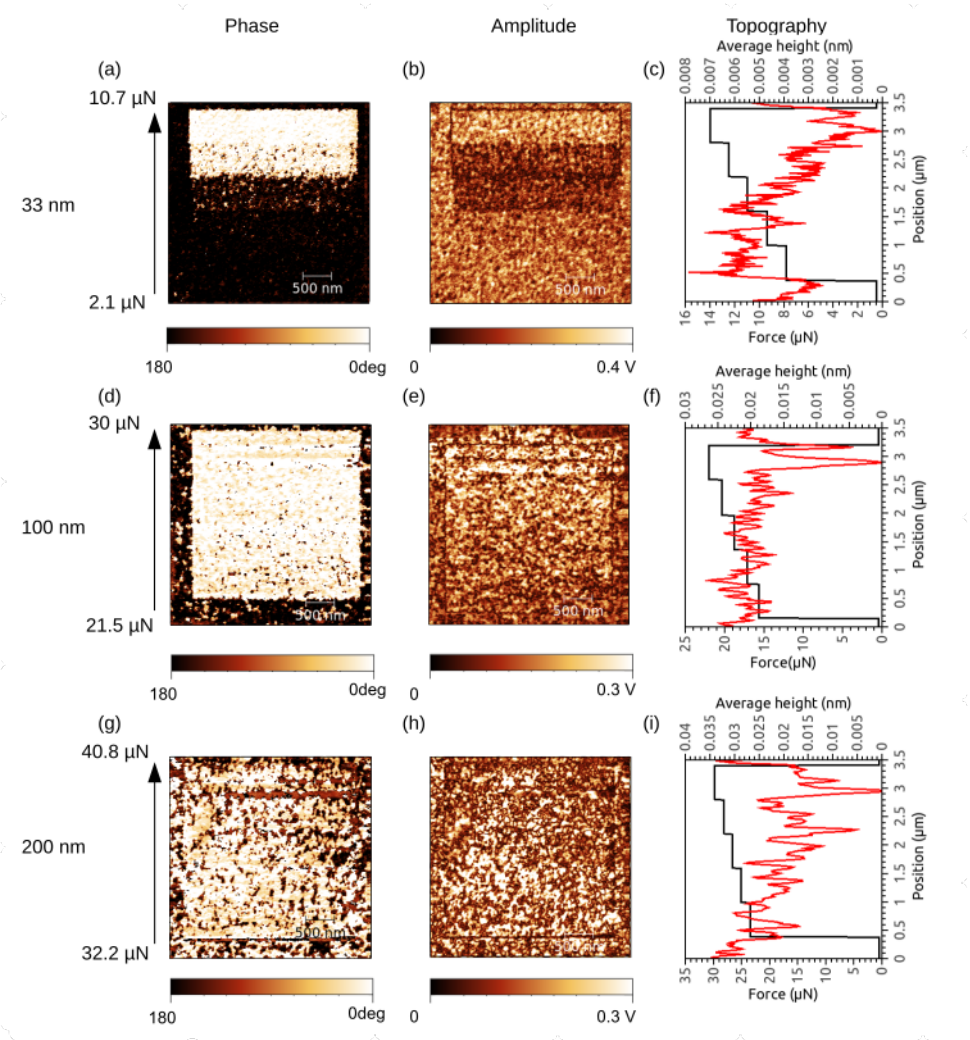

Figure 5.16: Ferroelectric domain switching using mechanical stress for sol-gel PZT samples of different thickness (a), (d) and (g) phase image (b), (e) and (h) amplitude image and (c), (f) and (i) section profile and force plot. The size of all images is 3.5 μm and the switching was obtained with a badly conductive tip. The spatial evolution of the applied force (black solid line) is shown alongside the topography (red solid line), as a function of the vertical tip position.

This section proves that mechanical switching of domains is possible with badly conductive tip in samples at least up to 200 nm thick. However, the effect of indentation and non uniform switching suggest that it would be challenging to switch domains mechanically with thicker samples. This section also proves that the switching is not the result of electrical discharges from the sample through the tip, although

conductive tips should facilitate the switching by evacuating charges.

5.2.2.2 Effect of the crystallization on the mechanical switching

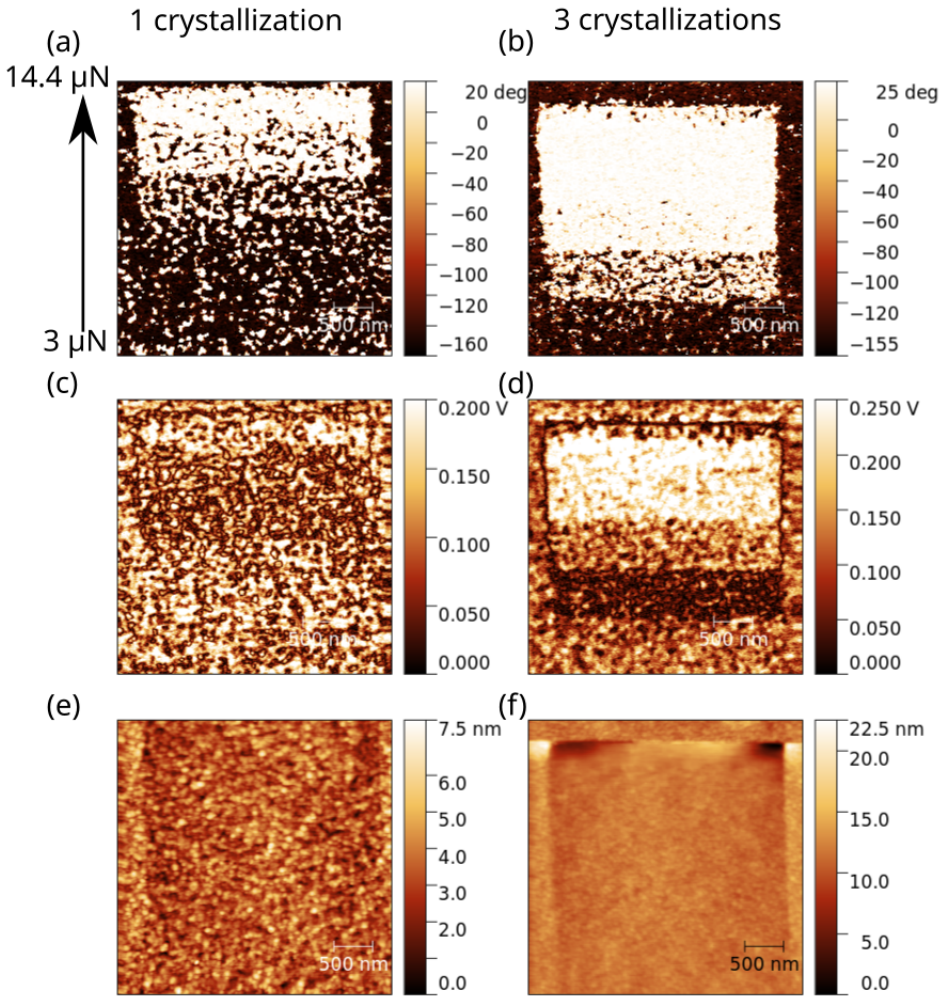

Figure 5.17: Mechanical switching for the sol_{100} sample and the $sol_{100/3c}$ sample. (a) and (b) PFM phase images, (c) and (d) PFM amplitude image, and (e) and (f) topography.

Besides the sol_{100} sample, the sample of the same thickness but with three crystallizations ($sol_{100/3c}$) was also considered. Experiments were performed to compare both samples from the point of view of the mechanical switching of domains. Since the range of forces of the soft conductive tip was not high enough to switch mechanically the polarization in the sample with one crystallization, the experiments had to be performed with a hard badly conductive tip.

The comparison was obtained with a protocol similar to the one presented in the previous section and in Section 5.2.1.3, where 5 different forces are applied to

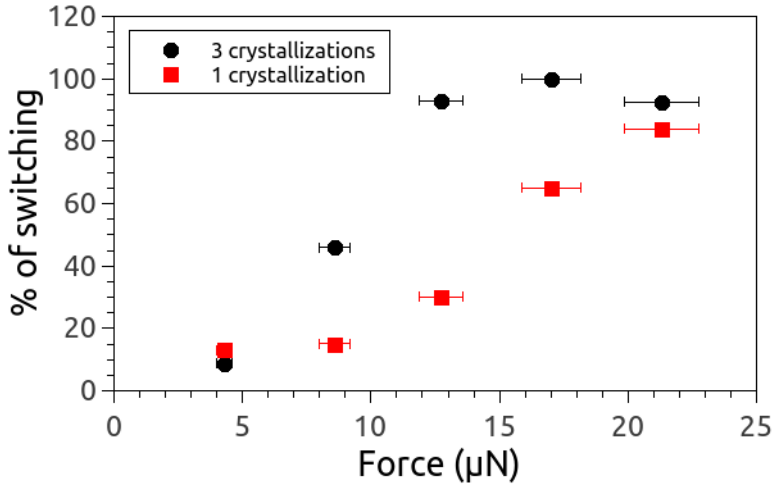

Figure 5.18: Plot of the percentage of switching against the force with a badly conductive tip for the sol_{100} and the $sol_{100/3c}$ samples.

the samples. The results in Fig. 5.17 show that mechanical switching occurs for lower forces in the $sol_{100/3c}$ sample. However, the topography shows that while the sol_{100} sample was barely altered by the force, the $sol_{100/3c}$ sample had a big change in the topography. Although it is known that the topography of the sample changes when electrically switching the sample (Section 4.2.6), the last region seems slightly damaged even presenting domains that did not switch.

It is possible to determine the threshold forces of both samples by plotting the percentage of switched domains as shown in Fig. 5.18. After interpolation, the threshold force for the sol_{100} sample is 19.3 μN and 11.4 μN for the $sol_{100/3c}$ sample. While the value of the sol_{100} is closer to the one obtained in the previous section, the value for the $sol_{100/3c}$ sample is smaller than the one found for the sol_{33} sample. This is a remarkable change and can be related with changes in the structure. To find the origin of this behavior, the samples were studied by STEM.

In Fig. 5.19 a and b, STEM-HAADF images are presented for the sol_{100} and the $sol_{100/3c}$ samples respectively. Both samples present cavities in the film as was previously mention in Section 4.2.6. Compared with the sol_{100} sample, the $sol_{100/3c}$ has more cavities and they are closer to the surface (80 nm from the interface with the bottom electrode for $sol_{100/3c}$ and over 15 nm for sol_{100}).

To study the relationship between crystallization and cavities, STEM-HAADF images of five different samples (sol_{33}, sol_{66}, sol_{100}, $sol_{100/3c}$ and sol_{200}, see Fig. E.2 in Appendix E) were processed using the Gwyddion software to determine the percentage of projected area and the average size of cavities (see Appendix E). The results in Fig. 5.19 c and d clearly show that the percentage of area covered by

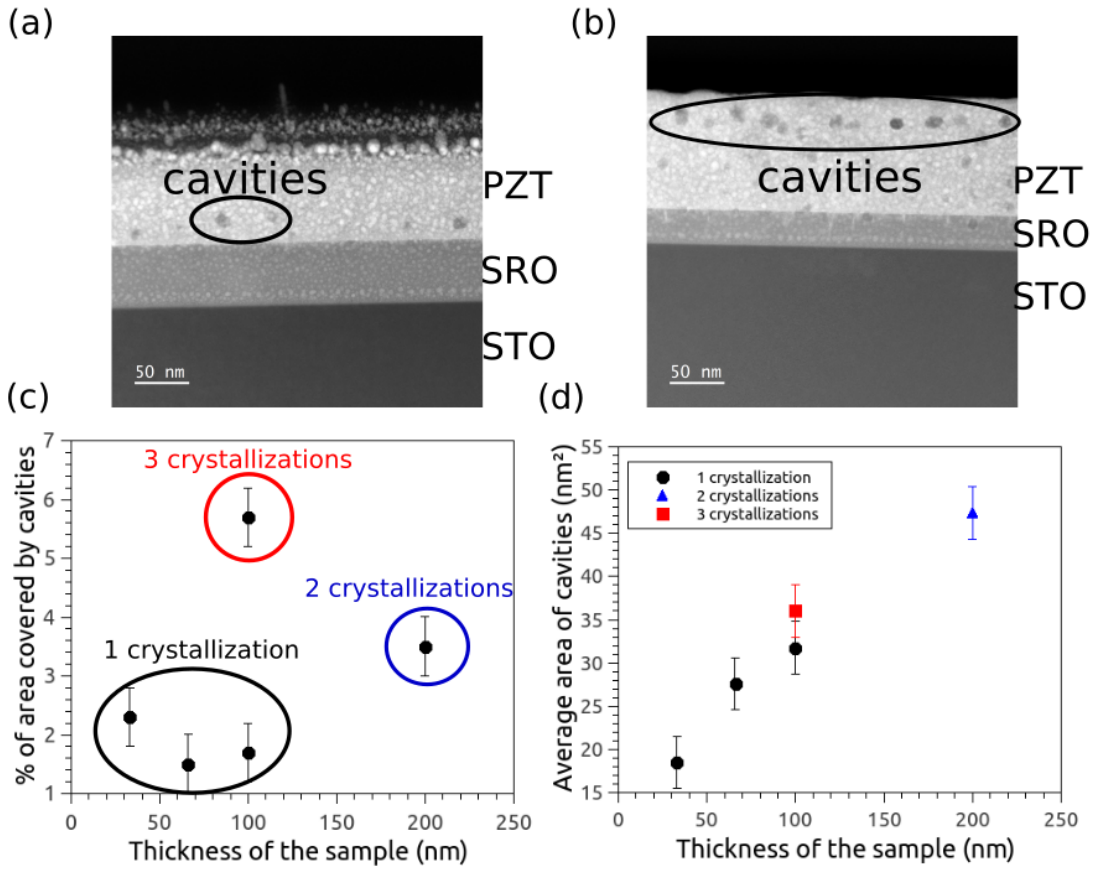

Figure 5.19: STEM-HAADF images of (a) sol_{100} and (b) $sol_{100/3c}$ with visible cavities. Plot of (c) percentage of area covered by cavities and (d) average area of cavities against the thickness of the sample.

cavities increases with the number of crystallizations, while the size of the cavities increases with the thickness. This increased percentage of cavities with the crystallizations could be the origin of the decrease threshold force in the $sol_{100/3c}$ sample. To complement these results, the samples were studied with RBS.

RBS results shown in Fig. 5.20 confirmed that the samples have the same composition, but the signal after the Pb peak decreases less for the 3 crystallizations sample, which can be associated with a surface roughness or in this case, with cavities at the surface. Furthermore, when estimating the thickness of the films with RBS, the 3 crystallizations film was found to be less thick. This is not due to an actual change of the thickness, but due to lower density of the film from the presence of cavities. The difference of density between both samples is 4.2%, which is close to the difference in the percentage of cavities between both samples (4%)

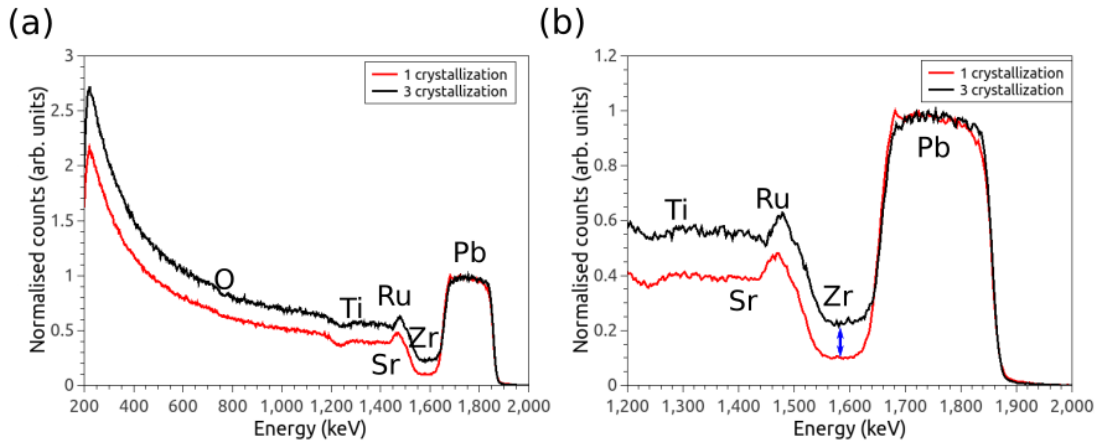

Figure 5.20: (a) RBS spectra and (b) peak of Pb for the sol_{100} and the $sol_{100/3c}$ samples. A clear difference between both signals is present after the Pb peak (see blue arrow). This difference can be linked to porosity or roughness in the sample.

It cannot be totally excluded that the cavities could be created by the FIB preparation, but the complementary results by RBS and the correlation between the localization of cavities and crystallizations suggests that they have an origin in the sample synthesis. They might correspond to regions with defects or less density that are more affected by the FIB milling or they might actually be real cavities in the sample. Although it is difficult provide a definite answer at this stage, all the results seem to correlate with the density of cavities in the films. These cavities will help stabilize domains created mechanically by clamping them, thus facilitating the mechanical switching of ferroelectric domains. Indeed, results in the literature suggest that microstructures may help achieve mechanical switching of domains (Li et al., 2021).

5.2.3 Discussion

In the previous sections, the mechanical switching has been discussed in terms of force. However, the pressure is responsible for the switching, not directly the applied force. While using the force for comparison is valid when the same tip is used, working with different tips must be discussed in terms of pressure threshold. To calculate the pressure, the contact area is obtained from the Hertz's model by using the young's modulus and the poisson's ratio of PZT (82.1 GPa and 0.39 respectively (Casset et al., 2012; Nazeer et al., 2009)), Pt-Ir tips (178 GPa and 0.382 respectively (Merker et al., 2001)) and polycrystalline diamond (1142 GPa and 0.069 respectively (Werner et al., 1993)).

To obtain the contact area it is necessary to know the radius of curvature of the

tip. The tips were observed using scanning electron microscope (SEM, Appendix C). However, wearing was observed for the conductive tip after the mechanical switching experiments. Indeed, the radius measured after experiments can be almost double the radius of a new tip as shown in Fig. 5.21. To account for this issue, mechanical switching experiments presented in this work were never performed with a new tip. Even using a worn tip, the uncertainty on the radius can be considered big since it is not possible to know the exact radius of the tip at the moment of the switching. In that sense, diamond tips seem more stable and their radii change less.

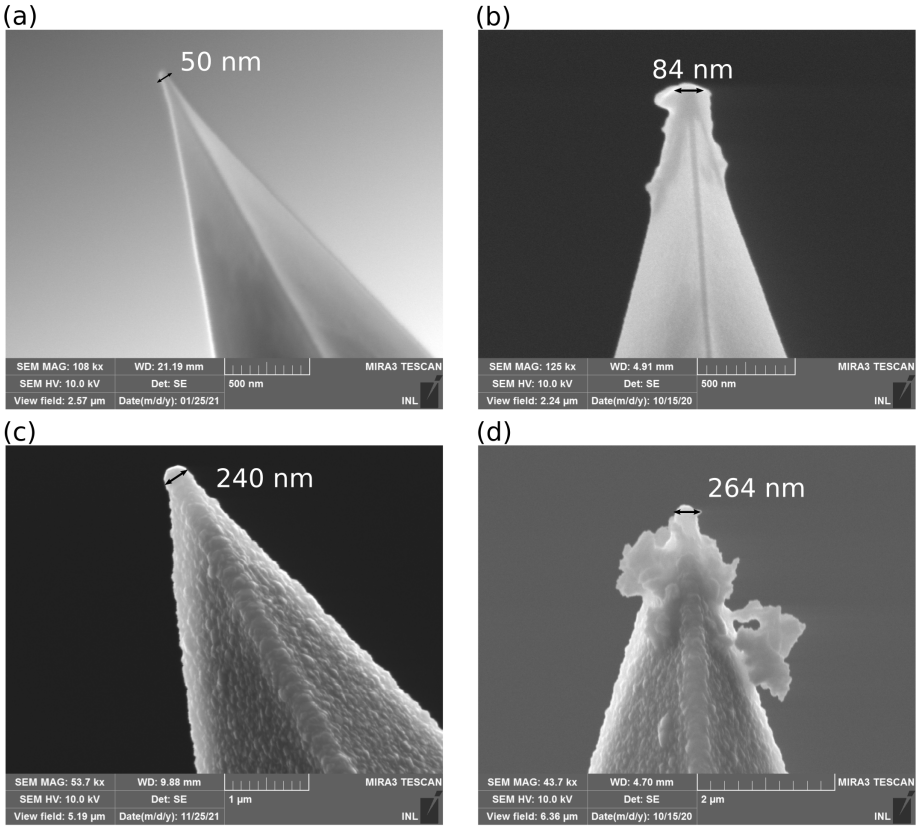

Figure 5.21: (a) New soft conductive tip (Pt-Ir) and (b) the same kind of tip after usage. (c) New hard badly conductive tip (diamond) and (d) the same kind of tip after mechanical switching experiments.

By applying the Hertz's model to the force thresholds measured previously in this work with a conductive and a badly conductive tip, a comparison between tips is shown in Fig. 5.22, suggesting that the pressure threshold is similar for both tips. However, with such big uncertainties it is possible that any difference between both is inside the error bars.

In conclusion, our results suggest that mechanical switching with a badly conductive tip requires the same pressure that with a conductive tip. Furthermore, all points present a linear behavior that shows an increase of the pressure threshold

with the thickness. It would be interesting for future experiments to study the effect of the conductivity of the tip, which should change the behavior of compensation charges, on the mechanical switching by applying more complex models like the DMT and the JKR, explained in Section 3.2.1.

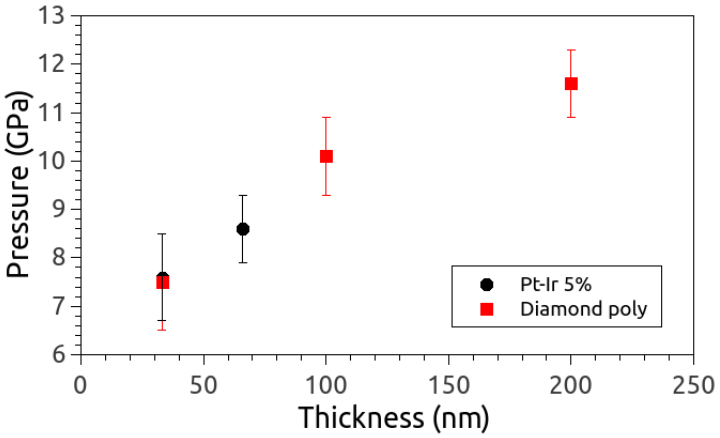

Figure 5.22: Plot of the pressure threshold against the thickness. The pressure threshold was obtained by applying Hertz's model to the results obtained in sol_{33}, sol_{66}, sol_{100} and sol_{200}.

5.3 Mechanical switching in the BFO sample

Mechanical switching was observed in the BFO sample, however using high forces (around 9 μN) led to indentation of tens of nm in the sample. This being the main limitation of the experiment, it was not possible to switch more than 75% of domains nor determine the threshold force. However, it was possible to perform experiments with both the conductive and the badly conductive tip.

An experiment was designed to determine if the switching was also possible in the in-plane direction. A badly conductive diamond tip scanned the sides of a square in different slow and fast axes while applying a force, with the objective of obtaining similar results to those obtained in Section 4.4.3. Then the region was scanned with a conductive tip to determine the configuration of domains. Results shown in Fig. 5.23 suggest that mechanical switching is possible by enlarging the down domains already present in the sample, as can be seen when comparing with the as-grown top region. The in-plane polarization showed a small change in contrast with the other regions, it is possible that the in-plane polarization of the down domains is enlarged when a pressure is applied, which results in an in-plane switching. Nevertheless, the in-plane polarization does not seem to be affected by the direction of scan.

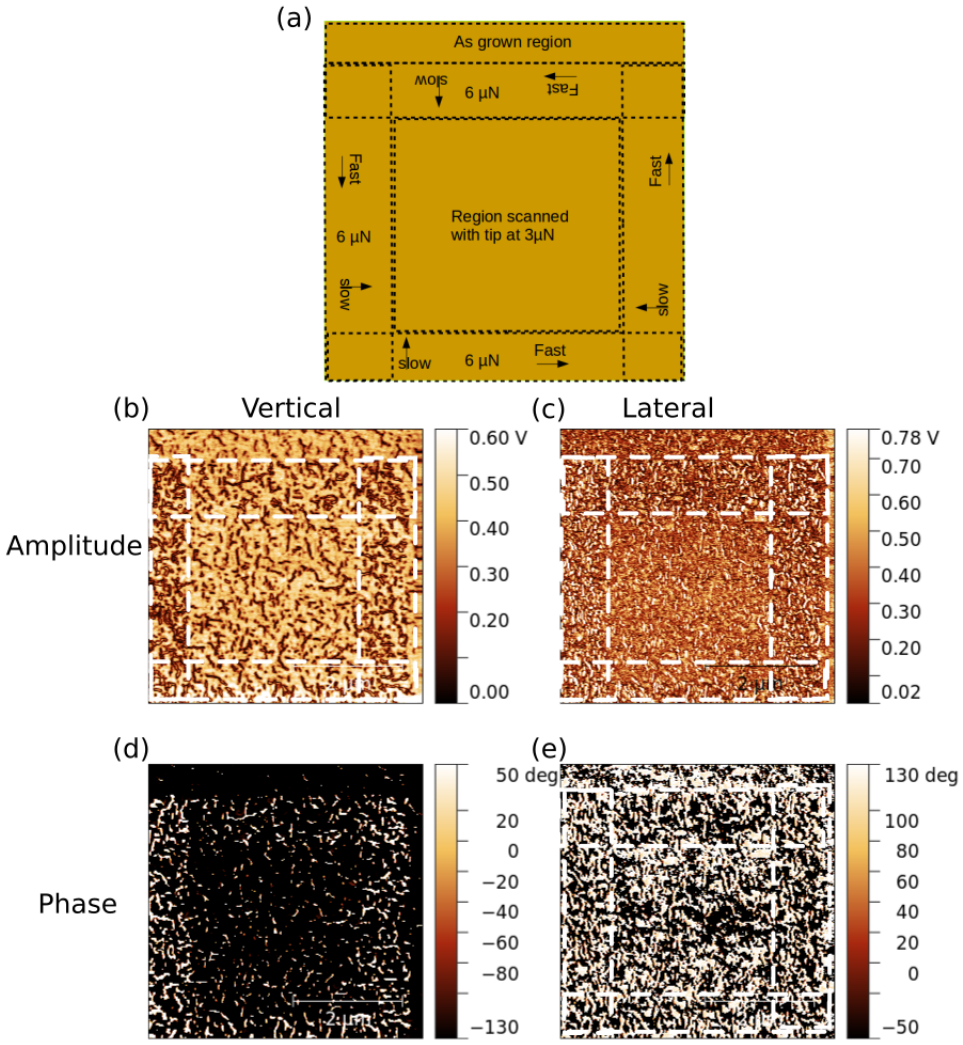

Figure 5.23: (a) schematic of force applied in the sample and their direction. (b) Vertical and (c) lateral PFM amplitude images. (d) Vertical and (e) lateral PFM phase images.

These results suggest that a mechanical control of ferroelectric domains in BFO is possible. However, other kind of tips should be used to be able to apply high forces without indentation. In that sense smaller tips of softer materials such as silicon could be used in future experiments.

In the literature, it was possible to switch the in plane polarization in BFO (Park et al., 2018) by using flexoelectric trailing fields. However, the substrate used was miscut in order to not allow 109° switching. This might be the key to achieve mechanical in-plane switching and the reason why it was not observed in this work.

5.4 Conclusions

In this chapter, the ability to switch ferroelectric domains by the application of a force from the AFM tip was studied in PZT and BFO thin films. It showed that the mechanical control of domains is possible in both BFO and PZT samples. However, the forces needed to switch domains in BFO were close to the indentation force.

It was possible to switch domains in sol-gel PZT samples up to 200 nm thick. This switching was achieved with both conductive and badly conductive tip ensuring that the phenomena is obtained through mechanical stimulus. The comparison between PLD and sol-gel grown films suggests that the presence of defects in the sol-gel films contributes to the switching of such a thick films by a pressure. It was observed that a sample with a higher density of cavities switched with a lower force than a sample with less cavities. These results suggest that large defects like nm-size cavities help to stabilize mechanically created domains.

It was possible to determine the threshold force for the 33, 66, 100 and 200 nm thick sol-gel films. The thickness of the material appears to be a parameter to tune the threshold forces. However, other ways exist such as applying an electric field before switching mechanically, which may inject charges in the material that in turn will screen the electric field created by the force applied.

Mechanical switching is not only possible, but desired in situations where leakage currents are to be avoided. Furthermore, this switching can be tuned by controlling parameters such as the thickness, the defect density and the charges injected in the film.

Conclusions

This work was focused on the study of ferroelectric domain switching by electrical and mechanical means. Piezoresponse force microscope (PFM) was the main tool for this study, which allows for imaging and manipulation of domains. The materials chosen were tetragonal $Pb[Zr_xTi_{1-x}]O_3$ (PZT) and $BiFeO_3$ (BFO) thin films grown either by sol-gel or pulsed laser deposition (PLD).

In the first chapter, after an introduction to the concept of dielectric polarization, ferroelectricity was introduced as an intrinsic property of materials, which originates from certain crystallographic point groups, and is characterized by hysteresis loops. Ferroelectricity allowed to define ferroelectric domains and domain walls, which are the main focus of study of this work. PZT and BFO were introduced as ferroelectric materials with different possible directions of the polarization. This chapter ends with a section dedicated to domain walls and their specific properties such as the possibility of having higher conductivity than the rest of the sample or be a zone of charge accumulation.

The second chapter was focused on the techniques of growth and structural, and chemical characterization of the samples. The main techniques used for the growth of thin films, sol-gel and PLD, are introduced together with the techniques of deposition of $SrRuO_3$ (SRO) electrodes. Finally these samples are studied by X-ray diffraction (XRD), scanning transmission electron microscopy (STEM), Rutherford backscattering spectrometry (RBS) and secondary ion mass spectrometry (SIMS).

The main tools of this thesis are derived from atomic force microscope (AFM), and are the focus of the third chapter. The first section was dedicated to AFM and its possible modes, with a special emphasis on contact mode. An important part of this chapter was dedicated to PFM and its capabilities to detect ferroelectric polarization, as well as all the possible artifacts observed using this technique. C-AFM was also introduced at the end of this chapter.

The results on the electrical control of ferroelectric domains were presented in the fourth chapter. In the first section, an explanation on how to switch out-of-plane and in-plane was performed. The second section was dedicated to the results

obtained with PZT samples grown by sol-gel. These results included the study of the as-grown domains, the influence of relative humidity in the growth of domains, the electrical characterization of the samples and the effects of variations in the sample structure. After this section, an electrical characterization of PZT samples grown by PLD was presented together with the study of hillocks in one of the samples. In the fourth section, the BFO sample was studied electrically with focus on the control of in-plane polarization and the tip degradation. It was shown that stripped domains can be created by changing the scanning direction of the AFM while a voltage is applied. Finally, the electrical conductivity at domain walls was not evidenced in PZT samples, and the tip degradation did not allow to explore this aspect in BFO. Overall, this chapter showed how to control electrically ferroelectric domains in PZT and BFO thin films.

The fifth chapter was focused on the mechanical control of domains. In the first section was dedicated to explain the possible mechanisms allowing for a ferroelectric domain to switch mechanically under and AFM tip. In the second section, the results obtained for PZT samples were presented, switching has been obtained with a conductive and a non conductive tip. It was possible to determine a threshold force for each sample, which depends on the tip used, and observe mechanical switching in samples up to 200 nm thick. This threshold force increases with the thickness and can be tuned by previously applying an electric field. Furthermore, it is suggested that nanometer-size defects like cavities in the sample, which can be controlled by the growth process, can decrease the threshold force of the samples. Finally, mechanical switching was observed in BFO, but limited by indentation in the sample. In summary, this chapter showed that mechanical switching was possible for all our samples and can be tuned by the previous application of an electric field, the thickness of the films and potentially by the concentration and distribution of nanometer-size defects like cavities.

Perspectives

Perspectives on the electrical control of domains

In this work it was possible to grow ferroelectric layers with reliable and stable ferroelectric properties to control the electrical polarization. This work can be continued with a series of experiments that are mostly related with the conductivity of domain walls and measurements under different atmospheres.

From the point of view of the effects of the atmosphere, only the sol-gel PZT samples were studied under nitrogen. This study could be repeated with the PLD-grown PZT and BFO samples in order to verify if they exhibit the same behavior, and in the case of BFO observe how the atmosphere affects the in-plane manipulation of domains. Furthermore, it could also be possible to work in vacuum with the Omicron microscope that belongs to INL. It has been reported in the literature that PZT samples show domain wall conductivity in these conditions (Guyonnet et al., 2011). A thorough comparison between the sol-gel PZT samples and the PLD PZT samples would be interesting to evaluate to what extent the concentration and localization of defects, like cavities, affect also the conductivity in vacuum.

As shown in section 1.4.3.2, most results reported in the literature show conductivity in BFO domain walls. In the literature, PFM experiments were done in air with diamond doped tips that should be harder and decrease electrostatic effects. To find conductivity in the BFO sample, trying new tips that would also change the contact potential and avoid oxidation is an option. A change of the atmosphere could also solve the problem of degradation of the tip for the BFO sample. This could be done either with nitrogen or with Omicron, our ultra high vacuum microscope. If these solutions work, the control of in-plane polarization would give a way to continue this work, from the materials point of view to the design of devices around the idea of domain wall conductivity. For example, it would be possible to control the conductivity of a region by changing the distribution of in-plane polarization. It could also be interesting to observe these conductive domain walls with STEM to better characterize their atomic structure.

Perspectives on the mechanical control of domains

This work focuses on the study of the force applied and the mechanical switching obtained. To compare results obtained with different tips, the Hertz's model was applied after measuring the tip radii with SEM and with the Young's modulus obtained from the literature. To improve this comparison different models as those introduced in section 3.2.1, Derjaguin-Müller-Toporov (DMT) and Johnson-Kendall-Roberts (JKR), could be applied. Furthermore, it could be interesting to obtain the Young's modulus of the samples studied instead of using ones from literature to verify that any difference of ferroelectric behavior between samples does not arise from the value of the Young's modulus. In the literature, there are methods to measure the Young's modulus from the contact models (J. Roa et al., 2011), unfortunately they could not be performed due to time constraints. An alternative is to use peak-force tapping mode to obtain the Young's modulus and measure the radius of the tip either with SEM or other methods, such as the one from the reference (J. Roa et al., 2011).

The microscopy facility in Lyon acquired recently a new Icon Bruker microscope capable of peak-force tapping mode. Using this device it should be possible to obtain the Young's modulus. This information would be key to understand if the difference in the density and distribution of cavities observed between sol_{100} and $sol_{100/3c}$ affect their mechanical properties.

Another way to continue the work on PZT could be to use harder conductive tips, which would allow to perform SS-PFM on the thicker PZT samples. This could be interesting to determine the origin of the switching in these samples, since it is known that bulk electrochemistry and ferroelasticity play a role, although the relative contribution of these two phenomena to the switching observed remains unknown. The changes of the SS-PFM loops could be related with the different mechanisms. For example, if the material switches because of a bias, the switching can be related with flexoelectricity or bulk effects, while a ferroelastic switching should not present a bias increasing with the force in the loops. These studies should be complemented with more structural and chemical studies by STEM and XRD.

The identification of the mechanisms at play during the mechanical switching could also be more specifically studied. This requires a better knowledge of the flexoelectric effects and ionic motions that could be involved. This work was exclusively experimental and it appears that the support of phase field simulations could help understanding the possible energy landscapes that give rise to a given domain configuration, and the influence of the flexoelectric tensors. Deeper analysis of the

kinetics of the mechanical switching could help deciding the importance of the ionic motion, which is slower than physical effects. Furthermore, the influence of the presence of cavities in the films could also be explored using phase field simulations.

Finally, the mechanical switching of domains in BFO was challenging in this work. Other results in the literature reported that it was possible using tips with a smaller radius (Park et al., 2018) and with an elastic constant that lies between the two kinds of tips used in this work. Increasing the pressure applied instead of the force while using softer tips may allow for the flexoelectric effect to play a bigger role and switch the in-plane polarization. In that case, it would be interesting to try and recreate stripe domains results obtained electrically by applying a force.

Specifically for the in-plane polarization of BFO, the effect of a stress applied in the in-plane direction would complete the results obtained in this work, as it would provide some control in the switching of any kind of domain. To progress in this direction, dedicated sample holders could be used that could allow to bend the sample in such a way that a controlled stress is applied. By simulating the stress field using a finite element software, it would be possible to design the sample-holder so that the desired stress is applied.

These perspectives are ways to build upon the results obtained in this thesis, and would help to better understand the mechanical switching phenomena observed.

Appendices

Appendix A

List of thin films

Name	Material	Deposition method	Thickness	Electrode
sol_{33}	PZT 20:80	Sol-gel	33 nm	SRO
sol_{66}	PZT 20:80	Sol-gel	66 nm	SRO
sol_{100}	PZT 20:80	Sol-gel	100 nm	SRO
sol_{133}	PZT 20:80	Sol-gel (2 crystallizations)	133 nm	SRO
sol_{166}	PZT 20:80	Sol-gel (2 crystallizations)	166 nm	SRO
sol_{200}	PZT 20:80	Sol-gel (2 crystallizations)	200 nm	SRO
$sol_{100/3c}$	PZT 20:80	Sol-gel (3 crystallizations)	100 nm	SRO
$sol_{100/new}$	PZT 20:80	Sol-gel (older solution)	100 nm	SRO
PLD_{20}	PZT 25:75	PLD	20 nm	SRO
PLD_{40}	PZT 25:75	PLD	40 nm	SRO
BFO	BFO	PLD	30 nm	LSMO

Table A.1: Table of the thin films studied in this thesis with their composition, deposition method, thickness and bottom electrode.

Appendix B

Configuration of the x-ray diffraction experiments at INL

To obtain the x-ray diffraction patterns, a Rigaku Smartlab equipped with a Cu rotating anode was routinely used with incident optics being set to parallel beam configuration (parabolic multilayer mirror, selectable parallel beam slit) with monochromatic incident radiation using a Ge(220) two-bounce monochromator. Receiving optics were in this case 5 degrees Soller slits, and a point scintillator counter. The alignment of optics was performed using the calibrated Rigaku center slit and the programmed Rigaku's routine to provide incident monochromatic (Cu $K_{\alpha 1}$ radiation) parallel beam. A schematic view of this montage is shown in Fig. F.1 configuration 1.

For some particular measurements, in view to obtain a more reduced background signal and lateral divergence, the parallel beam configuration (selectable parallel beam slit) was used with 5 degrees Soller slits in the incident beam and also 5 degress Soller slits in the receiving optics, using in addition to the Ge (400) two-bounce analyzer to monochromatize the beam before the scintillator counter. The calibration of the goniometer for this configuration was performed using Rigaku's medium resolution parallel beam routine, and using the Rigaku center slit. The alignment on the Ge (400) 2-bounce analyzer was subsequently realized to select monochromatic Cu $K_{\alpha 1}$ radiation. A schematic view of this montage is shown in Fig. F.1 configuration 2.

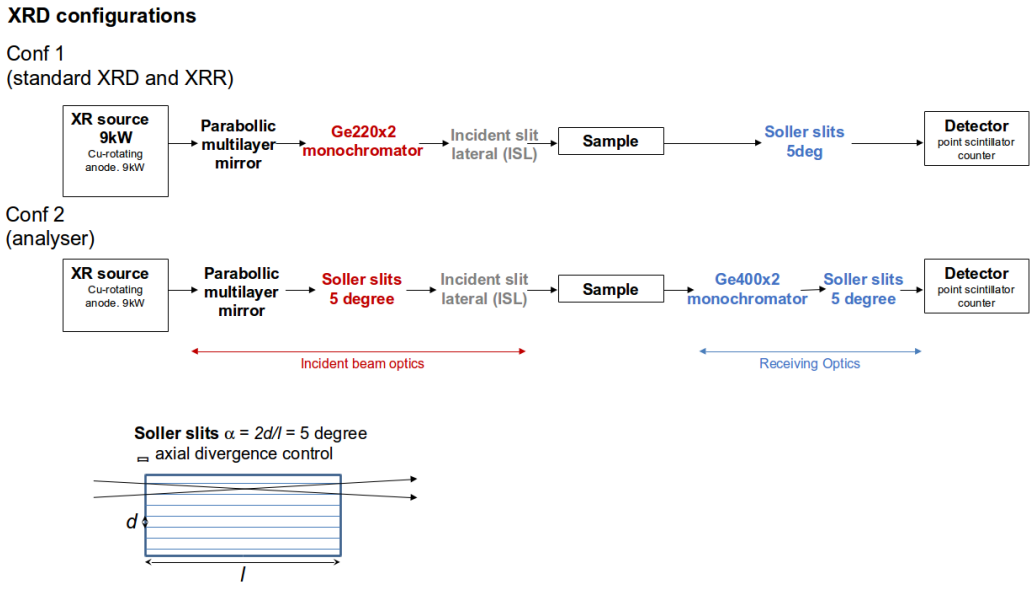

Figure B.1: Configuration 1 (Conf 1) and configuration 2 (Conf 2) used for the x-ray reflectometry and diffraction experiments.

Appendix C

Scanning electron microscopy

The scanning electron microscope (SEM) also uses a focused beam of electrons to obtain an image. The main difference is that the electrons detected are not transmitted through the sample, rather they are basckscattered electrons or secondary electrons emitted by atoms excited by the beam. For this reason, the sample does not need to be in a thin form and the energies used are in the range of tens of keV instead of hundreds.

In this work the SEM was used to measure the radius of AFM tips, however the interested reader can find more information about the technique in the references (Oatley et al., 1966; Vernon-Parry, 2000). The experiments were performed by Bejamin Fornacciari in a MIRA Tescan microscope at energies of 10 keV and in secondary electrons mode.

Appendix D

Focused ion beam preparation of STEM lamellae

Focused ion beam (FIB) milling is a technique similar to scanning electron microscopy, where a focused beam of ions is used to image or mill a sample. In this work, a focused gallium ion beam was used to mill thin lamellae of the PZT samples in cross-section geometry, to observe them with STEM. Information about the preparation of lamellae with FIB can be found in the literature, for example the review of Giannuzi and Stevie (Giannuzzi and Stevie, 1999).

The instrument for this work was NVison 40 fabricated by Zeiss, composed of an electronic column Gemini I and an ionic column SIINT Zeta Ga+, which allows for SEM observation too. The voltage used was 30 kV with intensities going from 13 nA to 40 pA. After the lamella is prepared, it is cleaned with a lower voltage of 5 kV. This work was performed by Solène Brottet at INL.

Appendix E

Data processing of STEM images for the study of cavities

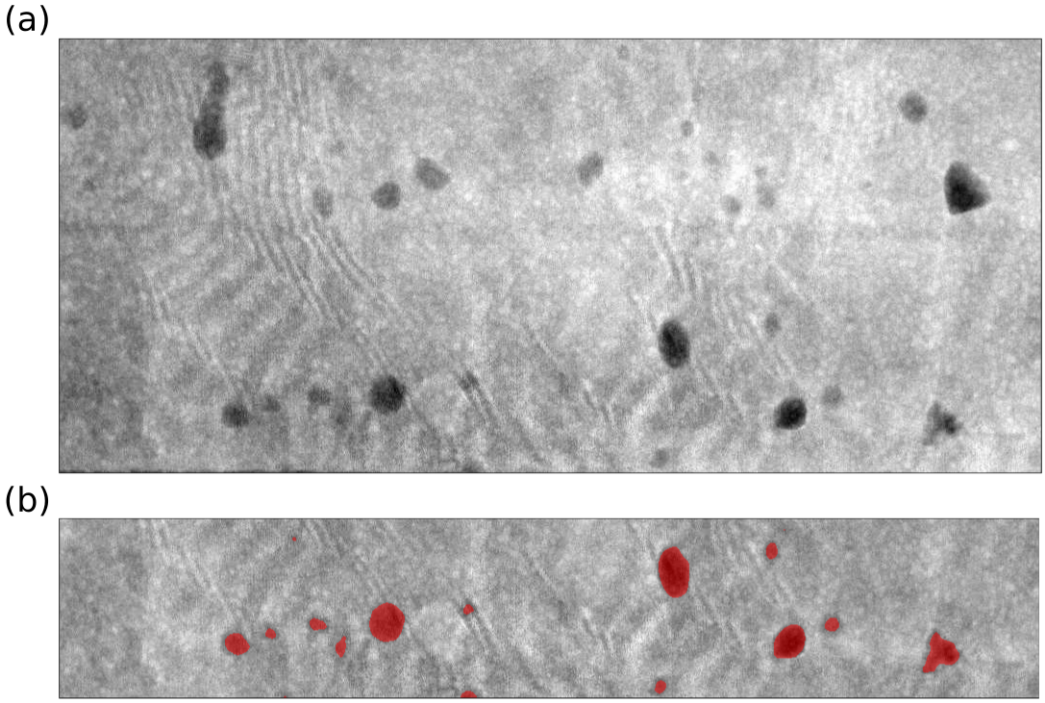

Figure E.1: (a) Original STEM image of the sol_{200} samples. (b) Bottom part of the image cut for image processing. The regions in red have been selected by the software as cavities.

To obtain the statistics about cavities in each sample, the grain analysis tool of Gwyddion software (Nečas and Klapetek, 2012) was used. This tool presents different methods to select grains in an image, in the case of domains the thresholding tool was used since PFM phase images present a clear threshold between up and down domains. However, the contrast in STEM-HAADF images is not always uniform, which can lead the software to detect cavities that do not exist. For instance,

the top part of the STEM-HAADF image in Fig. E.1 a appears brighter than the bottom part.

To solve this problem, the image was divided in smaller images with similar contrast (Fig. E.1 b). A flattening filter was used in these smaller images to make the contrast even more uniform. Then, the mark by segmentation option of the grain analysis was used to obtain the marked cavities as shown in Fig. E.1 b. This option uses the classical Vincent algorithm for watershed in digital space (Vincent and Soille, 1991). Finally, all the information obtained for each image subdivision was put together taking into account the size and number of cavities to obtain a total evaluation of the original image.

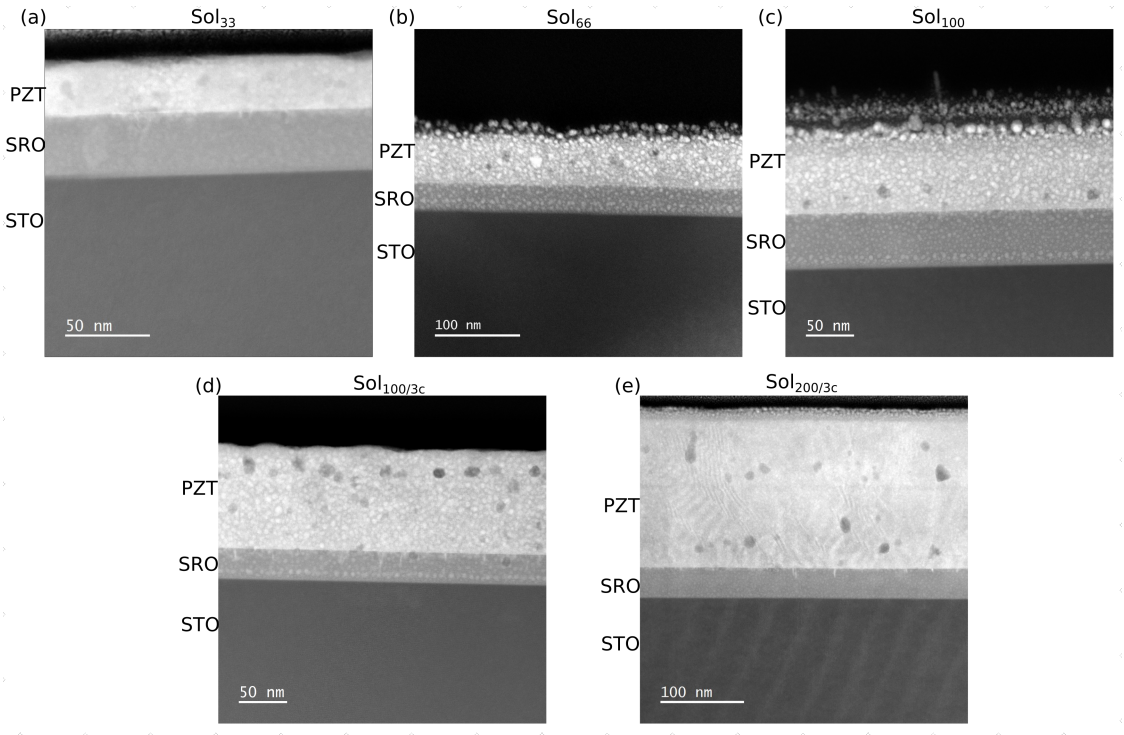

Figure E.2: (a) Original STEM images used for the study of cavities (a) sol_{33}, (b) sol_{66}, (c) sol_{100}, (d) $sol_{100/3c}$ and (e) sol_{200}

Sample	Total area	Area covered by cavities	%
sol_{33}	5,684.25 nm^2	136.42 nm^2	2.4 %
sol_{66}	17,494.86 nm^2	260.1 nm^2	1.5 %
sol_{100}	28,280 nm^2	492 nm^2	1.7 %
$sol_{100/3c}$	32,806 nm^2	1,882.3 nm^2	5.7%
sol_{200}	67,002 nm^2	2,336.6 nm^2	3.5 %

Table E.1: Table of samples and the corresponding projected area and projected area covered by cavities. In the last column, the percentage of projected area covered by cavities is written.

Appendix F

Topography of sol-gel films

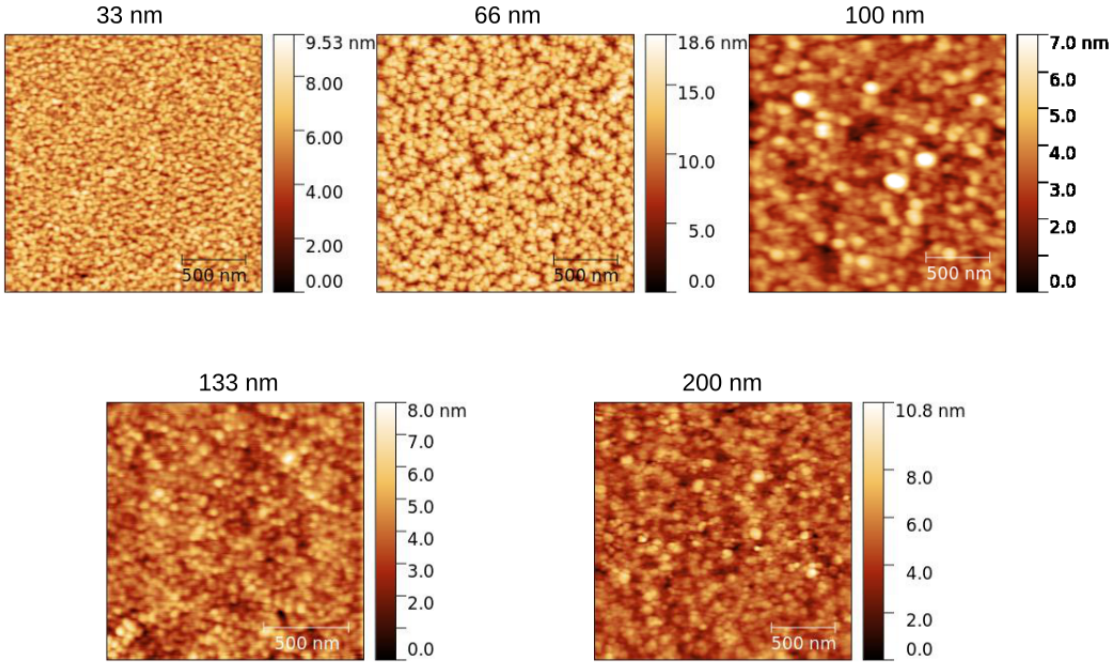

Figure F.1: Topography of sol_{33}, sol_{66}, sol_{100}, sol_{133} and sol_{200}.

Bibliography

Abdollahi, A., Domingo, N., Arias, I., and Catalan, G. (2019). Converse flexoelectricity yields large piezoresponse force microscopy signals in non-piezoelectric materials. *Nature Communications*, 10(1):1–6.

Ahart, M., Somayazulu, M., Cohen, R. E., Ganesh, P., Dera, P., Mao, H. K., Hemley, R. J., Ren, Y., Liermann, P., and Wu, Z. (2008). Origin of morphotropic phase boundaries in ferroelectrics. *Nature*, 451(7178):545–548.

Alsubaie, A., Sharma, P., Liu, G., Nagarajan, V., and Seidel, J. (2017). Mechanical stress-induced switching kinetics of ferroelectric thin films at the nanoscale. *Nanotechnology*, 28(7):1–8.

Arredondo, M., Saunders, M., Petraru, A., Kohlstedt, H., Vrejoiu, I., Alexe, M., Hesse, D., Browning, N. D., Munroe, P., and Nagarajan, V. (2009). Structural defects and local chemistry across ferroelectric-electrode interfaces in epitaxial heterostructures. *Journal of Materials Science*, 44(19):5297–5306.

Baibich, M. N., Broto, J. M., Fert, A., Van Dau, F. N., Petroff, F., Eitenne, P., Creuzet, G., Friederich, A., and Chazelas, J. (1988). Giant magnetoresistance of (001)Fe/(001)Cr magnetic superlattices. *Physical Review Letters*, 61(21):2472–2475.

Balke, N., Choudhury, S., Jesse, S., Huijben, M., Chu, Y. H., Baddorf, A. P., Chen, L. Q., Ramesh, R., and Kalinin, S. V. (2009). Deterministic control of ferroelastic switching in multiferroic materials. *Nature Nanotechnology*.

Balke, N., Gajek, M., Tagantsev, A. K., Martin, L. W., Chu, Y. H., Ramesh, R., and Kalinin, S. V. (2010). Direct observation of capacitor switching using planar electrodes. *Advanced Functional Materials*, 20(20):3466–3475.

Balke, N., Jesse, S., Li, Q., Maksymovych, P., Baris Okatan, M., Strelcov, E., Tselev, A., and Kalinin, S. V. (2015). Current and surface charge modified hysteresis loops in ferroelectric thin films. *Journal of Applied Physics*, 118(7).

Barthel, E. (2008). Adhesive elastic contacts: JKR and more. *Journal of Physics D: Applied Physics*, 41(16):163001.

Bartic, A. T., Wouters, D. J., Maes, H. E., Rickes, J. T., and Waser, R. M. (2001). Preisach model for the simulation of ferroelectric capacitors. *Journal of Applied Physics*, 89(6):3420–3425.

Binnig, G. (1986). Atomic force microscope and method for imaging surfaces with atomic resolution - US Patent 4724318.

Binnig, G., Quate, C. F., and Gerber, C. (1986). Atomic Force Microscope. *Physical Review Letters*, 56(9):930–933.

Binnig, G. and Rohrer, H. (1983). Scanning tunneling microscopy. *Surface Science*, 126(1-3):236–244.

Blaser, C. and Paruch, P. (2015). Subcritical switching dynamics and humidity effects in nanoscale studies of domain growth in ferroelectric thin films. *New Journal of Physics*, 17:1–9.

Brennecka, G. L., Ihlefeld, J. F., Maria, J. P., Tuttle, B. A., and Clem, P. G. (2010). Processing technologies for high-permittivity thin films in capacitor applications. *Journal of the American Ceramic Society*, 93(12):3935–3954.

Brugère, A. (2011). *Cinétique de formation et stabilité des domaines ferroélectriques créés par un Microscope à Force Atomique : Etude de films minces monocristallins de LiTaO 3 en vue d'applications mémoires*. PhD thesis, INSA Lyon.

Budd, K. D., Dey, S. K., and Payne, D. A. (1985). Sol-gel processing OF $PbTiO_3$, $PbZrO_3$, PZT, and PLZT thin films. *British Ceramic Proceedings*, (36):107–121.

Cao, Y., Li, Q., Chen, L. Q., and Kalinin, S. V. (2015). Coupling of electrical and mechanical switching in nanoscale ferroelectrics. *Applied Physics Letters*, 107(20).

Cao, Y., Morozovska, A., and Kalinin, S. V. (2017). Pressure-induced switching in ferroelectrics: Phase-field modeling, electrochemistry, flexoelectric effect, and bulk vacancy dynamics. *Physical Review B*, 96(18).

Caron, A., Rabe, U., Reinstädtler, M., Turner, J. A., and Arnold, W. (2004). Imaging using lateral bending modes of atomic force microscope cantilevers. *Applied Physics Letters*, 85(26):6398–6400.

Casset, F., Devos, A., Sadtler, S., Le Louarn, A., Emery, P., Le Rhun, G., Ancey, P., Fanget, S., and Defay, E. (2012). Young modulus and Poisson ratio of PZT thin film by Picosecond Ultrasonics. *IEEE International Ultrasonics Symposium, IUS*, pages 2180–2183.

Castle, B., Li, A., Coutu, R., Hengehold, R., and Van Nostrand, J. (2011). Tunneling atomic force microscopy characterization of cuprous oxide thin films. *Proceedings of the IEEE Conference on Nanotechnology*, pages 1470–1473.

Catalan, G., Béa, H., Fusil, S., Bibes, M., Paruch, P., Barthélémy, A., and Scott, J. F. (2008). Fractal dimension and size scaling of domains in thin films of multiferroic $BiFeO_3$. *Physical Review Letters*, 100(2):35–38.

Catalan, G., Lubk, A., Vlooswijk, A. H., Snoeck, E., Magen, C., Janssens, A., Rispens, G., Rijnders, G., Blank, D. H., and Noheda, B. (2011). Flexoelectric rotation of polarization in ferroelectric thin films. *Nature Materials*, 10(12):963–967.

Catalan, G., Schilling, A., Scott, J. F., and Gregg, J. M. (2007). Domains in three-dimensional ferroelectric nanostructures: Theory and experiment. *Journal of Physics Condensed Matter*, 19(13).

Cattan, E., Manceau, J. F., Haccart, T., Biwersi, S., Velu, G., Remiens, D., and Bastien, F. (1999). Remanent piezoelectric constant of PZT thin films. *Ferroelectrics*, 224(1-4):307–314.

Chen, L., Cheng, Z., Xu, W., Meng, X., Yuan, G., Liu, J., and Liu, Z. (2016). Electrical and mechanical switching of ferroelectric polarization in the 70 nm $BiFeO_3$ film. *Scientific Reports*, 6(September 2015):1–8.

Chen, Q. N., Ou, Y., Ma, F., and Li, J. (2014). Mechanisms of electromechanical coupling in strain based scanning probe microscopy. *Applied Physics Letters*, 104(24):1–5.

Chen, W., Liu, J., Ma, L., Liu, L., Jiang, G. L., and Zheng, Y. (2018). Mechanical switching of ferroelectric domains beyond flexoelectricity. *Journal of the Mechanics and Physics of Solids*, 111:43–66.

Chu, W.-K., Mayer, J. W., and Nicolet, M.-A. (1978). Concepts of Backscattering Spectrometry. In *Backscattering Spectrometry*, pages 54–88.

Covaci, C. and Gontean, A. (2020). Piezoelectric energy harvesting solutions: A review. *Sensors (Switzerland)*, 20(12):1–37.

Craciun, F., Lippert, T., and Dinescu, M. (2020). *Pulsed Laser Deposition: Fundamentals, Applications, and Perspectives.*

Crassous, A., Sluka, T., Tagantsev, A. K., and Setter, N. (2015). Polarization charge as a reconfigurable quasi-dopant in ferroelectric thin films. *Nature Nanotechnology.*

Dakin, T. W. (2006). Conduction and polarization mechanisms and trends in dielectric. *IEEE Electrical Insulation Magazine*, 22(5):11–28.

Damjanovic, D. (1998). Ferroelectric, dielectric and piezoelectric properties of ferroelectric thin films and ceramics. *Reports on Progress in Physics*, 61(9):1267–1324.

Damjanovic, D. (2006). *Hysteresis in piezoelectric and ferroelectric materials*, volume 3.

Das, S., Wang, B., Cao, Y., Rae Cho, M., Jae Shin, Y., Yang, S. M., Wang, L., Kim, M., Kalinin, S. V., Chen, L. Q., and Noh, T. W. (2017). Controlled manipulation of oxygen vacancies using nanoscale flexoelectricity. *Nature Communications*, 8(1):1–8.

Dawber, M., Rabe, K. M., and Scott, J. F. (2005). Physics of thin-film ferroelectric oxides. *Reviews of Modern Physics*, 77(4):1083–1130.

Domingo, N., Gaponenko, I., Cordero-Edwards, K., Stucki, N., Pérez-Dieste, V., Escudero, C., Pach, E., Verdaguer, A., and Paruch, P. (2019). Surface charged species and electrochemistry of ferroelectric thin films. *Nanoscale*, 11(38):17920–17930.

Ederer, C. and Spaldin, N. A. (2005). Weak ferromagnetism and magnetoelectric coupling in bismuth ferrite. *Physical Review B - Condensed Matter and Materials Physics*, 71(6):1–4.

Edwards, D., Brewer, S., Cao, Y., Jesse, S., Chen, L. Q., Kalinin, S. V., Kumar, A., and Bassiri-Gharb, N. (2016). Local probing of ferroelectric and ferroelastic switching through stress-mediated piezoelectric spectroscopy. *Advanced Materials Interfaces*, 3(7):1–9.

Eng, L. M. (1999). Nanoscale domain engineering and characterization of ferroelectric domains. *Nanotechnology*, 10(4):405–411.

Farokhipoor, S. and Noheda, B. (2011). Conduction through 71° domain walls in BiFeO3 thin films. *Physical Review Letters*, 107(12):3–6.

Fearn, S. (2015). *An Introduction to Time-of-Flight Secondary Ion Mass Spectrometry (ToF-SIMS) and its Application to Materials Science*. 2053-2571. IOP Publishing.

Feldman, L. C., Mayer, J. W., and Grasserbauer, M. (1987). Fundamentals of surface and thin film analysis. In *Analytica Chimica Acta*, volume 199, page 288.

Fina, I., Fábrega, L., Langenberg, E., Mart, X., Sánchez, F., Varela, M., and Fontcuberta, J. (2011). Nonferroelectric contributions to the hysteresis cycles in manganite thin films: A comparative study of measurement techniques. *Journal of Applied Physics*, 109(7):0–6.

Foeth, M., Sfera, A., Stadelmann, P., and Buffat, P. A. (1999). A comparison of HREM and weak beam transmission electron microscopy for the quantitative measurement of the thickness of ferroelectric domain walls. *Journal of Electron Microscopy*, 48(6):717–723.

Fousek, J. and Janovec, V. (1969). The orientation of domain walls in twinned ferroelectric crystals. *Journal of Applied Physics*, 40(1):135–142.

Ganpule, C. S., Roytburd, A. L., Nagarajan, V., Hill, B. K., Ogale, S. B., Williams, E. D., Ramesh, R., and Scott, J. F. (2002). Polarization relaxation kinetics and 180° domain wall dynamics in ferroelectric thin films. *Physical Review B - Condensed Matter and Materials Physics*, 65(1):1–7.

Gaponenko, I., Tückmantel, P., Karthik, J., Martin, L. W., and Paruch, P. (2015). Towards reversible control of domain wall conduction in $Pb(Zr_{0.2}Ti_{0.8})O_3$ thin films. *Applied Physics Letters*.

García, R. and Paulo, A. S. (1999). Attractive and repulsive tip-sample interaction regimes in tapping-mode atomic force microscopy. *Physical Review B - Condensed Matter and Materials Physics*, 60(7):4961–4967.

García, R. and Pérez, R. (2002). *Dynamic atomic force microscopy methods*, volume 47.

Gautier, B., BrugÈre, A., and Gidon, S. (2012). Impact of the ambient humidity on the kinetics of formation of ferroelectric domains in monocrystalline $LiTaO_3$. *International Journal of Nanoscience*, 11(4):1–5.

Genenko, Y. A., Glaum, J., Hoffmann, M. J., and Albe, K. (2015). Mechanisms of aging and fatigue in ferroelectrics. *Materials Science and Engineering B: Solid-State Materials for Advanced Technology*, 192(C):52–82.

Giannuzzi, L. A. and Stevie, F. A. (1999). A review of focused ion beam milling techniques for TEM specimen preparation. *Micron*, 30(3):197–204.

Goldschmidt, V. M. (1929). Crystal structure and chemical constitution. A lecture delivered before the faraday society on thursday, 14th march, 1929. *Transactions of the Faraday Society*, 25:253–283.

Gomez, A., Puig, T., and Obradors, X. (2018). Diminish electrostatic in piezoresponse force microscopy through longer or ultra-stiff tips. *Applied Surface Science*, 439:577–582.

Grandfond, A., Gautier, B., Militaru, L., Albertini, D., and Descamps-Mandine, A. (2014). Spurious phenomena occurring during current measurement on ultra-thin dielectric layers: From electro-thermal effects to surface damage. *Journal of Applied Physics*, 115(13):0–7.

Gross, L., Mohn, F., Moll, N., Liljeroth, P., and Meyer, G. (2009). The chemical structure of a molecule resolved by atomic force microscopy. *Science*, 325(5944):1110–1114.

Grossmann, M., Lohse, O., Bolten, D., Boettger, U., Schneller, T., and Waser, R. (2002). The interface screening model as origin of imprint in $PbZr_xTi_{1-x}O_3$ thin films. I. Dopant, illumination, and bias dependence. *Journal of Applied Physics*, 92(5):2680–2687.

Gruverman, A. (1996). Scanning force microscopy for the study of domain structure in ferroelectric thin films. *Journal of Vacuum Science & Technology B: Microelectronics and Nanometer Structures*, 14(2):602.

Gruverman, A., Auciello, O., and Tokumoto, H. (1998). Imaging and control of domain structures in ferroelectric thin films via scanning force microscopy. *Annual Review of Materials Science*, 28(1):101–123.

Gruverman, A., Rodriguez, B. J., Kingon, A. I., Nemanich, R. J., Tagantsev, A. K., Cross, J. S., and Tsukada, M. (2003). Mechanical stress effect on imprint behavior of integrated ferroelectric capacitors. *Applied Physics Letters*, 83(4):728–730.

Guo, E. J., Roth, R., Das, S., and Dörr, K. (2014). Strain induced low mechanical switching force in ultrathin $PbZr_{0.2}Ti_{0.8}O_3$ films. *Applied Physics Letters*, 105(1):0–5.

Güthner, P. and Dransfeld, K. (1992). Local poling of ferroelectric polymers by scanning force microscopy. *Applied Physics Letters*, 61(9):1137–1139.

Guyonnet, J., Gaponenko, I., Gariglio, S., and Paruch, P. (2011). Conduction at domain walls in insulating $Pb(Zr_{0.2}Ti_{0.8})O_3$ thin films. *Advanced Materials*.

Harnagea, C., Alexe, M., Hesse, D., and Pignolet, A. (2003). Contact resonances in voltage-modulated force microscopy. *Applied Physics Letters*, 83(2):338–340.

Hourani, W. (2011). *Caractérisation des courants de fuite à l ' échelle nanométrique dans les couches ultra-minces d ' oxydes pour la microélectronique Présentée devant L ' Institut National des Sciences Appliquées de Lyon Le grade de Docteur*. PhD thesis, INSA Lyon.

Huang, W., Yuan, F. G., and Jiang, X. (2016). *Flexoelectric effect, materials, and structures*. Elsevier Ltd.

Hutter, J. L. and Bechhoefer, J. (1993). Calibration of atomic-force microscope tips. *Review of Scientific Instruments*, 64(7):1868–1873.

J. Roa, J., Oncins, G., Diaz, J., Sanz, F., and Segarra, M. (2011). Calculation of Young's Modulus Value by Means of AFM. *Recent Patents on Nanotechnology*, 5(1):27–36.

Jacobs, T. D., Mathew Mate, C., Turner, K. T., and Carpick, R. W. (2013). Understanding the tip-sample contact: An overview of contact mechanics from the macro- to the nanoscale. In *Scanning Probe Microscopy for Industrial Applications: Nanomechanical Characterization*, number June 2016, pages 15–48.

Jaffe, B., Cook, W. R., and Jaffe, H. (1971). *Piezoelectric Ceramics*. Elsevier.

Jesse, S., Guo, S., Kumar, A., Rodriguez, B. J., Proksch, R., and Kalinin, S. V. (2010). Resolution theory, and static and frequency-dependent cross-talk in piezoresponse force microscopy. *Nanotechnology*, 21(40).

Jia, C. L., Urban, K. W., Alexe, M., Hesse, D., and Vrejoiu, I. (2011). Direct observation of continuous electric dipole rotation in flux-closure domains in ferroelectric $Pb(Zr, Ti)O_3$. *Science*, 331(6023):1420–1423.

Johnson, K. L., Kendall, K., and Roberts, A. D. (1971). Surface energy and the contact of elastic solids. *Proceedings of the Royal Society of London. A. Mathematical and Physical Sciences*, 324(1558):301–313.

Jungk, T., Hoffmann, Á., and Soergel, E. (2007). Consequences of the background in piezoresponse force microscopy on the imaging of ferroelectric domain structures. *Journal of Microscopy*, 227(1):72–78.

Kalinin, S. V., Jesse, S., Tselev, A., Baddorf, A. P., and Balke, N. (2011). The role of electrochemical phenomena in scanning probe microscopy of ferroelectric thin films. *ACS Nano*, 5(7):5683–5691.

Kalinin, S. V., Kim, Y., Fong, D. D., and Morozovska, A. N. (2018). Surface-screening mechanisms in ferroelectric thin films and their effect on polarization dynamics and domain structures.

Kalinin, S. V., Rodriguez, B. J., Jesse, S., Shin, J., Baddorf, A. P., Gupta, P., Jain, H., Williams, D. B., and Gruverman, A. (2006). Vector piezoresponse force microscopy. *Microscopy and Microanalysis*, 12(3):206–220.

Kao, K. C. (2004). Electric Polarization and Relaxation. In *Dielectric Phenomena in Solids*, pages 41–114. Elsevier.

Kholkin, A. L., Kalinin, S. V., Roelofs, A., and Gruverman, A. (2007). *Review of ferroelectric domain imaging by piezoresponse force microscopy*, volume 2.

Khomskii, D. (2009). Classifying multiferroics: Mechanisms and effects. *Physics*, 2.

Kiguchi, T., Shimizu, T., Shiraishi, T., and Konno, T. J. (2020). Epitaxial growth mechanism of $Pb(Zr,Ti)O_3$ thin films on $SrTiO_3$ by chemical solution deposition via self-organized seed layer. *Journal of the Ceramic Society of Japan*, 128(8):501–511.

Kim, Y., Kumar, A., Tselev, A., Kravchenko, I. I., Han, H., Vrejoiu, I., Lee, W., Hesse, D., Alexe, M., Kalinin, S. V., and Jesse, S. (2011). Nonlinear phenomena in multiferroic nanocapacitors: Joule heating and electromechanical effects. *ACS Nano*, 5(11):9104–9112.

Kittel, C. (1946). Theory of the structure of ferromagnetic domains in films and small particles. *Physical Review*, 70(11-12):965–971.

Kittel, C. (1949). Physical Theory of Ferromagnetic Domains. *Reviews of Modern Physics*, 21(4):541–583.

Klinov, D. and Magonov, S. (2004). True molecular resolution in tapping-mode atomic force microscopy with high-resolution probes. *Applied Physics Letters*, 84(14):2697–2699.

Landau, L. and Lifshitz, E. (1935). On the theory of the dispersion of magnetic permeability in ferromagnetic bodies. *Perspectives in Theoretical Physics*, 169(14):51–65.

Lee, D., Behera, R. K., Wu, P., Xu, H., Sinnott, S. B., Phillpot, S. R., Chen, L. Q., and Gopalan, V. (2009). Mixed Bloch-Néel-Ising character of 180°ferroelectric domain walls. *Physical Review B - Condensed Matter and Materials Physics*, 80(6):2–5.

Li, Q., Wang, B., He, Q., Yu, P., Chen, L.-Q., Kalinin, S. V., and Li, J.-F. (2021). Ferroelastic Nanodomain-mediated Mechanical Switching of Ferroelectricity in Thick Epitaxial Films. *Nano Letters*, 21(1):445–452.

Lichtensteiger, C., Fernandez-Pena, S., Weymann, C., Zubko, P., and Triscone, J. M. (2014). Tuning of the depolarization field and nanodomain structure in ferroelectric thin films. *Nano Letters*, 14(8):4205–4211.

Lichtensteiger, C., Weymann, C., Fernandez-Pena, S., Paruch, P., and Triscone, J. M. (2016). Built-in voltage in thin ferroelectric $PbTiO_3$ films: The effect of electrostatic boundary conditions. *New Journal of Physics*, 18(4).

Liu, Q. (2014). *Optimization of Epitaxial Ferroelectric PZT Thin-Film Capacitor Properties*. PhD thesis, INSA Lyon.

Lu, H., Bark, C. W., Esque De Los Ojos, D., Alcala, J., Eom, C. B., Catalan, G., and Gruverman, A. (2012a). Mechanical writing of ferroelectric polarization. *Science*, 335(6077):59–61.

Lu, H., Kim, D. J., Bark, C. W., Ryu, S., Eom, C. B., Tsymbal, E. Y., and Gruverman, A. (2012b). Mechanically-induced resistive switching in ferroelectric tunnel junctions. *Nano Letters*, 12(12):6289–6292.

Lu, H., Tan, Y., McConville, J. P., Ahmadi, Z., Wang, B., Conroy, M., Moore, K., Bangert, U., Shield, J. E., Chen, L. Q., Gregg, J. M., and Gruverman, A. (2019). Electrical Tunability of Domain Wall Conductivity in $LiNbO_3$ Thin Films. *Advanced Materials*, 1902890:1–7.

Luo, Y., Li, X., Chang, L., Gao, W., Yuan, G., Yin, J., and Liu, Z. (2013). Upward ferroelectric self-poling in (001) oriented PbZr0.2Ti0.8O3epitaxial films with compressive strain. *AIP Advances*, 3(12):0–8.

Maranganti, R., Sharma, N. D., and Sharma, P. (2006). Electromechanical coupling in nonpiezoelectric materials due to nanoscale nonlocal size effects: Green's function solutions and embedded inclusions. *Physical Review B - Condensed Matter and Materials Physics*, 74(1):1–14.

Martin, Y., Williams, C. C., and Wickramasinghe, H. K. (1987). Atomic force microscope-force mapping and profiling on a sub 100-Å scale. *Journal of Applied Physics*, 61(10):4723–4729.

Mattox, D. M. (2010). *Handbook of Physical Vapor Deposition (PVD) Processing*. Elsevier.

McGilly, L. J., Feigl, L., Sluka, T., Yudin, P., Tagantsev, A. K., and Setter, N. (2016). Velocity Control of 180° Domain Walls in Ferroelectric Thin Films by Electrode Modification. *Nano Letters*.

Merker, J., Lupton, D., Töpfer, M., and Knake, H. (2001). High temperature mechanical properties of the platinum group metals: Elastic properties of platinum, rhodium and iridium and their alloys at high temperatures. *Platinum Metals Review*, 45(2):74–82.

Merz, W. J. (1954). Domain formation and domain wall motions in ferroelectric $BaTiO_3$ single crystals. *Physical Review*, 95(3):690–698.

Mitsui, T. and Furuichi, J. (1953). Domain structure of rochelle salt and KH_2PO_4. *Physical Review*, 90(2):193–202.

Molotskii, M. (2003). Generation of ferroelectric domains in atomic force microscope. *Journal of Applied Physics*, 93(10 1):6234–6237.

Morozovska, A. N., Eliseev, E. A., and Kalinin, S. V. (2006). Domain nucleation and hysteresis loop shape in piezoresponse force spectroscopy. *Applied Physics Letters*, 89(19):21–24.

Morozovska, A. N., Eliseev, E. A., Li, Y., Svechnikov, S. V., Maksymovych, P., Shur, V. Y., Gopalan, V., Chen, L. Q., and Kalinin, S. V. (2009). Thermodynamics of nanodomain formation and breakdown in scanning probe microscopy: Landau-Ginzburg-Devonshire approach. *Physical Review B - Condensed Matter and Materials Physics*, 80(21):1–12.

Morozovska, A. N., Eliseev, E. A., Tagantsev, A. K., Bravina, S. L., Chen, L. Q., and Kalinin, S. V. (2011). Thermodynamics of electromechanically coupled mixed ionic-electronic conductors: Deformation potential, Vegard strains, and flexoelectric effect. *Physical Review B - Condensed Matter and Materials Physics*, 83(19):1–10.

Muller, V. M., Derjaguin, B. V., and Toporov, Y. P. (1983). On two methods of calculation of the force of sticking of an elastic sphere to a rigid plane. *Colloids and Surfaces*, 7(3):251–259.

Murrell, M. P., Welland, M. E., O'Shea, S. J., Wong, T. M., Barnes, J. R., McKinnon, A. W., Heyns, M., and Verhaverbeke, S. (1993). Spatially resolved electrical measurements of SiO_2 gate oxides using atomic force microscopy. *Applied Physics Letters*, 62(7):786–788.

Natali, M., Garoli, D., Rigato, V., and Romanato, F. (2011). Structural characterization of lead zirconate titanate thin films prepared on different electrodes and on silicon substrates. *Journal of Vacuum Science & Technology A: Vacuum, Surfaces, and Films*, 29(6):061505.

Nazeer, H., Abelmann, L., Tas, N. R., van Honschoten, J. W., Siekman, M. H., and Elwenspoek, M. C. (2009). Determination of Young's modulus of PZT and $Co_{80}Ni_{20}$ thin films by means of micromachined cantilevers. *Proc. Micromechanics and Microsystems Europe*, 172:278–281.

Nečas, D. and Klapetek, P. (2012). Gwyddion: An open-source software for SPM data analysis. *Central European Journal of Physics*, 10(1):181–188.

Nguyen, T. D., Mao, S., Yeh, Y. W., Purohit, P. K., and McAlpine, M. C. (2013). Nanoscale flexoelectricity. *Advanced Materials*, 25(7):946–974.

Oatley, C. W., Nixon, W. C., and Pease, R. F. (1966). Scanning Electron Microscopy. *Advances in Electronics and Electron Physics*, 21(C):181–247.

Okino, H., Sakamoto, J., and Yamamoto, T. (2003). Contact-resonance piezoresponse force microscope and its application to domain observation of Pb(Mg1/3Nb2/3)O3-PbTiO3 single crystals. *Japanese Journal of Applied Physics, Part 1: Regular Papers and Short Notes and Review Papers*, 42(9 B):6209–6213.

Pabst, G. W., Martin, L. W., Chu, Y. H., and Ramesh, R. (2007). Leakage mechanisms in $BiFeO_3$ thin films. *Applied Physics Letters*, 90(7):23–25.

Park, S. M., Wang, B., Das, S., Chae, S. C., Chung, J. S., Yoon, J. G., Chen, L. Q., Yang, S. M., and Noh, T. W. (2018). Selective control of multiple ferroelectric switching pathways using a trailing flexoelectric field. *Nature Nanotechnology*, 13(5):366–370.

Paruch, P., Giamarchi, T., Tybell, T., and Triscone, J. M. (2006). Nanoscale studies of domain wall motion in epitaxial ferroelectric thin films. *Journal of Applied Physics*, 100(5).

Paruch, P. and Triscone, J. M. (2006). High-temperature ferroelectric domain stability in epitaxial $PbZr_{0.2}Ti_{0.8}O_3$ thin films. *Applied Physics Letters*, 88(16):2004–2007.

Paruch, P., Tybell, T., and Triscone, J. M. (2001). Nanoscale control of ferroelectric polarization and domain size in epitaxial $Pb(Zr_{0.2}Ti_{0.8})O_3$ thin films. *Applied Physics Letters*, 79(4):530–532.

Peter, F. (2006). *Piezoresponse Force Microscopy and Surface Effects of Perovskite Ferroelectric Nanostructures*. PhD thesis.

Pintilie, L., Ghica, C., Teodorescu, C. M., Pintilie, I., Chirila, C., Pasuk, I., Trupina, L., Hrib, L., Boni, A. G., Georgiana Apostol, N., Abramiuc, L. E., Negrea, R., Stefan, M., and Ghica, D. (2015). Polarization induced self-doping in epitaxial $Pb(Zr_{0.20}Ti_{0.80})O_3$ thin films. *Scientific Reports*, 5:1–14.

Polla, D. L. and Francis, L. F. (1998). Processing and characterization of piezoelectric materials and integration into microelectromechanical systems. *Annual Review of Materials Science*, 28(1):563–597.

Preisach, F. (1935). Über die magnetische Nachwirkung. *Zeitschrift fur Physik*, 94(5-6):277–302.

Privratská, J. and Janovec, V. (1997). Pyromagnetic domain walls connecting antiferromagnetic non-ferroelastic magnetoelectric domains. *Ferroelectrics*, 204(1-4):321–331.

Prosandeev, S., Lisenkov, S., and Bellaiche, L. (2010). Kittel law in $BiFeO_3$ ultrathin films: A first-principles-based study. *Physical Review Letters*, 105(14):1–4.

Rabe, U. (2006). Atomic Force Acoustic Microscopy BT - Applied Scanning Probe Methods II: Scanning Probe Microscopy Techniques. In *Applied Scanning Probe Methods*, volume II, pages 37–90.

Rödel, J. and Li, J. F. (2018). Lead-free piezoceramics: Status and perspectives. *MRS Bulletin*, 43(8):576–580.

Rodriguez, B. J., Callahan, C., Kalinin, S. V., and Proksch, R. (2007a). Dual-frequency resonance-tracking atomic force microscopy. *Nanotechnology*, 18(47).

Rodriguez, B. J., Callahan, C., Kalinin, S. V., and Proksch, R. (2007b). Dual-frequency resonance-tracking atomic force microscopy. *Nanotechnology*, 18(47):475504.

Rodriguez, B. J., Gruverman, A., Kingon, A. I., Nemanich, R. J., and Cross, J. S. (2004). Three-dimensional high-resolution reconstruction of polarization in ferroelectric capacitors by piezoresponse force microscopy. *Journal of Applied Physics*, 95(4):1958–1962.

Roelofs, A., Pertsev, N. A., Waser, R., Schlaphof, F., Eng, L. M., Ganpule, C., Nagarajan, V., and Ramesh, R. (2002). Depolarizing-field-mediated 180° switching in ferroelectric thin films with 90° domains. *Applied Physics Letters*, 80(8):1424–1426.

Sanchez-Santolino, G., Tornos, J., Hernandez-Martin, D., Beltran, J. I., Munuera, C., Cabero, M., Perez-Muñoz, A., Ricote, J., Mompean, F., Garcia-Hernandez, M., Sefrioui, Z., Leon, C., Pennycook, S. J., Muñoz, M. C., Varela, M., and Santamaria, J. (2017). Resonant electron tunnelling assisted by charged domain walls in multiferroic tunnel junctions. *Nature Nanotechnology*, 12(7):655–662.

Schaab, J., Skjærvø, S. H., Krohns, S., Dai, X., Holtz, M. E., Cano, A., Lilienblum, M., Yan, Z., Bourret, E., Muller, D. A., Fiebig, M., Selbach, S. M., and Meier, D. (2018). Half wave rectifying domain walls. *Nature Nanotechnology*, 13(1028).

Schröder, M., Haußmann, A., Thiessen, A., Soergel, E., Woike, T., and Eng, L. M. (2012). Conducting domain walls in lithium niobate single crystals. *Advanced Functional Materials*.

Schrödinger, E. (1912). Studien über Kinetik der Dielektrika, den Schmelzpunkt, Pyro und Piezoelektrizität. *Akademie der Wissenschaften in Wien Mathem.-Naturw. Klasse 2a*, 121(November):1937–1972.

Schwarzkopf, J., Braun, D., Hanke, M., Uecker, R., and Schmidbauer, M. (2017). Strain engineering of ferroelectric domains in in $K_xNa_{1-x}NbO_3$ epitaxial layers. *Frontiers in Materials*, 4(August).

Scott, J. F., Kammerdiner, L., Parris, M., Traynor, S., Ottenbacher, V., Shawabkeh, A., and Oliver, W. F. (1988). Switching kinetics of lead zirconate titanate submicron thin-film memories. *Journal of Applied Physics*, 64(2):787–792.

Scott, J. F. and Paz De Araujo, C. A. (1989). Ferroelectric memories. *Science*, 246(4936):1400–1405.

Seidel, J., Maksymovych, P., Batra, Y., Katan, A., Yang, S. Y., He, Q., Baddorf, A. P., Kalinin, S. V., Yang, C. H., Yang, J. C., Chu, Y. H., Salje, E. K., Wormeester, H., Salmeron, M., and Ramesh, R. (2010). Domain wall conductivity in La-doped $BiFeO_3$. *Physical Review Letters*, 105(19):2010–2012.

Seidel, J., Martin, L. W., He, Q., Zhan, Q., Chu, Y. H., Rother, A., Hawkridge, M. E., Maksymovych, P., Yu, P., Gajek, M., Balke, N., Kalinin, S. V., Gemming, S., Wang, F., Catalan, G., Scott, J. F., Spaldin, N. A., Orenstein, J., and Ramesh, R. (2009). Conduction at domain walls in oxide multiferroics. *Nature Materials*.

Seol, D., Kim, B., and Kim, Y. (2017). Non-piezoelectric effects in piezoresponse force microscopy. *Current Applied Physics*, 17(5):661–674.

Seol, D., Park, S., Varenyk, O. V., Lee, S., Lee, H. N., Morozovska, A. N., and Kim, Y. (2016). Determination of ferroelectric contributions to electromechanical response by frequency dependent piezoresponse force microscopy. *Scientific Reports*, 6(April):1–10.

Shafer, P., Zavaliche, F., Chu, Y. H., Yang, P. L., Cruz, M. P., and Ramesh, R. (2007). Planar electrode piezoelectric force microscopy to study electric polarization switching in $BiFeO_3$. *Applied Physics Letters*, 90(20):65–68.

Sharma, P., Zhang, Q., Sando, D., Lei, C. H., Liu, Y., Li, J., Nagarajan, V., and Seidel, J. (2017). Nonvolatile ferroelectric domain wall memory. *Science Advances*, 3(6):1–9.

Shin, J., Nascimento, V. B., Geneste, G., Rundgren, J., Plummer, E. W., Dkhil, B., Kalinin, S. V., and Baddorf, A. P. (2009). Atomistic screening mechanism of ferroelectric surfaces: An in situ study of the polar phase in ultrathin $BaTiO_3$ films exposed to H_2O. *Nano Letters*, 9(11):3720–3725.

Shin, Y. H., Grinberg, I., Chen, I. W., and Rappe, A. M. (2007). Nucleation and growth mechanism of ferroelectric domain-wall motion. *Nature*, 449(7164):881–884.

Shur, V. Y. (2006). Domain engineering in lithium niobate and lithium tantalate: Domain wall motion. *Ferroelectrics*, 340(1 PART 1):3–16.

Shur, V. Y., Rumyantsev, E. L., Nikolaeva, E. V., Shishkin, E. I., Batchko, R. G., Miller, G. D., Fejer, M. M., and Byer, R. L. (2000). Regular ferroelectric domain array in lithium niobate crystals for nonlinear optic applications. *Ferroelectrics*, 236(1):129–144.

Skaliukh, A. (2018). About Mathematical Models of Irreversible Polarization Processes of a Ferroelectric and Ferroelastic Polycrystals. In *Ferroelectrics and Their Applications*. InTech.

Sluka, T., Bednyakov, P., Yudin, P., Crassous, A., and Tagantsev, A. (2016). Charged Domain Walls in Ferroelectrics. In *Springer Series in Materials Science*, volume 228, pages 103–138.

Sluka, T., Tagantsev, A. K., Damjanovic, D., Gureev, M., and Setter, N. (2012). Enhanced electromechanical response of ferroelectrics due to charged domain walls. *Nature Communications*, 3.

Soergel, E. (2011). Piezoresponse force microscopy (PFM). *Journal of Physics D: Applied Physics*, 44(46).

Strelcov, E., Kim, Y., Yang, J. C., Chu, Y. H., Yu, P., Lu, X., Jesse, S., and Kalinin, S. V. (2012). Role of measurement voltage on hysteresis loop shape in Piezoresponse Force Microscopy. *Applied Physics Letters*, 101(19).

Sutor, A., Rupitsch, S. J., and Lerch, R. (2010). A Preisach-based hysteresis model for magnetic and ferroelectric hysteresis. *Applied Physics A: Materials Science and Processing*, 100(2):425–430.

Tabor, D. (1977). Surface forces and surface interactions. *Journal of Colloid And Interface Science*, 58(1):2–13.

Thakre, A., Kumar, A., Song, H. C., Jeong, D. Y., and Ryu, J. (2019). Pyroelectric energy conversion and its applications—flexible energy harvesters and sensors. *Sensors (Switzerland)*, 19(9).

Thomas, L., Hayashi, M., Jiang, X., Moriya, R., Rettner, C., and Parkin, S. (2007). Resonant amplification of magnetic domain-wall motion by a train of current pulses. *Science*, 315(5818):1553–1556.

Tressler, J. F. (2008). Piezoelectric transducer designs for sonar applications. *Piezoelectric and Acoustic Materials for Transducer Applications*, pages 217–239.

Tsuchiya, K., Kitagawa, T., and Nakamachi, E. (2003). Development of RF magnetron sputtering method to fabricate PZT thin film actuator. *Precision Engineering*, 27(3):258–264.

Tybell, T., Paruch, P., Giamarchi, T., and Triscone, J. M. (2002). Domain Wall Creep in Epitaxial Ferroelectric [Formula presented] Thin Films. *Physical Review Letters*, 89(9):8–11.

Valasek, J. (1921). Piezo-electric and allied phenomena in Rochelle salt. *Physical Review*, 17(4):475–481.

Vasudevan, R. K., Matsumoto, Y., Cheng, X., Imai, A., Maruyama, S., Xin, H. L., Okatan, M. B., Jesse, S., Kalinin, S. V., and Nagarajan, V. (2014). Deterministic arbitrary switching of polarization in a ferroelectric thin film. *Nature Communications*, 5:1–8.

Vats, G., Ravikant, Schoenherr, P., Kumar, A., and Seidel, J. (2020). Low-Pressure Mechanical Switching of Ferroelectric Domains in $PbZr_{0.48}Ti_{0.52}O_3$. *Advanced Electronic Materials*, 6(10):1–7.

Vegard, L. (1921). Die Konstitution der Mischkristalle und die Raumfüllung der Atome. *Zeitschrift fur Physik*, 5(1):17–26.

Vernon-Parry, K. (2000). Scanning electron microscopy: an introduction. *III-Vs Review*, 13(4):40–44.

Vincent, L. and Soille, P. (1991). Watersheds in digital spaces: an efficient algorithm based on immersion simulations. *IEEE Transactions on Pattern Analysis and Machine Intelligence*, 13(6):583–598.

Vogel, A., Sarott, M. F., Campanini, M., Trassin, M., and Rossell, M. D. (2021). Monitoring Electrical Biasing of $Pb(Zr_{0.2}Ti_{0.8})O_3$ Ferroelectric Thin Films In Situ by DPC-STEM Imaging. *Materials*, 14(16):4749.

Wade, R. H. (1962). The determination of domain wall thickness in ferromagnetic films by electron microscopy. *Proceedings of the Physical Society*, 79(6):1237–1244.

Wang, B., Lu, H., Bark, C. W., Eom, C. B., Gruverman, A., and Chen, L. Q. (2020). Mechanically induced ferroelectric switching in $BaTiO_3$ thin films. *Acta Materialia*, 193:151–162.

Wang, Y., Zhao, H., Zhang, L., Chen, J., and Xing, X. (2017). $PbTiO_3$-based perovskite ferroelectric and multiferroic thin films. *Physical Chemistry Chemical Physics*, 19(27):17493–17515.

Warren, W. L., Dimos, D., Pike, G. E., Tuttle, B. A., Raymond, M. V., Ramesh, R., and Evans, J. T. (1995). Voltage shifts and imprint in ferroelectric capacitors. *Applied Physics Letters*, 67(1995):866.

Waser, R., Böttger, U., and Tiedke, S. (2005). *Polar Oxides: Properties, Characterization, and Imaging.*

Weeks, B. L., Vaughn, M. W., and Deyoreo, J. J. (2005). Direct imaging of meniscus formation in atomic force microscopy using environmental scanning electron microscopy. *Langmuir*, 21(18):8096–8098.

Werner, M., Hein, S., and Obermeier, E. (1993). Elastic properties of thin polycrystalline diamond films. *Diamond and Related Materials*, 2(5-7):939–942.

Whyte, J. R. and Gregg, J. M. (2015). A diode for ferroelectric domain-wall motion. *Nature Communications.*

Williams, D. B. and Carter, C. B. (2009). *Transmission Electron Microscopy.* Springer US, Boston, MA.

Xiong, W., Liu, J., Ma, L., Chen, W., and Zheng, Y. (2020). Tip-force-induced ultrafast polarization switching in ferroelectric thin film: A dynamical phase field simulation. *Journal of Applied Physics*, 128(1):0–12.

Xu, F., Trolier-McKinstry, S., Ren, W., Xu, B., Xie, Z. L., and Hemker, K. J. (2001). Domain wall motion and its contribution to the dielectric and piezoelectric properties of lead zirconate titanate films. *Journal of Applied Physics*, 89(2):1336–1348.

Xu, K., Sun, W., Shao, Y., Wei, F., Zhang, X., Wang, W., and Li, P. (2018). Recent development of PeakForce Tapping mode atomic force microscopy and its applications on nanoscience. *Nanotechnology Reviews*, 7(6):605–621.

Yanev, V., Rommel, M., Lemberger, M., Petersen, S., Amon, B., Erlbacher, T., Bauer, A. J., Ryssel, H., Paskaleva, A., Weinreich, W., Fachmann, C., Heitmann, J., and Schroeder, U. (2008). Tunneling atomic-force microscopy as a highly sensitive mapping tool for the characterization of film morphology in thin high-k dielectrics. *Applied Physics Letters*, 92(25):90–93.

Zheng, W., Qiu, X., Li, C., Zheng, C., Ge, X., Li, A., and Wu, D. (2014). Mechanical switching of ferroelectric polarization in ultrathin $BaTiO_3$ films: The effects of epitaxial strain. *Applied Physics Letters*, 104(4):1–6.

Zubko, P., Catalan, G., and Tagantsev, A. K. (2013). Flexoelectric Effect in Solids. *Annual Review of Materials Research*, 43(1):387–421.

FOLIO ADMINISTRATIF

THESE DE L'UNIVERSITE DE LYON OPEREE AU SEIN DE L'INSA LYON

NOM : GONZALEZ CASAL DATE de SOUTENANCE : 28/01/2022

Prénoms : Sergio

TITRE : Electromechanical control of ferroelectric domains in $Pb(Zr,Ti)O_3$ and $BiFeO_3$ thin films

NATURE : Doctorat Numéro d'ordre : AAAALYSEIXXXX

Ecole doctorale : EEA

Spécialité : Électronique, micro et nano-électronique, optique et laser

RESUME :
Les matériaux ferroélectriques montrent une polarisation spontanée qui peut être basculée par l'application d'un champ électrique. Cette polarisation à l'échelle nanométrique est localisée dans des régions appelées domaines ferroélectriques. Récemment, il a été rapporté que les domaines peuvent être contrôlés par une stimulation mécanique. Ce travail est centré sur l'étude des domaines au moyen de la microscopie à force atomique (AFM) et des techniques dérivées comme la microscopie à force piézoélectrique (PFM), qui permet l'application simultanée des stimulations électriques et mécaniques. Dans ce contexte, deux matériaux ferroélectriques différents ont été considéré: $Pb(Zr,Ti)O_3$ (PZT) et $BiFeO_3$ (BFO).
PZT a permis l'étude de la distribution des domaines hors du plan et des paramètres qui affectent leurs basculements électrique et mécanique, comme l'influence de la méthode de synthèse sur les propriétés ferroélectriques d'un matériau de même composition, ainsi que de l'atmosphère de mesure (humidité) et de l'épaisseur de l'échantillon. Nos résultats montrent qu'il est possible de contrôler la force nécessaire pour faire basculer mécaniquement les domaines. En parallèle, BFO a permis l'étude de la polarisation dans le plan et sa manipulation avec la composante du champ électrique localisée dans le plan de l'échantillon. Nous avons mis en évidence par la spectroscopie à commutation PFM (SS-PFM) un phénomène de contamination de la pointe qui rend l'interprétation des mesures difficile.
Puisque l'AFM et la PFM sont des techniques de surface, ce travail a été complété par des analyses structurales des échantillons obtenus par des techniques comme la diffraction des rayons X (x-ray diffraction, XRD), la microscopie électronique en transmission à balayage (scanning transmission electron microscopy, STEM) et la spectrométrie de rétrodiffusion Rutherford (Rutherford backscattering spectrometry, RBS).

MOTS-CLÉS : Ferroélectrique, AFM, PFM, Électromécanique, Domaines, $PbZr_{0.2}Ti_{0.8}O_3$, $BiFeO_3$

Laboratoire (s) de recherche : Institut des Nanotechnologies de Lyon (INL, UMR 5270), Matériaux : Ingénierie et Sciences (MATEIS, UMR 5510)

Directeur de thèse: Brice GAUTIER

Composition du jury : Patrycja PARUCH, Nathalie LEMEE, Silvana MERCONE, Sylvia MATZEN, Łukasz BOROWIK, Damien DELERUYELLE et Ingrid CAÑERO-INFANTE